



UNIVERSITÄT
DES
SAARLANDES

Derivatization and design of transition metal oxides and sulfides for advanced and sustainable battery technology

Dissertation
zur Erlangung des Grades
der Doktorin der Ingenieurwissenschaften
der Naturwissenschaftlich-Technischen Fakultät
der Universität des Saarlandes

vorgelegt von

BEHNOOSH BORNAMEHR

Saarbrücken, Aug 2023

Tag des Kolloquiums: 1. Dezember 2023
Dekan: Prof. Dr. Ludger Santen
Berichterstattung: Prof. Dr. Volker Presser
Priv.-Doz. Dr.-Ing. Guido Falk
Vorsitzende Person: Priv.-Doz. Dr. André Schäfer
Akad. Mitarbeiter*In: Prof. Dr. mont. Christian Motz

ACKNOWLEDGMENT

This work has been carried out from July 2021 to July 2023 at the INM – Leibniz Institute for New Materials, Saarbrücken. The work has been made possible through funding from Deutsche Forschung Gemeinschaft (DFG) under project number 452180147. I thank the board of INM and the Leibniz Association for supporting me in my career development.

I gratefully acknowledge the support of my supervisor Prof. Volker Presser, head of the INM Energy Materials Group for his great care, understanding, and scientific insight. I have been privileged to have him as my mentor and my Ph.D. supervisor and be able to perform research in collaboration with many other great scientists and researchers as a result. In parallel, I thank Prof. Markus Gallei, head of the polymer group at the University of Saarland for being my second Ph.D. supervisor and supporting me through scientific discussions, and providing me with methods and materials to explore my research topic.

I thank the employees at INM, as well as at the university of Saarland, for the support they provided to me as a Ph.D. student so I can bring my Ph.D. journey to its destination. For their great support among many others, I fail not to mention the following group members: Dr. Samantha Husmann, Dr. Emmanuel Pamete Yambou, Stefanie Arnold, Mohammad Torkamanzadeh, external collaborators: Dr. Michael Elsässer at the University of Salzburg, Dr. Jeffry Urban and Dr. Chaochao Dun at Berkeley National Laboratory, and Dr. Aldo Zarbin at the University of Parana. INM colleagues: Dr. Marcus Koch, Aude Hättich, Robert Drumm, and Andrea Jung. Master students Amila Beganovic, and Hiba El Gaidi. External employees at Saarland University Dr. Theo Jäger, Dr. Flavio Soldera.

TABLE OF CONTENT

1	<i>Introduction and Motivation</i>	1
2	<i>Theoretical Background</i>	3
2.1	History of energy storage	3
2.2	Li-ion battery principles	4
2.2.1	Storage mechanism	5
2.2.2	Development	9
2.3	Present challenges for next-generation batteries	10
2.3.1	Energy	11
2.3.2	Power	12
2.3.3	Cost	13
2.3.4	Safety	14
2.3.5	Sustainability	16
2.4	Advanced materials for next-generation batteries	19
2.4.1	Chemistry: Derivatization	19
2.4.2	Morphology: Design	21
2.4.3	Improvement beyond derivatization and design	25
3	<i>Approach and overview</i>	27
4	<i>Results and discussion</i>	30
4.1	Prussian blue and its analogues as functional template materials: control of derived structure compositions and morphologies	30
4.2	Mixed Cu–Fe sulfide derived from polydopamine-coated Prussian blue analogue as a lithium-ion battery electrode.....	30
4.3	Surfactant-stabilization of vanadium iron oxide derived from Prussian blue analog for lithium-ion battery electrodes	30
4.4	Mechanically stable, binder-free, and free-standing vanadium trioxide/carbon hybrid fiber electrodes for lithium-ion batteries.....	30
4.5	Recent advances in nanoengineering of electrode-electrolyte interfaces to realize high-performance Li-ion batteries	30
5	<i>Conclusion and outlook</i>	125
6	<i>Abbreviations</i>	129
7	<i>References</i>	130

ZUSAMMENFASSUNG

Diese Dissertation befasst sich mit der Entwicklung elektrochemischer Energiespeicher, die die Leistung bestehender Lithium-Ionen-Batterien übertreffen. Die Forschung untersucht das Design und die Modifikation von Metalloxiden und -sulfiden, um die elektrochemische Leistung kommerzieller Batterieelektroden zu verbessern, und stellt die damit verbundenen Herausforderungen dar. Durch den Einsatz spezifischer Designstrategien und Derivatisierungsmethoden werden neuartige Materialien mit einzigartigen Eigenschaften synthetisiert, die sich von denen in kommerziellen Batterien unterscheiden.

Für jedes untersuchte Material wird die Beziehung zwischen seiner elektrochemischen Leistung und verschiedenen anderen Materialeigenschaften untersucht, um bestehende Einschränkungen zu beseitigen. Im Falle der selbsttragenden Fasern wird der Einfluss der mechanischen Flexibilität auf die elektrochemischen Eigenschaften analysiert. Bei den Konversionsmaterialien wird der nachteilige Shuttle-Effekt oder das Ätzen der Elektroden durch das Aufbringen einer stabilen Beschichtung zum Schutz der aktiven Komponente vor Degradation abgeschwächt. Die Arbeit zielt darauf ab, pH-neutrale Synthesen und Niedertemperatur-Derivatisierung zu verwenden, um die Auswirkungen von aggressiven Komponenten und energiereichen Verfahren zu verringern, und stellt die Herausforderungen dar, die sich daraus ergeben.

Darüber hinaus werden in dieser Arbeit ergänzende Ansätze zur Verbesserung der Grenzfläche zwischen Elektrode und Elektrolyt nach Modifizierung des Elektrodenmaterials durch Werkstofftechnik untersucht. Diese Strategien werden eingehend untersucht und als mögliche Lösungen zur Verbesserung der Gesamtleistung der Energiespeicher vorgestellt.

ABSTRACT

This Ph.D. thesis focuses on developing electrochemical energy storage devices that outperform existing lithium-ion batteries. The research investigates the design and modification of metal oxides and sulfides to enhance the electrochemical performance of commercial battery electrodes and presents the challenges met. By employing specific design strategies and derivatization methods, novel materials with unique properties are synthesized, distinct from those found in commercial batteries.

For each material studied, the thesis examines the relationship between its electrochemical performance and various other material properties to address existing limitations. In the case of self-standing fibers, the influence of mechanical flexibility on electrochemical properties is analyzed. Similarly, for the conversion-type materials, the detrimental shuttling effect or electrode etching is mitigated by applying a stable coating to protect the active component from degradation. In parallel, this thesis aims to use pH-neutral syntheses and low-temperature derivatization to reduce the effect of harsh components and high-energy procedures and presents the challenges that arise from this.

Additionally, this work explores complementary approaches to enhance the interface between the electrode and electrolyte after modifying the electrode material through materials engineering. These strategies are thoroughly investigated and presented as potential solutions to improve the overall performance of energy storage devices.

1 INTRODUCTION AND MOTIVATION

Energy storage is crucial to effectively achieve sustainable goals and to reduce our global carbon footprint since a large share of carbon emissions is caused by using fossil fuels for energy generation, and a transition to renewable energy sources demands an effective energy storage infrastructure. **Figure 1** shows the global carbon dioxide equivalent emissions by sector. The energy sector accounts for 73.2% of the emissions and is the largest contributor. Under this sector, a large share of emissions stems from fossil fuel-based electricity production or direct fossil fuel consumption for transport.[1] To decrease the emissions, the electricity that is mainly generated from fossil fuels must shift to renewable energy sources. The same applies to the transport sector, which is transitioning from internal combustion to electric vehicles (EVs). While renewable energy is free of charge, the challenge of harnessing and accessing this energy at times of need remains an expensive hurdle.

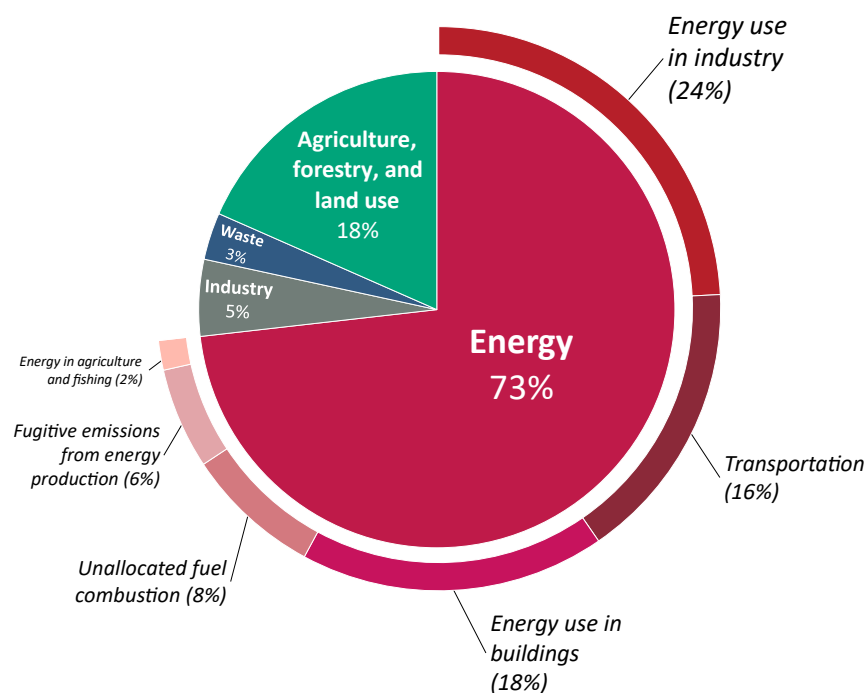


Figure 1 Equivalent CO₂ global emissions by sector in 2016. [1]

To solve this challenge, electrochemical energy storage has become the leading enabler among different energy storage systems.[2, 3] Due to their state of commercial availability, high efficiency, and high energy density, Li-ion batteries are explored to replace most applications that require energy storage. From hearing aids to large trucks, we use this battery

type to run and answer our daily needs. **Figure 2** shows the growth of Li-ion battery use in different applications from 2015 to 2030 (estimated).[2]

More than 60% of the costs for this advanced technology lie in the raw materials, mainly to produce the electrodes.[4] While the demand for Li-ion batteries increases yearly, the raw materials supply chain is challenged by the COVID pandemic and the Ukraine-Russia war, further increasing raw materials cost for Li-ion batteries, which are all critical for the European union (EU).[5] However, to increase sustainability in materials, societal and environmental baselines must be addressed in addition to the economic baseline. [6] Therefore, research and development of new electrode materials that improve these baselines are central columns to making the energy transition bridge sustainable. The key ingredients in the path toward new materials are advanced design and derivatization methods to enable next-generation Li-ion batteries. This thesis introduces different methods in detail to design rational morphologies such as self-standing fibers and core shells for new hybrids of metal oxides and sulfides. It then explains the additional steps after design and derivatization to increase the electrochemical performance of battery materials.

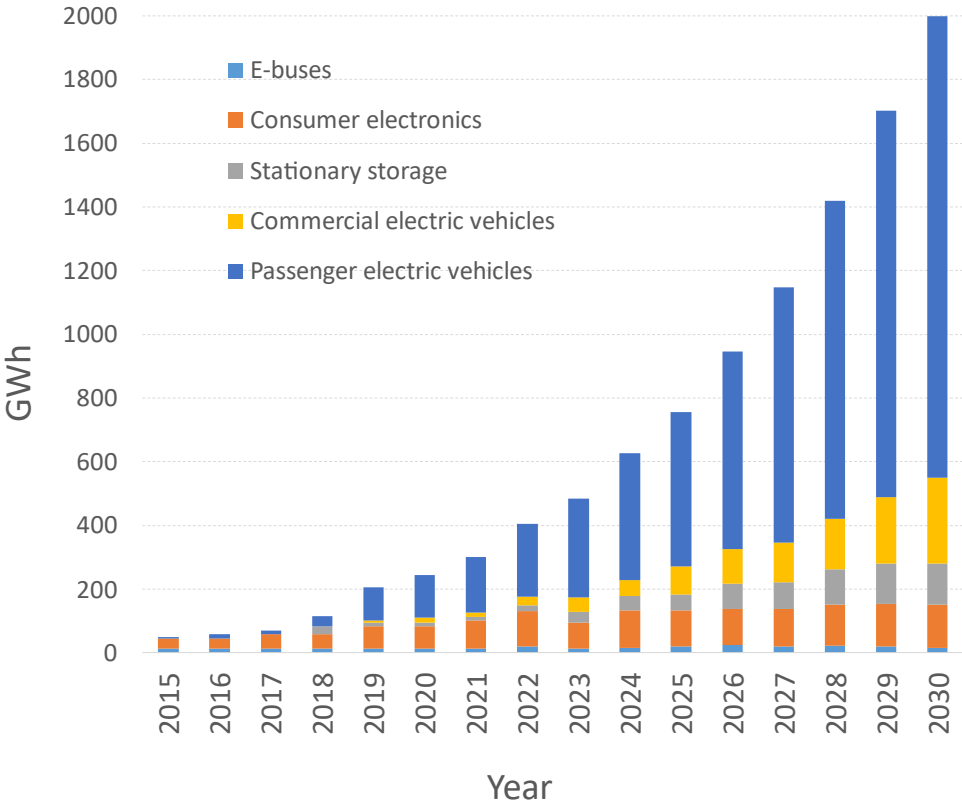


Figure 2 Growth of Li-ion batteries in gigawatt hours for different applications.[2]

2 THEORETICAL BACKGROUND

2.1 History of energy storage

The history of energy storage encompasses a journey of technological advancements spanning several centuries.[7] The story begins in 1800 with the invention of the Voltaic Pile by the Italian physicist Alessandro Volta. [8] Consisting of alternating layers of zinc and copper separated by cardboard soaked in an electrolyte solution, the Voltaic Pile was the world's first practical battery. [9] It produced a steady electric current, providing a reliable source of energy. Volta's groundbreaking achievement laid the foundation for further experimentation and research into battery technologies. In the early 19th century, the field of energy storage grew following several inventions. In 1859, French scientist Gaston Planté developed the lead-acid battery, which marked a significant milestone in the history of batteries. [10] The lead-acid battery was the first rechargeable battery and found widespread use in various applications, including telegraphy, early electric lighting, and later, in the automotive industry. [11, 12] Due to their reliability and scalability, lead-acid batteries found prominence and enduring legacy. [13]

The late 19th and early 20th centuries witnessed the emergence of several battery chemistries, each with unique characteristics and applications. In 1881, French inventor Camille Alphonse Faure further improved the lead-acid battery by introducing a pasted plate design, enhancing its capacity and performance. This development paved the way for the lead-acid battery's widespread adoption in automobiles, providing a source of power for the rapidly growing transportation sector. [14] Around the same time, the nickel-cadmium (NiCd) battery, invented by Swedish engineer Waldemar Jungner in 1899, gained prominence. The NiCd battery offered higher energy density and longer cycle life compared to lead-acid batteries. It became a popular choice for portable applications and was widely used in early portable radios and flashlights. [15, 16] However, the cadmium used in NiCd batteries raised environmental concerns due to its toxicity[17], leading to a shift towards alternative chemistries in the future.

As the world entered the digital age, a new era of portable electronic devices emerged, necessitating smaller, lighter, and more powerful energy storage solutions. This demand led to the development of the first commercial lithium battery in the 1970s. Several other

rechargeable battery technologies were developed, especially targeting stationary applications such as vanadium-flow and sodium-sulfur batteries. [18-20] These batteries, however, had a large volume and were not tailored for use in portable devices. Yet, it wasn't until 1991 that Sony Corporation introduced the first practical rechargeable lithium-ion battery. The Li-ion battery was a significant breakthrough, offering higher energy densities, longer lifespans, and reduced self-discharge rates compared to previous battery technologies. Its lightweight and compact design made it ideal for portable electronics such as laptops, smartphones, and digital cameras. [21]

The success of Li-ion batteries revolutionized energy storage and facilitated the widespread adoption of EVs and renewable energy systems. [2, 5] With increasing global CO₂ emissions and its future risks [22], countries need to transition their energy source from fossil fuels to renewables across all sectors.[23] While this is the long-term solution to reducing CO₂ emissions, it fully alters the energy storage infrastructure [24] and requires large investments.[25] Fossil fuels hold a global 61.3% share as the source of electricity production [26] and an 80% share as the primary energy source for consumption.[27] In contrast to fossil fuels, the amount of renewable energy cannot be predicted or managed at all times due to intermittency and requires a storage system to ensure a stable supply for consumers, especially during peak demand periods. A shortage of power for short periods in the industry can drastically affect a country's gross domestic product, especially those reliant on manufacturing. This was, for example, a €600 million loss in Germany per one hour of blackout in 2013. [28, 29] Li-ion batteries play a pivotal role in driving the global transition toward sustainable energy sources. The ability to store energy efficiently and deliver it when needed is instrumental in enabling the integration of renewable energy technologies such as solar and wind into the grid.

2.2 Li-ion battery principles

The concept of the Li-ion battery was developed and studied in the 1970s and 1980s based on the movement of Li-ion as the working ion to charge and discharge the battery (rocking chair concept), and several studies enabled them to become stable and usable in room temperature.[30] This battery technology was commercialized in 1991 and steadily grew in the market, while the price fell by more than tenfold with further development and extended use until this day.[31] **Figure 3** shows the schematic of a Li-ion cell, its main components, and

major developments that enabled Li-ion battery commercialization.[30] The inventors of the Li-ion battery, John Goodenough, Stanley Whittingham, and Akira Yoshino were awarded the Nobel Prize in Chemistry in 2019 for their contribution to the development of the Li-ion battery.[32] Similar battery technologies, such as Li-sulfur, Li-air, all solid-state Li-ion, and post-Li batteries, were further studied and have been under constant development.[21, 33]

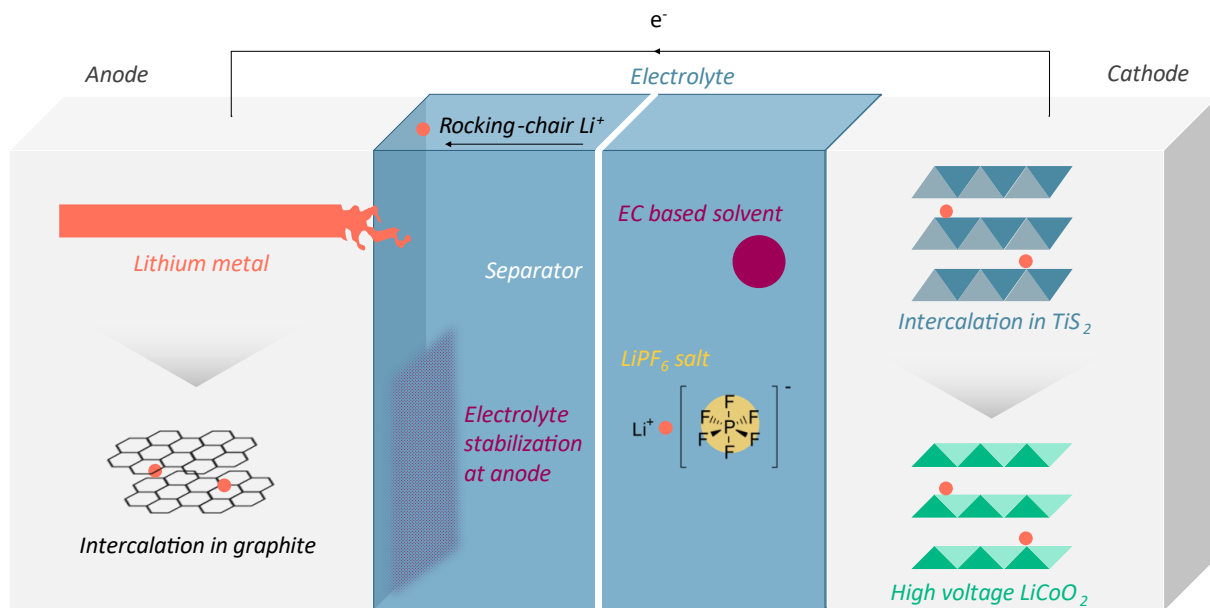


Figure 3 Main components of a Li-ion cell and discovered concepts used to achieve stable performance for commercial Li-ion batteries. Lithium and electron flow are shown for the charge step. Adapted from [30].

2.2.1 Storage mechanism

To understand the storage mechanism in Li-ion batteries, each cycle can be broken down into the charge and discharge steps. The framework of the conventional Li-ion cell is made of two electrodes immersed in an organic electrolyte with dissolved lithium salt (LiPF₆).[34] These electrodes are separated by a porous polymeric membrane that conducts ions but keeps the electrodes away from each other. In the case of direct contact between the electrodes, the cell is internally short-circuited and releases a high amount of energy.[35]

When the cell is charging, it follows the mechanism of an electrolytic cell, and during discharge, it acts as a galvanic cell.[36] Therefore, the oxidation and reduction at the electrodes are swapped in charge and discharge. However, the discharge nomenclature is

applied to batteries in general, and the electrode operating at higher potential is referred to as the cathode [37] (usually a mixed metal oxide), and the electrode operating at lower potential as the anode (usually a conductive carbon powder).[38]

The specific capacity of anode and cathode material is the charge that can be stored per unit mass for each material. This is expressed in Ah/g and determined by the number of redox processes at a different potential. Every change in the material's oxidation state causes the release or uptake of an electron. A Li⁺ ion is released or uptaken in parallel to keep the charge neutrality. The theoretical specific capacity can be calculated according to **Equation 1**, where n is the number of exchanged electrons (or lithium ions), F is the Faraday constant, and M is the molar mass of the electrode material.[35]

$$\textit{Theoretical capacity per gram} = \frac{n \times F}{M} \qquad \textbf{Equation 1}$$

After assembling, the cell has a voltage equal to the potential difference between the electrodes.[39] For simplification, we take the primary chemistry of the commercial cell with lithium cobalt oxide (LCO) as the cathode material and graphite as the anode material. With LCO redox potential at 4-5 V vs. Li/Li⁺ and graphite at ~0.1 V vs. Li/Li⁺, this chemistry offers a cell with a working voltage of 3.0-4.2 V, resulting in a nominal voltage of 3.6 V.[40] Since the cell energy results from the cell voltage multiplied by the capacity, the anode and cathode are chosen based on their potential to result in a high cell voltage and increase the energy; however, this voltage is limited by the electrochemical stability of the used electrolyte or other components such as the current collector and the binder. [41]

The common carbonate-based electrolyte used in commercial Li-ion batteries is made of a mixture of the non-linear ethylene carbonate (EC) and at least one linear carbonate such as dimethyl carbonate (DMC), diethyl carbonate (DEC), and ethyl methyl carbonate (EMC) that lower the melting point of EC (36 C) [42] to be used at room temperature and simultaneously withstand about 4 V potential window from 1.0 V to 4.7 V vs. Li/Li⁺. [30] This stability window is determined by the lowest unoccupied molecular orbital (LUMO) and the highest occupied molecular orbital (HOMO). When the cell is assembled, the LUMO must be higher than the electrochemical potential of the anode (μ_a), and HOMO needs to be lower than the electrochemical potential of the cathode (μ_c) to remain stable.[41]

Graphite has a Li-intercalation potential of ~ 0.1 V vs. Li/Li^+ , while the stability range of the electrolyte starts from 1 V vs. Li/Li^+ . This potential difference causes the reduction and decomposition of electrolytes at the anode surface and results in the formation of the solid electrolyte interphase (SEI). Electrolyte oxidation can also happen at the cathode interface to form cathode electrolyte interphase (CEI) if the cathode potential is higher than the electrolyte HOMO potential [43] These interphases act as a bridge in the electrode-electrolyte potential difference, protecting the electrolyte from further reactions with the electrodes, and enable stable cycling of the battery. As a result, the potential window of electrolyte E_g widens to V_o with the formation of stable SEI and CEI [34, 44] (Figure 4).

When the cell is charged, reduction at the anode and oxidation at the cathode occur. At the reduction sites, lithium ions in the electrolyte are absorbed in the anode and intercalated in the graphite layers. At the same time, intercalated lithium in the LCO layers is released in the electrolyte.[41] Therefore, in Li-ion batteries, electrode reduction is equal to lithiation or lithium introduction, and oxidation is equal to delithiation or lithium removal.

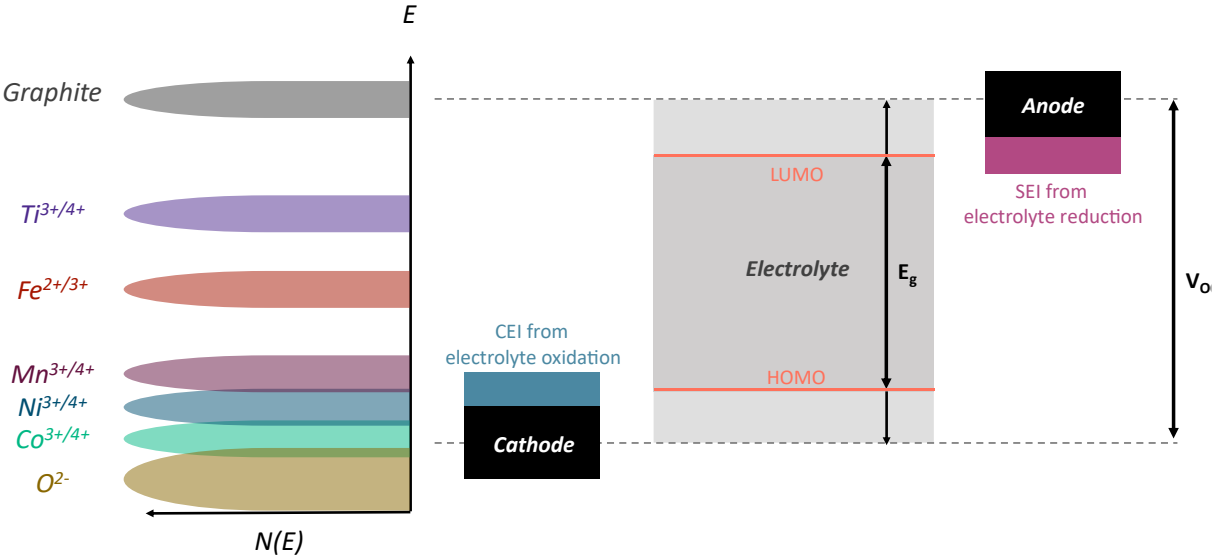


Figure 4 Fermi energies of some cathode and anode redox pairs and their effect on widening the electrolyte potential window. If the electrolyte potential window does not overlap with the electrodes, the anode reduces the electrolyte and forms SEI at the anode/electrolyte interface, and the cathode oxidizes the electrolyte and produces CEI at the cathode/electrolyte interface. Adapted from [44].

Lithiation and delithiation in batteries are primarily performed by Faradaic processes. That means the charge is stored when the active material undergoes chemical redox processes.[45] For example, in LCO, the cobalt atom is in the Co^{3+} oxidation state, which is oxidized to Co^{4+} during charging, and through this oxidation, a Li-ion is released from the LCO lattice. This is the major difference compared to other electrochemical storage systems, such as electrical double-layer capacitors that are governed by electrostatic (non-Faradaic) ion electrosorption.[20, 46] These redox processes determine the electrode's potential and are studied in depth for different materials.[41] Voltammograms and charge-discharge curves are usually recorded to observe the redox processes and their potential.[37] **Figure 5** shows the cyclic voltammogram and galvanostatic charge-discharge curve of LCO during charge and discharge and how these two electrochemical plots are connected.

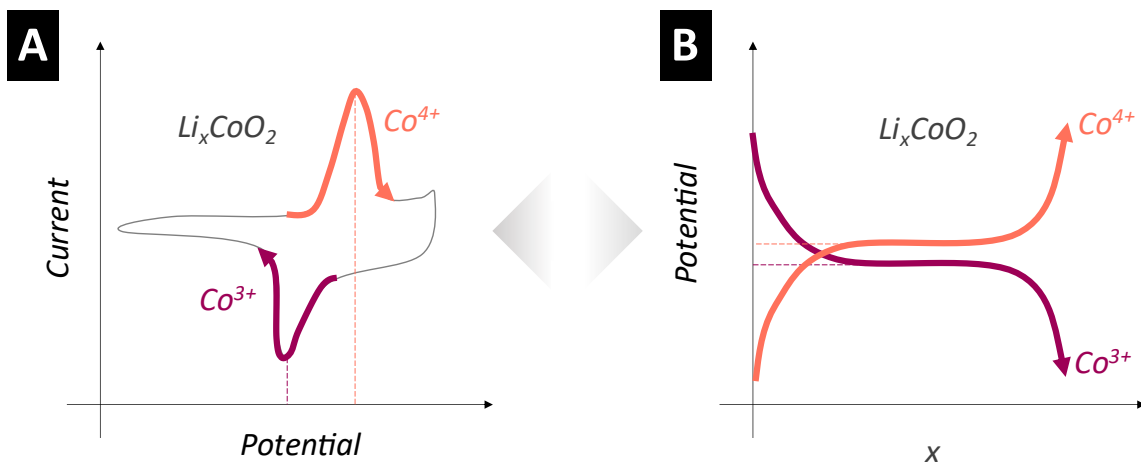


Figure 5 Cyclic voltammogram of LCO with the redox peaks for $\text{Co}^{4+}/\text{Co}^{3+}$ during charge and discharge (A) and galvanostatic charge-discharge curves for LCO (B). Sharp redox peaks in the voltammogram translate to elongated plateaus in charge-discharge curves and indicate Faradaic energy storage via redox reactions.

In addition to the active material where the reduction and oxidation processes occur, two other components, namely the conductive carbon additive and the binder, are used in the electrode.[47, 48] The role of the carbon additive is to increase the conductivity of the active material. At the same time, the binder, often polyvinylidene fluoride (PVdF), keeps the carbon additive and active material particles in contact, as well as adhesion to the current collector, and ensures electron pathways are maintained during cycling.[49] Since binder and carbon

additives are usually inactive, they are kept at a minimum amount, so the highest possible capacity is achieved per unit mass of the electrode.[50]

Regarding the lithiation mechanism, both LCO and graphite have a layered structure and intercalate lithium ions between these layers.[51] Insertion-type materials are also used in present battery cathodes that work similarly to the intercalation materials but insert the lithium in their interstitial lattice sites. Two main groups are the spinel and olivine materials with lithium manganese oxide (LMO) and lithium iron phosphate (LFP) as examples.[21]

2.2.2 Development

Most of the history of Li-ion battery development is focused on electrode research, as they directly determine the cell capacity and working voltage.[21] Lithium metal was used as the anode in the early batteries due to its high capacity (3,860 mAh/g) and low redox pair potential (-3.04 V vs. the standard hydrogen electrode (SHE) equal to 0.0 V vs. Li/Li⁺) [52]. However, lithium ions may not homogeneously plate during charging as a layer but rather form dendrites.[53, 54] These dendrites offer shorter diffusion paths when grown towards the cathode. Therefore, after many cycles, they constantly grow until they can finally pass through the separator, reach the cathode, and short the cell from the inside.[55, 56]

For the cathode, the first intercalation material of TiS₂ was reported by Whittingham, which was able to be reversibly charged and discharged against lithium metal anode [57] and commercialized by Exxon in the late 1970s. [40] The cell voltage was low due to the redox pairs of titanium and sulfur, but the structure and cycling performance inspired researchers to further work on intercalation cathode materials. Mizushima et al. [58] reported LCO with a layered structure that could reversibly be lithiated and delithiated at room temperature without undergoing bond breakage and reformation while simultaneously offering potentials higher than 4.0 V vs. Li/Li⁺. LCO also had lithium atoms in the molecule, eliminating the need for a metallic lithium anode.[59] This improved the safety and after further studies in the 1980s, was successfully used versus a graphite anode in the first generation of commercialized Li-ion batteries by SONY in 1991.[35]

LCO can release up to 50% of its lithium ions, translating to half of its theoretical capacity of 274 mAh/g. For a full delithiation, voltages up to 5 V vs. Li/Li⁺ were needed, making electrolyte and LCO unstable. In addition, cobalt is not abundant and, therefore high in cost compared to

other rock-forming transition metals.[60] The commercial LCO chemistry was therefore tailored over time by introducing cheaper or more stable transition metals such as Ni, Al, and Mn into the structure to reduce the price and increase the capacity. This resulted in a variety of cathode chemistries in the market.[61] Among commercialized chemistries, lithium nickel cobalt aluminum oxide $\text{LiNi}_{0.8}\text{Co}_{0.15}\text{Al}_{0.05}\text{O}_2$ (NCA), lithium nickel manganese oxide $\text{Li}(\text{Ni}_{0.5}\text{Mn}_{0.5})\text{O}_2$ (NMO), lithium nickel manganese cobalt oxide (NMC) in different transition metal ratios can be named.[62] Other commercialized insertion-type materials in spinel structure, including lithium manganese oxide $\text{Li}_x\text{Mn}_2\text{O}_4$ (LMO) [63] and in olivine structure lithium iron phosphate LiFePO_4 (LFP) are noteworthy. Each of these chemistries has its certain shortcoming and advantages, making them desired in different applications. **Table 1** shows a summary of these chemistries, their energy density, and their working voltage as the decisive parameter for their applications.

Table 1 Common chemistries of commercialized Li-ion batteries and their specifications.[64]

Symbol	Cathode	Anode	Cell voltage (V)	Specific energy (Wh/kg)
NCA	LiNiCoAlO_2	Graphite	3.65	130
NMC	LiNiCoCoO_2	Graphite	3.8-4.0	170
LFP	LiFePO_4	$\text{Li}_4\text{Ti}_5\text{O}_{12}$	2.3-2.5	100
LMO	LiMnO_4	Graphite	4.0	120
LCO	LiCoO_2	Graphite	3.7-3.9	140

2.3 Present challenges for next-generation batteries

The state-of-the-art Li-ion batteries are usually compared based on the electrodes used in the cell and known as the different cell chemistries.[65] This assessment is done in a variety of performance parameters depending on the battery application, such as the electrochemical performance at different temperatures and potential ranges, their self-discharge, their cost of production, their safety during service, and environmental impacts such as recyclability, raw material toxicity, and energy needed for production. To improve these key parameter indicators, three main strategies are followed. First, tailoring the present components such as mixing silicon with graphite to increase the capacity. Second, replacing the components for example non-flammable aqueous electrolytes instead of organic carbonate-based ones,[66]

or using cheaper cathodes to decrease the cell cost such as LFP instead of NMC.[67] And third, developing post-lithium technologies, such as sodium-ion batteries. [68]

To compare these systems, five major parameters of energy, power, cost, safety, and sustainability are relevant in every technology and application and therefore discussed further in detail.

2.3.1 Energy

The cell's energy can be measured per unit mass (specific energy; Wh/kg) or volume (energy density; Wh/L), depending on the application and requirements.[69] This is achieved by multiplying the achievable cell capacity and working voltage window and the most critical parameter for portable electronic devices as larger energy means more charge stored in the battery and less frequent charging.[70]

Due to lithium ions' lightweight and small size, a high specific energy and energy density compared to other battery types can be reached at the cell level.[65, 71] The battery energy density and specific energy decrease through the scale-up due to the addition of several components such as the separator, current collectors, and cooling system from the cell level to the module level that add to the mass and volume without contributing to the lithium storage capacity. Therefore, energy is calculated in each step depending on the external components in the battery. **Figure 6** shows the steps in the scale-up of the electrode material to a pack for two chemistries of graphite || NCA and graphite-SiO_x || LFP parallel to their energy density and specific energy changes, showing that the theoretical active material energy is reduced by 5- to 10-fold when it reaches the pack level.[67]

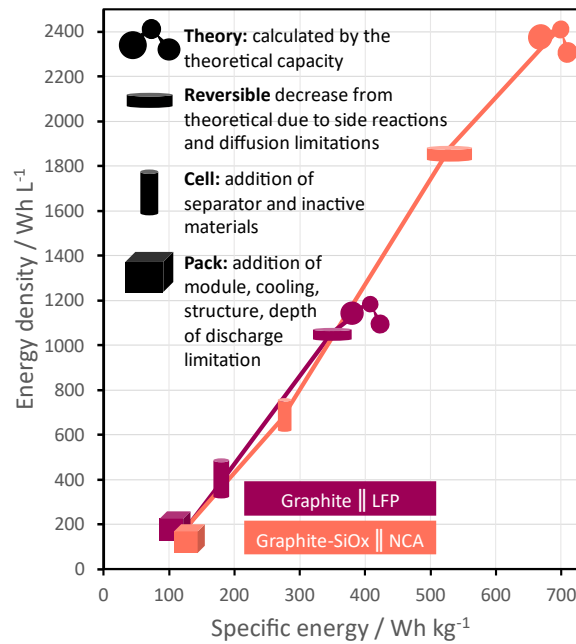


Figure 6 Energy density and specific energy change from theoretical achievable to pack level for graphite || NCA and graphite-SiO_x || LFP chemistries. Adapted from [67].

2.3.2 Power

Like energy density, power can be measured per mass or volume unit, resulting in specific power (W/kg) and power density (W/L), respectively. Power is used to measure how fast the stored energy can be inserted or withdrawn from the battery and is of significant importance for electric mobility since long charging times cause range anxiety in the consumer.[72] To mitigate this, various strategies from material to pack level are used to offer fast charging times.

At the cell level, conductivity (active material, electrolyte, and SEI), lithium dissolution in the electrolyte, and electrode porosity and tortuosity [73] play a direct role in quick lithium ion transfer and effective charge and discharge.[74] A battery can be forced to charge at higher rates, but if the material and electrolyte do not conduct the current, instead of storing lithium ions Ohmic polarization at the electrode takes place, resulting in lower energy in the battery and lithium plating on the anode.[75] **Figure 7** shows the path of lithium ions during cycling and material properties at the cell level that aid lithium transfer and therefore increase achievable power.[72]

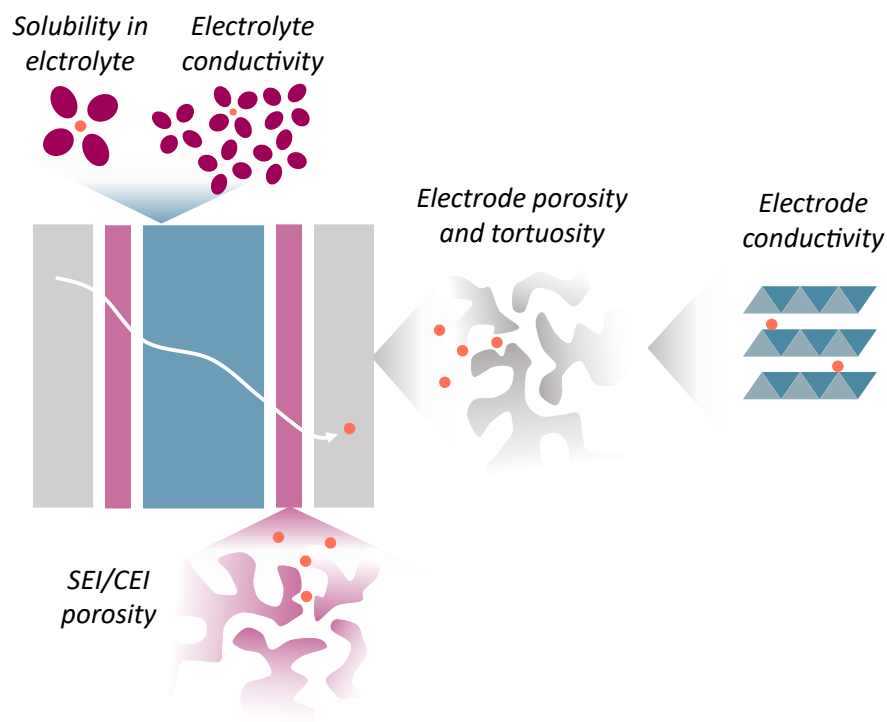


Figure 7 Path of lithium ions between the electrodes during cycling and the effect of cell components on lithium ion transfer. Adapted from [72].

2.3.3 Cost

Since the commercialization of Li-ion batteries, the price per kilowatt hour has decreased by 97% for different cell types.[76] This price decline can be broken down into battery component costs, including electrode materials, electrolytes, and inactive components. **Figure 8A** shows the price decline for different cell types in the last decade, and **Figure 8B** shows the share of different battery components in cost decline for the 1995-2000 period compared to 2010-2015.[31] These graphs indicate that all parts of the battery have been subject to cost decline and that the cathode material is the most cost-intensive component of battery production. However, while the manufacturing costs fall steadily as the technology becomes more mature, the raw materials costs are highly volatile depending on the supply chain.[60, 77]

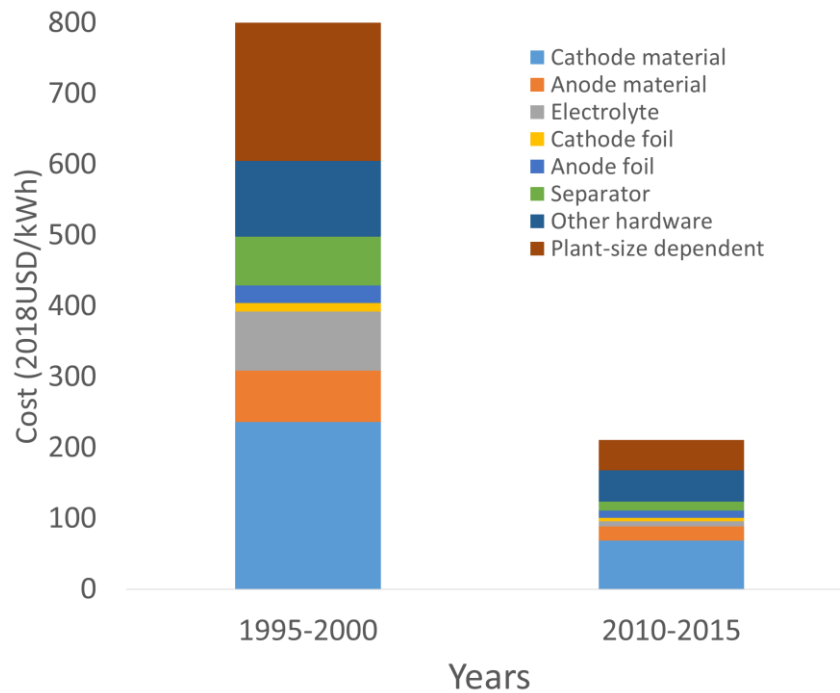


Figure 8 Cost breakdown of a battery cell into its hardware components and the comparison for 1995-2000 and 2010-2015.[31]

Still, the main contributor to the cost decline for Li-ion batteries is the reduced cost of the cathode materials, with over 20% contribution due to charge capacity increase per volume and over 15% due to lower cathode material price.[31] This shows the improvement in the cathode material in terms of higher performance and lower costs plays the largest role in the battery cost decline. Estimation studies show slight volatility in the main raw materials price used in these batteries namely lithium, graphite, cobalt, nickel, and manganese can hinder the battery price decline in the following years. [60]

Most of these raw materials are on the European Commission’s list of critical minerals and metals [78, 79], and in addition to their criticality, their volatile costs with increasing demand accelerate research and development of new electrode chemistries for present Li-ion batteries and new technologies such as post-Li-ion technologies.

2.3.4 Safety

The safety hazards posed by using Li-ion batteries can be divided into three stages of battery life: Before application, during service, and after the end of life. Certainly, the safety considerations also strongly depend on the target application (electric vehicles vs. mobile

computing, for example). The hazards before and after the application are mainly connected to the environmental impact during mining or waste disposal and will be discussed under their sustainability issue (chapter 2.3.4).[80] Here the focus is put on safety hazards during the utilization of batteries which are mainly connected to the thermal runaway of the cell.

The Li-ion battery can be strained under different circumstances, such as thermal, mechanical, and electrical abuse. However, all these issues result in the same detrimental effect on the battery called thermal runaway. This can be summarized as the effect caused by a series of exothermic reactions that increase the battery temperature and instability accompanied by gas detection. The sharp temperature increase accelerates the battery's chemical reaction, destabilizes the battery's active material, and can lead to a fire hazard.[81]

The use mentioned earlier can trigger thermal runaway through different mechanisms. Mechanical abuse, for example, results in destructive deformation due to an applied force to the battery.[82] This can be due to a collision, for example, a car crash, or the penetration of the battery by external sharp objects and subsequent damage to the separator and internal short circuit between the electrodes.[83] Electrical abuse mainly results from external factors such as external electric shocks, short circuits, and water exposure. However, mismanagement of the applied current or voltage on the battery causes overcharge or over-discharge, subsequently increasing the cell temperature.[84] Thermal abuse can result from electrical and mechanical abuse, or directly from thermal shocks and local heating. To protect the battery, several safety standards are followed beyond the cell level to ensure the module's safety. This includes the introduction of cooling systems, cushions, and a battery management system.[81, 85]

All these safety issues, however, are rooted in the cell level and largely dependent on the electrode chemistry which defines the safe voltage window and charge and discharge states, as well as the electrolyte used in the cell. [86] Regarding the electrolyte, although the organic carbonate-based solvents form a stable SEI layer on the negative anode, they are extremely flammable and also unstable above 4.3 V vs. Li/Li⁺. [87] In parallel, the high resistive nature of SEI can pose additional thermal risks. For salt, LiPF₆ is the common choice due to its high conductivity but a safety risk due to the low thermal stability temperature of 50 °C and the formation of corrosive HF.[88]

For the positive electrode, safety issues strongly depend on the material. Commercialized LCO cathode material, for example, becomes unstable in structure if more than 50% of the lithium atoms are removed from the layers. For lithium nickel oxide LiNiO_2 (LNO), the lithium-depleted oxide has a strong oxidizing nature and can oxidize the electrolyte that it encounters.[89] NCA has a low thermal stability of 200 °C investigated by differential scanning calorimetry.[90] Olivine-type LFP is a safer choice compared to the layered oxides due to the robust structure and high thermal stability, however, this comes at the cost of a lower energy density. [91]

For internal reactions on the cell level, advanced engineering and understanding of the electrode and electrolyte materials are essential, as well as increasing the thermal resistance of the separator to avoid its burning and internal shorting of the cell.[86] This includes an understanding of the cell stability potential and temperature window, stability of the electrodes and electrolyte at different charge and discharge rates, and engineering of the electrode/electrolyte interfaces.

2.3.5 Sustainability

For a technology to be sustainable, economic, social, and environmental impacts need to be considered.[6] This includes the costs of the raw materials and covers the safety hazards of the overall technology. Therefore, here we focus on the environmental impacts of Li-ion batteries. The total environmental impact of the cell can be broken down into the impact of chemical composition, synthesis process and processing, implementation in the system, and end of life (EOL).[92]

The choice of raw materials directly affects the impact of chemical composition. Elements that can be found in the biosphere and naturally exchanged by other compartments impose a lower environmental impact.[93] These elements can be recycled in nature and are shown in green in **Figure 9**. Additionally, using organic compounds derived from nature can provide a sustainable option for use in electrodes while reducing toxicity.[92] Two major setbacks of organic compounds are their lower cycle life and low volumetric capacity due to the large size of the molecules.[94]

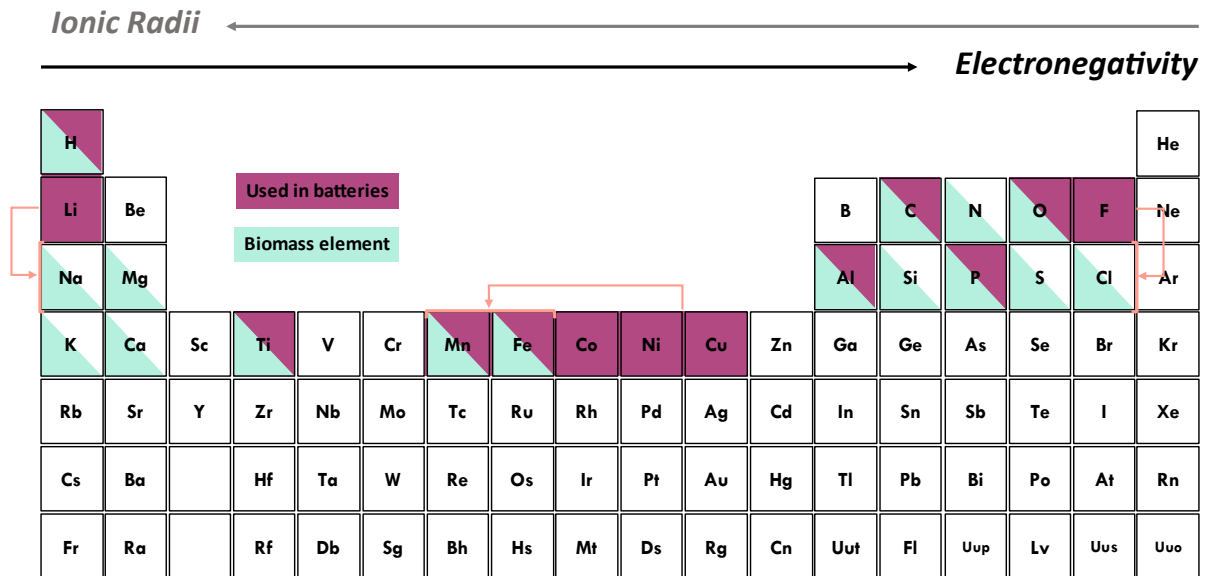


Figure 9 Periodic table showing the elements used in Li-ion batteries and elements that are degraded in nature in green. Shift to these biomass elements decrease the environmental impact of the batteries.[92]

During the material synthesis and processing, a large amount of energy is consumed when using high temperatures.[92] Reducing heat treatment steps and the utilized temperature for synthesis and introducing CO₂-consuming reactions for latter processing decrease the environmental impact of this stage.[95, 96] Implementing the processed material in the next step is mainly done by slurry preparation from the electrode components. Drying of the electrodes and dry room conditioning contribute to the largest share of energy consumed during cell manufacturing.[97] The main reason is the use of organic solvents such as N-methyl-2-pyrrolidone (NMP) for slurry preparation that needs a high temperature of 140 °C to be fully removed. This pricey solvent is then recovered by vaporization to save costs. [98, 99] NMP particularly poses severe toxicity issues in addition. Other organic solvents such as dimethyl sulfoxide (DMSO) and triethyl phosphate (TEP) are investigated as a greener option with fewer safety hazards, while at the same time providing the same slurry rheology and compatibility with PVdF binder. [100, 101] Still, aqueous solvents, dry electrode processing, and solvent-free self-standing electrode production would decrease the energy and cost needed for electrode preparation and simplify manufacturing. [99, 102] **Figure 10** shows the share of energy consumed for different components in battery cell manufacturing for a graphite-LMO cell chemistry. [97]

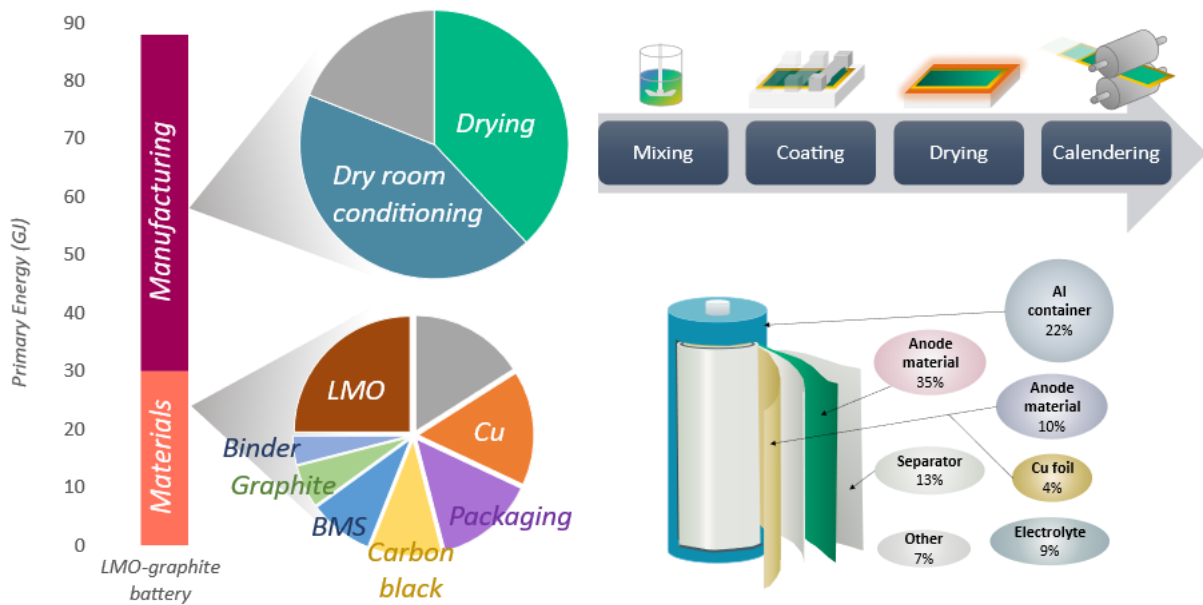


Figure 10 Energy consumption for battery materials and cell manufacturing with the respective share of different components for an LMO battery pack. Adapted from [97].

Li-ion batteries that have reached the end of their useful life in one application, such as electric vehicles or consumer electronics, can still retain a significant portion of their original capacity. These batteries can be repurposed for secondary applications, including energy storage systems for homes, businesses, or even grid-scale applications. [103] By repurposing these batteries for a second life, their value is maximized, reducing the need for new battery production and minimizing environmental impact. Additionally, the repurposing of Li-ion batteries for secondary applications can help offset the cost of battery replacements and provide an economic incentive for adopting renewable energy and energy storage solutions. Proper management and testing are crucial to ensure the safety and reliability of Li-ion batteries in their second life. [104] Challenges that are faced in large-scale use of EV batteries for a second life in industry, residential, or grid application are the requirements of the second life application in terms of safety and warranties, and the mismatch of different EV batteries. [105]

2.4 Advanced materials for next-generation batteries

The challenges mentioned above accelerate the research and development of electrode materials for next-generation batteries. An increase in demand and electrochemical performance requirements are driving forces in cost reduction and energy density enhancement.[106] Simultaneously, national, and international regulations and standards drive an increase in safety and sustainability.[24, 107, 108]

Two main areas in materials engineering are needed to address current challenges and to support these developments for next-generation batteries. First, the chemistry resulting from the derivatization method, and second, the morphology resulting from the design strategy.[62] New electrode compositions can be created by tuning the composition during derivatization,[109] while for design rational morphologies are engineered with respect to particle size, shape, and porosity by tuning the synthesis and processing parameters.[110] These two fields are highly interconnected. For example, certain design strategies are needed for enabling complex compositions, otherwise, stable cycling will not be achievable.[111] After careful engineering of the composition and morphology, further improvement at the electrode/electrolyte interface can be implemented to complement the advancement of the electrode materials and enhance the performance.

2.4.1 Chemistry: Derivatization

Current commercial layered and insertion-type compounds are limited in the attainable capacity due to the definite number of lithiation spaces per active material mass unit.[21] For this reason, other groups of electrode materials namely conversion and alloying-type materials are researched to enable higher capacities.[112] In these materials, lithium reacts with the active electrode material to form a new product or an alloy.[113] The conversion and alloying reactions can accommodate a larger number of lithium ions, and therefore reach higher capacities, but also undergo a larger volume expansion during lithiation which is detrimental to the structure stability.[114] This expansion causes the detachment of particles and the loss of electric pathways by pulverization and as a result, less material will be accessible for lithiation after each cycle and capacity fades quickly. Additionally, pulverization exposes new surfaces of the active material to the electrolyte and as a result, the continuous

formation of SEI on new surfaces depletes the lithium reservoir and increases the electric impedance.[109]

Depending on the redox potential and the counter electrode, they can be candidates for the cathode or anode side. Alloying elements such as Si, Sn, Sb, Ge, and P that bind with Li at lower potentials are investigated as anode materials and can be added to a graphite matrix or other layered active material with less volumetric expansion to dampen the capacity fading of alloying material.[106] Sulfur also reacts with lithium at potentials lower than 3 V vs. Li/Li⁺ but is used as a cathode material in batteries.[115] At higher potentials, transition metal oxides and sulfides are present. Depending on the metallic element, the redox potential varies greatly from ~1 V to ~5 V vs. Li/Li⁺. **Figure 11A** shows the potential of different transition metal oxides and sulfides. [41] With every redox pair a Li-ion is added or removed to the material; therefore, to increase the specific energy in a cell, researchers aim to increase the redox pairs per unit mass of active material as well cathode redox potential.[33]

To increase the number of transferred electrons while improving stability, mixed metal compounds are pursued to achieve higher capacities compared to single metal compounds. With this strategy, the volumetric expansion is broken down into multiple steps.[116] For example, if all the capacity is reliant on the Fe^{2+/3+}, all volumetric expansion takes place at the redox potential of iron. But with the presence of other redox pairs, lithiation, and delithiation occurs stepwise and less strain is put on the material during the process which increases the cycle life and cycling stability.[62] A drawback to the mixed compound is the possibility of one-sided reactions and material deterioration. Especially at larger voltage windows, the mixed compound decomposes into more thermodynamically stable species during lithiation and does not convert to its initial mixed composition during delithiation.[117]

Another approach to increase the energy is to tailor the bonding energies of the material to increase the potential of electrode redox pairs.[118] A successful example of this is the development of LFP. In the phosphate polyanion PO₄, strong P-O bonding decreases the π-bond Fe-O covalence, therefore increasing the Fe^{2+/3+} redox potential from 2.5 V vs. Li/Li⁺ in Fe₂O₃ to 3.5 V vs. Li/Li⁺ in LFP. Different phosphate groups and other polyanions such as SO₄, and BO₄ were tested to examine their effect on the iron redox peak.[119] **Figure 11B** shows the iron redox peak shift for different phosphate groups relative to lithium with the lowest energy for LFP, translating to the highest potential.[120]

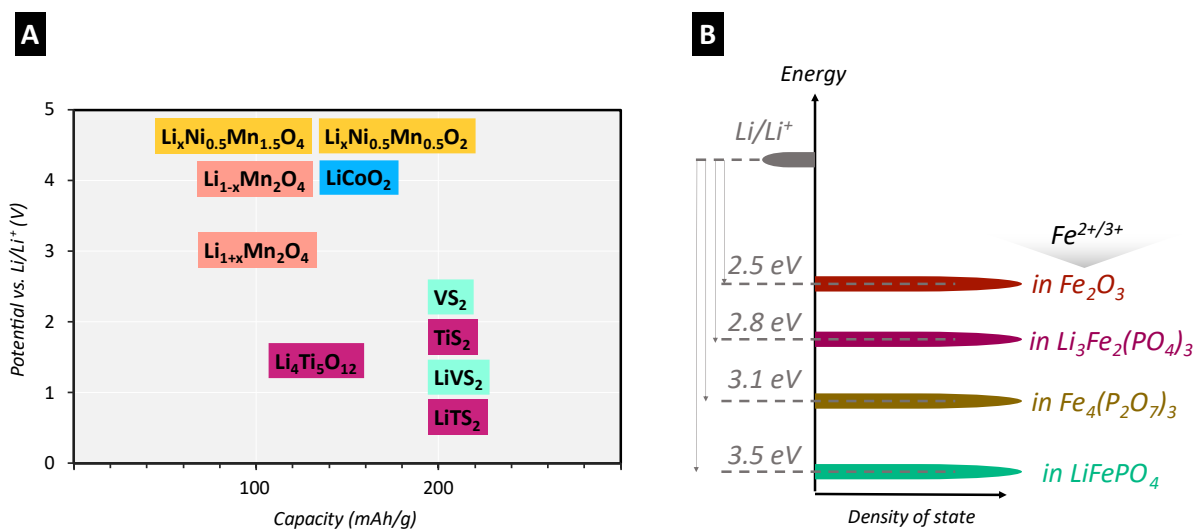


Figure 11. A Examples of transition metal oxide and sulfides (Ti: red, V: green, Mn: orange, Co: blue, mixed: yellow) with their approximate capacity and potential vs. Li/Li⁺. Adapted from [41]. **B** Fermi energy levels of Fe^{2+/3+} relative to lithium for different iron phosphates.

Adapted from [120].

Because of the higher electronegativity of oxygen versus sulfur and higher achievable redox potentials, current cathode materials are focused on metal oxides.[44] However, metal sulfides can provide higher capacities due to the available sulfur that takes part in redox reactions.[115] While redox of oxygen atoms at high potentials produces free oxygen radicals that are detrimental to battery stability, sulfur can be reduced and oxidated alongside the transition metals while providing a high theoretical capacity of 1675 mAh/g.[41] The drawback is the loss of sulfur due to the solubility of lithium polysulfide species Li₂S_x (3 ≤ x ≤ 8) in the electrolyte and its shuttling between the electrodes.[121] This phenomenon decreases the charge efficiency and results in the capacity fading of the active material.[122] Therefore, the sulfide compounds need a design strategy to preserve the sulfur element from shuttling and avoid its loss.[123]

2.4.2 Morphology: Design

In addition to materials' chemistry, morphology design plays an essential role in achievable capacity. Different design strategies are utilized to decrease lithium diffusion length and to increase specific surface and conductivity. For certain compounds such as sulfides and other conversion and alloying type material, caging and coating strategies are commonly used to retain the particles and active elements intact.[124, 125] Synthesis methods and parameters

are here critical to design rational morphologies such as fibers [126], core-shells [127], nanoparticles [114], and hollow structures. [128] Among many synthesis methods, co-precipitation at room temperature, [92] hydrothermal or solvothermal synthesis at temperatures 100-200 °C,[129] and solid-state synthesis at temperatures 800-1000 °C are standard synthesis procedures in the order of consumed energy.[130]

With an increase in temperature, higher crystallinity is achieved, but control over morphology is more difficult as the particle growth rate increases. Through standard co-precipitation up to 100 °C, nanoparticles are commonly produced.[131] An example of this synthesis method is the formation of Prussian blue analogs (PBA) that can be tuned in size and morphology.[132] Smaller particles with finer features reduce lithium diffusion length, relieve the mechanical stress from cycling, and provide more reactive sites.[133] Combining co-precipitation with other methods such as anion and cation exchange, enables more intricate features including pores and advanced hollow morphologies.[134] These strategies increase the efficiency of the material by providing access to new parts of the material that was not easily reachable in a bulk particle (**Figure 12**).[135]

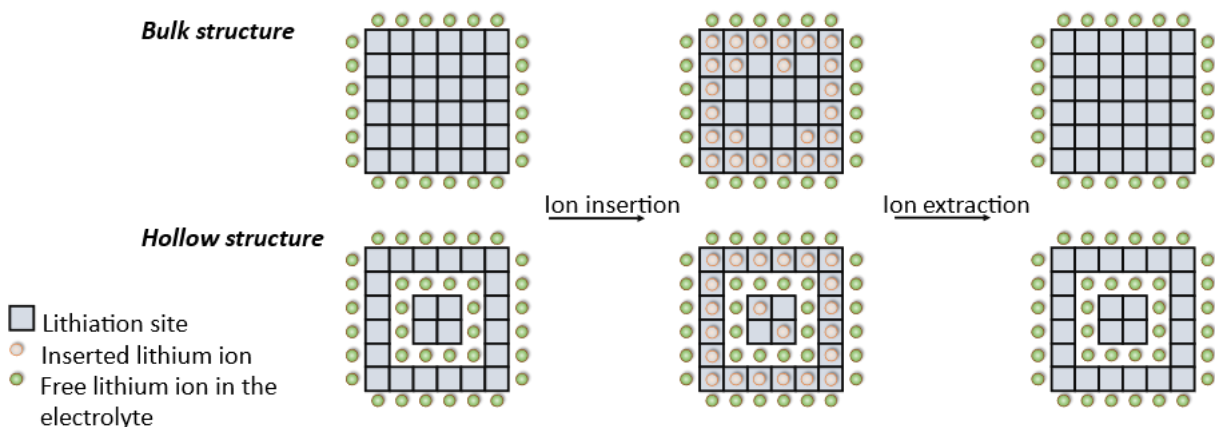


Figure 12 Comparison of a bulk and hollow structure and the role of morphology design in material efficiency by increasing the available surface area and shortening the diffusion length. Adapted from [135].

Hydrothermal and solvothermal methods can be used to produce 2D and wire morphologies due to the present temperature and concentration gradients in the media and the directional growth of the particles.[136] These structures are effective in providing a higher specific area and shortening the diffusion path. To achieve a higher degree of crystallinity or deriving

oxides, an additional heat treatment step is followed in the furnace and careful attention to the treatment parameters is needed to avoid structure collapse.[129]

Solid-state synthesis is performed by combining powder precursors and heating them to high temperatures to obtain the target compound. Due to the high temperatures used in this method, synthesis and processing take place simultaneously and further heat treatments are not carried out. This method is commonly used for commercial cathode materials by combining lithium precursors of LiOH or Li₂CO₃ and that of transition metals. High temperatures and long processing times make this method energy intensive and difficult to structure tuning. Using a microwave-assisted method can decrease the needed temperature for this synthesis.[130]

In addition to these standard methods, two synthesis approaches that provide flexibility in morphology design and are researched as battery material synthesis methods are template-directed synthesis and electrospinning. Templating enables the design of hollow structures and core-shells and can be performed via soft templating using organic materials such as surfactants,[137] and polymers[138] or hard templating using inorganic ones such as silica.[139] For this, a template is used as the substrate for the growth or deposition of the target material. Usually, a chemical or thermal treatment then removes the hard and soft template, respectively while the target material remains present and retains the template shape.[140] The template removal additionally creates porosity in the remaining shell, which is advantageous for lithium diffusion.[141] **Figure 13** schematically shows the steps in a template-directed synthesis.[142] This method is comparable to carbon coating of active material particles; a popular and common strategy to increase the conductivity of the active material or to protect it from direct etching and deterioration by the electrolyte.[129] However, in core-shell structures, more space can be provided between the core and the shell. This gives more room for core volume expansion and reduces the possibility of shell fracture and material loss.

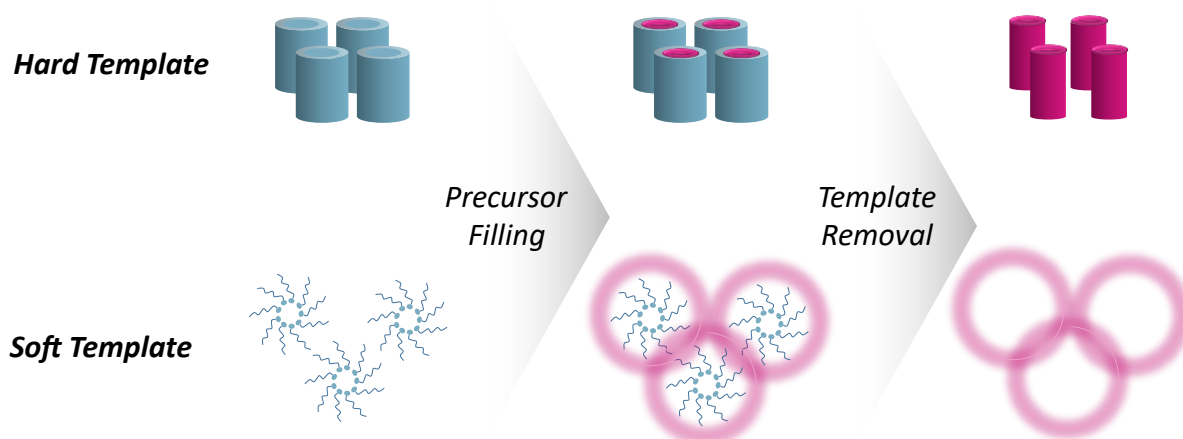


Figure 13 Schematic representation of hard templating and soft templating mechanism.

Adapted from [142].

While coating and core-shell design are effective strategies to create a protective layer on the active material, electrospinning is used to synthesize continuous fibers of the active material, increase the surface area, as well as enable self-standing electrodes.[143] For this, a solution, melt, or sol-gel of the active material is prepared [144] and connected to a needle at high voltages of 15-30 V versus a conductive substrate below the needle in the form of a flat plate or a rotating cylinder.[145] The applied voltage creates a jet of the electrospinning fluid, which exits the needle and dries as continuous fibers upon deposition on the substrate.[146] Several parameters affect the stability of the jet, including the humidity and the temperature of the atmosphere, applied voltage, and distance between the needle and the substrate, and need to be carefully optimized for the used fluid. [147-150] These continuous fibers form a non-woven fibrous mat and are then heat-treated to form compounds such as oxides and sulfides as battery electrode materials.[151]

Figure 14 illustrates a schematic representation of the electrospinning method.[152] The precursor solution is often prepared in a polymer matrix to ensure the continuity of the fibers and stable sol-gel consistency.[153] The polymer matrix is transformed into a carbon shell or a carbonaceous network after the heat treatment. The conductivity of this network can be increased by higher heat-treatment temperatures, but a full transformation of the polymer to carbon causes the collapse of fibers due to the increased brittleness and loss of ductility.[154] For direct use of electrospun fiber mats as self-standing electrodes without subsequent coating preparation, it is therefore essential to pay attention to the mechanical stability of the fibers during the heat treatment.[155]

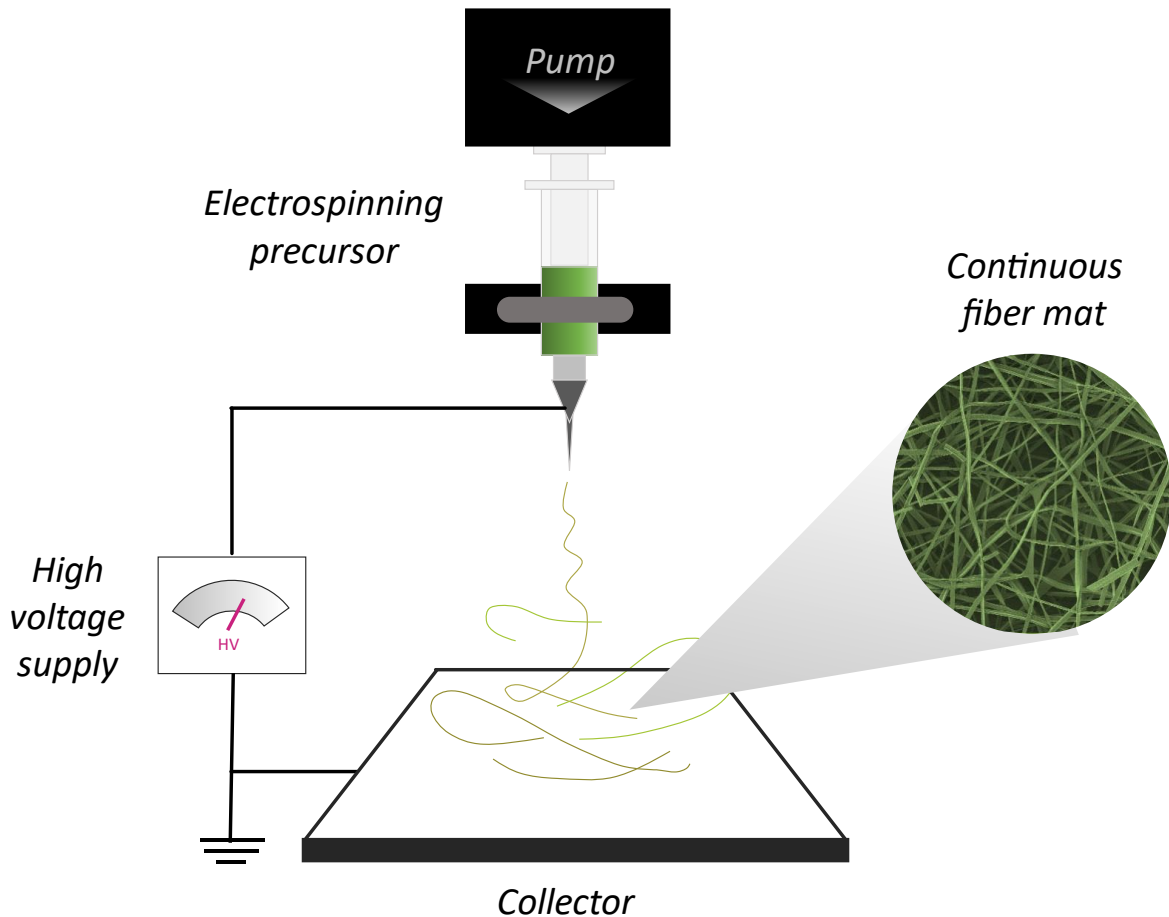


Figure 14 Schematic representation of an electrospinning setup with a plate substrate as fiber collector. Adapted from [152].

2.4.3 Improvement beyond derivatization and design

Electrochemical performance and cell reactions depend not only on the electrode materials but also on the electrode/electrolyte interface at which corrosion of the electrode material takes place and capacity is lost due to metal dissolution in the electrolyte.[156] While hybridization of the electrode particles by using protective layers such as carbon coating can improve the material's stability, the electrolyte interface can also be further engineered to improve the SEI and CEI layers and increase the conductivity in these interphases.

The strategies used at the electrode and electrolyte interface are very dependent on the electrolyte, namely liquid and solid electrolytes since the composition of the formed interphase at the electrode/electrolyte interface is highly dependent on the nature of the present electrolyte.[157] Generally, the surface of the electrodes can be modified by creating a coating layer with respect to the electrolyte and the interphase nature to increase the

stability against corrosive reactions.[158] Synthesis methods such as co-precipitation, solvothermal, sol-gel, atomic layer deposition, and ball-milling can be employed for this target and are chosen based on the coating thickness, and degree of parameter control such as temperature and pH.[159]

Additionally, using additives in the electrolyte can affect the formed interphase between the electrode and electrolyte and increase cycling stability.[160] Although an easier approach than tuning the electrode materials surface, this lacks the selectivity on the cathode or anode and affects both electrodes. Apart from chemical tuning, testing parameters, and electrode preparation can be used to further improve the performance stability. This can be for example in the form of conditioning via a constant current or voltage in the electrochemical conditioning [161], or changing pressure and mass loading of the electrode material in the coating preparation.[162]

3 APPROACH AND OVERVIEW

The present thesis comprises three sections to explore advanced Li-ion battery electrodes while simultaneously designing them for higher sustainability. The first section introduces design and derivatization principles. These principles are then applied through four chapters in section two. The third section then completes these reports, showing complementary steps to electrode design and derivatization to improve the battery performance. An overview of these sections is shown in **Figure 15**.

Section 1: Chapter 1 reviews PBAs as a template for the derivatization of a variety of transition metal compounds such as oxides, sulfides, phosphides, nitrides, porous carbons, and metal alloys. Further advanced structure designs are also explained. Due to the extensiveness and complexity of strategies for design and derivatization from Prussian blue analogs, they are broken down into three steps: pre-treatment, derivatization, and post-treatment, and the effect of each step on the final product has been explained. Finally, this chapter introduces the principles of design and derivatization using PBAs, later used for core chapters.

Section 2: To apply the principles introduced in **Section 1**, three chapters are introduced in **Section 2**. Every chapter has three points of focus: using design or derivatization principles, oxide or sulfide material chemistry optimization, and improvement of an aspect to increase the material sustainability. These aspects sequentially are raw materials choice, synthesis and processing, electrode preparation, performance, and lifetime optimization. For material synthesis, parameters such as pH and temperature are brought to the ambient conditions to save energy costs by heating or reducing the hazards of using acidic pHs. In the next step, the processing is improved. Here, we target the heat treatment of the synthesized precursor into its respective sulfide or oxide and reduce the treatment temperature and duration or change the reactive gas to CO₂ to decrease the carbon footprint. The third step is electrode preparation, where organic and toxic solvents and the subsequent solvent drying can be avoided. Finally, all the steps are optimized for electrochemical performance and the lifetime of the battery material. The work starts with pure derivatization and then how morphology design affects material's derivatization.

The first original work is introduced in **Chapter 2** and emphasizes on the derivatization of mixed metal sulfide from iron-copper PBA and the challenges that come with the

derivatization of mixed metal compounds. Non-EU-critical elements were used, and a treatment for 10 min was employed for the derivatization of the sulfide material. Here we coat the particles during synthesis and show that the coating agent directly affects the synthesis and particle size.

Chapter 3 covers a mixed metal oxide of iron and vanadium, a complex system which can deteriorate during cycling. The work focuses on derivatization from iron-vanadium PBA and its stabilization via surfactant for electrochemical energy storage. At the same time, material design principles are introduced to remove the use of binder and wet coating preparation. Self-standing electrodes were prepared by dispersion in ethanol and vacuum filtration to reduce environmental impact during the electrode preparation. Subsequent heat treatment also took place under CO₂ flow and by infrared heating.

Chapter 4 explores an advanced design strategy using electrospinning methodology to produce single metal oxide vanadium trioxide and optimize its fiber design. The synthesized electrospun fibers were used directly as free-standing electrodes without slurry preparation. The use of electrospinning eliminates the drying process and the use of solvent and binder. Here, the mechanical properties of the fibers and their effect on the electrochemical properties are assessed.

Section 3: Chapter 5 reviews complementary steps to the design and derivatization to further stabilize the performance of advanced battery materials. This is explained by engineering the electrode/electrolyte interface for both the anode and cathode to increase their lifetime. The methods of choice need to be tailored based on the composition of the electrode, and the electrolyte, as well as how they interfere with each other such as the corrosiveness of the electrolyte towards the active material. Some of these complementary steps can be integrated into the synthesis and processing of the electrode material, for example by using atomic layer deposition to form an artificial coating on the active material.

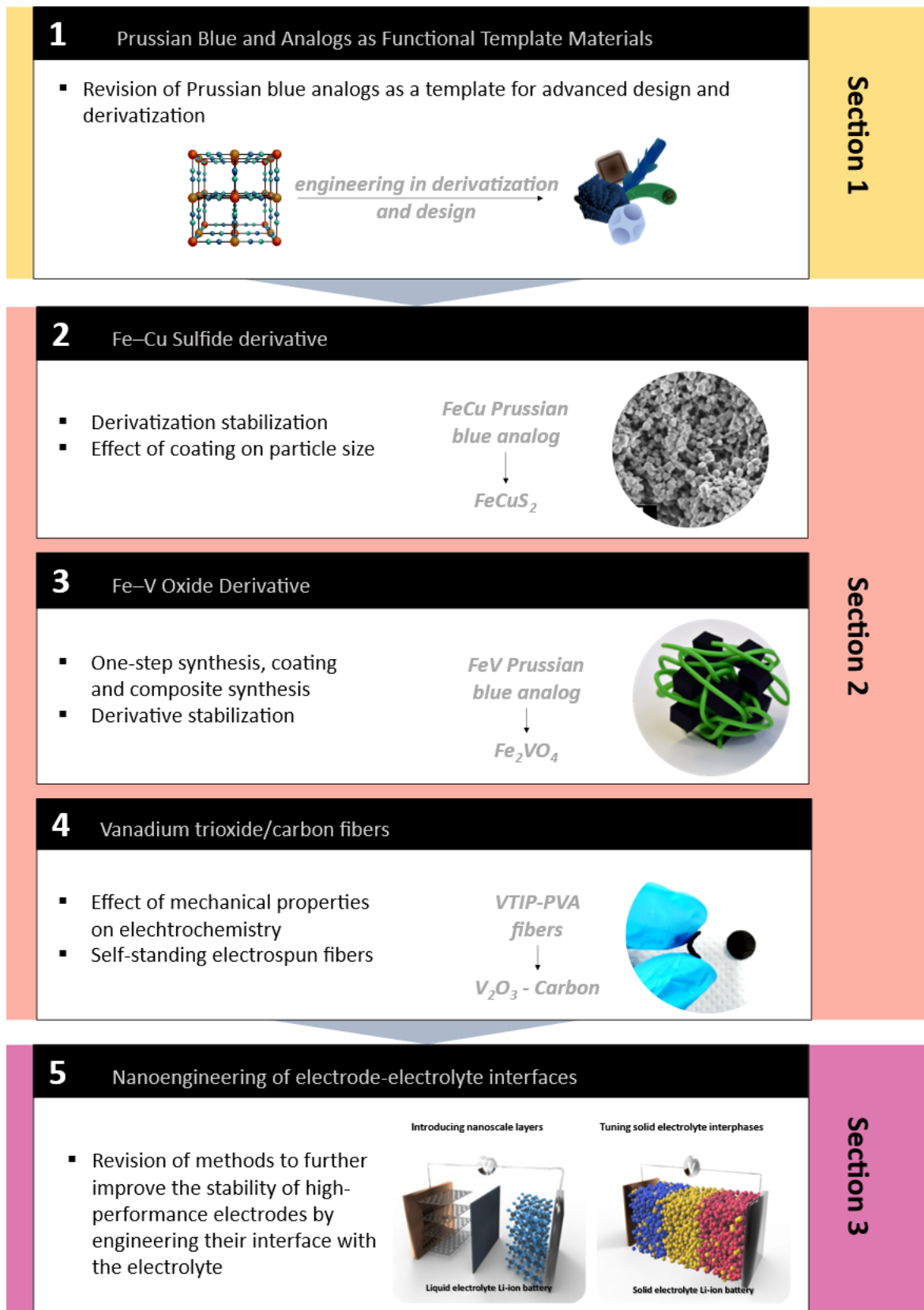


Figure 15. Chapter overview of results and discussion

4 RESULTS AND DISCUSSION

- 4.1 Prussian blue and its analogues as functional template materials: control of derived structure compositions and morphologies**
- 4.2 Mixed Cu–Fe sulfide derived from polydopamine-coated Prussian blue analogue as a lithium-ion battery electrode**
- 4.3 Surfactant-stabilization of vanadium iron oxide derived from Prussian blue analog for lithium-ion battery electrodes**
- 4.4 Mechanically stable, binder-free, and free-standing vanadium trioxide/carbon hybrid fiber electrodes for lithium-ion batteries**
- 4.5 Recent advances in nanoengineering of electrode-electrolyte interfaces to realize high-performance Li-ion batteries**

Prussian blue and its analogues as functional template materials: control of derived structure compositions and morphologies

Behnoosh Bornamehr^{1,2}, Volker Presser^{1,2,3*},

Aldo J. G. Zarbin^{4,*}, Yusuke Yamauchi^{5,6,*}, Samantha Husmann^{1*}

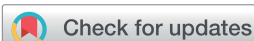
- ¹ INM – Leibniz Institute for New Materials, Campus D2 2, 66123, Saarbrücken, Germany
- ² Department of Materials Science & Engineering, Saarland University, Campus D2 2, 66123, Saarbrücken, Germany
- ³ saarene – Saarland Center for Energy Materials and Sustainability, Campus C4 2, 66123 Saarbrücken, Germany
- ⁴ Department of Chemistry, Federal University of Paraná (UFPR), CP 19032, 81531-980 Curitiba, PR, Brazil
- ⁵ School of Chemical Engineering and Australian Institute for Bioengineering and Nanotechnology (AIBN), The University of Queensland, Brisbane, QLD 4072, Australia
- ⁶ International Center for Materials Nanoarchitectonics (WPI-MANA), National Institute for Materials Science (NIMS), 1-1 Namiki, Tsukuba, Ibaraki 305-0044, Japan

Citation:

Bornamehr, B., Presser, V., Zarbin, A.J., Yamauchi, Y. and Husmann, S., 2023. Prussian blue and its analogues as functional template materials: control of derived structure compositions and morphologies. *Journal of materials chemistry A*, 11(20), pp.10473-10492.

Own contributions:

Writing – original draft

Cite this: *J. Mater. Chem. A*, 2023, 11, 10473

Prussian blue and its analogues as functional template materials: control of derived structure compositions and morphologies

Behnoosh Bornamehr,^{ID} ^{ab} Volker Presser,^{ID} ^{*abc} Aldo J. G. Zarbin,^{ID} ^{*d}
Yusuke Yamauchi,^{ID} ^{*ef} and Samantha Husmann,^{ID} ^{*a}

Hexacyanometallates, known as Prussian blue (PB) and its analogues (PBAs), are a class of coordination compounds with a regular and porous open structure. The PBAs are formed by the self-assembly of metallic species and cyanide groups. A uniform distribution of each element makes the PBAs robust templates to prepare hollow and highly porous (hetero)nanostructures of metal oxides, sulfides, carbides, nitrides, phosphides, and (N-doped) carbon, among other compositions. In this review, we examine methods to derive materials from PBAs focusing on the correlation between synthesis steps and derivative morphologies and composition. Insights into catalytic and electrochemical properties resulting from different derivatization strategies are also presented. We discuss challenges in manipulating the derivatives' properties, give perspectives of synthetic approaches for the target applications and present an outlook on less investigated grounds in Prussian blue derivatives.

Received 6th December 2022
Accepted 17th February 2023

DOI: 10.1039/d2ta09501g

rsc.li/materials-a

1. Introduction

Prussian blue (PB) is a well-known classic coordination compound that has risen from an old painting pigment to a widely studied electrode material.¹ PB and its analogues (PBAs) combine the presence of redox-active metallic species and an open porous structure that can accommodate ions with little or no volumetric change. Such characteristics are attractive for energy storage, catalysis, sensing, and biomedical applications, among others.^{2–5} Recently, PBAs have gained growing interest as a template material for preparing porous derivatives.^{6,7} By providing metal species, carbon, and nitrogen from cyanide ligands combined with a well-structured, stable, and highly porous framework, they enable sacrificial templating (or template-engaged/self-template) methods. Templating is a very effective tool to synthesize more complex porous and hollow structures, and many different (hetero)nanostructures derived

from PBAs have already been described.^{8–10} Calcination methods produce oxides,^{11–13} while annealing generates carbides,^{14,15} alloys,^{16,17} or metal nanoparticles with different compositions.^{18–22} Pre-treatments can regulate the morphology of the derivatives or introduce heteroatoms.^{22–24}

Nevertheless, fast and simultaneous reports within the past few years have led to many PBA derivative (hereafter referred to as PBDs) compositions and morphologies with little control over the product, where even different derivatives are obtained under similar processing conditions. This lack of understanding of how PBA characteristics and the derivatization process affect the composition, structure, and morphology of PBDs, makes the control and prediction of the final product a current challenge. Despite that, PBDs perform very well in electrocatalysis, batteries, and capacitors, far surpassing counterparts obtained by different methods. A comprehensive summary of the PBA derivatization methods and correlation with PBD composition, morphology, and properties is particularly interesting in this context.

Most reviews on PBDs focus on specific applications such as energy storage,^{6,9,10,25} catalysis,^{10,26} and the environment.⁹ Nevertheless, very few describe the synthetic methods to obtain PBDs; noteworthy are the compilation of Fe-based PBDs prepared by Li *et al.*,¹³ and the revisions of Zakaria *et al.*²⁷ and Azhar *et al.*²⁸ that largely focus on PBA modification prior to derivatization. The growing chemical compositions and structure complexity described for PBDs require an overview of the synthesis routes and steps and the approaches utilized for each composition group (oxides, sulfides, carbides, *etc.*).

^a*INM – Leibniz Institute for New Materials, Campus D2 2, 66123, Saarbrücken, Germany. E-mail: volker.presser@leibniz-inm.de; husmann.samantha@gmail.com*

^b*Department of Materials Science & Engineering, Saarland University, Campus D2 2, 66123, Saarbrücken, Germany*

^c*Saarene – Saarland Center for Energy Materials and Sustainability, Campus C4 2, 66123 Saarbrücken, Germany*

^d*Department of Chemistry, Federal University of Paraná (UFPR), CP 19032, 81531-980 Curitiba, PR, Brazil. E-mail: aldozarbin@ufpr.br*

^e*School of Chemical Engineering and Australian Institute for Bioengineering and Nanotechnology (AIBN), The University of Queensland, Brisbane, QLD 4072, Australia. E-mail: y.yamauchi@uq.edu.au*

^f*International Center for Materials Nanoarchitectonics (WPI-MANA), National Institute for Materials Science (NIMS), 1-1 Namiki, Tsukuba, Ibaraki 305-0044, Japan*



In this review, we introduce the concept of using the PB family of compounds as template materials and present their characteristics and advantages, and their potential to be used as precursors for novel materials. In addition, we will examine the strategies adopted in the PBA synthesis to create specific template structures. The different derivatization methods will be summarized in terms of composition and morphology, addressing the approaches for introducing additional elements and creating complex structures. This will provide a guide map for the derivatization of new compositions and gives a better insight into planning the synthesis route for the intended application. As many of the derivatives are used as catalysts and energy storage electrodes, some examples of different processing methods for PBD fabrication and the effect of the steps and the attained morphology on the performance in these specific applications will be demonstrated. Finally, we will elaborate on the key aspects of PBA templating that dictate the composition and morphology of the derivatives and will discuss the challenges in achieving control over material design.

2. Prussian blue and its analogues as template materials

Prussian blue is the oldest reported coordination compound, yet it is still the subject of intense research to the present day.⁹ PB was initially discovered as a pigment at the beginning of the 18th century. However, after its structural characterization and discovery of its redox properties in the 1970s,^{29,30} this material found interest in other areas of application such as (bio)sensors and absorption, filtration and purification, energy storage and conversion, and drug delivery, among others.^{31–33}

As coordination compounds, the primary structure of the PBA family is based on two metal centres bridged through cyanide ligands in an octahedral arrangement, formally denoted as hexacyanomethylates. A PBA presents a general formula $A_xM[M'(CN)_6]_y\Box_{1-y}\cdot nH_2O$, where M and M' are transition metals coordinated to the nitrogen and carbon of CN ligands, respectively (Fig. 1A); A is normally an alkali cation, \Box stands

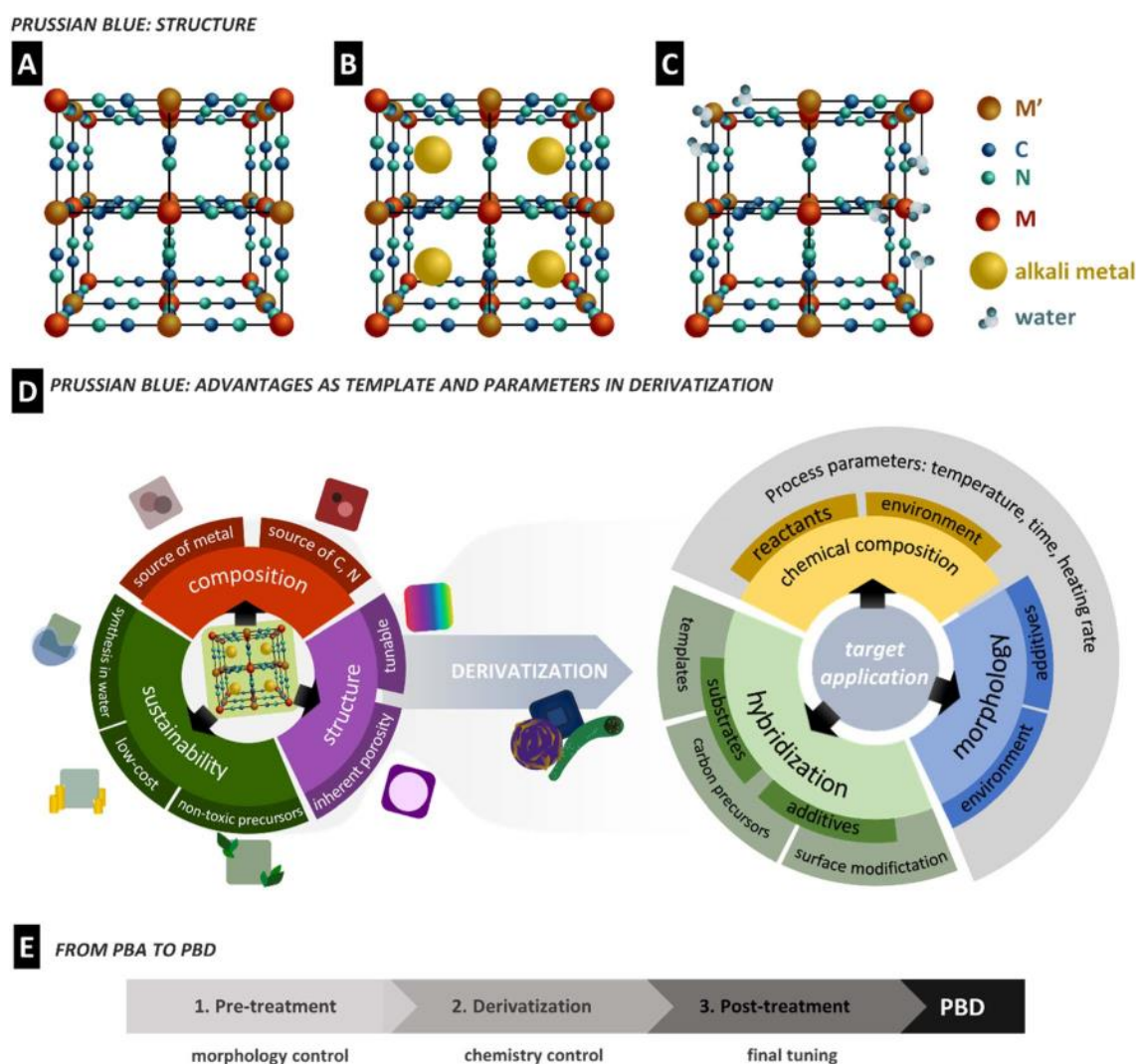


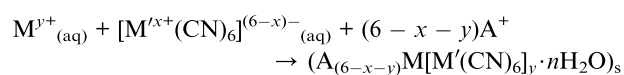
Fig. 1 (A) Theoretical PBA lattice. (B) Defect-free “soluble” PBA with alkali ions in the lattice. (C) “Insoluble” PBA lattice with defects and water molecules filling the defect sites. (D) PBA characteristics useful for templating and the parameters affecting the PBD properties. (E) The proposed approach for PBD derivatization in three steps, and the main feature of each step.



for possible lattice vacancies, and coordinated water can eventually occupy defects or uncoordinated sites. In the case of PB, the metal centres are Fe(III) and Fe(II) species, resulting in the formula $AFe^{III}[Fe^{II}(CN)_6]$. The defective and alkali-free structure is often referred to as insoluble, while the highly organized and alkali-containing one is defined as soluble PB (Fig. 1A–C).¹⁰ These terms do not correlate with PBA solubility in water or solvents. The cubic structure formed from the octahedral coordination of both metals leads to a porous framework, while the strong bonding energy of the cyanide ligands gives rigidity to the material.³⁴ During redox reactions of the metallic centres, ions can be stored in the porous lattice, while the structure rigidity prevents significant strain or expansion, enabling stable ion insertion processes.³⁵ The properties and the size of the interstitial sites can be tuned by the metal character through replacing one or both Fe centres with several other transition metals such as cobalt, manganese, and nickel, leading to PBAs.³⁶ These characteristics combined allow a PBA to be selective towards specific ions, which has significant implications on its application performance and possibilities.^{37,38}

In 1984, Itaya *et al.* demonstrated the catalytic effect of Prussian white (PB reduced form) on H_2O_2 reduction, which led to almost 40 years of exponential research on PB in analytical bio-sensors.³⁹ As a consequence, novel PBAs were described, bringing new electrochemical properties that naturally diversify PBAs' application as electrode materials. Much of PBAs' outstanding performances arise from combining (multi) metallic centres and the described open framework structure, often compared to metal–organic frameworks (MOFs). Unlike MOFs, PBAs are water and air-stable under standard ambient conditions,⁴⁰ are easy to synthesize, and present a high concentration of redox-active species per cell volume. In addition, the short cyanide ligands create easy access to the metallic species while holding the structure, which is often a drawback of the bulky ligands in MOFs.^{41,42} Though restricted in terms of ligand nature, PBAs with many different combinations of transition metals have been described.¹¹

An appealing characteristic of PBAs to be used as a template is that they are biocompatible.⁴³ At the same time, their synthesis is normally performed by a fast, easy, and water-based co-precipitation method using relatively cheap precursors. It is cost-effective and shows a high degree of sustainability. The co-precipitation synthesis of PBAs generally consists of the drop-wise addition of an MX salt solution ($X = Cl^-$, NO_3^- , SO_4^{2-} , *etc.*) to a solution of $A_{6-x}[M^x(CN)_6]$. The M ion coordinates to the $[M^x(CN)_6]$ unit, while A ions can be incorporated into the structure in a generic reaction that can be expressed as:



Parameters like the concentration of precursors, pH, temperature, and mixing rate, among others, influence the composition, crystallinity, defect content, and particle size.^{44,45} Surfactants or carbonaceous materials are often added to control the shape or reduce the particle size. In contrast,

additional M salts can be added during co-precipitation to produce more complex compositions,^{15,28} resulting in a gradient composition between two (or more) PBAs.^{46,47} An intrinsic parameter that affects the particle size is the solubility of the PBA and therefore, its formation speed. This must be considered while changing the chemistry of the PBA and designing its size and morphology. The solubility difference can itself be used to stabilize unstable PBAs. For example, a core–shell PBA on PBA structure can be synthesized by covering soluble vanadium hexacyanoferrate (VHCF) with copper hexacyanoferrate (CuHCF), which has a lower solubility.⁴⁸ The synthetic approaches and the interplay of the controlling variables over PBA characteristics and morphology are extensively reviewed. These will not, therefore, be discussed in depth here.^{28,49,50} Nevertheless, understanding PBA synthesis and particle growth is of great importance, as well as understanding their versatility in composition and morphology, as they influence the PBDs derived from such materials. Therefore, we recommend that anyone interested in the PBD topic investigate PBA synthesis literature to be able to successfully tailor PBDs.

PBA characteristics are often pursued in electrode materials, such as metal oxides and sulfides. Nano and microporosity are well known to benefit the electrochemical properties of materials as they increase the surface area, facilitate ion transport and improve electron mobility. Complex synthetic methods are often developed to achieve highly porous/hollow morphologies of well-known electrode materials and to improve performance.^{51,52} In this context, PBAs have recently started to be used as templates to produce porous derivatives (Fig. 1D). Since the PBA structure benefits from the presence of C, N, and metallic elements, it can also accomplish self-templating.

Derivatization of PB and PBAs can be performed *via* multiple approaches, but thermal treatment is mostly used due to its versatility. By controlling the temperature and atmosphere, for example, using a carrier gas that reacts with the PBA, the derivative chemistry can be altered in various ways. Therefore, carbides, metal-containing compounds, or simply metal alloys can be derived through thermal treatment. Other methods, such as liquid and hydrothermal syntheses, have also been used to derive metallic compounds and show the diversity in the synthesis of PBDs, however, with far less extent compared to the thermal procedures.²⁷ The next section will provide an overview of the PBA derivatization strategies and steps through which different morphologies and compositions can be obtained.

3. PBD synthesis strategies

Synthesis of PBDs can be very versatile and sometimes lengthy; however, they can be roughly broken down into three main steps: pre-treatment, derivatization, and post-treatment. The derivatization is the key step, and it is defined here as the step that causes the conversion of a PBA into other materials (oxides, sulfides, carbides, *etc.*). Often a pre-treatment is performed before derivatization, occasionally followed by post-treatment to complete the entire procedure. Each of these steps is chosen strategically to result in a specific attribute of the



Table 1 Process steps and methods to achieve PBDs and their key features and limitations

Step	Method	Features	Limitations
Pre-treatment; modification of PBA characteristics	Template	Control of the macrostructure “Cubic-free” morphology possible Addition of new components/more complex composition Hollowness possible	Multi-step/time demanding Possible unwanted elements from the template
	Directed growth	Control of the microstructure (normally by using salt/surfactants) Normally achieved in one step High parameter sensibility: fine-tuning Hollowness and porosity possible (also combined with etching)	Less morphology variety than templates (cubic-derived morphology only) High parameter sensibility: difficult to control
	Etching	Added porosity and/or hollowness	High sensibility to media and PBA characteristics Etching process depends on PBA crystallinity Particles >100 nm to avoid structure collapse Normally requires a combined hydrothermal process
		Time-dependent morphology: fine-tuning Combined with directed growth for morphological control	Limited to specific ions (normally oxide/hydroxide salts) Not all metal species can be exchanged Generally limited to N-coordinated metal
	Ion exchange	Preparation of non-stable PBAs More complex M/M' compositions Additional metals can be incorporated Combined with etching for control of exchanged ions and/or added porosity	
	Coating	Control of the particle size Incorporation of additional elements that can be used in the derivatization step Protection against coarsening in derivatization	Normally limited to carbon coatings Sometimes, multi-step process/time demanding
	Hybrid/composite	Added functionality to PBAs and PBDs	Not always homogeneous component distribution Possible reaction of an added component in the derivation process
Derivatization; conversion from a PBA to a PBD	Thermal	Accomplishes the widest variety of chemical compositions Time- and temperature-dependent compositions: tuning possible Possible porosity due to PBA shrinkage	Possible loss of morphology, especially at high T (coated samples can help mitigate) Less control over product than liquid-driven methods Sublimation or salt decomposition required for added elements (F, P, Se, etc.)
		Hydrothermal	Control of porosity through reaction time Larger variety of precursor salts Less energy intensive Can be combined with an acid/base for added porosity and hollowness Can produce an M'-free PBD with the aid of S-containing salts
	Liquid	High complexity in morphology and metallic composition Can replace an N-coordinated metal	So far, limited to hydroxides So far, limited to pristine cubic PBAs Slower process
	Post-treatment; final tuning of composition and morphology	Etching	Carbon products through metal leaching Addition of porosity and/or hollowness Removal of specific metallic species
Thermal		Improved crystallinity Achieved carbon graphitization	Can cause morphology collapse Can modify composition during crystallization
Composite		Added functionality to PBDs Versatility in composition and morphology Can support PB as a substrate	Lower interaction between the added component and PBD compared to pre-treatment Additional steps/time demanding

material, such as the morphological, physical, or chemical properties, and aid the material's performance in its target application. Each step can be taken *via* a single or multiple

processes. For example, two pre-treatment strategies or two steps of derivatizations can be used. However, adding each step brings an extra challenge while extending time and energy



demands. Pre-treatment steps are usually employed to control the morphology of the PBA, but morphology engineering is realizable only on particles with a minimum size to tolerate intricate architecture. Derivatization is the main step in defining PBD chemistry. However, this change in chemistry needs a high degree of control on process parameters to preserve the structure designed by pre-treatment. At last, post-treatment steps are used to fine-tune the product by etching away unwanted products or adding porosities, but this comes at the cost of high temperatures or the use of harsh acids. Therefore, understanding the full journey from a PBA to a PBD is essential to design an effective derivatization. A summary of the derivatization steps and methods covered in this review and an overview of their key features are described in Table 1.

3.1 Pre-treatment

Any treatment procedure that retains the PBA character, that is, being a hexacyanometallate, is considered a pre-treatment. Here, we summarize the strategies used in the pre-treatment to alter the PBA morphology and composition and make it ready for derivatization. These can be divided into templating and directed growth, etching, ion exchange, coating, and composite formation (Fig. 2A). We provide examples of the synthesis of PBA particles that were further used to prepare PBDs. The work on composition, morphology, and size control of PBA particles is extensive. Many pioneering and outstanding examples were left out simply because there is no work on producing PBDs from those structures, in particular, the anisotropic growth of PBAs to produce sheets, tubes, rods, or other nanostructures.^{53,54} Most of the reported studies and the examples presented here are PBDs with cubic-derived morphology. This is evidence that many possibilities in PBD research remain unexplored.

3.1.1 Templating and directed growth. PBAs are sometimes synthesized through the templating strategy to control the particle shape and size. The templated PBA is then used as a template to form the PBD. Most PBAs naturally grow as cubic particles ranging from a few nanometers to a few micrometres, depending on the synthesis parameters such as solution concentration and temperature. The PBA templating strategies can act in two directions: introduce porosity and hollowness in the particle microstructure, or direct the macrostructure of the bulk material. PBAs can grow around the template material that is afterward removed to create hollow structures. This can be done, for example, through soft-templating by the use of polymers and surfactants, which are further removed, leaving a hollow PBA shell. By using different surfactants in $\text{Co}(\text{NO}_3)_2$ solution, Liu *et al.* were able to prepare different morphologies of cobalt hexacyanoferrate (CoHCFE).⁵⁵ The nature of the surfactant can direct how the particles will grow. In this example, sodium dodecyl benzene sulfonate (SDBS) forms droplets covered by the cobalt salt, leading to CoHCFE-covered SDBS spheres (Fig. 2B and C). Sodium dodecyl sulfate (SDS) covers the particle surface, producing SDS-covered CoHCFE cubes. Upon heat treatment of the PBA to produce FeCo oxides,

the surfactant is removed, leading to porous cubes, hollow spheres, or nanoparticles.⁵⁵

Hard templating has also been used to regulate the microstructure. Hard templating has the advantage of more flexibility in terms of shape and size due to the rigid structure compared to soft templates. Traditional methods like coating silicon particles and subsequent etching with acid can be employed for this. Nevertheless, a better way to induce hollowness and porosity is by using sacrificial templates, where the particle also takes part in the PBA reaction and is consumed, leaving an empty core. For example, Nai *et al.* prepared CoHCFE nano-frames in the presence of trisodium citrate.⁵⁶ Initially, typical cubes of CoHCFE are formed. However, with increased reaction time, the inner part of the cubes is consumed and reprecipitated at the edges of the original cubes, producing porous frames after 36 h of reaction. The citrate plays a key role as it protects the (100) faces of the cubes, leaving exposed reactive (110) edges. The size of the precursor cubes and the size of the resulting frames could also be tuned by using the concentration of the reactants. They observed that the soluble K-rich phase is the preferred structure at the frames compared to the inner cube, resulting in a less defective material.

Preferential growth engineering is a common approach in pre-treatment, and tailored morphologies can be synthesized based on the coverage of certain edges or faces of the crystal. For example, Nai *et al.*⁵⁷ explored epitaxial growth in CoHCFE to result in intricate structures such as frames, cages, and boxes. In this study, the initial PBA is formed rapidly, but over a longer holding time, a K-rich CoFe PBA starts forming on top of the original CoHCFE cubes. Due to higher activity at the corners and edges, the second phase starts nucleating from these sites. A higher growth rate was observed in the presence of PVP, and full coverage of the PBA template forms cages. Different citrate concentrations at this stage further ripened the shell into a solid or open frame. The authors explain the different morphologies by the different planes that PVP ([100]) and citrate ([111]) protect, and the influence of concentrations on the growth kinetics (Fig. 2D–F).⁵⁷

Hard templating is a common approach for tuning the macrostructure of the particles. The template can function as a substrate for the growth of the PBA material, for example, using layered structures like graphene or MXenes to create PBA sheets, or wires to create PBA core-shell fibres or hollow tubes. Wang *et al.* used a nickel foam to grow different metallic structures like Co_3O_4 nanosheets, $\text{Cu}(\text{OH})_2$ nanowires, or $\text{Ni}(\text{OH})_2$ nanoparticles.⁵⁸ These materials were used as metal precursors to form different PBAs at the surface of the macrostructure. In this case, the template is not removed and takes part in the derivatization process, resulting in highly porous 3D structures.⁵⁸ This is a common strategy to guarantee that the template actively acts as a structure support, source of elements, or results in conductive carbon species.

3.1.2 Etching. Etching of a PBA is normally performed to achieve porosity and hollowness because this characteristic is desired in many applications for its high specific surface area. In the etching process, the etchant acts on the most reactive or weakest part, normally the corners or edges, producing cages.



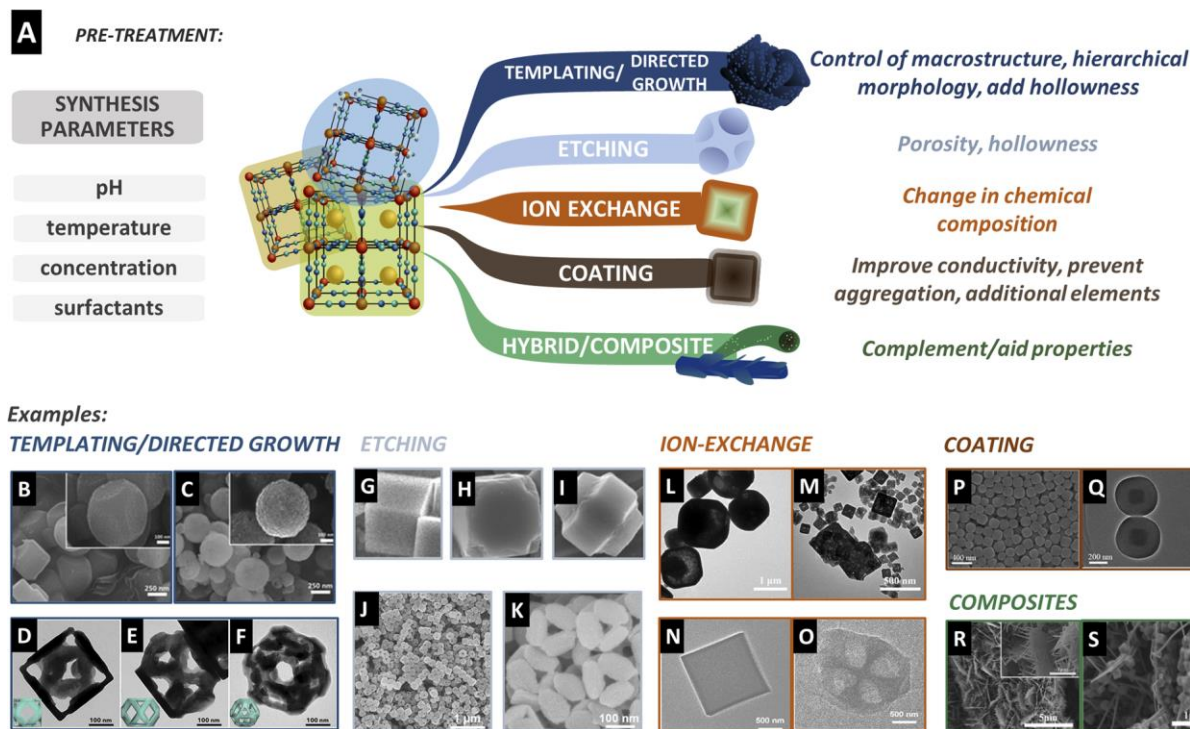


Fig. 2 (A) Strategies to modify PBA particles before derivatization, with the common target results. These treatments are performed in parallel to the synthesis parameters such as the pH, temperature, or concentration of the salts. (B) Co–Fe PBA precursor and (C) resulting porous spheres prepared by soft-templating. Reproduced from ref. ⁵⁵ with permission from the Royal Society of Chemistry. (D–F) Directed growth of the CoHCFe precursor after resting in the presence of trisodium citrate. Reproduced with permission from ref. ⁵⁷. Copyright 2018 Elsevier. (G–I) Etching procedure of the cubic precursor in the presence of HCl⁵⁹ and (J and K) in the presence of ammonia.²³ (G–I) were reproduced from ref. ⁵⁹ with permission from the Royal Society of Chemistry. (J and K) were reproduced with permission from ref. ²³. Copyright 2017 WILEY-VCH Verlag GmbH & Co. KGaA, Weinheim. (L and M) TEM images of MnHCFe after the reaction with Co(NO₃)₂ in the absence (L) and presence (M) of C₂H₅OH creating porous CoHCFe cubes. Reproduced with permission from ref. ⁶². Copyright 2021 Elsevier B.V. (N) Cubic precursors before and (O) after cation exchange due to the solubility difference. Reproduced with permission from ref. ²². Copyright 2021 Wiley-VCH GmbH. (P) SEM image of the PB precursor and (Q) TEM image of core–shell spheres after coating with resorcinol formaldehyde. Reproduced with permission from ref. ⁶⁷. Copyright 2019 American Chemical Society. (R) NiCo arrays on carbon cloth as a substrate before and (S) after PBA cube formation. Reproduced with permission from ref. ⁷⁵. Copyright 2019 Elsevier B.V.

However, protective agents like polymers or surfactants can direct the etching process, for example, toward the cube faces, producing frames, or the interior, leading to hollow cubes. One of the first studies on the selective etching of PBAs was performed by Hu *et al.*, where the faces of PB cubes were protected by cetyltrimethylammonium bromide (CTAB), creating elongated cuboids in the presence of HCl.⁵⁹ In the absence of CTAB, the etching is random, while with its presence, a selectivity is observed for directional etching. In Fig. 2G–I, the etching of the cubes from corners, which have higher energy, is shown over-time, leading to the elongated-cube morphology, while faces are protected by CTAB (Fig. 2I). Similarly, hot etching of PB mesocrystals in the presence of polyvinylpyrrolidone (PVP) can produce hollow particles.⁶⁰ In this method, mesocrystals and PVP were strategically chosen to promote the etching inside the particles. In comparison, single PB crystals are defect-free and do not have a high energy grain boundary to let the HCl molecules diffuse inside the particles. Therefore, the etching starts at the surface and creates superficial voids. The role of PVP is to bind with the iron atoms in PB and control the etching rate. A thicker PVP layer inhibits etching, while too little PVP cannot

guarantee the uniformity of the hollow particles. Depending on the particle size and temperature, these particles can be transformed upon calcination into different phases of iron oxide.⁶¹ Most PBAs are unstable in basic media. Thus, using bases like NaOH or NH₄OH became common to etch them. Nevertheless, the presence of OH[−] can start the simultaneous formation of metal oxide/hydroxide, directly leading to PBDs.⁸ Therefore, the concentration, temperature, and/or etching time must be carefully controlled. The use of ammonia has consistently been demonstrated to preferentially etch the corners of the cubic structures of different PBA compositions, indicating a reliable way to form hollow cages.^{22–24}

Fig. 2J and K shows an example of nickel hexacyanoferrate (NiHCFe) cages produced by ammonia etching.²³ As the etching depends on defect density, a less crystalline PBA will induce a faster etching rate, leading to over-etching and collapse of the cubes at prolonged etching times.²³ Due to the increased surface area, hollow particles are attractive for improving the performance in applications directly affected by the available surface area and mass diffusion. Consequently, etching has been further developed and utilized with other synthesis conditions,



like milder etchants such as urea.²⁰ The control of the etching rate is a crucial part of tailoring the morphology, producing uniform hollow/porous particles, and avoiding structure collapse during the etching or derivatization step. For added control of the chemical composition of the PBA, etching can also be carried out along with ion exchange.

3.1.3 Ion exchange. The ion exchange process is a solubility- and equilibrium-driven method to modify the PBA chemical composition and comprises two sub-categories of anion and cation exchange. Most of the time, this process also changes the morphology, creating core-shell structures, hollow particles, or other hierarchical structures. Similar to etching, depending on the conditions, ion exchange can also directly lead to PBDs rather than simply modifying PBA characteristics, for example, with NaOH treatments, as will be discussed further.⁸ The advantage of the PBA co-precipitation method is that one PBA can be a seed for the growth of a second PBA composition, creating core-shell structures. The difference in solubility of the two phases promotes ion-exchange processes, which can change the morphology by creating yolk-shell or completely hollow materials. The difference in PBA solubility compared to that of other metal salts can also be used to prepare PBA compositions that are normally not stable by direct co-precipitation. For example, cobalt in cobalt hexacyanocobaltate (CoHCCo) can be partially exchanged for Mo by adding MoO₄ to a CoHCCo suspension²² (Fig. 2N and O). Mo occupies the M-NC sites due to the weaker character of the Co-NC bond compared to that of Co-CN. This site occupancy later plays an essential role in the derivatization process, leading to a hybrid composed of Mo₂N and Co₃O₄. In PBAs, the coordination of the metal to the carbon of cyanide has a much stronger character than the one to nitrogen. Therefore, in many ion-exchange strategies, only the M-NC can be replaced in the original structure. Even in the case of complete dissolution of the PBA to react with the salt additive, the new metal ion will react with the [M^{x+}(CN)₆]^{(6-x)-} unit, retaining the M'-CN character. Zhang *et al.* combined etching with ion exchange to modify chemical composition while creating porosity.²⁴ When cubes of nickel hexacyanocobaltate (NiHCCo) are mixed with ammonia, the corners are etched, creating hollow cages. At prolonged times, the etching continues at the edges until the six cube faces are separated, leading to plate-like morphology. If palladium salt is mixed with NiHCCo and ammonia, Pd ions partially replace Ni (as they are coordinated with nitrogen). Interestingly, ion exchange accelerates the morphology change caused by ammonia, directly leading to PdNiHCCo plates rather than hollow cages. Even if the NiHCCo cubes are first etched and then mixed with Pd, hollow cages cannot be accomplished, indicating that ion exchange preferentially takes place at the edges, causing dissolution and collapse of the cubes. A similar cation exchange based on this principle was conducted by synthesizing a more soluble manganese hexacyanoferrate (MnHCFe) and then adding cobalt nitrate that replaced Mn atoms to form CoHCFe in the presence of C₂H₂OH (Fig. 2L and M).⁶² Ion-exchange in this way can be regarded as similar to the templating method, and the initial PBA before ion-exchange is regarded as the sacrificial template.

3.1.4 Coating and surface modification. The coating of PBA particles is performed to improve the electrical conductivity of PBDs as most of the derivatives, like metal oxides, or sulfides, have intrinsic low conductivity. As a secondary effect, the coating can also prevent particle aggregation and coarsening during derivatization.⁶³ Some studies report the successful capitalization of carbon atoms of cyanide ligands as the source to produce conductive carbon within the PBDs.²⁴ Nevertheless, this is achieved under specific and mild conditions like low temperature (<400 °C) and a N₂ atmosphere, which is unsuitable for most derivatization processes. Therefore, the coating step is usually performed with a carbon precursor that can later be converted into a conductive carbon shell. The coating can be performed by using polymers that bind to the material. This binding ability can be an inherent property of the polymer or has to be facilitated by treating the surface and adding elements that ease the attachment of the coating precursor to the substrate. Two main examples are resorcinol formaldehyde (RF) and polydopamine (PDA).⁶³⁻⁶⁷ RF can be used as a shell on PBA particles to produce core-shell morphology (Fig. 2P and Q). These particles can then be converted to a yolk-shell by heat treatment. A RF resin shell can be implemented on particles by using a surfactant, such as CTAB, that is stabilized on the PB particle surface and promotes the polymerization of resorcinol and formaldehyde.⁶⁷ Coating with PDA can be performed in a single step and simultaneously with PBA co-precipitation.^{63,65} This is due to the self-polymerization of dopamine hydrochloride through its oxidation in the presence of Fe³⁺ or some other oxidized metals. The polymerization takes place by non-covalent bonding of Fe³⁺ and catechol. The pH of the solution or the presence of oxidative agents further promotes polymerization kinetically and thermodynamically.⁶⁵

A recent study observed that the incorporation of a PDA affected the particle size and material composition. In the synthesis of CuHCFe, the presence of a PDA coating stabilized potassium in the PBA crystal, which subsequently affected the final derivative composition.⁶³ Electrospinning is also an adopted strategy to cover the PBAs with polymeric carbon precursors. By dispersing the synthesized PBA particles in the spinning solution, fibres of PBAs embedded in a carbon matrix are produced. Upon heat treatment, the particles are converted into the targeted PBD, while the fibres can carbonize and form a network of conductive carbon.⁶⁸⁻⁷⁰ Besides acting upon conductivity, the PBA surface can be modified or coated with other materials that provide extra elements in the derivatization process. For example, adding thiols to the material can provide a source of sulfur to produce PBD metal sulfides.⁷¹ Anchoring metal precursors can alter the metallic derivative's composition and morphology. For example, CoHCCo cubes are modified with Ni(OH)₂, creating a core-shell composition. Upon sulfidation, both materials are converted, creating a CoS₂@NiS₂ hierarchical structure rather than a homogeneous mixture of CoS₂ and NiS₂.⁷²

3.1.5 Composites and hybrids. Creating composites or hybrids with other materials that do not necessarily change PBA particles but rather act as a support or active material in PBD



application is one of them. For example, carbon nanotubes (CNT),^{73,74} carbon cloth,⁷⁵ graphene,^{76,77} and nickel foam,^{58,78–80} among others, can act as a substrate for particle growth or simply anchoring. In cases where direct anchoring of PB on the substrate is impossible or inefficient, a second substrate can be used. Fig. 2R and S show an example where NiCo arrays were first formed by a hydrothermal procedure on carbon cloth, and then NiHCCo was formed on the arrays.⁷⁵ These substrates are rather stable up to high temperatures and do not actively change PBA particles nor modify them upon derivatization. However, they act as a support for a PBD material while improving mechanical and electrical properties. Materials with target properties can also be added that do not necessarily decompose or react during the derivatization process. Wang *et al.* modified the surface of PB cubes with CeO₂ nanoparticles.⁸¹ The modification occurs through a redox reaction between Ce(OH)²⁺, formed due to hydrolysis of hexamethylenetetramine, and Fe(III) species of PB. This mechanism leads to an intimate interaction between the as-produced CeO₂ particles and the PB surface, preventing the aggregation or segregation of the particles during heat treatment.

3.1.6 Other approaches. Simply modifying PBA synthetic conditions can also significantly change the morphology or composition. For example, by varying the ratio between Co²⁺ and [Fe(CN)₆]³⁻ in solution, the morphology of CoHCFe can progress from rounded cubes to nanoframes.⁸² At the same time, increased ageing time can lead to hollow particles, which is possibly a greener alternative to the etching methods. Most of the PBA studies rely on co-precipitation. There are alternative synthetic methods for PBA preparation, for example, electro-deposition which can better control particle size, or the hydrothermal method, which can tune porosity. Wang *et al.*¹⁵ controlled manganese hexacyanocobaltate (MnHCCo) morphology and porosity by varying reaction times during hydrothermal processing. The particles evolve from rounded cubes to cross-shaped etched faces.¹⁵ The morphology is then retained upon pyrolysis. In this case, no pre-treatment *per se* is applied, but the PBA synthesis is rationally designed. As previously mentioned, the synthetic routes for controlling PBA composition, growth, and morphology are plenty, and many (if not most) of them remain unexplored for PBD synthesis.²⁸ The combination of the synthesis routes and parameters with pre-treatment methods gives space for improving the control over PBD morphology and composition and better tuning of their properties.

3.2 Derivatization

We define derivatization as the step in which a PBA is used as a template/precursor and converted into another material. The two widely adopted methods are hydrothermal and thermal syntheses, through which many chemical compositions can be derived. They are usually relatively simple and fast methods with great scalability potential. Liquid methods are far less reported. However, they enable complex compositions and morphologies. The following metallic compounds have been reported as derivatives from PBAs: carbides, oxides, sulfides,

fluorides, hydroxides, nitrides, phosphides, phosphosulfides, selenides, and selenophosphides. In addition, metal alloys or pure metals and carbon can be derived from PBAs by extra steps, besides composites or hybrids within these compositions. A primary factor separating each group of compounds is the temperature of the treatment. Because they have different thermal stabilities, one can control the dominant phase by controlling the temperature. Both thermal and hydrothermal treatments can be used for lower-temperature treatments, but only thermal procedures can be conducted for higher temperatures. The final chemistry of the derived compound depends on the environment during derivatization, besides the (pre-treated) PBA composition itself. In thermal treatments, the atmosphere can carry the reactive element, for example, oxygen (in synthetic air or O₂) or nitrogen (in NH₃). It can also be a carrier of the reactive material typically placed upstream in the furnace or mixed with the PBA. The gas can also be an inert component, enabling the synthesis of carbides, for example.

Similarly, additional salts can be placed in the media to promote specific compositions in hydrothermal or liquid methods. For example, by hydrothermal treatment of a Co–Ni PBA with ammonium thiomolybdate, mixed Ni–Co–Mo sulfide can be derived.⁸³ Here, an overview of the derivatization strategies is provided for each compound group. These procedures are summarized and shown schematically in Fig. 3 and Table 2.

3.2.1 Oxides. These compounds were the first and most widely reported PBDs, as they can be easily prepared through a simple standalone thermal step, or subsequent to hydrothermal, and liquid methods.^{8,11,12,22,55–59,61,67,69,81,84–87} During thermal treatment, oxidation can be achieved in open air, synthetic air, or oxygen. To successfully derive metal oxide or mixed metal oxides from PBAs, the temperature and duration of the treatment have to be controlled with precision. A broad range of temperatures from 250 °C to 900 °C can be implemented for oxide derivatization, depending on the desired oxide phase. PB has been extensively investigated to produce iron oxides, given the two iron centres present in its structure. A great compilation focused on PB-derived Fe_xO_y can be found elsewhere.¹³ In general, the thermal decomposition of PB enables the stabilization of other phases of Fe₂O₃ rather than α -Fe₂O₃. The crystallinity and resulting phase depend not only on the temperature but also on the PB particle size and morphology. In a multi-step approach, Liu *et al.* reported yolk-shell spheres of Fe₂O₃@C that were further treated to produce sulfides (Fig. 3C).⁶⁷ Hu *et al.* prepared hollow PB particles of different sizes based on the PVP method.⁶⁰ When calcined at 250 °C, the smaller particles (110 nm) led to a mixture of amorphous and γ -Fe₂O₃, while the larger ones (190 nm) resulted in the γ -phase only.⁶¹ Similarly, when calcined at 400 °C, the large particles oxidized into single α -Fe₂O₃ while the smaller ones were composed of a mixture of α - and γ -Fe₂O₃. In addition, if standard non-hollow small PB cubes (110 nm) are heat-treated, no crystallinity is achieved even at 400 °C. This indicates that the smaller the surface area, the slower the crystallization and conversion. When different metals are present in the structure, more complexity is added to the oxidation of PBAs. Since most metals have a high oxygen affinity, homogeneous



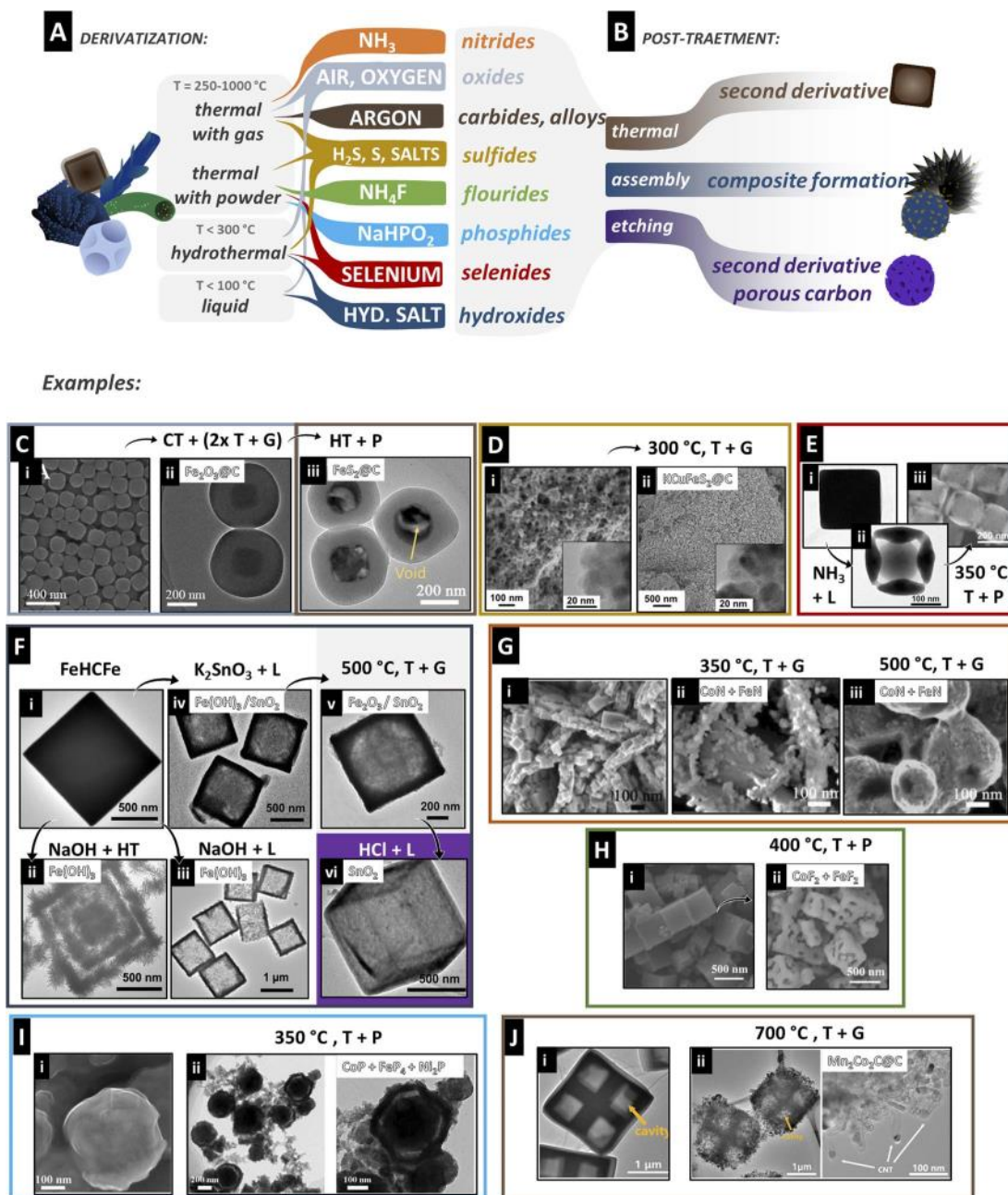


Fig. 3 (A and B) Overview of typical compounds derived from PBAs and the common route for derivatization. (C) Consecutive treatments of PB to obtain $\text{FeS}_2\text{@C}$ yolk-shell structures. Coating with resorcinol followed by 2-step annealing leads to a $\text{Fe}_2\text{O}_3\text{@C}$ yolk-shell (ii). Further hydrothermal treatment with thioacetamide leads to the final derivative. Reproduced with permission of ref. ⁶⁷. Copyright 2019 American Chemical Society. (D) Carbon-coated mixed metal sulfide nanoparticles obtained by thermal treatment in $\text{H}_2\text{S}/\text{Ar}$ gas. Reproduced with permission of ref. ⁶⁵. Copyright 2022 American Chemical Society. (E) Cages of mixed selenides obtained through etching with ammonia solution (ii) followed by thermal treatment with Se powder in N_2 . Reproduced with permission of ref. ²³. Copyright 2017 WILEY-VCH Verlag GmbH & Co. KGaA, Weinheim. (F) Several derivatives obtained from PB by different methods: (ii and iii) treatment with NaOH produces multi-shelled (ii) or hollow (iii) metal hydroxide cubes with hydrothermal treatment (ii) or in room temperature solution (iii). (iv) New metals can be incorporated by the dissociation of metal oxide salts and form partially hollow cubes of hydroxide/oxide mixtures that can be heat treated in air to form oxides (v) and further etched with acid to remove one phase (vi) creating single metal oxide hollow cubes. Reproduced with permission of ref. ⁸. Copyright 2013 American Chemical Society (G) Hierarchical metal nitrides coated on Ni foam/ $\text{Co}(\text{OH})_2$ obtained by thermal treatment with NH_3 . The higher the temperature, the more coarsening occurs (ii and iii). Reproduced with permission of ref. ⁵⁸. Copyright 2018 WILEY-VCH Verlag GmbH & Co. KGaA, Weinheim. (H) Porous cubes of metal fluoride mixtures directly obtained from thermal treatment with NH_4F in argon. Reproduced with permission of ref. ²¹. Copyright 2019 Elsevier B.V. (I) Ternary mixed metal phosphide core-shell particles are obtained by annealing with NaH_2PO_2 in N_2 . Reproduced with permission of ref. ¹⁰². Copyright 2021 American Chemical Society. (J) Porous hollow cross-shaped frames of mixed metal carbide@carbon nanotubes obtained by direct annealing of the PBA in Ar. Reproduced with permission of ref. ¹⁵. Copyright 2020 Wiley-VCH GmbH. CT: coating, T + P: thermal + powder, T + G: thermal with gas, HT: hydrothermal, L: liquid.



Table 2 Examples of the PBA derivatization process and application of the resulting PBD^c

PBA, morphology	Pre-treatment (method) ^{a,b} , conditions, morphology	Derivatization (method) ^b , conditions, morphology	Post-treatment	PBD	Application	Ref
NiTCNi, nanoplates		(T + P), NaH ₂ PO ₄ , Ar, 300 °C, 2 h, porous nanoplates (L) 2 M NaOH, RT, 10 min, amorphous porous nanoplates (T + G), air, 300 °C, 1 h, porous nanoplates		Ni ₃ P ₄ + Ni ₂ P + C Ni(OH) ₂ NiO	OER OER OER	105
CoHCFe, cubes	(ET + HT), urea, frames	(T + P) NaH ₂ PO ₄ , N ₂ , 300 °C, 2 h, porous nanoframes		Co _{0.6} Fe _{0.4} P + C + N	HER and OER	20
CoHCCo, cubes	(CT + L), Ni(NO ₃) ₂ + urea, core-shell	(T + P), thiourea, N ₂ , 350 °C, 2 h, core-shell		CoS ₂ @NiS ₂	Capacitor	72
FeHCFe, cubes	(ET + HT), 0.2 M NaOH, hollow box	(T + G), air, 300 °C, 6 h, hollow box		α -Fe ₂ O ₃ α -Fe ₂ O ₃	Li-ion battery	8
NiHCCo, cubes	(ET), RT, 0.2 M NaOH, yolk-shell porous box	(T + G), air, 300 °C, 6 h, yolk-shell porous box		SnO ₂ , porous hollow box	Li-ion battery	16
NiHCCo, cubes	(ET + IE), K ₂ SnO ₃ · 3H ₂ O, Fe(OH) ₃ /SnO ₂ hollow box	(T + G), air, 500 °C, 6 h, α -Fe ₂ O ₃ /SnO ₂ hollow box	HCl etching	NiCo alloy@C	OER	94
NiHCCo, cubes	(TP), electrospinning nanofibers	(T + G), air, 200 °C, 2 h, nanofibers	Thermal annealing 800 °C, Ar/H ₂	NiS ₂ NiCo + C	Solar cells Li-S battery	65
CoHCFe, cubes on Co(OH) ₂ sheets	(ET + IE), (NH ₄) ₂ S, hierarchical microspheres	(T + P), sulfur, N ₂ , 350 °C, 2 h, hierarchical microspheres		NiCo + C	OER and HER	58
FeHCFe, cubes	(CT), PDA, core-shell	(T + G) Ar, 600 °C, 2 h, hollow nanocages (T + P) NaH ₂ PO ₄ , Ar, 400 °C, 2 h, hollow nanocages (T + G) air, 450 °C, 2 h, cubes (T + G) NH ₃ , 450 °C, 2 h, cubes (T + G, HT) Ar, 150 °C, 2 h, 600 °C, 2 h, yolk-shell Fe ₃ O ₄ @C	Hydrothermal, TAA, 160 °C, 20 h	Co ₃ O ₄ + Fe ₃ O ₄ Co _{3.47} N + Fe ₃ N FeS ₂ @C	Li-ion battery	67

^a ET: etching, IE: ion exchange, CT: coating, and TP: template. ^b T + P: thermal with gas, HT: hydrothermal, and L: liquid. ^c CoHCFe: cobalt hexacyanoferrate, FeHCFe: iron hexacyanoferrate (PB). HER: hydrogen evolution reaction. NiHCCo: nickel hexacyanocobaltate. NiTCNi: Ni[(H₂O)₂[Ni(CN)₄]_n · xH₂O]. OER: oxygen evolution reaction. RT: room temperature, and (TAA): thioacetamide.

derivatization might not occur at low temperatures and a short derivatization time. This might result in mixtures of single-metal oxides over mixed-metal oxides due to a higher oxygen affinity of one of the metallic species. For example, upon oxidation of CoHCFE nanoframes at 350 °C for 2 h, the resulting oxide is composed of a mixture of Co_3O_4 , CoFe_2O_4 , and K_2CoO_3 .⁵⁶ Meanwhile, oxidation of hollow nanocubes and nanospheres of CoHCFE at 500 °C for 3 h led to a single phase of $\text{Fe}_y\text{Co}_x\text{O}_4$.⁵⁵ Phase diagrams can be used as an estimation guide while reducing the strength of oxidation by decreasing the synthetic air-to-argon ratio or using carbon dioxide gas can help to achieve better control over oxidation. Li *et al.* reported a copolymer-co-morphology synthetic strategy to prepare spinel oxides, where metal ratios initially tuned the composition of the oxide in the PBA.¹¹ In this approach, Mn–Fe hexacyanocobaltate ($\text{Mn}_y\text{Fe}_{1-y}\text{HCCo}$) with different Mn/Fe ratios is prepared by simultaneous addition of FeCl_2 and $\text{Mn}(\text{NO}_3)_2$ to $\text{K}_3[\text{Co}(\text{CN})_6]$. When heat-treated at 500 °C for 1 h, spinel $\text{Mn}_x\text{Fe}_{1.8-x}\text{Co}_{1.2}\text{O}_4$ ($0 < x < 1.8$) hollow nano-dice are obtained. Besides tuning the composition, the decrease in the Mn content leads to a morphological progression from cubes to spheres, demonstrating that the chemical composition also plays a role in morphology control. In terms of morphology, shrinkage of PBA particle is normally reported when being oxidized due to the removal of the CN units. This is followed by an overall increase in surface roughness and surface area, which is desired in many applications. Though many studies report a direct templating of PBA into PBDs, that is, changing the composition but retaining the original PBA morphology, that is not always the case. Zhang *et al.* demonstrated the morphological evolution of PB cubes at different treatment temperatures.⁸⁵ When crystalline PB cubes of 1 μm are heat treated at 350 °C, the outer part of the cubes is oxidized, while the centre atoms diffuse outwards, creating a Fe_2O_3 shell-microbox. When the temperature is increased to 550 °C, there is particle coarsening, resulting in porous hollow microboxes, which further progress to a hierarchical structure of hollow boxes composed of Fe_2O_3 nanoplates at 650 °C. This shows that even in the absence of pre-treatments, hollowness and morphology can be tuned with heat treatment parameters. Hollowness in PBA particles through heat treatment has been explored for other compositions as well. This is achieved through the Kirkendall effect, where the difference in the diffusion of the metals, or the metals and the gas, leads to internal voids in the PBD particles. If well controlled, morphologies like yolk–shell can be achieved.⁸⁸

Though less explored, liquid methods are also used for deriving PBA into oxides. However, this is achieved by the initial derivatization of PBA into hydroxides and further thermal treatment of PBD–OH. Therefore, the liquid approaches will be discussed in the hydroxide section.

3.2.2 Sulfides and selenides. Derivatization of PBA to these chalcogenides can be performed by both hydrothermal and thermal procedures, while sulfides have also been achieved by liquid methods.^{23,67,71,72,75,76,83,89,90} In the thermal method, H_2S can be directly used, or sulfur powder can be heated to produce sulfur vapour and combined with H_2 gas to diffuse as H_2S gas in the PBA structure. Sometimes sulfur or sulfur-containing

additives are incorporated in the PBA particles in pre-treatment steps, acting as a source of sulfur during the heat treatment.⁷¹ Similar procedures can be performed by putting selenium powder in the upstream side of the furnace or simply mixing the ground powder with other reactants. Temperatures between 300 and 500 °C usually provide the necessary energy for the formation of homogeneous chalcogenides.^{72,75} Nevertheless, partial sulfidation/selenization through thermal methods is more difficult to control, normally resulting in complete conversion of the treated materials.^{63,71}

Bornamehr *et al.* were able to completely convert CuHCFE into chalcopyrite within only 10 minutes of treatment at 300 °C with H_2S gas.⁶³ In this work, the authors demonstrated the effect of the coating on the derivative composition. The polydopamine used to coat and control the particle size also led to a potassium-rich and less defective CuHCFE phase. As a result, the sulfide derived from the coated material was KCuFeS_2 , while for the uncoated, it was CuFeS_2 (Fig. 3D). This work also presents significantly smaller derivative particles (<100 nm) than the usual 0.5–2 μm range. Higher surface area can be achieved with smaller particles; however, it is more difficult to incorporate morphology complexity in this size range.

In the hydrothermal procedure, a sulfur-containing compound such as the Na_2S salt or thioacetamide can release S^{2-} anions and promote anion exchange in the PB lattice to form metal sulfide.^{67,91} For selenides, the selenium powder can be dissolved in water to use as the reactive environment in hydrothermal methods.⁹² Reaction temperatures for forming metal chalcogenides in hydrothermal synthesis are reported between 120 and 200 °C. However, the product of hydrothermal synthesis is often subjected to a subsequent thermal annealing process to achieve complete conversion and crystallinity. Liu *et al.* reported an interesting multi-step procedure to prepare yolk–shell spheres of $\text{FeS}_2@\text{C}$ derived from PB (Fig. 3C).⁶⁷ Initially, PB particles are coated with a resorcinol–formaldehyde resin (RF). Upon two-step annealing in Ar at 150 °C and 600 °C, the PB particles shrink and oxidize to Fe_2O_3 while the RF coating graphitizes into a carbon shell, forming a yolk–shell structure. The spheres were modified with thioacetamide, and through hydrothermal synthesis at 160 °C, $\text{FeS}_2@\text{C}$ yolk–shell particles were achieved. The coating prevents agglomeration and coarsening of particles, while annealing at higher temperatures is essential to achieve conductivity in the formed carbon shell. Another way to achieve sulfides with yolk–shell morphology is through the Kirkendall mechanism and ion exchange. This was performed, for example, by reacting cadmium hexacyanoferrate (CdHCFE) with Na_2S at 150 °C under 10 atm.⁹³ The S^{2-} ions are exchanged with $[\text{Fe}(\text{CN})_6]^{3-}$, forming CdS. As the Cd^{2+} ions diffuse outwards faster than S^{2-} can diffuse inwards, hollowness starts to appear between the surface and the centre of the cubes, resulting in a CdS yolk–shell structure. When NiHCCo is reacted with Na_2S at 100 °C, the cube faces are etched first, and the morphology evolves to NiS_x nanocages rather than yolk–shell structures.⁹¹ Using $(\text{NH}_4)_2\text{S}$ instead of Na_2S drastically changes the morphology. Huang *et al.* prepared hierarchical NiS_2 particles by treating NiHCCo cubes with $(\text{NH}_4)_2\text{S}$ by the hydrothermal method at 100 °C.⁹⁴



Through hydrolysis, OH^- and S_x^- are formed, and OH^- slowly etches the Ni^+ ions, leading to $\gamma\text{-NiOOH}$. At prolonged times, NiHCCo cubes are completely dissolved, and $\gamma\text{-NiOOH}$ is partially converted to NiS_x while the morphology evolves to hierarchical microspheres of $\gamma\text{-NiOOH}/\text{NiS}_x$. These particles are crystallized and converted to NiS_2 by thermal treatment at 350°C with sublimed sulfur powder. These last studies are the few examples where the metal from the $[\text{M}(\text{CN})_6]$ unit is completely removed from the final derivative, as no iron⁹³ or cobalt^{91,94} remains in the material. Nai *et al.* also utilized ammonia to prepare cages of NiHCFe ,²³ by heat treatment with Se powder at 350°C , obtaining a mixture of NiSe_2 and FeSe_2 (Fig. 3E). Like oxides, obtaining mixed metal chalcogenides rather than a mixture of single metal components also requires careful tuning of derivatization parameters. Selenide powder was also used as a post-treatment to dope $(\text{CoFe})\text{S}_2$.⁹⁵ Hollow cubes of CoHCFe were prepared in the presence of trisodium citrate and then mixed with sulfur powder. After heat treatment at 350°C for 2 h, $(\text{CoFe})\text{S}_2$ is formed. Mixing the sulfide with selenium powder and treating it at 250°C for 8 h leads to the Se-doped $(\text{CoFe})\text{S}_2$ hollow boxes. The inverse process, first selenization followed by sulfidation was also performed, resulting in $\text{S}-(\text{CoFe})\text{Se}_2$.

3.2.3 Hydroxides. The conversion of PBAs into hydroxides can be realized through liquid and hydrothermal procedures.^{8,58,94} Perhaps the most extensive example is the work by Zhang *et al.*⁸ In this work, PB cubes were transformed into different hollow and hierarchical cubes with different compositions driven by basic etching and ion exchange. In the presence of NaOH solutions, PB is converted to $\text{Fe}(\text{OH})_3$. The morphology of the resulting cubes depends on the NaOH concentration and temperature, generating yolk-shell, hollow cubes, or multi-shelled microboxes (Fig. 3F(ii) and (iii)). In the presence of MO_x salts ($\text{K}_2\text{SnO}_3 \cdot 3\text{H}_2\text{O}$, Na_2SiO_3 , Na_2GeO_3 , NaAlO_2 , or $\text{NaBO}_2 \cdot 4\text{H}_2\text{O}$), basic etching from salt hydrolysis and ion exchange takes place, resulting in homogeneous $\text{Fe}(\text{OH})_3/\text{MO}_x$ hollow cubes (Fig. 3F(iv)). Upon annealing, they can be converted into mixtures of Fe_2O_3 and MO_x (SnO_2 , SiO_2 , GeO_2 , *etc.*) and further single MO_x hollow cubes by etching out the Fe_2O_3 phase (Fig. 3F(v) and (vi)). This work demonstrates the versatility of changing morphology and composition by finely tuning reaction parameters.

As discussed in the sulfide section, $(\text{NH}_4)_2\text{S}_2$ can also go through hydrolysis, producing NH_3 and H_2S which are decomposed into OH^- and S_x^{2-} .⁹⁴ This leads to a simultaneous transformation of the PBA into oxyhydroxide and partial sulfidation with a complex morphology evolution. In general, the use of a metal salt rather than a strong base or ammonia leads to slower and more controlled derivatization into hydroxide. This is also a pathway to introduce new elements to the PBA/PBD structure, especially if they do not typically form stable PBA complexes, like Ge, Si, Al, and B in the work of Zhang *et al.*⁸ This strategy was also used by Hu *et al.* to form oxide mixtures of Fe and W.⁹⁶ By stirring PB cubes with Na_2WO_4 at 50°C , $\text{Fe}(\text{OH})_3/\text{WO}_{3-x}$ hollow cages are formed. Through calcination at 550°C for 6 h, $\text{Fe}_2\text{O}_3/\text{W}_{18}\text{O}_{49}$ composites are then obtained. The liquid methods allow the synthesis of more complex or hierarchical

structures, which is usually not the case for thermal treatments. Therefore, PBD-OH is typically used as a precursor for other PBD compositions like PBD-oxides, instead of direct oxidation of PBAs, and PBD-sulfides, by heat treatment with sulfur powder.⁹⁴

3.2.4 Fluorides and nitrides. These compounds remain little explored and are mainly synthesized by thermal procedures. For nitrides, derivatization can be achieved with the aid of NH_3 gas.^{58,97} Some studies capitalized on the nitrogen from CN ligands and prepared metal nitrides as well.²² Nevertheless, most commonly, nitrogen from CN is either removed or results in N-doped carbon rather than metal nitrides. Of the few reports on nitrides, the majority covers the conversion of PB into Fe_2N , and most metals/compositions are still to be studied.^{97,98} Wang *et al.* demonstrated that under an NH_3 flow, CoHCFe templated over $\text{Co}(\text{OH})_2/\text{nickel}$ foam is converted into a mixture of FeN and CoN.⁵⁸ At a lower temperature (325°C), interconnected nanosheets are obtained. When the temperature increases to 350°C , 450°C , and 500°C , coarsening and coalescence occur, resulting in complete loss of the initial nanostructure (Fig. 3G). The higher the temperature, the less nitrogen is incorporated into the material, resulting in mixtures of nitrides with different stoichiometric ratios. Wang *et al.* described the formation of FeCoNiN on nickel foam (NF) by treatment of $\text{CoHCFe}/\text{Ni}(\text{OH})_2/\text{NF}$ with ammonia. However, the large amount of Ni suppresses more structural and composition insights into Co- and Fe-derived components, with evidence of Ni_3N .⁹⁹ Fluoride-based PBDs are also quite limited, though more restricted in terms of synthetic approaches, given the toxicity and hazards of fluorinated compounds, especially at high temperatures. One report uses the templating approach to grow NiHCFe onto $\text{Ni}(\text{OH})_2/\text{Ni}$ foam nanosheets.⁷⁹ This material is then fluorinated by a thermal process through the decomposition of NH_4F at 350°C for 2 h and the effect of the NH_4F ratio and temperature were evaluated. They show that fluorine suppresses the release and decomposition of CN units, producing a more stable hierarchical structure compared to that of the same sample annealed in argon. Fluorination results in F-doped NiFeOOH rather than a fluoride compound. Nevertheless, F-doping plays an important role in the catalytic activity of the material. Differently, when bare CoHCFe cubes are heat treated at 400°C with NH_4F , etched porous cubes of CoF_2 and FeF_2 mixtures are formed (Fig. 3H),²¹ indicating that Co/Fe mixtures might be more prone to fluorination than Ni/Fe.

3.2.5 Phosphides and phosphor-containing compounds. Due to their high hydrogen evolution activity as catalyst and their low cost as opposed to the noble metals, different phosphor-containing compounds have been investigated as PBDs, being the emerging PBD class of compounds after the pioneering oxides.^{20,64,65,74,75,77,78,80,82,100,101} Metal phosphides are derived by a thermal procedure using NaH_2PO_2 powder under an inert gas flow such as Ar or N_2 . Similar to selenization and sulfidation, the powder can be mixed with the reactants or placed on the upstream side of the tube.^{20,65} Zhou *et al.*¹⁰² prepared mixtures of 3 different phosphides by treating FeHCCo with NiCl_2 to form NiFeHCCo , and further heat treatment with NaH_2PO_2 in N_2 . The heating leads to a core-shell



structure that could be related to the higher concentration of Ni at the surface (Fig. 3I). As observed for the derived-oxides, the PBA composition also affects the morphology of the derived phosphide. Ding *et al.* prepared CoHCFe, NiHCFe, and MnHCFe by co-precipitation and phosphorized them under the same conditions (400 °C, Ar, and NaH₂PO₂). After the heat treatment, all materials present a rough surface. However, NiFe–P shows higher particle coarsening while MnFe–P presents small particles adhered to the cubes.¹⁰¹ The addition of Se or S powder can result in the formation of selenophosphide or phosphosulfides.^{75,89} Similar to other thermal treatments, a temperature range of 300–500 °C has shown the best resulting products in terms of homogeneity. For example, Liu *et al.* performed sulfidation, phosphorization, and phosphosulfidation of NiHCFe, to evaluate the effect of time and temperature on the composition and morphology.⁸⁹ At 350 °C and under a N₂ flow in the presence of both sulfur and NaH₂PO₂, the cubic morphology evolves to smaller nanosheets after 1 h of annealing, leading to a complete loss of the cubic shape and morphing into nanoflowers after 2.5 h. The flower morphology is not obtained in the absence of either sulfur or NaH₂PO₂, and only deformed and shrunk cubes are produced. Analysis of composition indicates that the flowers are mixed metal phosphosulfide (NiFe)PS₃ rather than individual phosphosulfides. In another phosphide derivatization, similar to the RF strategy, NiHCCo 450 nm cubes were coated by dopamine through the self-polymerization process prior to derivatization.⁶⁵ The material was first annealed at 600 °C to ensure carbonization of the coating while forming a Ni–Co alloy. This results in carbon-coated NiCo hollow cubes. The PBD was then treated with NaH₂PO₂ at 400 °C to convert the alloy into a mixed NiCo phosphide. Jiang *et al.* also utilized dopamine for PBD preparation. They demonstrated a tubular PB morphology rather than the usual cubes.⁶⁴ After coating tubular PB particles with dopamine, the material was converted to carbon-coated FeP. They used the original PB as a cathode and the PBD FeP as an anode in a sodium-ion battery full cell. In many cases, the PBAs are combined with carbon structures prior to the phosphorization process.^{65,74,77} The carbon structures, like carbon nanotubes and graphene, enhance the overall electronic conductivity of the derivative and anchor the PBD particles, demonstrating improved catalytic performances compared to the bare PBD.⁷⁷

3.2.6 Alloys, carbides, and carbon. By heating the PBAs in an inert atmosphere such as Ar, without providing other elements, alloys and metal carbides can be obtained.^{13–17,24,62,65,68,70,84,103,104} For example, the treatment parameters used for oxidation in air can be replicated under Ar to produce a metallic alloy/carbon composite.⁸⁴ While mild conditions will form alloys and carbon mixtures, the formation of carbides requires higher temperatures (>500 °C). This can make it challenging to achieve carbides with different morphological features like high porosity and hollowness. As demonstrated by Wang *et al.*, highly porous cages of MnHCCo can be prepared through prolonged reaction times (Fig. 3J).¹⁵ Nevertheless, when annealed at 700 °C for 2 h, the structures with higher hollowness degrees collapsed. The presence of metal and carbon at high temperatures and under inert

conditions can also favour the growth of by-products like carbon nanotubes, affecting the final morphology of the PBD product.¹⁵ After the derivatization of the metal carbide or alloy/C mixture, porous carbon can be produced through a subsequent etching of the metallic species, for example, by using HF or HCl. This carbon material with high porosity can be very attractive for absorption applications.^{103,104}

3.3 Post-processing

Some PBD synthesis methods involve post-processing steps to reach the desired product quality and characteristics. This can be liquid etching to remove impurities or additives, such as removing metals in the derivative to produce porous carbon.¹⁰³ Simultaneous with etching, more intricate morphologies can be achieved due to ion exchange.⁸ Etching can also be utilized as a post-processing step that removes unwanted phases. For instance, if two oxide phases are formed after derivatization, and one is undesired or detrimental to the performance, it can be selectively etched. It also causes *in situ* porosity formation that can be beneficial to the target product.⁸⁶ Post-processing can also be in the form of mono- or multi-stage annealing, resulting in higher hybridization and graphitization degrees or higher crystallinity of the PBD phases. The PBD particles can be further incorporated into other materials, for example, within MXene layers, to form MXene/PBD composites.⁸⁷ Though they do not fundamentally relate to the PBA derivatization process, these steps affect the resulting PBD composite properties for their target application.

4. PBD properties: structure design and applications

Understanding the structure/property correlation is a key step to enabling PBD use for different applications. Therefore, the derivatization procedure's steps are often engineered to achieve a specific structure. The structure design can be reviewed from two perspectives: first, the elaboration on the PBD synthesis route in each step of pre-treatment, derivatization, and post-treatment; and second, the formation of hybrids and composites by assembling PBAs and other components together. The result of these design strategies is either a final sophisticated morphology such as hierarchical and multi-walled structures that aid the material with improved surface area, mechanical properties, and other characteristics that are beneficial to the final application, or in a chemical composition that improves conductivity, magnetic properties, *etc.* Since each chemical group (carbides, phosphides, oxides, *etc.*) have a diverse effect on performance, the effect of composition can be studied for a particular application, as described in previous revisions.^{6,9,10,25,26} Here, attention will be focused on the effect of morphology on the properties and applications.

4.1 Structure design and PBD characteristics

Pre-treatment usually has a crucial effect on the structure design, mainly when etching and ion exchange are employed. For example, by using PVP or citrate, crystal growth can be



controlled to result in a frame or box morphology.⁵⁷ The derivatization step can heavily influence the PBD structure.^{84,105} Sometimes, due to different precursors (sulfur, selenium, or NaH_2PO_2 powder) and different growth mechanisms of the derivative crystals, the same structure evolves into different morphologies.^{19,89} Heat-treatment parameters can also affect the design. It has been shown that treating PBA particles under the same atmosphere but with different temperatures can result in different oxide morphologies.⁸⁵

Besides the synthesis parameters, even morphological attributes such as the cavity size in the PBA can affect the subsequent derivative morphology. This has been shown for different iron oxide phases derived from PB cages with different cavity sizes under the same derivatization parameters.⁶¹ Particle sizes start from around 200 nm when designing more complex and hierarchical structures. The morphology of smaller particles is usually limited to dense cubic shapes that are not well developed and grown. Smaller particles are more prone to collapse when inducing hollowness and porosity and do not provide the necessary volume for morphology design. Furthermore, methods to modify particle morphology rely on protecting specific planes/surfaces and/or attacks on reactive sites. This requires well-structured particles with high crystallinity. The high surface energy of smaller particles makes it more difficult to control and guide morphology changes.

While the elemental composition of PBDs can be relatively easy to control, the resulting phases and stoichiometry rely on many kinetic and thermodynamic aspects of the derivatization process. A key aspect of PBA composition is the relatively limited amount of stable metalocyanide salts, typically varying between $[\text{Fe}^{\text{II/III}}(\text{CN})_6]^{4-/3-}$ and $[\text{Co}(\text{CN})_6]^{3-}$, sometimes $[\text{Mn}(\text{CN})_6]^{3-}$ or $[\text{Ru}(\text{CN})_6]^{4-}$, though the latter is quite cost-prohibitive. Therefore, most PBA compositions consist of $\text{M}[\text{M}'(\text{CN})_6]$ with $\text{M}' = \text{Fe}, \text{Co}, \text{Mn}$, and sometimes Ru . Even though the M element could vary through a large portion of transition metals, nearly all studies report on PBAs with $\text{M} = \text{Fe}, \text{Co}, \text{Ni}$, and Mn . A few examples of alternative metals already reported – though not all for PBD synthesis – are $\text{Cu}, \text{V}, \text{Mg}, \text{Zn}, \text{Cd}, \text{Ag}, \text{Ti}, \text{Pd}$, and Mo (Fig. 5). Mixing different M units has become one strategy to increase composition complexity or stabilize different metals in the lattice that would not form a standalone PBA, where even a high entropy PBA with 5 different M is described.^{11,106} In principle, mixing different $[\text{M}'(\text{CN})_6]^{6-x}$ units are also possible and has been successfully reported.¹⁰⁷ However, the versatility remains limited. Besides, the M unit can be more easily replaced in the structure in pre-treatment procedures like ion exchange due to the lower $\text{M}-\text{NC}$ bonding strength, providing more flexibility in composition design. The composition of the PBDs will be modified in the derivatization process by incorporating, for example, O, S , or P , and eliminating N and C from the ligands while retaining the metal species (in the absence of post-treatment). Therefore, to some extent, it is possible to predict probable chemical components of PBDs. Nevertheless, the derivatization parameters and morphological features of the PBA precursor will affect the resulting phases. Higher porosity and hollowness provide a larger surface area that can accelerate the conversion or

facilitate the diffusion of the metallic species, resulting in different phases or segregation of components, for example, metal oxides *versus* mixed metal oxides.^{55,56,61}

Though not covered in this review, the PBA synthetic strategy presents many possibilities for altering morphology and composition. Most of the examples presented here involve the synthesis of PBA by co-precipitation and further modifying the surface, morphology, or composition through pre-treatment and derivatization. The synthesis parameters in co-precipitation can also be tuned to change morphology, like the solvent (H_2O , ethanol), temperature, pH or M/M' concentration ratio. A few template strategies utilize different materials as the support for PBA nucleation, directing the 3D macro-structure,^{58,79,108} or as a support and metallic source, where the template itself reacts with the metalocyanide salt to form a PBA, creating better interaction between the template and PBA.¹⁰⁹ Nevertheless, other synthesis methods and processings exist. One approach involves the single-precursor synthesis through the decomposition of $[\text{M}'(\text{CN})_6]$ salt, either by acid-induced or hydrothermal methods.^{110,111} This enables the slow release of M' ions, creating highly crystalline nanoparticles below the 100 nm range, though $\text{M} = \text{M}'$ limits the composition. Electrodeposition has the same controlled nucleation and growth effect but allows for a more varied composition ($\text{M} \neq \text{M}'$), especially if the M source is immobilized in the electrode.^{112–114} Electrodeposition can also orient the morphology¹¹⁵ and create PBA composites with the electrode material, for example, carbon nanotubes¹¹² or graphene.¹¹⁶ Layer-by-layer assembly is another method for controlled orientation of PBA particles while modifying the surface with potential active materials for derivatization, like polymers (for carbonization and conductivity), thiols or amides (for sulfides or N-doped materials), or nanoparticles (for an additional metallic source and compositional complexity).^{80,117,118} Though carbon coating through surface modification is the standard strategy to induce conductivity while avoiding particle aggregation, there are other ways to achieve that, such as electrospinning. Electrospun carbon fibers provide high porosity, conductivity, and specific surface area. PBA particles can be assembled inside the electrospun fibers by electrospinning the PBA particles^{16,68,69} or anchoring the particles on the electrospun carbon fibers.¹⁰⁰ After derivatization, the carbonized fibers act as a conductive matrix for the PBD while providing flexibility and mechanical stability.

4.2 PBD morphology and applications

The applications of PBDs are varied since they can present many compositions. The most attention is given to electrochemical applications such as catalysis, energy storage, and conversion. The effect of properties on the application can be discussed from two viewpoints, namely, the effect of chemical composition and the effect of structure and morphology. The chemical composition results from the used precursor and the media chosen for derivatization. This is usually better controlled and easily tailored, though unpredicted or secondary phases can be formed during the derivatization. The unwanted phases can be



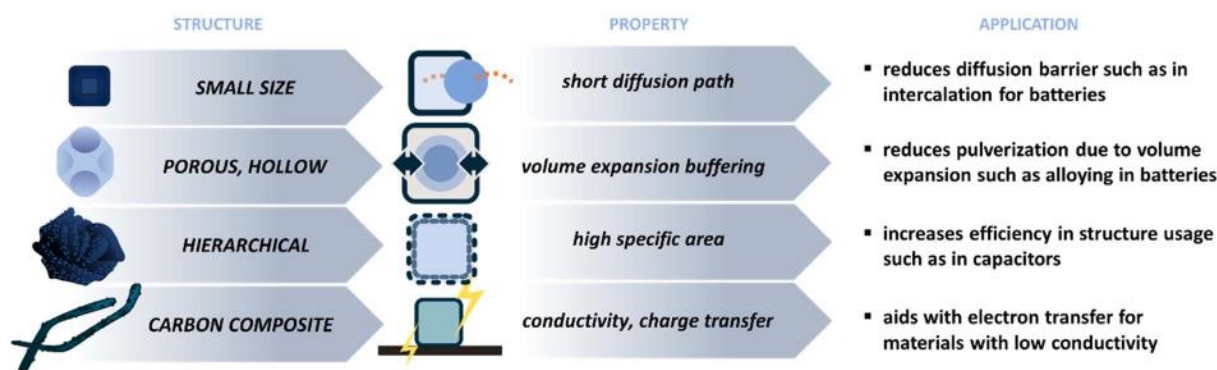
structure, properties, and applications

Fig. 4 Main strategies to tune the structure of PBDs, their resulting properties, and examples in applications that are affected by such strategies.

controlled by changing processing parameters or etching the extra phases as a post-treatment step. The chemical composition will have different effects depending on the application, as the target properties will vary. Therefore, here the properties and their effect on the application are focused on the morphology since there are similar morphological features that are beneficial to different applications, for example, tailoring the structure for smaller particle size to reduce the diffusion paths and increase the reaction rate. Typical morphological features are depicted in Fig. 4, and some examples are addressed in Table 2. These standard features can be divided into the following.

4.2.1 Small particle size. Decreasing the particle size is the most common approach to enhance properties, especially in electrochemical applications. This is a rather simple step that enhances electron transfer and element diffusion by reducing the diffusion paths. This method is extensively explored in the PBA application. It uses the synthesis parameters, such as the salt concentration during co-precipitation or the pH to control the growth of the nuclei. A careful treatment keeps the small size attribute of the template. Therefore, studies on the derivatization of the PBA usually do not focus on the effect of the derivative particle size on the properties but rather use strategies in the pre-treatment step to control the PBA size. Li *et al.*¹³ provided an overview of PB derivatives and the effect of temperature and environment on the particle size and phase change, and their application in energy storage and conversion. By cross-comparing different reported studies, they showed that a larger particle size usually results in higher crystallinity due to smaller surface area and defects. The effect of particle shape can also be observed in parallel to the size effect. For example, a nanosphere morphology can provide better mechanical stability than a nano-cubic structure and enhance the stability during the cycling of a battery electrode. However, with the same diameter, a cubic structure provides a higher surface area. Liu *et al.*⁵⁵ prepared porous nanospheres and nanocubes of iron-cobalt oxide. With the similar size of both morphologies, the spheres provided higher capacity and stability when tested as a lithium-ion battery anode material compared to the cubes

due to the higher cobalt loading and better porosity achieved during the processing.

4.2.2 Hollow and porous structures. This method benefits applications that rely on high surface area and fast diffusion. Nevertheless, such properties can also be achieved by reducing the particle size or through sheet morphologies. Their ability to buffer volume expansions in applications where redox and conversion reactions occur makes hollow structures characteristic and attractive. The most prominent example is metal-ion batteries, which rely on the diffusion of ions (like lithium or sodium) into and out of the particles in each charge and discharge step. Depending on the material, alloying reactions can also be part of the charge storage mechanism, which presents a much more significant volumetric expansion (100–400%). Zhang *et al.*⁸ provided extensive work on hollow metal oxide boxes. They compared the effect of box layers on the stability of the material as an electrode for Li-ion batteries. A higher number of box layers showed better cycling stability, indicating better structural stability during the charge and discharge. For the synthesis of PBDs, they employed all three steps with ion exchange as the pre-treatment by using NaOH, which simultaneously derived iron hydroxide from the PB template, followed by an annealing step to produce crystalline iron oxide. In another report, Liu *et al.*⁶⁷ prepared yolk-shell spheres by coating PB particles with resorcinol formaldehyde. They performed initial annealing and hydrothermal treatment *via* thioacetamide to prepare FeS₂ yolks and carbon shells. The present free space between the yolk and the shell provides room for volumetric expansion, which occurs during the conversion reactions for lithiation and de-lithiation. The shell is not an active material and does not aggregate during the reactions; therefore, a stable cycling performance is achieved.

4.2.3 Hierarchical structure. Hierarchical materials enable macrostructure arrangements with complex morphologies that provide a higher accessible surface area which is critical for applications reliant on surface activity such as catalysis or solar cells. Huang *et al.* prepared nickel sulfide mesospheres made of an assembly of 2D nanoflakes and compared the performance of this material to a similar nickel sulfide phase in nanoparticle



morphology as a catalyst for solar cells.⁹⁴ They started with NiHCCo and performed ion exchange and etching to remove cobalt by using $(\text{NH}_4)_2\text{S}$ salt and further derivatization *via* a thermal treatment by using sublimed sulfur powder. The hierarchical nanosphere material presented better long-term stability and faster electrolyte regeneration, assigned to lower resistance and diffusion impedance compared to the nanoparticles.

4.2.4 Carbon composite. Using carbonaceous materials with a high ratio of sp^2 hybridized carbon atoms increases the conductivity, whether when used as a carbon coating, a substrate, or a matrix, and is a standard approach in applications that rely on facile electron transfer. Forming a coating has the added benefit of the entrapment of unwanted species. Wu *et al.*⁶⁵ explored bimetallic Ni–Co phosphide as a separator and polysulfide mediator in Li–S batteries. To prevent polysulfide shuttling during battery cycling, they designed carbon-coated hollow cages of NiCo phosphide. Although the results are not compared to a coating-less counterpart, successful polysulfide mediation is demonstrated. For this, two strategies are combined: first, a hollow structure to mitigate the volume expansion in polysulfide adsorption, and second, the carbon coating by using polydopamine to entrap these species and increase the capacity stability of the cell. A rather less explored strategy is employing electrospinning to either decorate electrospun fibres by the PBD or to directly electrospin the PBA/D. A 1D structure can be produced by controlling the fibre size and

providing a high surface area and active site availability. Moreover, the polymer-based fibre can be heat treated and used as a carbon substrate to increase the overall conductivity of the composite.⁷⁰ For example, Wei *et al.*¹⁰⁰ prepared FeCo phosphide on nitrogen-doped carbon fibres through electrospinning. They further annealed and calcined the material and then performed a second derivatization by using NaH_2PO_2 powder as the phosphor source. Electrospinning provides a high surface area and access sites to evenly distributed particles while protecting them from agglomeration due to the open fibre morphology, which aids in the catalytic performance.

5. Summary and outlook

The Prussian blue family of compounds emerged as a new class of precursors/templates for synthesizing advanced materials. They provide a source of different metallic species, carbon, and nitrogen arranged in open framework cubic structures. The cubic morphology can be tuned into various complex, hierarchical, and porous/hollow structures, while composition can be changed through surface modification and ion exchange processes. In addition, the template synthesis is water-based and usually low-cost, making it a sustainable and scalable derivatization template. Such structures can be converted into a wide array of metal-based compound compositions whose morphology is a direct product of the PBA template. Conversion is achieved by different derivatization methodologies, mainly

OUTLOOK:

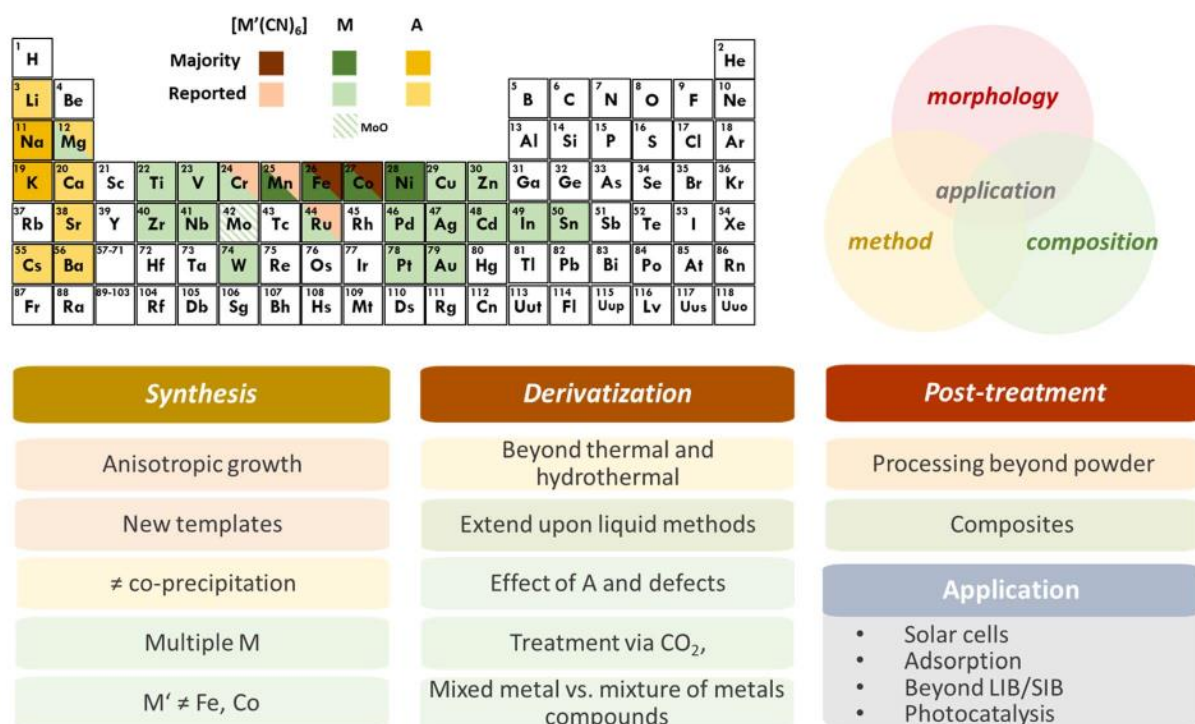


Fig. 5 Outlook on PBDs. Many compositions remain unexplored. Further investigating new synthetic methods, composites and material processing can improve PBD performance in current and new applications.



consisting of thermal and hydrothermal methods. Most derivatives are characterized by increased surface area and homogeneous morphology and composition. The different PBDs and their composites have enhanced performance for several applications, such as catalysis and diverse energy storage technologies.

Though PBD reports are quickly growing, several aspects of using PBAs as templates are overlooked. First, regardless of the increased interest in PBDs, most reports are restricted to a limited number of synthetic approaches and compositions. In addition to the classic PBA synthesis route *via* a liquid method, cyanogels can aid in expanding the PBA chemistry past the transition metal combinations.^{119,120} The extensive work on PBA synthesis and particle control should be taken advantage of to explore and achieve a well-tailored PBA template for derivatization. In terms of composition, much can be done by temperature control, while the ratio of metals will play a defining role in the phases that can be obtained. Combining multiple M species could also contribute to a more diverse range of compositions. For example, the gradient synthesis of PBAs is an unexplored method for PBDs.^{46,47} The gradient enables complex compositions, a mixture of different metal species, and could easily create PBDs with $M_1@M_2$ core-shell structures. Even though PBAs with different M species have been reported, most PBD studies consist of $M = \text{Fe, Co, Ni, and Mn}$ (Fig. 5). Meanwhile, a challenge is posed for compositions without Fe and Co, given the availability of $[M(\text{CN})_6]$ salts. Currently, ion-exchange synthesis seems to be the only described way to remove M' species, besides specific acid washing for Fe removal.

PBA can show different structures with lower or higher degrees of defects (as in the soluble and insoluble forms) and cation content. However, there is still a lack of understanding of whether and how such defects and cations influence the derivative. For example, a few studies observed the presence of alkali-containing phases in the resulting derivative arising from the PBA alkali-rich structure.^{56,63} The counter-cation largely influences PBA structure and properties,¹¹² therefore, more attention should be given to counter-cations present in the PBA synthesis, as it is retained in derivatization through heat treatment. For example, adding Li^+ in the PBA synthesis could lead to a lithiated PBD phase for energy storage applications. The lack of counter-cations in PBA is associated with a defective structure. Defect engineering is a promising method to introduce inherent conductivity rather than adding other components like carbon, for example, in metal oxides. More insight into the effect of defects in the original PBA structure would help better to design PBA synthesis and pre-treatment for defect-oriented PBDs.

In terms of derivatization methods, liquid methods remain limited, even though they have the advantage of mild/room temperature conditions which can prevent the collapse of highly porous/hollow structures. More elaborate compositions and complex morphologies could arise from diving into liquid ion exchange and etching methods during the pre-treatment and derivatization steps. In this case, post-processing could be limited to low-temperature treatments to induce

crystallization, while temperatures for graphitization might be prohibitive. Besides, new experimental approaches could be considered for transforming PBAs into PBDs, like plasma-assisted and electrochemical methods.

When using multiple metallic components, a challenge is to derive single-phase compounds. The weaker bond between $M\text{-NC}$ compared to that between $M'\text{-CN}$ will likely promote better diffusion of M species upon the heat treatment, which can lead to phase separation.¹²¹ Using a gas with lower reactivity (*e.g.*, CO_2) instead of synthetic air can lower the oxidation rate and retain carbon species. Using H_2S gas instead of sublimed sulfur powder also provides a stable sulfur supply that can result in better homogeneity and control in size and phase.

Much was discussed in terms of morphology change and design during PBD synthesis steps. However, that is mainly done starting from cubic particles. Elaborating on the anisotropic growth of PBA particles could unlock a new range of morphologies and properties of PBDs.^{53,54} Expanding on the templating of PBA during their synthesis could also increase the morphological complexity of the resulting PBD. So far, nickel foam is the main adopted substrate for PB growth. Nevertheless, template-oriented growth can be widely varied to produce films, rods, wires, and arrays, among others.^{7,122–125}

Most PBA derivatization results in PBD powders for electrochemical applications. This means processing into electrode materials with the aid of binder, carbon, solvents, and coating processes. Exploring new combinations of PBA synthesis and derivatization like electrospinning, aerogels, 3D printed structures, or self-supporting films can enable the preparation of free-standing and flexible PBD materials. Similarly, the PBDs can also be further processed in post-treatment steps to create new composites or assemblies that are not possible before the derivatization method, for example, the addition of conductive polymers (that would otherwise decompose in the treatments), MXenes (that could themselves convert into oxides, sulfides, *etc.*), nanoparticles (that would coarsen), *etc.*

In terms of application, PBAs are primarily used as templates due to the porous structure with ion-compatible voids and high surface area desired in catalysis and energy storage. Nevertheless, each compound class (oxides, sulfides, carbides, *etc.*) has numerous applications. Both selenides and sulfides have essential applications in solar cells, and only a few reports of PBDs address such use.^{90,94} Waste treatment is also an overlooked potential application of PBDs. The high porosity and surface area make them ideal for absorption, while the tunable voids and metallic species can induce selectivity towards specific compounds. The HER and OER are primarily studied in the widely explored catalysis field. However, (photo)catalytic degradation could greatly benefit from such structured materials. Iron species are known to provide high photocatalytic efficiency. The straightforward implementation of additional metals like Ti, Sn, or Zn in the PBA synthesis can further tune the catalytic activity. At the same time, target pre-treatment and derivatization can result in a highly active material. Similarly, other energy storage systems besides Li-ion, Li-S, and Na-ion batteries could capitalize on the combination of the



composition and structure of PBDs. For example, the catalytic properties could be used in the ORR in Li–air and Zn–air cathodes.

Using PBA as precursors and templates is an exciting strategy to get unique, specific, and sophisticated materials aiming at target properties and applications. The PBD properties strongly correlate to the PBA structure/composition and the experimental steps employed to derivate the PBA. Exciting scientific and technological challenges emerge from this topic. We expect this review to be useful for chemists, physicists, materials scientists, and engineers interested in exploring this fascinating subject.

Conflicts of interest

There are no conflicts to declare.

Acknowledgements

S. H. acknowledges the funding of the PBDS project (HU 2959/2-1) by the German Research Foundation (DFG, Deutsche Forschungsgemeinschaft). The INM authors thank Eduard Arzt (INM) for his continuing support. A. J. G. Z. thanks INCT Nanocarbono, INCT NanoVida, CAPES, and CNPq for financial support.

References

- 1 A. A. Karyakin, *Electroanalysis*, 2001, **13**, 813–819.
- 2 X. Wang and L. Cheng, *Coord. Chem. Rev.*, 2020, **419**, 213393.
- 3 Q. Wang, J. Li, H. Jin, S. Xin and H. Gao, *InfoMat*, 2022, e12311.
- 4 H. Yi, R. Qin, S. Ding, Y. Wang, S. Li, Q. Zhao and F. Pan, *Adv. Funct. Mater.*, 2020, **31**, 2006970.
- 5 S. Zhao, Z. Guo, K. Yan, X. Guo, S. Wan, F. He, B. Sun and G. Wang, *Small Struct.*, 2021, **2**, 2000054.
- 6 J. Nai and X. W. Lou, *Adv. Mater.*, 2018, **31**, 1706825.
- 7 B. Kong, C. Selomulya, G. Zheng and D. Zhao, *Chem. Soc. Rev.*, 2015, **44**, 7997–8018.
- 8 L. Zhang, H. B. Wu and X. W. Lou, *J. Am. Chem. Soc.*, 2013, **135**, 10664–10672.
- 9 X. Wu, Y. Ru, Y. Bai, G. Zhang, Y. Shi and H. Pang, *Coord. Chem. Rev.*, 2022, **451**, 214260.
- 10 X. Song, S. Song, D. Wang and H. Zhang, *Small Methods*, 2021, **5**, 2001000.
- 11 X. Li, L. Yuan, J. Wang, L. Jiang, A. I. Rykov, D. L. Nagy, C. Bogdan, M. A. Ahmed, K. Zhu, G. Sun and W. Yang, *Nanoscale*, 2016, **8**, 2333–2342.
- 12 C.-H. Chuang, L.-Y. Hsiao, M.-H. Yeh, Y.-C. Wang, S.-C. Chang, L.-D. Tsai and K.-C. Ho, *ACS Appl. Energy Mater.*, 2020, **3**, 11752–11762.
- 13 Y. Li, J. Hu, K. Yang, B. Cao, Z. Li, L. Yang and F. Pan, *Mater. Today Energy*, 2019, **14**, 100332.
- 14 B. He, P. Kuang, X. Li, H. Chen, J. Yu and K. Fan, *Chem.–Eur. J.*, 2020, **26**, 4052–4062.
- 15 X. Wang, A. Dong, Z. Zhu, L. Chai, J. Ding, L. Zhong, T. T. Li, Y. Hu, J. Qian and S. Huang, *Small*, 2020, **16**, 2004614.
- 16 B. Zhang, J. Shan, J. Yu, W. Wang, W. Li, N. Li and Y. Li, *Int. J. Hydrogen Energy*, 2021, **46**, 8871–8884.
- 17 D. Liu, R. Qiang, Y. Du, Y. Wang, C. Tian and X. Han, *J. Colloid Interface Sci.*, 2018, **514**, 10–20.
- 18 Q. Wang, Y. Zhao, W. Luo, W. Jiang, J. Fan, L. Wang, W. Jiang, W.-x. Zhang and J. Yang, *Chem. Commun.*, 2018, **54**, 5887–5890.
- 19 A. R. Mule, B. Ramulu and J. S. Yu, *Small*, 2022, **18**, 2105185.
- 20 Y. Lian, H. Sun, X. Wang, P. Qi, Q. Mu, Y. Chen, J. Ye, X. Zhao, Z. Deng and Y. Peng, *Chem. Sci.*, 2019, **10**, 464–474.
- 21 C. Pei, H. Chen, B. Dong, X. Yu and L. Feng, *J. Power Sources*, 2019, **424**, 131–137.
- 22 T. Wang, P. Wang, W. Zang, X. Li, D. Chen, Z. Kou, S. Mu and J. Wang, *Adv. Funct. Mater.*, 2022, **32**, 2107382.
- 23 J. Nai, Y. Lu, L. Yu, X. Wang and X. W. Lou, *Adv. Mater.*, 2017, **29**, 1703870.
- 24 H. Zhang, Q. Jiang, J. H. Hadden, F. Xie and D. J. Riley, *Adv. Funct. Mater.*, 2021, **31**, 2008989.
- 25 J. Chen, L. Wei, A. Mahmood, Z. Pei, Z. Zhou, X. Chen and Y. Chen, *Energy Storage Mater.*, 2020, **25**, 585–612.
- 26 L.-M. Cao, D. Lu, D.-C. Zhong and T.-B. Lu, *Coord. Chem. Rev.*, 2020, **407**, 213156.
- 27 M. B. Zakaria and T. Chikyow, *Coord. Chem. Rev.*, 2017, **352**, 328–345.
- 28 A. Azhar, Y. Li, Z. Cai, M. B. Zakaria, M. K. Masud, M. S. A. Hossain, J. Kim, W. Zhang, J. Na, Y. Yamauchi and M. Hu, *Bull. Chem. Soc. Jpn.*, 2019, **92**, 875–904.
- 29 H. J. Buser, D. Schwarzenbach, W. Petter and A. Ludi, *Inorg. Chem.*, 1977, **16**, 2704–2710.
- 30 V. D. Neff, *J. Electrochem. Soc.*, 1978, **125**, 886–887.
- 31 B. Nayebe, K. P. Niavol, B. Nayebe, S. Y. Kim, K. T. Nam, H. W. Jang, R. S. Varma and M. Shokouhimehr, *Mol. Catal.*, 2021, **514**, 111835.
- 32 Z. Qin, Y. Li and N. Gu, *Adv. Healthcare Mater.*, 2018, **7**, 1800347.
- 33 W. J. Li, C. Han, G. Cheng, S. L. Chou, H. K. Liu and S. X. Dou, *Small*, 2019, **15**, 1900470.
- 34 M. Hu, N. L. Torad and Y. Yamauchi, *Eur. J. Inorg. Chem.*, 2012, **2012**, 4795–4799.
- 35 Z. Shadike, D.-R. Shi, M.-H. Cao, S.-F. Yang, J. Chen and Z.-W. Fu, *J. Mater. Chem. A*, 2017, **5**, 6393–6398.
- 36 W. Zhang, H. Song, Y. Cheng, C. Liu, C. Wang, M. A. N. Khan, H. Zhang, J. Liu, C. Yu and L. Wang, *Adv. Sci.*, 2019, **6**, 1801901.
- 37 S. Klink, Y. Ishige and W. Schuhmann, *ChemElectroChem*, 2017, **4**, 490–494.
- 38 V. Krishnan, A. L. Xidis and V. Neff, *Anal. Chim. Acta*, 1990, **239**, 7–12.
- 39 K. Itaya, N. Shoji and I. Uchida, *J. Am. Chem. Soc.*, 1984, **106**, 3423–3429.
- 40 A. Mohammad, P. J. Faustino, M. A. Khan and Y. Yang, *Int. J. Pharm.*, 2014, **477**, 122–127.
- 41 Q. Hu, X. Huang, Z. Wang, G. Li, Z. Han, H. Yang, X. Ren, Q. Zhang, J. Liu and C. He, *J. Mater. Chem. A*, 2020, **8**, 2140–2146.



- 42 L. Xiao, Z. Wang and J. Guan, *Coord. Chem. Rev.*, 2022, **472**, 214777.
- 43 P. Dvořák, M. Günther, U. Zorn and A. Catsch, *Naunyn-Schmiedeberg's Arch. Pharmacol.*, 1971, **269**, 48–56.
- 44 Z. Chu, Y. Liu and W. Jin, *Biosens. Bioelectron.*, 2017, **96**, 17–25.
- 45 H. Ming, N. L. Torad, Y.-D. Chiang, K. C.-W. Wu and Y. Yamauchi, *CrystEngComm*, 2012, **14**, 3387–3396.
- 46 S. Jeon, C. H. Li and D. R. Talham, *Cryst. Growth Des.*, 2021, **21**, 916–925.
- 47 Y. Li, C. H. Li and D. R. Talham, *Nanoscale*, 2015, **7**, 5209–5216.
- 48 T.-U. Choi, G. Baek, S. G. Lee and J.-H. Lee, *ACS Appl. Mater. Interfaces*, 2020, **12**, 24817–24826.
- 49 G. Du and H. Pang, *Energy Storage Mater.*, 2021, **36**, 387–408.
- 50 L. Catala and T. Mallah, *Coord. Chem. Rev.*, 2017, **346**, 32–61.
- 51 Z. Li, H. B. Wu and X. W. D. Lou, *Energy Environ. Sci.*, 2016, **9**, 3061–3070.
- 52 B. Li and H. C. Zeng, *Adv. Mater.*, 2019, **31**, 1801104.
- 53 F.-X. Bu, M. Hu, W. Zhang, Q. Meng, L. Xu, D.-M. Jiang and J.-S. Jiang, *Chem. Commun.*, 2015, **51**, 17568–17571.
- 54 M. Cao, X. Wu, X. He and C. Hu, *Chem. Commun.*, 2005, 2241–2243.
- 55 L. Liu, Z. Hu, L. Sun, G. Gao and X. Liu, *RSC Adv.*, 2015, **5**, 36575–36581.
- 56 J. Nai, B. Y. Guan, L. Yu and X. W. Lou, *Sci. Adv.*, 2017, **3**, e1700732.
- 57 J. Nai, J. Zhang and X. W. D. Lou, *Chem*, 2018, **4**, 1967–1982.
- 58 Y. Wang, J. Ma, J. Wang, S. Chen, H. Wang and J. Zhang, *Adv. Energy Mater.*, 2019, **9**, 1802939.
- 59 M. Hu, J.-S. Jiang and Y. Zeng, *Chem. Commun.*, 2010, **46**, 1133–1135.
- 60 M. Hu, S. Furukawa, R. Ohtani, H. Sukegawa, Y. Nemoto, J. Reboul, S. Kitagawa and Y. Yamauchi, *Angew. Chem., Int. Ed.*, 2012, **51**, 984–988.
- 61 M. Hu, A. A. Belik, M. Imura, K. Mibu, Y. Tsujimoto and Y. Yamauchi, *Chem. Mater.*, 2012, **24**, 2698–2707.
- 62 Y. Qiu, H. Yang, Y. Cheng, B. Wen and Y. Lin, *Appl. Surf. Sci.*, 2022, **571**, 151334.
- 63 B. Bornemann, V. Presser and S. Huisman, *ACS Omega*, 2022, **7**, 38674–38685.
- 64 M. Jiang, L. Ren, Z. Hou, W. Hua, D. Lei, Y. Cao, Y. Zhang and J.-G. Wang, *J. Power Sources*, 2023, **554**, 232334.
- 65 Z. Wu, S. Chen, L. Wang, Q. Deng, Z. Zeng, J. Wang and S. Deng, *Energy Storage Mater.*, 2021, **38**, 381–388.
- 66 N. P. Wickramaratne, V. S. Perera, B.-W. Park, M. Gao, G. W. McGimpsey, S. D. Huang and M. Jaroniec, *Chem. Mater.*, 2013, **25**, 2803–2811.
- 67 Y. Liu, W. Wang, Q. Chen, C. Xu, D. Cai and H. Zhan, *Inorg. Chem.*, 2019, **58**, 1330–1338.
- 68 D. Yin, C. Han, X. Bo, J. Liu and L. Guo, *J. Colloid Interface Sci.*, 2019, **533**, 578–587.
- 69 D. Meng, C. Zhang, Y. Liang, W. Qiu, F. Kong, X. He, M. Chen, P. Liang and Z. Zhang, *J. Colloid Interface Sci.*, 2021, **599**, 280–290.
- 70 F. Chen, S. Zhang, R. Guo, B. Ma, Y. Xiong, H. Luo, Y. Cheng, X. Wang and R. Gong, *Composites, Part B*, 2021, **224**, 109161.
- 71 B. Wang, X. Wang, Z. Wang, K. Srinivas, X. Zhang, B. Yu, D. Yang, W. Zhang, T.-C. Lau and Y. Chen, *Chem. Eng. J.*, 2021, **420**, 130481.
- 72 S.-C. Wang, D. Xiong, C. Chen, M. Gu and F.-Y. Yi, *J. Power Sources*, 2020, **450**, 227712.
- 73 S. Husmann and A. J. G. Zarbin, *Chem.–Eur. J.*, 2016, **22**, 6643–6653.
- 74 Z. Ding, H. Yu, X. Liu, N. He, X. Chen, H. Li, M. Wang, Y. Yamauchi, X. Xu and M. A. Amin, *J. Colloid Interface Sci.*, 2022, **616**, 210–220.
- 75 Q. Zong, Y. Zhu, Q. Wang, H. Yang, Q. Zhang, J. Zhan and W. Du, *Chem. Eng. J.*, 2020, **392**, 123664.
- 76 X. Xu, H. Liang, F. Ming, Z. Qi, Y. Xie and Z. Wang, *ACS Catal.*, 2017, **7**, 6394–6399.
- 77 Y. Du, J. Chen, L. Li, H. Shi, K. Shao and M. Zhu, *ACS Sustainable Chem. Eng.*, 2019, **7**, 13523–13531.
- 78 S. Li, L. Bai, H. Shi, X. Hao, L. Chen, Z. Ma, X. Qin and G. Shao, *Int. J. Hydrogen Energy*, 2021, **46**, 27883–27890.
- 79 F. Ma, Q. Wu, M. Liu, L. Zheng, F. Tong, Z. Wang, P. Wang, Y. Liu, H. Cheng, Y. Dai, Z. Zheng, Y. Fan and B. Huang, *ACS Appl. Mater. Interfaces*, 2021, **13**, 5142–5152.
- 80 D.-W. Wang, Y.-D. Zhu, S. Lei, S.-M. Chen, Z.-G. Gu and J. Zhang, *J. Solid State Chem.*, 2021, **293**, 121779.
- 81 K. Wang, F. Zhang, G. Zhu, H. Zhang, Y. Zhao, L. She and J. Yang, *ACS Appl. Mater. Interfaces*, 2019, **11**, 33082–33090.
- 82 J. Huang, P. Xu, T. Gao, J. Huangfu, X.-j. Wang, S. Liu, Y. Zhang and B. Song, *ACS Sustainable Chem. Eng.*, 2019, **8**, 1319–1328.
- 83 X. Y. Yu, Y. Feng, Y. Jeon, B. Guan, X. W. Lou and U. Paik, *Adv. Mater.*, 2016, **28**, 9006–9011.
- 84 X. Liang, G. Wang, W. Gu and G. Ji, *Carbon*, 2021, **177**, 97–106.
- 85 L. Zhang, H. B. Wu, S. Madhavi, H. H. Hng and X. W. Lou, *J. Am. Chem. Soc.*, 2012, **134**, 17388–17391.
- 86 L. Hou, L. Lian, L. Zhang, G. Pang, C. Yuan and X. Zhang, *Adv. Funct. Mater.*, 2015, **25**, 238–246.
- 87 M. Zhang, J. Zhou, J. Yu, L. Shi, M. Ji, H. Liu, D. Li, C. Zhu and J. Xu, *Chem. Eng. J.*, 2019, 123170.
- 88 G. Tian, X. Ran, Q. Wang and D. Zhang, *Dalton Trans.*, 2022, **51**, 1032–1040.
- 89 Z. Liu, Y. Wang, R. Chen, C. Chen, H. Yang, J. Ma, Y. Li and S. Wang, *J. Power Sources*, 2018, **403**, 90–96.
- 90 Q. Zhang, Y. Zhang, T. Zhang, F. Li and L. Xu, *J. Alloys Compd.*, 2023, **930**, 167455.
- 91 X. Y. Yu, L. Yu, H. B. Wu and X. W. Lou, *Angew. Chem.*, 2015, **54**, 5331–5335.
- 92 H. Xu, K. Ye, K. Zhu, Y. Gao, J. Yin, J. Yan, G. Wang and D. Cao, *Inorg. Chem. Front.*, 2021, **8**, 2788–2797.
- 93 Y. Su, D. Ao, H. Liu and Y. Wang, *J. Mater. Chem. A*, 2017, **5**, 8680–8689.
- 94 S. Huang, H. Wang, Y. Zhang, S. Wang, Z. Chen, Z. Hu and X. Qian, *RSC Adv.*, 2018, **8**, 5992–6000.
- 95 Y. Song, X. Zhao and Z.-H. Liu, *Electrochim. Acta*, 2021, **374**, 137962.



- 96 X. Hu, X. Wang, X. Hu, C. Xie and D. Zeng, *Chem. Commun.*, 2019, **55**, 13386–13389.
- 97 W. Qi, S. Liu, F. Li, H. Jiang, Z. Cheng, S. Zhao and M. Yang, *Catal. Sci. Technol.*, 2019, **9**, 2571–2577.
- 98 Z. Cheng, A. Saad, S. Adimi, H. Guo, S. Liu, T. Thomas and M. Yang, *Mater. Adv.*, 2020, **1**, 1161–1167.
- 99 Z. Wang, S. Jiao, B. Wang, Y. Kang, W. Yin, X. Lv, Q. Zhang, Z. Zhang, Y. Chen and G. Pang, *Int. J. Hydrogen Energy*, 2021, **46**, 8345–8355.
- 100 B. Wei, G. Xu, J. Hei, L. Zhang and T. Huang, *Int. J. Hydrogen Energy*, 2021, **46**, 2225–2235.
- 101 X. Ding, W. Uddin, H. Sheng, P. Li, Y. Du and M. Zhu, *J. Alloys Compd.*, 2020, **814**, 152332.
- 102 X. Zhou, Y. Zi, L. Xu, T. Li, J. Yang and J. Tang, *Inorg. Chem.*, 2021, **60**, 11661–11671.
- 103 N. Wang, W. Ma, Z. Ren, Y. Du, P. Xu and X. Han, *J. Mater. Chem. A*, 2018, **6**, 884–895.
- 104 Y.-T. Zhuang, W. Gao, Y.-L. Yu and J.-H. Wang, *Carbon*, 2016, **108**, 190–198.
- 105 X.-Y. Yu, Y. Feng, B. Guan, X. W. D. Lou and U. Paik, *Energy Environ. Sci.*, 2016, **9**, 1246–1250.
- 106 M. Du, P. Geng, C. Pei, X. Jiang, Y. Shan, W. Hu, L. Ni and H. Pang, *Angew. Chem.*, 2022, **134**, e202209350.
- 107 A. Schmidt, S. Husmann and A. J. G. Zarbin, *J. Solid State Electrochem.*, 2018, **22**, 2003–2012.
- 108 B. Kong, J. Tang, C. Selomulya, W. Li, J. Wei, Y. Fang, Y. Wang, G. Zheng and D. Zhao, *J. Am. Chem. Soc.*, 2014, **136**, 6822–6825.
- 109 S. Husmann, E. S. Orth and A. J. G. Zarbin, *Electrochim. Acta*, 2019, **312**, 380–391.
- 110 S. Husmann, A. J. G. Zarbin and R. A. W. Dryfe, *Electrochim. Acta*, 2020, **349**, 136243.
- 111 X.-J. Zheng, Q. Kuang, T. Xu, Z.-Y. Jiang, S.-H. Zhang, Z.-X. Xie, R.-B. Huang and L.-S. Zheng, *J. Phys. Chem. C*, 2007, **111**, 4499–4502.
- 112 S. Husmann and A. J. G. Zarbin, *Electrochim. Acta*, 2018, **283**, 1339–1350.
- 113 C. M. Ferreira, M. K. Ramos and A. J. G. Zarbin, *Eur. J. Inorg. Chem.*, 2021, **2021**, 3373–3384.
- 114 M. K. Ramos and A. J. G. Zarbin, *Appl. Surf. Sci.*, 2020, **515**, 146000.
- 115 S. Nakanishi, G. Lu, H. M. Kothari, E. W. Bohannon and J. A. Switzer, *J. Am. Chem. Soc.*, 2003, **125**, 14998–14999.
- 116 L. C. Lopes, S. Husmann and A. J. G. Zarbin, *Electrochim. Acta*, 2020, **345**, 136199.
- 117 S. Lei, Q.-H. Li, Y. Kang, Z.-G. Gu and J. Zhang, *Appl. Catal., B*, 2019, **245**, 1–9.
- 118 R. N. Soek, A. Schmidt, H. Winnischofer and M. Vidotti, *Appl. Surf. Sci.*, 2016, **378**, 253–258.
- 119 Z. Fang, A. Zhang, P. Wu and G. Yu, *ACS Mater. Lett.*, 2019, **1**, 158–170.
- 120 P. Wu, A. Zhang, L. Peng, F. Zhao, Y. Tang, Y. Zhou and G. Yu, *ACS Nano*, 2018, **12**, 759–767.
- 121 P. L. Soni and V. Soni, *The Chemistry of Coordination Complexes and Transition Metals*, CRC Press, 2021.
- 122 F. Feng, S. Chen, X. Z. Liao and Z. F. Ma, *Small Methods*, 2019, **3**, 1800259.
- 123 P. Yang, J. Peng, Z. Chu, D. Jiang and W. Jin, *Biosens. Bioelectron.*, 2017, **92**, 709–717.
- 124 Y. Xian, Y. Hu, F. Liu, Y. Xian, L. Feng and L. Jin, *Biosens. Bioelectron.*, 2007, **22**, 2827–2833.
- 125 A. Johansson, E. Widenkvist, J. Lu, M. Boman and U. Jansson, *Nano Lett.*, 2005, **5**, 1603–1606.



Mixed Cu–Fe Sulfides Derived from Polydopamine-Coated Prussian Blue Analogue as a Lithium-Ion Battery Electrode

Behnoosh Bornamehr^{1,2}, Volker Presser,^{1,2,3,*} Samantha Husmann,^{1,*}

¹ *INM – Leibniz Institute for New Materials, Campus D2 2, 66123, Saarbrücken, Germany*

² *Department of Materials Science & Engineering, Saarland University, Campus D2 2, 66123, Saarbrücken, Germany*

³ *Saarene – Saarland Center for Energy Materials and Sustainability, Campus C4 2, 66123 Saarbrücken, Germany*

Citation:

Bornamehr, B., Presser, V. and Husmann, S., 2022. Mixed Cu–Fe Sulfides Derived from Polydopamine-Coated Prussian Blue Analogue as a Lithium-Ion Battery Electrode. *ACS omega*, 7(43), pp.38674-38685.

Own contributions:

Methodology, Investigation, Data Curation, Validation, Writing – original draft

Mixed Cu–Fe Sulfides Derived from Polydopamine-Coated Prussian Blue Analogue as a Lithium-Ion Battery Electrode

Behnoosh Bornamehr, Volker Presser,* and Samantha Husmann*

Cite This: *ACS Omega* 2022, 7, 38674–38685

Read Online

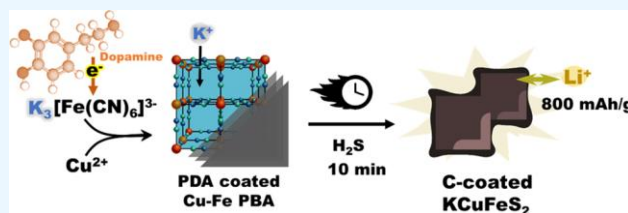
ACCESS |

Metrics & More

Article Recommendations

Supporting Information

ABSTRACT: Batteries employing transition-metal sulfides enable high-charge storage capacities, but polysulfide shuttling and volume expansion cause structural disintegration and early capacity fading. The design of heterostructures combining metal sulfides and carbon with an optimized morphology can effectively address these issues. Our work introduces dopamine-coated copper Prussian blue (CuPB) analogue as a template to prepare nanostructured mixed copper–iron sulfide electrodes. The material was prepared by coprecipitation of CuPB with in situ dopamine polymerization, followed by thermal sulfidation. Dopamine controls the particle size and favors K-rich CuPB due to its polymerization mechanism. While the presence of the coating prevents particle agglomeration during thermal sulfidation, its thickness demonstrates a key effect on the electrochemical performance of the derived sulfides. After a two-step activation process during cycling, the C-coated KCuFeS₂ electrodes showed capacities up to 800 mAh/g at 10 mA/g with nearly 100% capacity recovery after rate handling and a capacity of 380 mAh/g at 250 mA/g after 500 cycles.



1. INTRODUCTION

Lithium-ion batteries (LIBs) are essential technologies to carry present-day electrochemical charge storage in stationary and portable applications.^{1,2} Common cathode materials employ metal oxides composed of cobalt, nickel, and manganese with a layered structure that allows the facile, reversible, and electrochemically triggered insertion of Li⁺ ions between the layers with typical capacities of about 200 mAh/g.^{3–5} Elements such as cobalt and nickel are less common, cost drivers, and subject to geopolitical considerations and can be replaced by more common and widely available elements, such as copper and iron. Still, the low capacities of metal oxides commonly used in commercial batteries limit the performance, and other compounds are relevant to the investigation for achieving a higher energy density.⁶

Metal sulfides are actively explored to replace transition-metal oxides in new battery technologies.^{7,8} These compounds can undergo conversion reactions in addition to insertion and enable redox processes that transfer more electrons and therefore provide higher charge storage capacity.⁹ They are also more thermally stable and electronically conductive than their oxide counterparts.^{10,11} Copper iron sulfide is particularly attractive as it is nontoxic, cheap, and provides high natural abundance of its elements.¹² The material potential for use in energy storage has been demonstrated in LIB applications. For example, CuFeS₂ nanorods have shown high capacities of 633 mAh/g at 0.2 C when tested between 0.01 and 3.0 V vs Li/Li⁺ as LIB electrodes.¹³

Standard synthesis methods for these nanosulfides are energy-intensive, lack scalability, or are based on inorganic solvents. Therefore, greener methods to produce metal sulfides

can increase the sustainability of electrode production. However, a new synthesis method must be employed while addressing the limitation of the metal sulfides.^{8,14} The limiting factors causing performance degradation for metal sulfides are the relatively low electrical conductivity, significant volume expansion, and polysulfide shuttling during electrochemical cycling.^{15,16} To mitigate these drawbacks of metal sulfides, different strategies can be pursued. Adding carbon to the material can enhance the conductivity, while homogeneity and interaction in the nanoscale between the components significantly improve the performance.^{17–19} Nanodesigned structures can accommodate or buffer the volumetric expansion. Different morphologies have been used, such as hollow, hierarchical, and core–shell structures, or simply reducing the particle size as a strategy.²⁰ These approaches reduce ion diffusion path and volume expansion resulting from lithiation while trapping polysulfides.²¹ There are many methods to produce metal sulfides, but a simple means to incorporate morphology design is by deriving the metal sulfide from a template material.

Prussian blue (PB) is a porous and tunable material that consists of iron centers coordinated by cyanide ligands (Fe₄[Fe(CN)₆]₃ or AFe₃[Fe(CN)₆]₂, where A is an alkali

Received: July 5, 2022

Accepted: September 30, 2022

Published: October 17, 2022



metal).¹² PB synthesis is particularly facile when using a coprecipitation method in water, making it ideal for upscaling. By switching the metallic precursors, Prussian blue analogues (PBAs) can be synthesized, replacing the iron species in the lattice with other transition metals.²² PB and PBAs can then be used as templates for various derived compounds such as oxides, phosphides, nitrides, alloys, carbides, and chalcogenides, including metal sulfides.^{23–26}

In addition, PBAs are also very flexible in morphology design.²⁷ Different morphologies can be obtained by changing the PB synthesis parameters, such as hollow- or nanostructures and core–shell and hierarchical structures, which can help reduce the effects of volume expansion during cycling.²⁸ Often, the PBAs are combined with carbon species either by growing PBAs on the surface of conductive carbon substrates or coating PBAs with carbon or carbon precursors. For example, polydopamine (PDA) has been recently established as a coating agent, as it is easy to polymerize in aqueous media and form a coating layer on different substrates.^{29,30} Besides aiding in the conductivity and electrochemical stability of PB(A)s, carbon can control the size and morphology of the particles.^{31,32} These morphological attributes are then kept after the derivatization procedure. They are of critical importance in the case of metal sulfides for energy storage since they can mitigate volume expansion, increase conductivity, and shorten diffusion paths.³³

This work reports the successful derivatization of mixed iron–copper sulfide from copper hexacyanoferrate (analogous to PB) while describing the effect of PDA addition and its thickness on the morphology and electrochemical performance. In contrast to previous reports, we show that the PDA coating can be done at acidic pH, and the presence of PDA favors the stabilization of alkali metal ions in the structure. Through self-sacrificial thermal sulfidation, the material is converted into carbon-coated copper–iron sulfides. This enables a one-step water-based template synthesis, coating, and morphology design. Furthermore, complete conversion is achieved within 10 min under a mild temperature of 300 °C, which is, to the best of the authors' knowledge, the fastest for mixed-metal sulfide derivatization while still using a temperature lower than 400 °C. The thickness of the PDA coating plays a crucial role in stabilizing particle growth and morphology, which further determines the derivative performance as a Li-ion battery electrode.

2. EXPERIMENTAL SECTION

2.1. Synthesis of Cu-PBA. Dopamine hydrochloride (type: quality level 200), potassium ferricyanide ($K_3[Fe(CN)_6]$, $\geq 99.0\%$), and copper chloride ($CuCl_2$, $\geq 99.95\%$) were purchased from Sigma-Aldrich. All aqueous solutions were prepared with ultrapure water ($\rho > 18 M\Omega\cdot cm$), and a pH of 2 was adjusted with concentrated HCl (37%, Sigma). Bare copper hexacyanoferrate (denoted CuPB) was prepared by dropwise addition at a 40 mL/h rate of 100 mL aqueous solution of copper chloride (12.5 mmol/L) to 100 mL aqueous solution of potassium ferricyanide (25 mmol/L) under magnetic stirring. For the PDA-coated samples, 76 mg or 1 g of dopamine hydrochloride was first added to the $K_3[Fe(CN)_6]$ solution under stirring before the addition of $CuCl_2$ solution, yielding samples CuPB-PDA1 and CuPB-PDA2, respectively (Table 1). After the complete addition of $CuCl_2$, the mixture was stirred for 1 h more to ensure homogeneity and set to rest overnight for 18 h. The powder was then

Table 1. Synthesis Conditions to Prepare the Copper Hexacyanoferrate Template

	sample		
	CuPB	CuPB-PDA1	CuPB-PDA2
$K_3[Fe(CN)_6]$	100 mL, 25 mM, pH 2	100 mL, 25 mM, pH 2	100 mL, 50 mM, pH 2
$CuCl_2$	100 mL, 12.5 mM, pH 2	100 mL, 12.5 mM, pH 2	100 mL, 25 mM, pH 2
dopamine		76 mg (0.5 mmol)	1 g (6.5 mmol)
DAH/Fe (molar ratio)	0	0.1	2.6

collected via centrifugation, washed with distilled water to pH 5, washed twice with acetone, and dried in an oven at 80 °C for 18 h.

2.2. Sulfidation of Cu-PBA. The conversion of CuPB into sulfide was done in a Carbolite Gero H_2S tubular furnace. The CuPB powder was placed in the center of the quartz tube and purged with 100 sccm argon (99.999%) for 2 h. The furnace was heated to 300 °C at a heating rate of 5°/min and an Ar flow of 100 sccm. The temperature was then maintained for 10 min under a flow of 50 sccm of H_2S gas as reactant gas and 100 sccm Ar as protective gas. The product was collected after cooling the furnace to room temperature under 50 sccm of Ar gas flow. The sulfidized samples were denoted with an S to the name, for example, CuPB-S for the sulfidation product from CuPB. The yield after the sulfidation was the highest for the PDA-free sample (80%), and with the PDA increase, the yield decreased due to carbonization of the polymer, with the lowest percentage of 71% for the CuPB-PDA2 sample.

2.3. Material Characterization. Structural morphology was characterized by scanning electron microscopy (SEM) and elemental analysis via energy-dispersive X-ray (EDX) spectroscopy using a ZEISS GEMINI 500 microscope coupled with an X-max detector from Oxford Instruments, employing an acceleration voltage of 1 kV for imaging and 15 kV for spectroscopy. The samples were mounted on an aluminum stub fixed with carbon tape without additional conductive sputter coating. For elemental analysis, at least 20 points were chosen randomly, and the average amount of detected elements was calculated. The average particle size was calculated by measuring 100 particles under focus in the SEM images with the software ImageJ.

A 2100F system (JEOL) at 200 kV was used for transmission electron microscopy (TEM). The powder was dispersed in ethanol via an ultrasonic bath to prepare the samples and then dried on the copper grid coated with lacey carbon drop by drop.

For phase analysis, powder X-ray diffraction (XRD) was performed using a D8 Discover diffractometer (BRUKER AXS) with a copper source ($Cu K\alpha$, 40 kV, 40 mA), a Göbel mirror, and a 1 mm point focus. A two-dimensional VANTEC detector was used to cover an angular range of $20^\circ 2\theta$ for 1000 s and repeated three times to record an angular range of 10° – $80^\circ 2\theta$. All scans went through background subtraction and were normalized to (0,100). Rietveld refinement was done by HKL fits of the corresponding phases using the software TOPAS 6 from Bruker AXS.

Raman spectroscopy was conducted with a Renishaw inVia Raman microscope employing a 633 nm excitation wavelength (Nd-YAG laser) with a power of 87 μW at the focal point of the sample, with a numeric aperture of 0.75. Each spectrum was recorded with 20 s exposure time and accumulated five

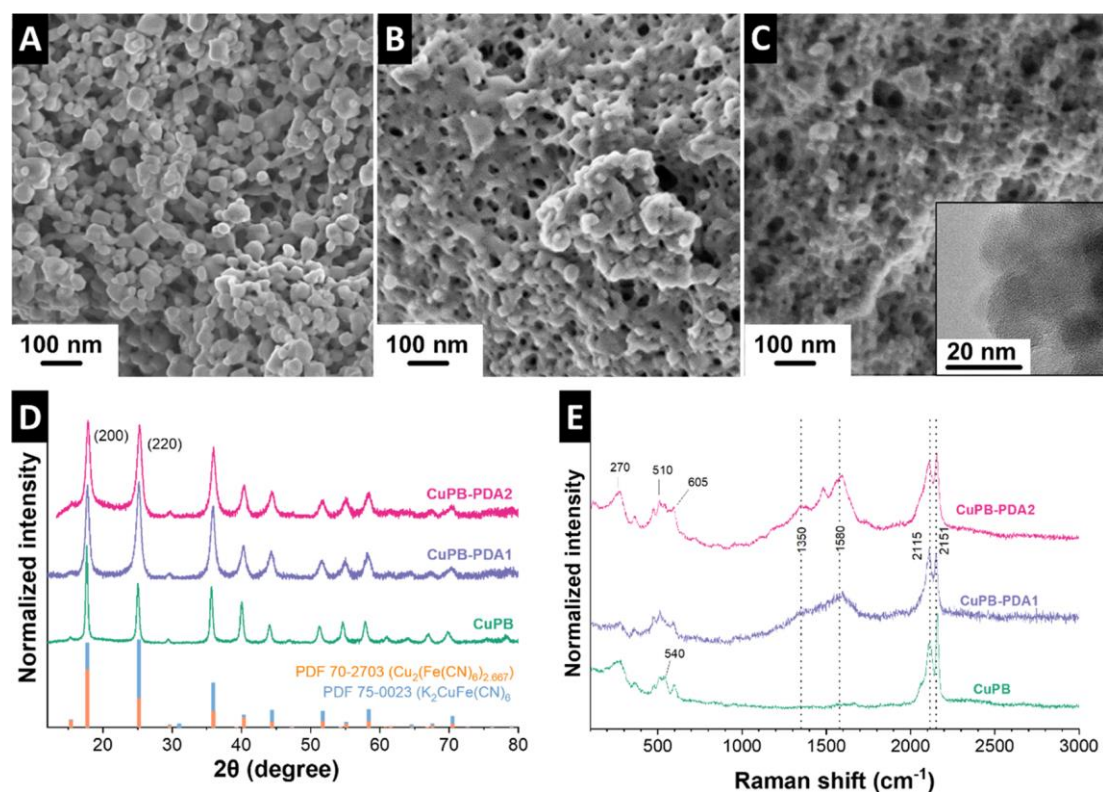


Figure 1. Scanning electron micrographs of the as-dried samples: (A) CuPB, (B) CuPB-PDA1, (C) CuPB-PDA2 (inset: transmission electron micrograph), and their respective (D) X-ray diffractograms and (E) Raman spectra.

times for each sample at least 10 points. Spectra were treated by cosmic ray removal and then normalized to (0,100).

A Netzsch TG-209-1 Libra system was used for thermogravimetric analysis (TGA) to analyze the mass changes when heating at 5 °C/min to 700 °C in synthetic air with Ar as protective gas.

2.4. Electrode Preparation. The powder material of each sample was finely ground and mixed with conductive carbon black (CB, C65, IMERYS Graphite & Carbon) and a binder poly(vinylidene fluoride) (PVDF, Sigma-Aldrich) in a mass ratio of 8:1:1. PVDF was first dissolved in *N*-methyl-2-pyrrolidone (NMP) with a mass ratio of 1:9 and stirred until it became homogeneous and then added to the mixture of the active material (AM) and conductive carbon. The consistency of the slurry was controlled by adding NMP and mixing in a speed mixer (DAC150.1 FVZ Hauschild). Initially, the dried powders of the active material and carbon black were mixed at 1000 rpm for 2 min. NMP was added in small amounts to produce a thick paste and mixed at 1000 rpm for 2 min, followed by 2500 rpm for 2 min. Then, the 10 mass % of PVDF in NMP was added to the paste and mixed at 800 rpm for 6 min. Small quantities of NMP were added and speed-mixed at 800 rpm for 2 min each time, and the consistency was checked. NMP addition continued until the mixture transitioned from the paste to a flowing viscous slurry. NMP addition was then ceased to avoid forming a runny dripping liquid. The coating was done using the doctor blade method with an automatic coater (MTI mini cast coater MSK-AFA-HC100) with a wet thickness of 200 μm onto the copper foil (MTI, 25 μm thickness). The coating was dried overnight at 110 °C in a vacuum oven and then cold press-rolled to a total thickness of 80 μm . The roll-pressed foil was punched into

circles with a diameter of 10 mm to be used as the electrode. The electrodes were individually weighed with a precision of 0.01 mg. We determined the film mass using bare Cu foil. To do so, 10 punched Cu foils with a diameter of 10 mm were weighed, and the average was subtracted from the total electrode mass. The mass was normalized by the active material content (i.e., 80%), and only electrodes containing more than 1 mg of active material were used in electrochemical testing to ensure reliable measurements. The average active material mass was 1.6 ± 0.3 mg and 2.0 ± 0.1 mg for CuPB-PDA1-S and CuPB-PDA2-S, respectively.

2.5. Electrochemical Characterization. For electrochemical measurements of half-cells, CR2032 coin cells were assembled. The Cu-coated disks were used as the working electrode and a lithium chip (11 mm) as the counter and reference electrode. Whatman GF/F glass fiber mats were punched into 18 mm diameter disks and used as a separator. LiPF_6 salt (1 mol/L) in a mixture of ethylene carbonate and dimethyl carbonate (EC/DMC, 1:1 by volume, Sigma, battery grade) was used as the electrolyte. Cyclic voltammetry (CV) was carried out using a BioLogic VMP-300 potentiostat/galvanostat and performed in a potential window of 0.01–3.0 V vs Li/Li^+ at scan rates of 0.05 and 0.5 mV/s. Galvanostatic charge/discharge with potential limitation (GCPL) measurements were done with an Arbin Battery Cycler in the potential range of 0.01–3.0 V vs Li/Li^+ to test the rate capability and cycling stability at rates of 250, 500, and 1000 mA/g. All of the electrochemical tests were done in a Binder climate chamber held at 25 ± 1 °C.

Table 2. Rietveld Refinement Results of CuPB, CuPB-PDA1, and CuPB-PDA2 Were Obtained from Fitting Structures of PDF 70-2703 and PDF 75-0023

	domain size (nm)		composition ratio (mass %)	cell parameter (Å)	
	Cu ₂ [Fe(CN) ₆]	K ₂ Cu[Fe(CN) ₆]	Cu ₂ [Fe(CN) ₆]/K ₂ Cu[Fe(CN) ₆]	Cu ₂ [Fe(CN) ₆]	K ₂ Cu[Fe(CN) ₆]
CuPB1-2	26	37	44/56	10.07	10.10
CuPB1-2_PDA1	12	17	25/75	10.02	10.01
CuPB1-2_PDA2	8	10	30/70	10.03	10.02

Table 3. Elemental Analysis of CuPB, CuPB-PDA1, and CuPB-PDA2 and Their Respective Sulfidized Samples

sample	element (atom %)						
	Cu	Fe	S	K	C	N	O
CuPB	10.1 ± 0.9	5.9 ± 1.7		0.7 ± 0.2	45.3 ± 0.9	35.8 ± 2.5	2.2 ± 2.5
CuPB-PDA1	9.2 ± 1.1	6.8 ± 2.3		5.7 ± 1.8	44.4 ± 2.0	30.5 ± 3.0	3.3 ± 0.6
CuPB-PDA2	7.4 ± 0.4	3.3 ± 0.4		2.4 ± 0.3	49.1 ± 0.4	32.0 ± 1.4	5.8 ± 0.2
CuPB-S	12.8 ± 2.6	41.8 ± 8.13	30.0 ± 3.1	1.9 ± 0.4	11.1 ± 3.9	0.2 ± 0.4	2.1 ± 0.5
CuPB-PDA1-S	24.7 ± 2.1	8.9 ± 0.8	23.1 ± 1.7	5.7 ± 1.4	32.4 ± 2.7	2.3 ± 0.7	3.0 ± 0.3
CuPB-PDA2-S	11.8 ± 1.3	6.1 ± 1.2	14.3 ± 2.6	4.2 ± 0.8	40.9 ± 4.6	5.3 ± 0.8	17.4 ± 3.4

3. RESULTS AND DISCUSSION

3.1. Synthesis of CuPB Using Dopamine. CuPB was prepared by coprecipitation, a well-established and straightforward method for synthesizing PB and PBA nanoparticles.¹² Ming et al. reported that the pH of the synthesis solution and the concentration of the precursor salts directly affect the morphology and the particle size. A defect-free structure has been shown to enhance the energy storage ability³¹ and is preferred here as a more homogeneous template for further derivatization. The 1:2 Cu/Fe ratio was employed to minimize introduced defects by a lack of cyanide ligands in the synthesis.³⁴

After adding the copper salt to the ferricyanide, a dark brown opaque solution was formed. In the synthesis of PDA-coated samples, dopamine hydrochloride was first dissolved in the ferricyanide solution prior to the addition of CuCl₂. When adding the dopamine, the color of the solution changed from the characteristic bright yellow of [Fe(CN)₆]³⁻ to deep red, which is assigned to the oxidation of dopamine by ferricyanide and reduction of Fe³⁺ to Fe²⁺. The color difference between the batches with and without dopamine is shown in Figure S1A,B, Supporting Information.

The morphology of the produced powders was studied by SEM (Figure 1). A higher amount of PDA in the solution has a visible effect on the morphology, namely, the connectivity increases among the PBA particles, and there is a general reduction in the particle size (Figure 1A–C). The particle size distribution was calculated by measuring the diameter of 100 particles of each sample from scanning electron micrographs resulting in an average particle size 24 ± 0.3 and 22 ± 0.6 nm for CuPB-PDA1, and CuPB-PDA2, respectively (Figure S1C). In the absence of dopamine or any protecting agent, PB particles present progressive nucleation, that is concomitant nucleation and growth, resulting in heterogeneous particle size distribution.³⁵ Due to less control over the nucleation and growth in the CuPB, a bimodal size distribution is observed, resulting in centers of 26 ± 0.6 and 43 ± 8 nm. The TEM inset in Figure 1C demonstrates the CuPB-PDA2 particles smaller than 20 nm and the amorphous PDA coating around them. These observations and the color change in the presence of dopamine indicate direct participation of PDA in the synthesis procedure, which is related to the dopamine polymerization

process. PDA is formed through the oxidative polymerization of dopamine. Therefore, a key step for PDA synthesis is the oxidation of dopamine, which commonly occurs in an alkaline environment and/or in the presence of an oxidizing agent.³⁶ Previous works have mentioned that one or both conditions are necessary for dopamine molecules to be activated through the deprotonation of the hydroxyl group and self-polymerize.^{37,38}

In the presence of transition metals, especially Fe³⁺, the hydroxyl groups of catechols can chelate to the metal species, forming a reversible noncovalent complex by donating a pair of nonbonding electron pairs to the iron ion. This results in the formation of mono- to tris-catechol-metal ion complexes depending on the concentration of Fe³⁺^{39,40} and the pH.⁴¹ Here, the ferricyanide ion can act as a mild oxidizing agent through coordination and electron transfer from dopamine. The reduced [Fe(CN)₆]⁴⁻ ions act as nucleation sites for PBA particle growth when the copper salt is added to the solution. The presence of oxidized dopamine around [Fe(CN)₆]⁴⁻ increases the distance between the nucleation sites, impedes particle growth, and results in smaller particles.

X-ray diffractograms of the produced samples are presented in Figure 1D. The diffractograms feature the characteristic reflections of a PB(A) cubic structure, matching both Cu₂[Fe(CN)₆] and K₂Cu[Fe(CN)₆] phases with a cubic system and space group of *Fm* $\bar{3}$ *m* (225) and *F* $\bar{4}$ *3m* (216), respectively. The samples containing PDA showed a higher (220) peak intensity than the (200) peak, indicating a possible better match with the K-rich phase. The uncoated CuPB sample also displays narrower peaks than the PDA-coated material, suggesting a larger particle size. These observations were further analyzed by Rietveld refinement (Table 2 and Figure S2). The Rietveld refinement reveals that all samples present a mixture of Cu₂[Fe(CN)₆] and K₂Cu[Fe(CN)₆], with the PDA-containing samples showing more of the K-rich phase. The amount of K-CuPB increased from 56% in CuPB to 75% and 70% in CuPB-PDA1 and CuPB-PDA2, respectively. The overall domain size of the CuPB material also tends to be larger than the other two. This aligns with the larger particles in scanning electron micrographs (Figures 1A and S1C). After the PDA addition, the crystallite size of both phases decreases significantly from 37 nm for K₂Cu[Fe(CN)₆] in the CuPB sample to 17 and 10 nm in CuPB-PDA1 and CuPB-PDA2, and

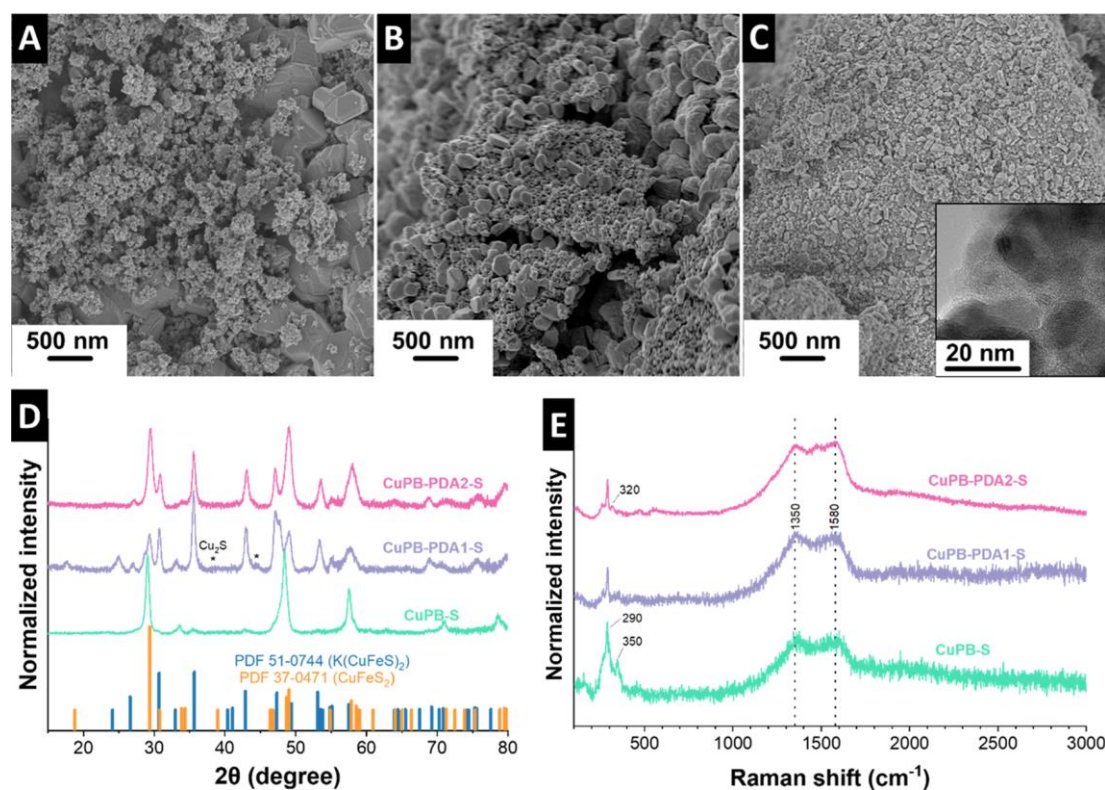


Figure 2. Scanning electron micrographs of the sulfidized sample: (A) CuPB-S, (B) CuPB-PDA1-S, (C) CuPB-PDA2-S (inset: transmission electron micrograph) and their respective (D) X-ray diffractograms and (E) Raman spectra.

for $\text{Cu}[\text{Fe}(\text{CN})_6]$, from 26 to 12 and 8 nm, respectively. This trend confirms the dopamine effect surrounding the $[\text{Fe}(\text{CN})_6]^{3-}$ ions during synthesis and controlling the particle size in both present phases.

The composition of the samples was further analyzed by energy-dispersive X-ray spectroscopy (Table 3). Analysis of the samples identified the following elements: copper, iron, potassium, carbon, nitrogen, and oxygen. In both samples with PDA, more potassium is observed (5.7 atom % in CuPB-PDA1 and 2.4 atom % in CuPB-PDA2), supporting the higher $\text{K}_2\text{Cu}[\text{Fe}(\text{CN})_6]$ phase content in these samples, while in the sample with no PDA, a very low amount of potassium was detected (0.7 atom %). This confirms that during the synthesis, the reduction of ferricyanide ions to $[\text{Fe}(\text{CN})_6]^{4-}$ favors the interaction of potassium ions for charge balance. The alkali-rich phase of PB materials is known to be less defective and more electrochemically stable. This PDA-induced effect could not only be used to produce more stable structures but also to incorporate other counterions like Li^+ , which could compensate for Li consumption during solid-electrolyte interphase (SEI) formation, for example. Detected potassium was higher in the CuPB-PDA1 sample but with a larger deviation, probably due to the lower homogeneity compared to the CuPB-PDA2 sample. The thicker PDA coating in CuPB-PDA2 also diminishes the signal intensity of CuPB-related components. Therefore, no straight relation between the coating thickness and potassium amount was concluded. Other elements present in the PDA molecule (carbon, nitrogen, and oxygen) slightly increased in the PDA-containing samples. The main change was the increase of oxygen from 2.2 atom % in CuPB to 5.8 atom % in CuPB-PDA2, while carbon went from 45.3 to 49.1 atom % in the same samples.

Figure 1E shows the Raman spectra of the samples before the derivatization. The set of bands from 200 to 700 cm^{-1} belong to the Fe–CN–Cu vibrations due to M–CN–M' bonds.⁴² Two bands at ~ 2115 and $\sim 2151\text{ cm}^{-1}$ correspond to A_{1g} and E_{1g} modes of $\nu(\text{CN})$ vibrations, respectively. The high-frequency one is usually associated with inner sphere metal species coordination (NC–M), in this case, Fe ions, due to stronger bond and π back-bonding effects. At the same time, the lower frequency corresponds to M'–NC effects.⁴³ The increase in the low-frequency mode after the PDA addition indicates the higher contribution of Cu–NC, which is associated with a less defective structure due to more Cu units.⁴⁴ In the presence of dopamine, the D-band and G-band of carbon are seen at 1350 and 1580 cm^{-1} , respectively, and we see further growth of the carbon signal with higher dopamine addition. The band at 1480 cm^{-1} between the D-band and the G-band appears with increased dopamine content and shows the functional groups in the PDA (e.g., –OH scissoring).⁴⁵ TGA analysis (Figure S3A, Supporting Information) confirms the presence of the carbon species by the difference in the mass loss between CuPB and CuPB-PDA2, indicating that approximately 10 mass % of the coated sample is carbon coating contribution.

3.2. Sulfidation of Cu-PB. The samples were further treated under H_2S to achieve mixed metal sulfide, resulting in the morphologies shown by scanning electron micrographs in Figure 2A–C. The sulfidation process was optimized to ensure total conversion of the CuPB precursor while avoiding particle growth. Figure 2D presents the X-ray diffractograms of the treated samples. All samples were fully sulfidized at $300\text{ }^\circ\text{C}$ after 10 min, as phase analysis shows that no remaining peaks from the PBA precursor are apparent. The resulting powder is

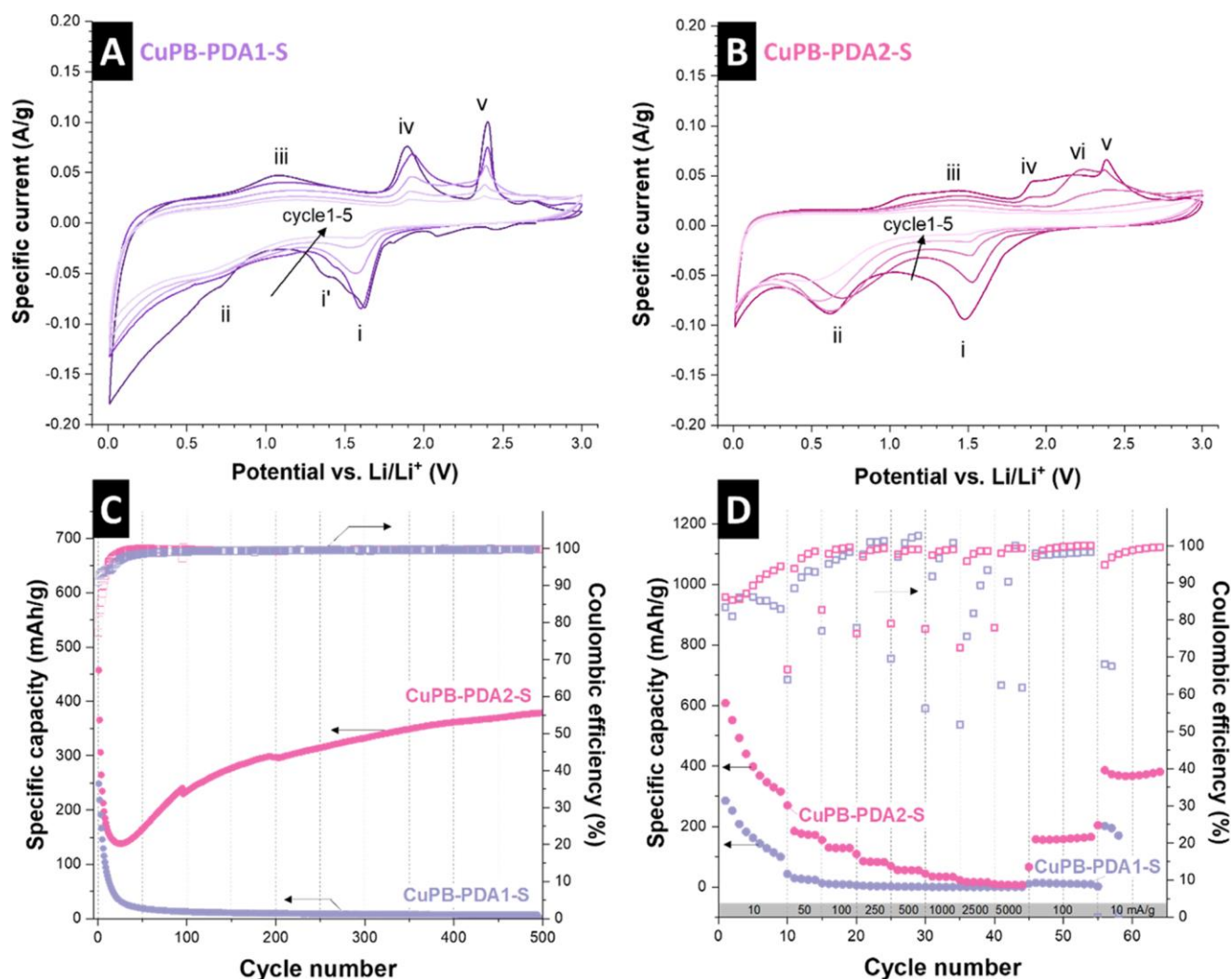


Figure 3. Cyclic voltammetry of (A) CuPB-PDA1-S and (B) CuPB-PDA2-S at 0.05 mV/s. (C) Cycling stability of CuPB-PDA1-S and CuPB-PDA2-S under a current rate of 250 mA/g. (D) Rate handling performance of CuPB-PDA1-S and CuPB-PDA2-S at different rates.

a crystalline mixed sulfide material. In the CuPB sample, the main peaks are attributed to tetragonal copper-iron sulfide (CuFeS_2) with the space group of $I42d$ (122) and a c/a unit cell ratio of 1.97, which indicates lattice expansion after the sulfidation. This phase change can significantly affect the structure, resulting in an inhomogeneous structure despite the short treatment time, as seen in the scanning electron micrographs (Figure 2A,B). There is a significant change in the product's composition when CuPB is coated with PDA. The new reflections correspond to the KCuFeS_2 phase (Figures 2D and S4). This observation confirms the previous characterization data, indicating the stabilization of potassium in the structure after adding the PDA to the PBA solution and its preservation in the structure after derivatization.

The presence and the amount of polydopamine affect the final derived sulfide composition. In the CuPB-PDA1-S sample, minor reflections other than those of tetragonal CuFeS_2 and KCuFeS_2 were indexed with CuS_x (Figure 2D), whereas the CuPB-PDA2-S sample only showed peaks conforming to CuFeS_2 and KCuFeS_2 . The more homogeneous phase structure in CuPB-PDA2-S can be due to a thicker polymer coating and, therefore, slower diffusion of sulfur in the

material and a more controlled derivatization and phase formation.

The initial sulfidized sample CuPB-S showed the largest particle size and morphology inhomogeneity, with particle size ranging from ~ 20 nm to $1 \mu\text{m}$ (Figure 2A). The derivatization process was more controlled and resulted in a more homogeneous structure upon the PDA addition. While large particles with micrometer range size and, at some parts, cracks were observed in CuPB-S and CuPB-PDA1-S (Figure S5A,B in Supporting Information), the morphology of the sample CuPB-PDA2-S showed better homogeneity and a consistent structure with a uniform sub-100 nm particle size (Figure 2C). This could be assigned to both the presence of a thicker PDA coating that prevents not only particle aggregation but also the characteristics of the CuPB precursor. Previous works on PB(A) synthesis^{36,46,47} show that the presence of defects, which is usually a result of insufficient cyanide bridging, changes the structure of the lattice from cubic and monoclinic and that this structure change is accompanied by the presence of water molecules in the lattice (referred as insoluble PB, even though is not related to its solubility). However, when alkali ions instead of water molecules are stabilized in the lattice (soluble PB), the formation of vacancies is suppressed, and a

lower defect-containing structure is formed. As the CuPB particle acts as a template and metallic source for the produced sulfides, the lower defect degree in the parent material aids in the homogeneity of the final product.

In the transmission electron micrographs shown in Figure 2C inset and Figure S5C,D, Supporting Information, the particles' crystallinity is confirmed, with a *d*-spacing of 0.301 nm, matching the (111) planes of the tetragonal CuFeS₂ phase at $\sim 29.5^\circ$ 2θ shown in Figure 2D. An amorphous carbon coating is also observed around the particles, indicating the successful employment of the PDA as a carbon shell precursor. This confirms that the coating amount controls the morphology and growth rate of the sulfide particles, leading to higher homogeneity of the resulting derivative.

In addition to the structure, chemical heterogeneity was also observed via EDX elemental analysis (Table 3). The potassium content remained with a similar trend within the samples. After the heat treatment, the nitrogen amount decreased in all samples from ~ 30 to 5 atom % or below, which shows the nitrogen removal from the cyanide ligand. Carbon was also reduced but in less extent, retaining ~ 11 , 32, and 41 atom % for CuPB-S, CuPB-PDA1-S, and CuPB-PDA2-S, respectively, which demonstrates a thicker coating in the CuPB-PDA2-S sample. After the sulfidation, the mean and standard deviation of iron in CuPB-S indicates an inhomogeneous structure. With PDA addition, more homogeneity in the chemical composition can be observed with a lower deviation in the spectrum values and a higher carbon content due to the thicker coating. The mass reduction of the PDA can explain the sensitivity of the material homogeneity to the PDA coating amount during the heat treatment due to the conversion of the intermediates in PDA.⁴⁸ If the polymer does not thoroughly coat the substrate or is lost during the heat treatment, it weakens the diffusion barrier. It causes overgrowth of sulfide particles where not enough coating covers the material, resulting in morphological and chemical heterogeneity. The presence of oxygen with 17.4 atom % in CuPB-PDA2-S can indicate the incomplete transformation of PDA to carbon.

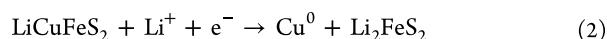
Raman spectra of the heat-treated samples are shown in Figure 2E. The bands at lower frequencies of 200–500 cm⁻¹ belong to the metal sulfide at ~ 290 , 320, and 350 cm⁻¹, corresponding to the A₁, B₂, and E_g modes of chalcopyrite metal-sulfur vibrations, respectively.^{49–51} The D-mode and G-mode related to carbon bands from the sp³ and sp² C–C bonding at 1350 and 1580 cm⁻¹, respectively, present narrowing after the thermal treatment, reflecting higher crystallinity of carbon as a result of the PDA heat treatment. In the CuPB-PDA2-S sample, the third band at ~ 1480 cm⁻¹ is still present, indicating that PDA intermediates do not fully transform into carbon, which is expected from the low heat treatment temperature and duration. TGA of the sulfidized samples without coating CuPB-S and with more coating CuPB-PDA2-S is shown in Figure S3B, Supporting Information. Similar mass change events occur at lower temperatures for CuPB-S compared to CuPB-PDA2-S, showing its higher sensitive for oxidation by the atmosphere and PDA protective effect. For CuPB-PDA2-S, the mass loss before 450 °C and the lower mass increase after 450 °C are due to the burning of the coating by oxygen. The coating also protects the sulfide particles from oxidation, and therefore, the mass increase and oxidation peaks are delayed in the latter sample, taking place at higher temperatures.

3.3. Electrochemical Performance as Li-Ion Battery Electrode.

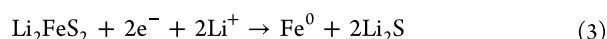
The electrochemical behavior of CuPB-PDA1 and CuPB-PDA2 electrodes operated as half-cells was explored for application in lithium-ion batteries. Figure 3A,B shows cyclic voltammetry of CuPB-PDA1-S and CuPB-PDA2-S, respectively. The voltammogram in Figure 3A shows three main reduction peaks at 1.60 V vs Li/Li⁺ (i), 1.38 V vs Li/Li⁺ (i'), and 0.68 V vs Li/Li⁺ (ii). Through the anodic sweep, three peaks are observed at 1.09, 1.92, 2.40 V vs Li/Li⁺ denoted as iii, iv, and v, respectively. The voltammogram of CuPB-PDA2-S (Figure 3B) shows reduction peaks at ca. 1.5 V vs Li/Li⁺ (i) and ca. 0.6 V vs Li/Li⁺ (ii). At the anodic sweep, the first cycle presents similar oxidation peaks at 1.45 V (iii), 1.90 V (iv), and 2.45 V (v) vs Li/Li⁺ and an additional peak at 2.22 V (vi). The latest two further broaden and merge, while all processes decay in intensity upon cycling. This profile is a combination of processes observed for Cu₂S and FeS₂, given the overall behavior of CuFeS₂. The mechanism of charge storage in CuFeS₂ starts with the intercalation of Li⁺ upon iron reduction, which is accompanied by a cathodic peak at ca. 1.65 V vs Li/Li⁺.⁵²



For the KCuFeS₂ phase, lithiation takes place by replacing potassium ions, forming Li_xK_{1-x}CuFeS₂.^{53,54} In the same potential range, the reduction and formation of metallic copper occur at ca. 1.5 V vs Li/Li⁺.⁵⁵



As we have CuFeS₂ and KCuFeS₂ phases in the samples, the broad reduction process between 1.75 and 1.25 V vs Li/Li⁺ can be assigned to the lithiation of CuFeS₂ and copper reduction of both phases. The subsequent conversion stage, which is accompanied by a broad peak from 0.8 to 0.5 V vs Li/Li⁺ is well in line with the SEI formation and reduction of Fe, which results in eq 3



Similarly, the first broad oxidation process (peak iii in both CuPB-PDA1-S and CuPB-PDA2-S) refers to the partial oxidation of iron to Fe²⁺ in Li₂FeS₂, followed by the peak at 1.90 V vs Li/Li⁺ due to conversion of Cu into Cu₂S. The processes above 2.0 V vs Li/Li⁺ relate to further delithiation of the Li₂FeS₂ species and partial oxidation of sulfur.⁵³ While the conversion of Cu is quite reversible, the iron species do not fully oxidize back at 3.0 V vs Li/Li⁺, indicating the presence of irreversible mechanisms.⁵⁵ A summary of the possible redox reactions for the CuFeS₂ system is presented in Table S1, Supporting Information.^{15,53,55,56}

Figure 3C shows the cycling stability of the samples at 250 mA/g. The capacity of CuPB-PDA1-S starts at 248 mAh/g and fades quickly after about 20 cycles. This is typical for sulfide materials when tested over an extended voltage window to potentials lower than 1.2 V vs Li/Li⁺.⁵³ Capacity fading occurs after a few cycles due to the volume expansion and disintegration of the material during the conversion reactions and shuttling of polysulfides. While coating of the particles is a common strategy to buffer expansion and limit the diffusion of polysulfides, the quality of coating and its homogeneity directly affect the performance.^{57–59} This is demonstrated by the significant improvement of long-term cycling of the sample CuPB-PDA2-S. An initial capacity decay is observed in the

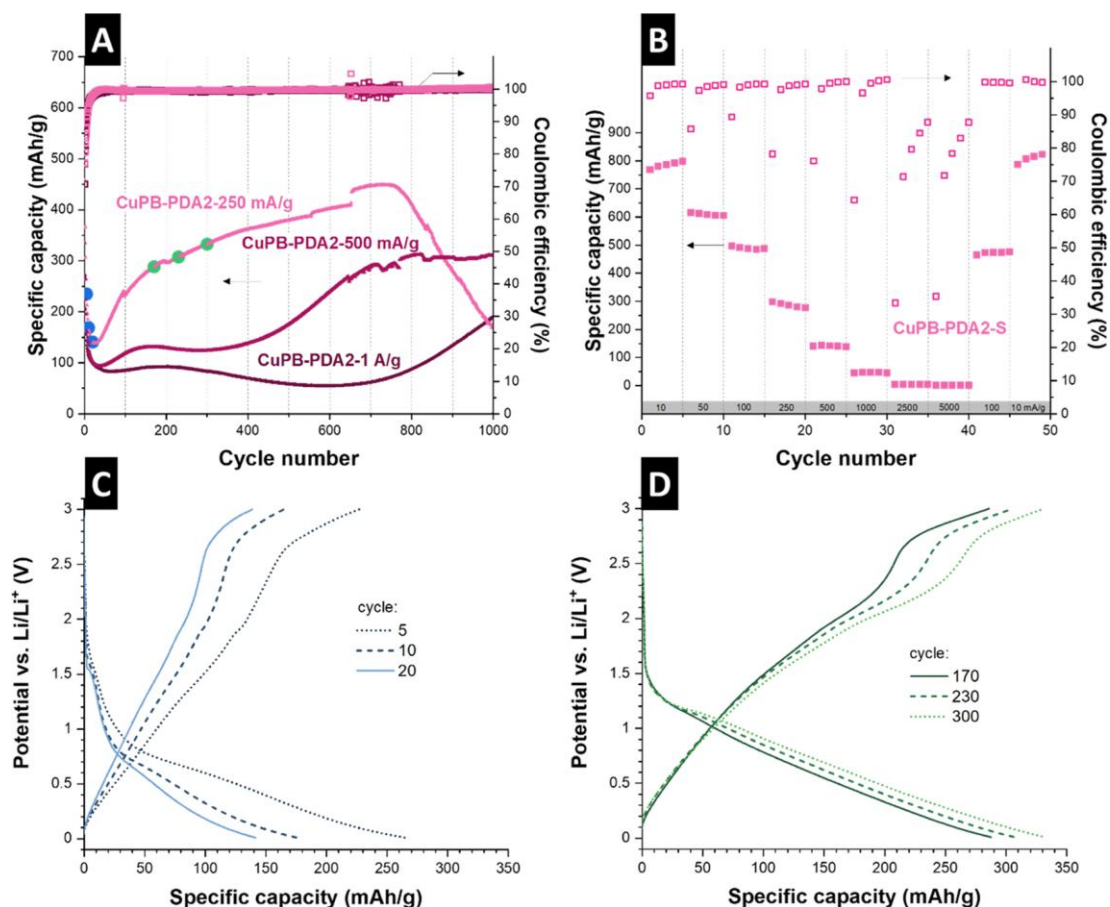


Figure 4. (A) Specific discharge capacity of CuPB-PDA2-S at 250, 500, and 1000 mA/g. (B) Rate handling of CuPB-PDA2-S at 250 mA/g after 500 cycles. (C, D) Galvanostatic charge and discharge curves of CuPB-PDA2-S from the chosen points in panel (A).

sample, starting from ~ 460 mAh/g and decreasing to ~ 150 mAh/g after 25 cycles. However, it then gradually increases to ~ 400 mAh/g. First, this demonstrates that the amount of the coating material directly affects the derivative performance. Nevertheless, it shows that the C-coated sulfide material requires activation to achieve its full capacity.

The Coulombic efficiency for CuPB-PDA2-S starts at ca. 80%, quickly rising above 95% in the first 25 cycles, corresponding to the initial capacity decay of this sample. This indicates the occurrence of irreversible reactions likely related to FeS₂ species as well as SEI formation. Nevertheless, further cycling presents steady Coulombic efficiencies in the range of 97–100%, which shows that the constant increase in capacity is possibly an activation process rather than phase transformations.⁵⁶ Figure 3D displays the discharge performance at different applied rates for CuPB-PDA1-S and CuPB-PDA2-S. At 0.01 A/g, CuPB-PDA2-S presents 607 mAh/g, which is higher than the reported theoretical capacity of 583 mAh/g for CuFeS₂.⁶⁰ This theoretical capacity is based on the four-electron process of iron and copper reduction. However, at the applied potential range, sulfur species also undergo reactions with lithium, contributing to the total capacity (Table S1, Supporting Information). Furthermore, the contribution of the carbon coating cannot be completely ignored, though the capacity from carbon should be limited due to the low graphitization degree. The initial capacity of CuPB-PDA1-S at 0.01 A/g is 285 mAh/g, less than half of CuPB-PDA2-S. This could be due to a more inhomogeneous structure both in

morphology and composition and the much larger particle size, leading to a less exposed surface area, as previously observed by scanning electron microscopy (Figure 2B).

The capacity of CuPB-PDA1-S is nearly zero at higher rates, except for the recovered ~ 200 mAh/g at the rate of 0.01 mA/g. With a thicker coating, CuPB-PDA2-S can deliver 200 mAh/g (0.50 A/g), 180 mAh/g (0.10 A/g), and 100 mAh/g (1.0 A/g). After cycling at higher rates for 40 cycles, the electrodes yield a residual capacity of 150 mA/g at 0.10 A/g and 380 mAh/g at 0.01 A/g. The combined characteristics of CuPB-PDA2-S help the material perform better as it has a smaller particle size, a higher amount of carbon for conductivity and connectivity, and a thicker carbon coating that provides mechanical stability under volumetric changes. Nevertheless, the overall performance is lower than expected for these mixed Cu and Fe sulfides. Similar to what is observed in the stability test, there is a fast capacity drop together with low Coulombic efficiency in the initial cycling.

To understand the behavior of CuPB-PDA2-S under cycling, stability tests were conducted at a rate of 500 mA/g and 1 A/g (Figure 4A). Cycling at higher rates showed that the increase in the capacity takes place in two steps that occur at larger intervals when tested at a faster rate. The first step of capacity increase finishes in the first 200 cycles, and its duration is less affected by the current rate. This is probably due to the carbon coating activation. Since no conditioning was done before the tests, the coating is not well-tailored for the diffusion of Li⁺ ions. After multiple cycling, more pores are opened, the more

Table 4. Performance Data of Copper and Iron Mixed and Unmixed Sulfide Electrodes for Li-Ion Batteries^a

active material	electrode composition	electrolyte	potential window (V vs Li/Li ⁺)	capacity values at different rates	reference
KCuFeS ₂ /CuFeS ₂ nanoparticles	AM/CB/PVDF 8:1:1	1 M LiPF ₆ EC/DMC	0.01–3.0	798 mAh/g at 0.01 A/g	this work
CuFeS ₂ nanorods	AM/acetylene black/PVDF 7:1.5:1.5	1 M LiPF ₆ EC/DMC/DEC	1.0–3.0	633 mAh/g at 0.2 C	15
	AM/acetylene black/PVDF 7:1.5:1	DOL/DME	1.0–3.0	675 mAh/g at 0.2 C	15
CuFeS ₂ quantum dots/carbon frame	AM/CB/PVDF 7:2:1	1 M LiPF ₆ EC/DMC	0.005–3.0	1150 mAh/g at 0.05 A/g	56
Natural chalcopyrite	AM/CB/CMC 7:1.5:1.5	1 M LiPF ₆ EC/DMC/DEC	0.01–3.0	990 mAh/g at 1 A/g	53
	AM/CB/sodium alginate 7:1.5:1.5	1 M LiPF ₆ EC/DMC	0.01–3.0	1010 mAh/g at 1 A/g	63
FeS ₂ -CNT	AM/carbon/PVDF 8:1:1	1 M LiTFSI DGE	1.0–3.0	695 mAh/g at 1 A/g	68
Cu ₂ S	AM/CB/PVDF 7:1.5:1.5	1 M LiPF ₆ in EMC	1.0–3.0	243 mAh/g at 0.5 C	67

^aAM = active material, CB: carbon black, EC: ethylene carbonate, DMC: dimethyl carbonate, DEC: diethyl carbonate DOL: 1, 3-dioxolane, DME: dimethyl ether, LiTFSI: lithium bis(trifluoromethanesulfonyl)imide, DGE: diethylene glycol dimethyl ether.

surface area is available to the ions, and diffusion takes place easier.¹³ It was previously demonstrated that the thickness and homogeneity of the coating significantly affect charge storage capacity and rate handling.^{59,61} Therefore, there is an optimal thickness to achieve the best electrochemical performance. While the thinner coating does not provide enough conductivity and mechanical stability, thicker coatings can limit Li⁺ diffusion through the active material, presenting decreased capacity and sluggish kinetics.

The second increase in the capacity starts after a different number of cycles depending on the current rate. When testing at 250 mA/g, the second increase is merged with the carbon activation and cannot be well defined. However, by increasing the current rate, the process is inhibited and can be well distinguished from the first step.

Several points were chosen from the stability curves at different rates (marked with different colors) to compare their charge and discharge profile (Figure S6, Supporting Information). The initial 5, 10, and 20 cycles from the current rate of 250 mA/g are shown in Figure 4C. All curves presented a similar profile during lithiation with a short plateau at ca. 1.5 V vs Li/Li⁺, and a second plateau starting at 0.75 V vs Li/Li⁺ extends to a long slope, referring to peaks (i) and (ii), respectively, previously observed in cyclic voltammetry (Figure 3B). The charge profile is characterized by a long slope from 0.01 to 2.0 V and a second slope from 2.5 to 3.0 V vs Li/Li⁺. The main difference between the tested rates is in the extent of the plateaus related to the conversion reactions, indicating that the material cannot be fully lithiated at higher rates.

After continuous cycling, the discharge profile changed in all of the rates, which indicates the change in the lithiation mechanism. The evolution of the new behavior was observed earlier in the sample cycled at 250 mA/g, already from the 160th cycle, and was accompanied by the formation of a new plateau at ~1.25 V vs Li/Li⁺ followed by a slope (Figure 4D). At this stage, a large portion of the capacity is recovered. Further charge/discharge curves at 250 mA/g showed the same profile with increased contribution of the 1.25 V plateau and the following slope, which leads to the capacity increase in the stability test.

For the material tested under 500 mA/g, the aforementioned transition occurs at later cycles (Figure S6, Supporting Information). Although the first changes and plateau formation at ~1.25 V vs Li/Li⁺ can be seen at the onset of the 160th cycle, it is after 400 cycles that this process is

intensified, leading to an increase in the capacity as observed in the profile of the 500th cycle. However, the processes are not fully stabilized, and both the plateau and the slope after it show a continuous increase in capacity. The same behavior occurs at 1 A/g, with the first profile change visible in the 160th cycle. At this rate, the material takes even more cycles to undergo the reaction with a plateau at 1.25 V vs Li/Li⁺, which is strong evidence of the reaction's dependence on diffusion.

Similar phenomena were previously described for CuFeS₂ and CuS species,^{62,63} where the capacity increase occurs after continuous cycling. Even though the charge storage mechanism of CuFeS₂ is usually described as a combination of lithiation of the mixed sulfide and further conversion reactions, the Cu–S system is much more complex, with several nonstoichiometric Cu_xS_y intermediates. Rate handling was done after 500 cycles at 250 mA/g to compare the rate handling of the material after its activation (Figure 4B). The behavior of the capacity changed drastically compared to that previously observed in Figure 3D. The initial capacity at 10 mA/g increased to 770 and 490 mAh/g at 100 mA/g. After cycling at higher rates, 790 and 470 mAh/g were recovered at those rates. As discussed previously, the theoretical capacity of CuFeS₂ is 587 mAh/g, while we find 438–587 mAh/g for K_xCuFeS₂ ($x \leq 1$). Higher capacities are normally described for CuFeS₂ and assigned to a transition from the Li–CuFeS₂ system to a combination of Li–FeS₂, LiFeS, Li–Cu₂S, and Li–S as described in the reactions of Table S1, Supporting Information.^{53,63}

The postmortem X-ray diffraction analysis of the cycled cells (Figure S7A, Supporting Information) showed that sharp peaks of elemental copper appear after the second capacity increase, and its amount increases upon more cycling. Since the postmortem XRD of the electrodes was done on the powder removed from the current collector, the observed copper peak arises from the sample. The presence of elemental copper has been reported to act as a polysulfide capturing agent,^{64,65} which prevents CuFeS₂ from enduring rapid capacity fading due to a polysulfide shuttling. Since copper is highly mobile and its diffusion in CuFeS₂ required less activation energy compared to Fe and K at room temperature,^{53,66} Cu leaves the lattice during lithiation, resulting in the formation of LiFeS₂ and metallic Cu.⁵⁴ Upon cycling, Cu_xS_y species are formed that can again reduce to Cu and Li₂S, generating the observed plateau at 1.25 V vs Li/Li⁺.⁵⁷ It is described that the reduction mechanism of Cu₂S to metallic

copper occurs through a displacement process, where copper is extruded from the formed Li_2S crystals and needs to diffuse through the particle.⁶⁷ Therefore, all of the processes involving the reduction of Cu-containing species depend on Cu diffusion. The need for Cu diffusion and phase conversion during cycling explains the lagging performance at higher rates. This can also explain the capacity increase upon continuous cycling, in which the carbon layer is slowly activated enabling faster charge mobility necessary for the conversion reactions.

Postmortem scanning electron micrographs (Figure S7B,C, Supporting Information) did not show any changes in the morphology of the active material or dissociation of the particles. This indicates that the conversion reactions do not lead to particle disruption or aggregation. This could be a reason for the increased capacity and stability in the rate handling after activation. Furthermore, the carbon coating and the small particle size contribute to the structure stability by limiting the volume expansion.

We see a significant influence of the PDA coating on electrochemical performance. A higher amount of coating enabled the material to activate through reversible conversion reactions and reach a stable capacity after the rate test. The summary of the results in this work is presented and compared with similar works in the literature in Table 4. Our results are comparable with synthetic nano CuFeS_2 works and demonstrate higher achieved capacities while using a more scalable and quicker synthesis procedure. Although we prepared the material by a facile method and showed a high-capacity recovery after the rate handling, the performance at higher rates is hindered due to limited diffusion possibly as a result of C-coating properties. The conductivity within the particles could be further improved by increasing the graphitization degree of the carbon coating or utilizing different carbon additives, while an intermediate coating thickness could help in the diffusion, enhancing the performance at higher rates.

4. CONCLUSIONS

Copper Prussian blue analogue (CuPBA) was synthesized in the presence of dopamine and used as a template to prepare carbon-coated mixed Cu–Fe sulfides. Dopamine alters the synthesis of CuPB through its oxidative polymerization process by reducing the ferricyanide precursor, favoring K-rich CuPB, and controlling the particle size by steric effects and formation of dopamine–Fe complex. Thus, PDA-coated CuPB particles are less defective and more homogeneous compared to bare CuPB. While the sole presence of PDA translates into a more K-rich phase, its quantity determines coating thickness. These two effects are correlated and cannot be disassociated. The material was thermally sulfidized under fast and mild conditions, producing homogeneous C-coated KCuFeS_2 nanoparticles. It was shown that the thickness of the coating is of great importance for the stable electrochemical performance of the iron–copper mixed-metal sulfide as the LIB electrode. At the same time, the thicker coating requires activation of the carbon layer to achieve higher capacity and better rate handling. During cycling, CuFeS_2 is gradually reduced to metallic copper and iron, resulting in the combination of redox processes of iron sulfide, copper sulfide, and lithium sulfide species. The presence of elemental copper and carbon coating impedes the shuttling of polysulfides during cycling. The material presents a diffusion-controlled activation process, with a capacity increase from 300 to 400 mAh/g at 250 mA/g, reaching 800 mAh/g at 10 mA/g. After activation of 500

cycles, the rate handling showed excellent capacity recovery and stability. The effect of PDA can impact future derivatization works on PB/PBA through their morphology and phase control.

■ ASSOCIATED CONTENT

Data Availability Statement

The data can be made available upon request.

Supporting Information

The Supporting Information is available free of charge at <https://pubs.acs.org/doi/10.1021/acsomega.2c04209>.

Material characterization of PDA-coated CuFe Prussian blue particles before and after sulfidation by Rietveld refinement and thermogravimetric analysis; additional transmission electron micrographs; and comprehensive electrochemistry data and its postmortem analysis for the sample CuPB-PDA2-S (PDF)

■ AUTHOR INFORMATION

Corresponding Authors

Volker Presser – INM—Leibniz Institute for New Materials, 66123 Saarbrücken, Germany; Department of Materials Science & Engineering, Saarland University, 66123 Saarbrücken, Germany; Saarene—Saarland Center for Energy Materials and Sustainability, 66123 Saarbrücken, Germany; orcid.org/0000-0003-2181-0590; Email: volker.presser@leibniz-inm.de

Samantha Husmann – INM—Leibniz Institute for New Materials, 66123 Saarbrücken, Germany; orcid.org/0000-0001-6157-214X; Email: samantha.husmann@leibniz-inm.de

Author

Behnoosh Bornamehr – INM—Leibniz Institute for New Materials, 66123 Saarbrücken, Germany; Department of Materials Science & Engineering, Saarland University, 66123 Saarbrücken, Germany

Complete contact information is available at: <https://pubs.acs.org/doi/10.1021/acsomega.2c04209>

Author Contributions

B.B.: methodology, investigation, data curation, validation, writing—original draft. V.P.: methodology, validation, supervision, funding acquisition, visualization, writing—review and editing. S.H.: conceptualization, methodology, validation, supervision, funding acquisition, writing—review and editing.

Notes

The authors declare no competing financial interest.

■ ACKNOWLEDGMENTS

S.H. acknowledges funding of the PBDS project (HU 2959/2) by the German Research Foundation (DFG, Deutsche Forschungsgemeinschaft). The authors thank Eduard Arzt (INM) for his continuing support.

■ REFERENCES

- (1) Moeller, K.-C. Overview of Battery Systems. In *Lithium-Ion Batteries: Basics and Applications*; Korthauer, R., Ed.; Springer, 2018; pp 5–9.
- (2) Leuthner, S. Lithium-Ion Battery Overview. In *Lithium-Ion Batteries: Basics and Applications*; Korthauer, R., Ed.; Springer, 2018; pp 14–17.

- (3) Guney, M. S.; Tepe, Y. Classification and assessment of energy storage systems. *Renewable Sustainable Energy Rev.* **2017**, *75*, 1187–1197.
- (4) Zhou, H.; Xin, F.; Pei, B.; Whittingham, M. S. What limits the capacity of layered oxide cathodes in lithium batteries? *ACS Energy Lett.* **2019**, *4*, 1902–1906.
- (5) Manthiram, A.; Song, B.; Li, W. A perspective on nickel-rich layered oxide cathodes for lithium-ion batteries. *Energy Storage Mater.* **2017**, *6*, 125–139.
- (6) Xie, D.; Mei, S.; Xu, Y.; Quan, T.; Härk, E.; Kochovski, Z.; Lu, Y. Efficient sulfur host based on yolk-shell iron oxide/sulfide-carbon nanospindles for lithium-sulfur batteries. *ChemSusChem* **2021**, *14*, 1404–1413.
- (7) Hu, Z.; Liu, Q.; Chou, S.-L.; Dou, S.-X. Advances and challenges in metal sulfides/selenides for next-generation rechargeable sodium-ion batteries. *Adv. Mater.* **2017**, *29*, No. 1700606.
- (8) Yu, X. Y.; Lou, X. W. Mixed metal sulfides for electrochemical energy storage and conversion. *Adv. Energy Mater.* **2018**, *8*, No. 1701592.
- (9) Goodenough, J. B. Energy storage materials: a perspective. *Energy Storage Mater.* **2015**, *1*, 158–161.
- (10) Nitta, N.; Wu, F.; Lee, J. T.; Yushin, G. Li-ion battery materials: present and future. *Mater. Today* **2015**, *18*, 252–264.
- (11) Huang, X.; Tang, J.; Luo, B.; Knibbe, R.; Lin, T.; Hu, H.; Rana, M.; Hu, Y.; Zhu, X.; Gu, Q.; et al. Sandwich-like ultrathin TiS₂ nanosheets confined within N, S codoped porous carbon as an effective polysulfide promoter in lithium-sulfur batteries. *Adv. Energy Mater.* **2019**, *9*, No. 1901872.
- (12) Liu, Y.; Che, Z.; Lu, X.; Zhou, X.; Han, M.; Bao, J.; Dai, Z. Nanostructured metal chalcogenides confined in hollow structures for promoting energy storage. *Nanoscale Adv.* **2020**, *2*, 583–604.
- (13) Ding, W.; Wang, X.; Peng, H.; Hu, L. Electrochemical performance of the chalcopyrite CuFeS₂ as cathode for lithium ion battery. *Mater. Chem. Phys.* **2013**, *137*, 872–876.
- (14) Theerthagiri, J.; Senthil, R. A.; Nithyadharseni, P.; Lee, S. J.; Durai, G.; Kuppusami, P.; Madhavan, J.; Choi, M. Y. Recent progress and emerging challenges of transition metal sulfides based composite electrodes for electrochemical supercapacitive energy storage. *Ceram. Int.* **2020**, *46*, 14317–14345.
- (15) Wang, Y.; Li, X.; Zhang, Y.; He, X.; Zhao, J. Ether based electrolyte improves the performance of CuFeS₂ spike-like nanorods as a novel anode for lithium storage. *Electrochim. Acta* **2015**, *158*, 368–373.
- (16) Wang, Q.; Jin, J.; Wu, X.; Ma, G.; Yang, J.; Wen, Z. A shuttle effect free lithium sulfur battery based on a hybrid electrolyte. *Phys. Chem. Chem. Phys.* **2014**, *16*, 21225–21229.
- (17) Ge, P.; Zhang, L.; Zhao, W.; Yang, Y.; Sun, W.; Ji, X. Interfacial bonding of metal-sulfides with double carbon for improving reversibility of advanced alkali-ion batteries. *Adv. Funct. Mater.* **2020**, *30*, No. 1910599.
- (18) Budak, Ö.; Srimuk, P.; Aslan, M.; Shim, H.; Borchardt, L.; Presser, V. Titanium niobium oxide Ti₂Nb₁₀O₂₉/carbon hybrid electrodes derived by mechanochemically synthesized carbide for high-performance lithium-ion batteries. *ChemSusChem* **2021**, *14*, 398–407.
- (19) Shim, H.; Lim, E.; Fleischmann, S.; Quade, A.; Tolosa, A.; Presser, V. Nanosized titanium niobium oxide/carbon electrodes for lithium-ion energy storage applications. *Sustainable Energy Fuels* **2019**, *3*, 1776–1789.
- (20) Zhao, Y.; Wang, L. P.; Sougrati, M. T.; Feng, Z.; Leconte, Y.; Fisher, A.; Srinivasan, M.; Xu, Z. A review on design strategies for carbon based metal oxides and sulfides nanocomposites for high performance Li and Na ion battery anodes. *Adv. Energy Mater.* **2017**, *7*, No. 1601424.
- (21) Husmann, S.; Zarbin, A. J. G.; Dryfe, R. A. W. High-performance aqueous rechargeable potassium batteries prepared via interfacial synthesis of a Prussian blue-carbon nanotube composite. *Electrochim. Acta* **2020**, *349*, No. 136243.
- (22) Zakaria, M. B.; Chikyow, T. Recent advances in Prussian blue and Prussian blue analogues: synthesis and thermal treatments. *Coord. Chem. Rev.* **2017**, *352*, 328–345.
- (23) Guo, Y.; Tang, J.; Wang, Z.; Sugahara, Y.; Yamauchi, Y. Hollow porous heterometallic phosphide nanocubes for enhanced electrochemical water splitting. *Small* **2018**, *14*, No. 1802442.
- (24) Nai, J.; Lou, X. W. Hollow structures based on Prussian blue and its analogs for electrochemical energy storage and conversion. *Adv. Mater.* **2019**, *31*, No. 1706825.
- (25) Kang, B. K.; Woo, M. H.; Lee, J.; Song, Y. H.; Wang, Z.; Guo, Y.; Yamauchi, Y.; Kim, J. H.; Lim, B.; Yoon, D. H. Mesoporous Ni-Fe oxide multi-composite hollow nanocages for efficient electrocatalytic water oxidation reactions. *J. Mater. Chem. A* **2017**, *5*, 4320–4324.
- (26) Wu, X.; Ru, Y.; Bai, Y.; Zhang, G.; Shi, Y.; Pang, H. PBA composites and their derivatives in energy and environmental applications. *Coord. Chem. Rev.* **2022**, *451*, No. 214260.
- (27) Zhong, L.; Mao, B.; Liu, M.; Liu, M.; Sun, Y.; Song, Y.-T.; Zhang, Z.-M.; Lu, T.-B. Construction of hierarchical photocatalysts by growing ZnIn₂S₄ nanosheets on Prussian blue analogue-derived bimetallic sulfides for solar co-production of H₂ and organic chemicals. *J. Energy Chem.* **2021**, *54*, 386–394.
- (28) Song, X.; Song, S.; Wang, D.; Zhang, H. Prussian blue analogs and their derived nanomaterials for electrochemical energy storage and electrocatalysis. *Small Methods* **2021**, *5*, No. 2001000.
- (29) Chen, X.; Zeng, S.; Muheyati, H.; Zhai, Y.; Li, C.; Ding, X.; Wang, L.; Wang, D.; Xu, L.; He, Y.; Qian, Y. Double-shelled Ni-Fe-P/N-doped carbon nanobox derived from a prussian blue analogue as an electrode material for K-ion batteries and Li-S batteries. *ACS Energy Lett.* **2019**, *4*, 1496–1504.
- (30) Peng, Z.; Qiu, X. Y.; Yu, Y.; Jiang, D.; Wang, H. T.; Cai, G. Y.; Zhang, X. X.; Dong, Z. H. Polydopamine coated Prussian blue analogue derived hollow carbon nanoboxes with FeP encapsulated for hydrogen evolution. *Carbon* **2019**, *152*, 16–23.
- (31) Ming, H.; Torad, N. L.; Chiang, Y.-D.; Wu, K. C.-W.; Yamauchi, Y. Size- and shape-controlled synthesis of Prussian Blue nanoparticles by a polyvinylpyrrolidone-assisted crystallization process. *CrystEngComm* **2012**, *14*, 3387–3396.
- (32) Lopes, L. C.; Husmann, S.; Zarbin, A. J. G. Chemically synthesized graphene as a precursor to Prussian blue-based nanocomposite: A multifunctional material for transparent aqueous K-ion battery or electrochromic device. *Electrochim. Acta* **2020**, *345*, No. 136199.
- (33) Husmann, S.; Booth, S. G.; Zarbin, A. J. G.; Dryfe, R. A. W. Electrodeposition of Prussian blue/carbon nanotube composites at a liquid-liquid interface. *J. Braz. Chem. Soc.* **2018**, *29*, 1130–1139.
- (34) Li, W.-J.; Han, C.; Cheng, G.; Chou, S.-L.; Liu, H.-K.; Dou, S.-X. Chemical properties, structural properties, and energy storage applications of prussian blue analogues. *Small* **2019**, *15*, No. 1900470.
- (35) Husmann, S.; Orth, E. S.; Zarbin, A. J. G. A multi-technique approach towards the mechanistic investigation of the electrodeposition of Prussian blue over carbon nanotubes film. *Electrochim. Acta* **2019**, *312*, 380–391.
- (36) Hurlbutt, K.; Wheeler, S.; Capone, I.; Pasta, M. Prussian blue analogs as battery materials. *Joule* **2018**, *2*, 1950–1960.
- (37) Liu, Y.; Ai, K.; Lu, L. Polydopamine and its derivative materials: synthesis and promising applications in energy, environmental, and biomedical fields. *Chem. Rev.* **2014**, *114*, 5057–5115.
- (38) Ryu, J. H.; Messersmith, P. B.; Lee, H. Polydopamine surface chemistry: A decade of discovery. *ACS Appl. Mater. Interfaces* **2018**, *10*, 7523–7540.
- (39) Liebscher, J.; Mrówczyński, R.; Scheidt, H. A.; Filip, C.; Hädäde, N. D.; Turcu, R.; Bende, A.; Beck, S. Structure of polydopamine: a never-ending story? *Langmuir* **2013**, *29*, 10539–10548.
- (40) Yang, J.; Stuart, M. A. C.; Kamperman, M. Jack of all trades: versatile catechol crosslinking mechanisms. *Chem. Soc. Rev.* **2014**, *43*, 8271–8298.

- (41) Zeng, H.; Hwang, D. S.; Israelachvili, J. N.; Waite, J. H. Strong reversible Fe³⁺-mediated bridging between dopa-containing protein films in water. *Proc. Natl. Acad. Sci. U.S.A.* **2010**, *107*, 12850–12853.
- (42) Holten-Andersen, N.; Harrington, M. J.; Birkedal, H.; Lee, B. P.; Messersmith, P. B.; Lee, K. Y. C.; Waite, J. H. pH-induced metal-ligand cross-links inspired by mussel yield self-healing polymer networks with near-covalent elastic moduli. *Proc. Natl. Acad. Sci. U.S.A.* **2011**, *108*, 2651–2655.
- (43) Moretti, G.; Gervais, C. Raman spectroscopy of the photosensitive pigment Prussian blue. *J. Raman Spectrosc.* **2018**, *49*, 1198–1204.
- (44) Kettle, S. F. A.; Diana, E.; Marchese, E. M. C.; Boccaleri, E.; Stanghellini, P. L. The vibrational spectra of the cyanide ligand revisited: the $\nu(\text{CN})$ infrared and Raman spectroscopy of Prussian blue and its analogues. *J. Raman Spectrosc.* **2011**, *42*, 2006–2014.
- (45) Ojwang, D. O.; Grins, J.; Wardecki, D.; Valvo, M.; Renman, V.; Häggström, L.; Ericsson, T.; Gustafsson, T.; Mahmoud, A.; Hermann, R. P.; Svensson, G. Structure characterization and properties of K-containing copper hexacyanoferrate. *Inorg. Chem.* **2016**, *55*, 5924–5934.
- (46) Figueiredo, M. L.; Martin, C. S.; Furini, L. N.; Rubira, R. J.; Batagin-Neto, A.; Alessio, P.; Constantino, C. J. Surface-enhanced Raman scattering for dopamine in Ag colloid: Adsorption mechanism and detection in the presence of interfering species. *Appl. Surf. Sci.* **2020**, *522*, No. 146466.
- (47) Asakura, D.; Okubo, M.; Mizuno, Y.; Kudo, T.; Zhou, H.; Ikeda, K.; Mizokawa, T.; Okazawa, A.; Kojima, N. Fabrication of a cyanide-bridged coordination polymer electrode for enhanced electrochemical ion storage ability. *J. Phys. Chem. C* **2012**, *116*, 8364–8369.
- (48) Wu, X.; Luo, Y.; Sun, M.; Qian, J.; Cao, Y.; Ai, X.; Yang, H. Low-defect Prussian blue nanocubes as high capacity and long life cathodes for aqueous Na-ion batteries. *Nano Energy* **2015**, *13*, 117–123.
- (49) Yu, X.; Fan, H.; Liu, Y.; Shi, Z.; Jin, Z. Characterization of carbonized polydopamine nanoparticles suggests ordered supramolecular structure of polydopamine. *Langmuir* **2014**, *30*, 5497–5505.
- (50) Parker, G. K.; Woods, R.; Hope, G. A. Raman investigation of chalcopryrite oxidation. *Colloids Surf., A* **2008**, *318*, 160–168.
- (51) Ohrendorf, F.; Haeuselner, H. Lattice dynamics of chalcopryrite type compounds. Part I. Vibrational frequencies. *Cryst. Res. Technol.* **1999**, *34*, 339–349.
- (52) Mernagh, T. P.; Trudu, A. G. A laser Raman microprobe study of some geologically important sulphide minerals. *Chem. Geol.* **1993**, *103*, 113–127.
- (53) Jiang, F.; Zhao, W.; Zhang, L.; Tian, Y.; Gao, X.; Ge, P.; Sun, W.; Chang, X.; Ji, X. Unraveling the mechanism of chalcopryrite's superior performance for lithium storage. *ACS Appl. Energy Mater.* **2021**, *4*, 5086–5093.
- (54) Conejeros, S.; Alemany, P.; Lluell, M.; Sanchez, V.; Llanos, J.; Padilla-Campos, L. Structural stability of quaternary ACuFeS₂ (A = Li, K) phases: a computational approach. *Inorg. Chem.* **2012**, *51*, 362–369.
- (55) Wu, X.; Zhao, Y.; Yang, C.; He, G. PVP-assisted synthesis of shape-controlled CuFeS₂ nanocrystals for Li-ion batteries. *J. Mater. Sci.* **2015**, *50*, 4250–4257.
- (56) Guo, P.; Song, H.; Liu, Y.; Wang, C. CuFeS₂ quantum dots anchored in carbon frame: superior lithium storage performance and the study of electrochemical mechanism. *ACS Appl. Mater. Interfaces* **2017**, *9*, 31752–31762.
- (57) Sun, W.; Tao, X.; Du, P.; Wang, Y. Carbon-coated mixed-metal sulfide hierarchical structure: MOF-derived synthesis and lithium-storage performances. *Chem. Eng. J.* **2019**, *366*, 622–630.
- (58) Husmann, S.; Budak, Ö.; Quade, A.; Frank, A.; Kruth, A.; Scheu, C.; Tolosa, A.; Presser, V. Electrospun vanadium sulfide / carbon hybrid fibers obtained via one-step thermal sulfidation for use as lithium-ion battery electrodes. *J. Power Sources* **2020**, *450*, No. 227674.
- (59) Cho, Y.-D.; Fey, G. T.-K.; Kao, H.-M. The effect of carbon coating thickness on the capacity of LiFePO₄/C composite cathodes. *J. Power Sources* **2009**, *189*, 256–262.
- (60) Smith, A. J.; Burns, J.; Dahn, J. A high precision study of the Coulombic efficiency of Li-ion batteries. *Electrochem. Solid-State Lett.* **2010**, *13*, A177.
- (61) Zhu, Z.; Cheng, F.; Chen, J. Investigation of effects of carbon coating on the electrochemical performance of Li₄Ti₅O₁₂/C nanocomposites. *J. Mater. Chem. A* **2013**, *1*, 9484–9490.
- (62) Li, R.; Wang, Y.; Zhou, C.; Wang, C.; Ba, X.; Li, Y.; Huang, X.; Liu, J. Carbon-stabilized high-capacity ferrous oxide nanorod array for flexible solid-state alkaline battery–supercapacitor hybrid device with high environmental suitability. *Adv. Funct. Mater.* **2015**, *25*, 5384–5394.
- (63) Zhang, Y.; Zhao, G.; Lv, X.; Tian, Y.; Yang, L.; Zou, G.; Hou, H.; Zhao, H.; Ji, X. Exploration and size engineering from natural chalcopryrite to high-performance electrode materials for lithium-ion batteries. *ACS Appl. Mater. Interfaces* **2019**, *11*, 6154–6165.
- (64) Wu, M.; Zhang, Y.; Li, T.; Chen, Z.; Cao, S.-a.; Xu, F. Copper sulfide nanoparticles as high-performance cathode materials for magnesium secondary batteries. *Nanoscale* **2018**, *10*, 12526–12534.
- (65) Zheng, S.; Yi, F.; Li, Z.; Zhu, Y.; Xu, Y.; Luo, C.; Yang, J.; Wang, C. Copper-stabilized sulfur-microporous carbon cathodes for Li–S batteries. *Adv. Funct. Mater.* **2014**, *24*, 4156–4163.
- (66) McDowell, M. T.; Lu, Z.; Koski, K. J.; Yu, J. H.; Zheng, G.; Cui, Y. In situ observation of divergent phase transformations in individual sulfide nanocrystals. *Nano Lett.* **2015**, *15*, 1264–1271.
- (67) Shi, C.; Li, X.; He, X.; Zhao, J. New insight into the interaction between carbonate-based electrolyte and cuprous sulfide electrode material for lithium ion batteries. *Electrochim. Acta* **2015**, *174*, 1079–1087.
- (68) Lu, J.; Lian, F.; Guan, L.; Zhang, Y.; Ding, F. Adapting FeS₂ micron particles as an electrode material for lithium-ion batteries via simultaneous construction of CNT internal networks and external cages. *J. Mater. Chem. A* **2019**, *7*, 991–997.

Recommended by ACS

Ternary Copper Iron Sulfide Microflowlers Anchored on Reduced Graphene Oxide for Water Splitting

Srinivasan Swathi, Dhayalan Velauthapillai, et al.

APRIL 19, 2023

ACS APPLIED NANO MATERIALS

READ

Preintercalated Copper Hexacyanoferrate as a Long-Time Cycle Cathode Material for Aqueous Aluminum-Ion Batteries

Jia Zheng, Ting Sun, et al.

APRIL 10, 2023

ACS SUSTAINABLE CHEMISTRY & ENGINEERING

READ

Enhanced Electrochemical Performance of CuO Capsules@CDs Composites for Solid-State Hybrid Supercapacitor

Sengodan Prabhu, Aharon Gedanken, et al.

APRIL 20, 2023

ENERGY & FUELS

READ

Ethanolamine-Induced Synthesis of Sesame Cake-like Cu/Ag Nanosheets with High Activity for the Reduction of p-Nitrophenol to p-Aminophenol

Jie Chen, Yiwei Dong, et al.

JUNE 02, 2023

ACS APPLIED NANO MATERIALS

READ

Get More Suggestions >

**Mixed Cu-Fe sulfides derived from polydopamine-coated Prussian blue analog
as Lithium-ion battery electrode**

Behnoosh Bornamehr^{1,2}, Volker Presser^{1,2,3*}, Samantha Husmann^{1*}

¹ *INM – Leibniz Institute for New Materials, Campus D2 2, 66123, Saarbrücken, Germany*

² *Department of Materials Science & Engineering, Saarland University, Campus D2 2, 66123, Saarbrücken, Germany*

³ *Saarene – Saarland Center for Energy Materials and Sustainability, Campus C4 2, 66123 Saarbrücken, Germany*

* Corresponding authors:

volker.presser@leibniz-inm.de (VP), samantha.husmann@leibniz-inm.de (SH)

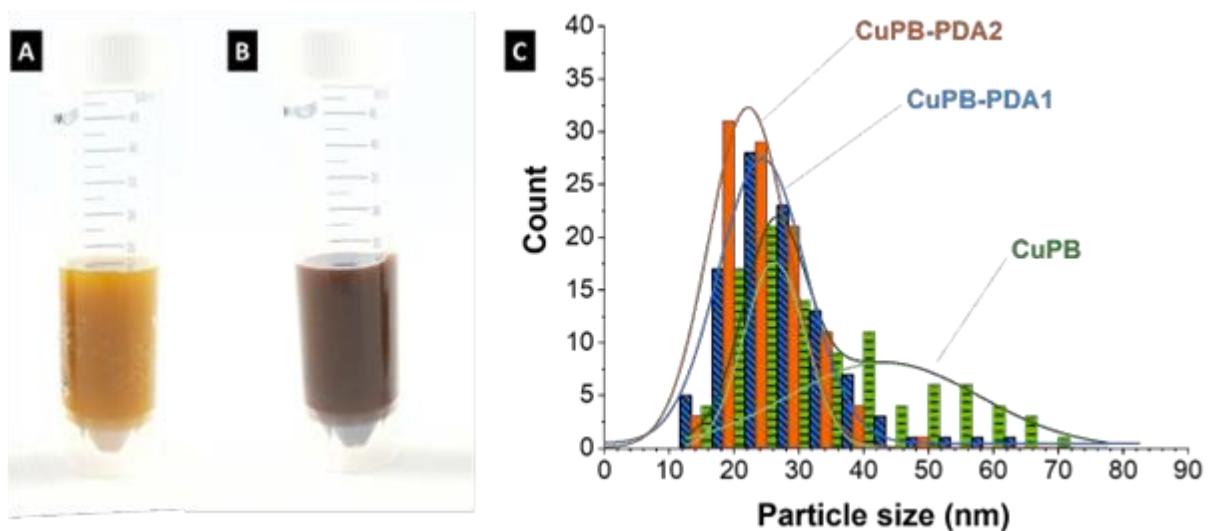


Figure S1. A) Photograph of CuFe PBA without PDA with yellow color and B) photograph of CuFe PBA with PDA with dark red color. C) Particle size distribution histogram of CuPB, CuPB-PDA1, CuPB-PDA2 measured by using 100 particles from scanning electron micrographs.

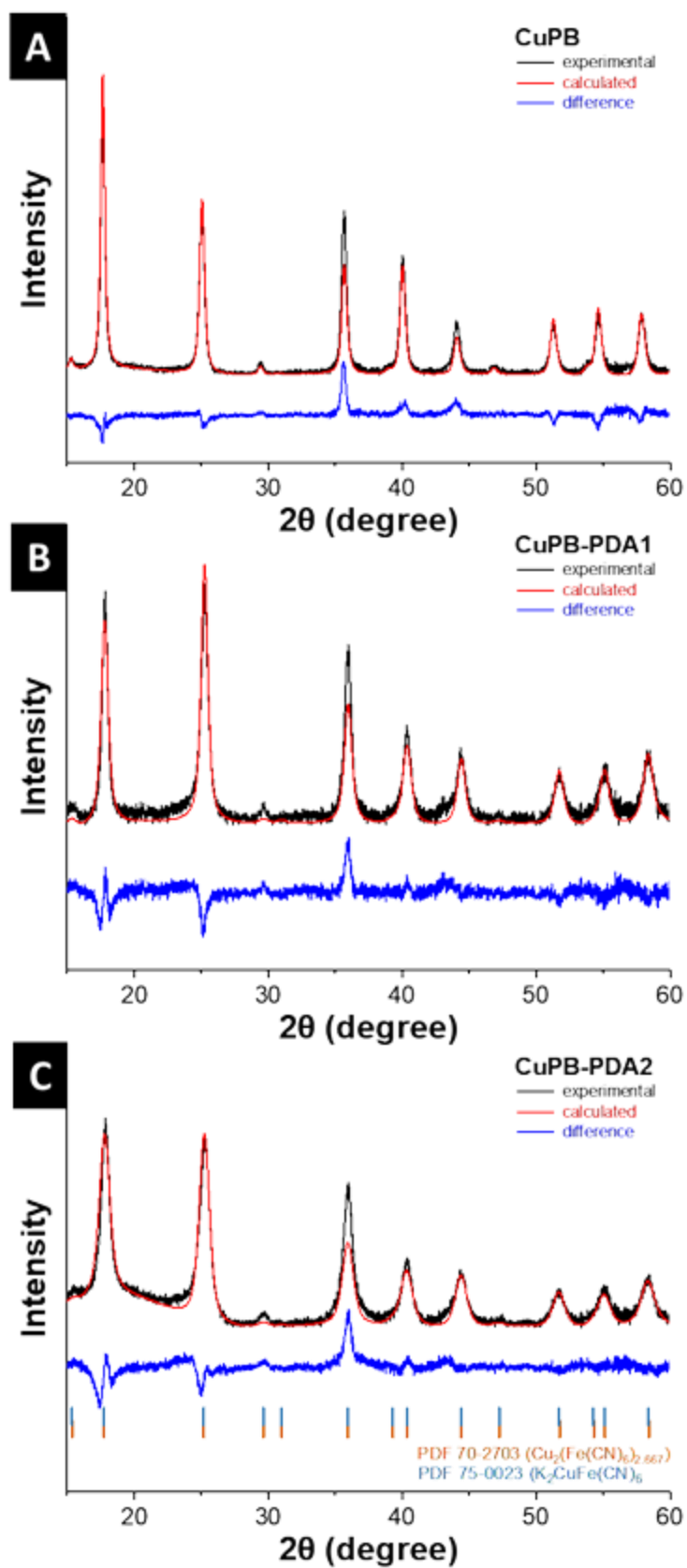


Figure S2: Rietveld fit from powder X-ray diffraction of the CuPB particles with and without PDA coatings: A) CuPB, B) CuPB-PDA1, and C) CuPB-PDA2.

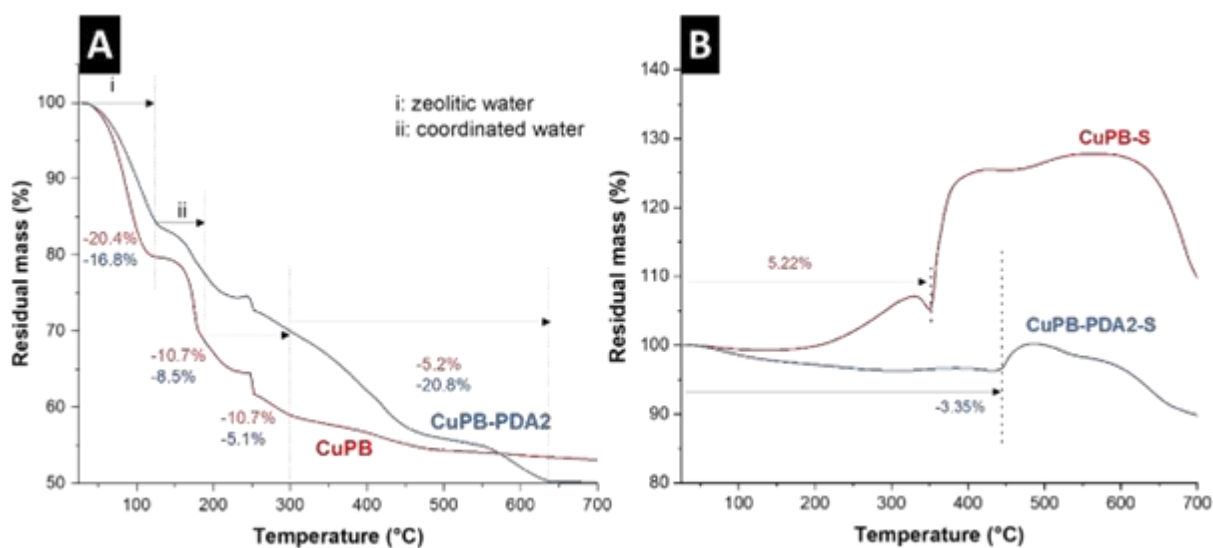


Figure S3. A) Thermograms of CuPB and CuPB-PDA2 and B) CuPB-S and CuPB-PDA2-S.

Heating was done under 5°C/min, Syn. air.

Method of calculating the amount of carbon from the thermograms: The mass loss below 200 °C can be assigned to the elimination of zeolitic/coordinated water (to 100 °C and 200 °C respectively). The next step is the mass loss due to the CN group removal, which occurs after the structural water removal and continues with a gradual slope contributing to the changes of 200 °C to 650 °C in the CuPB sample. In the CuPB-PDA2 sample, in addition to the cyanide bond loss, PDA is removed via the oxidation with air. Since the mass loss between 200-500 °C is 15.9% for the CuPB and 25.9% for CuPB-PDA2, the mass loss due to the polymer is calculated to be the difference which is 10 mass% of the CuPB-PDA2 sample.

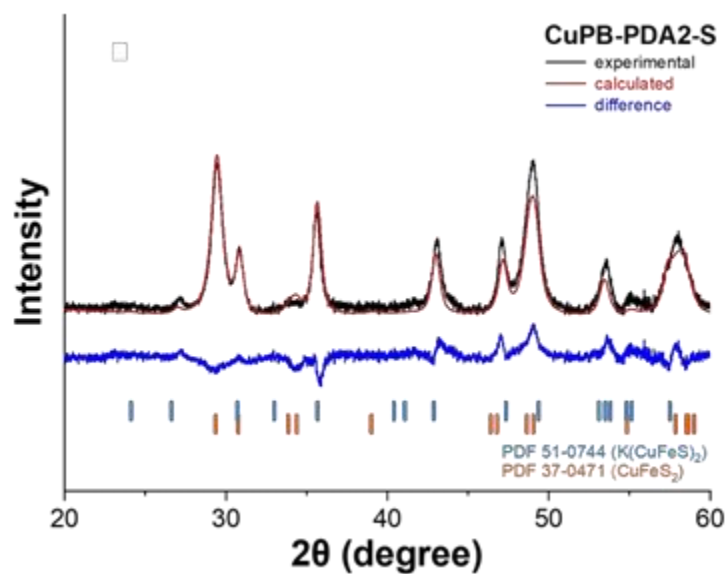


Figure S4: Rietveld fit from powder X-ray diffraction of the CuPB-PDA2 after sulfidation.

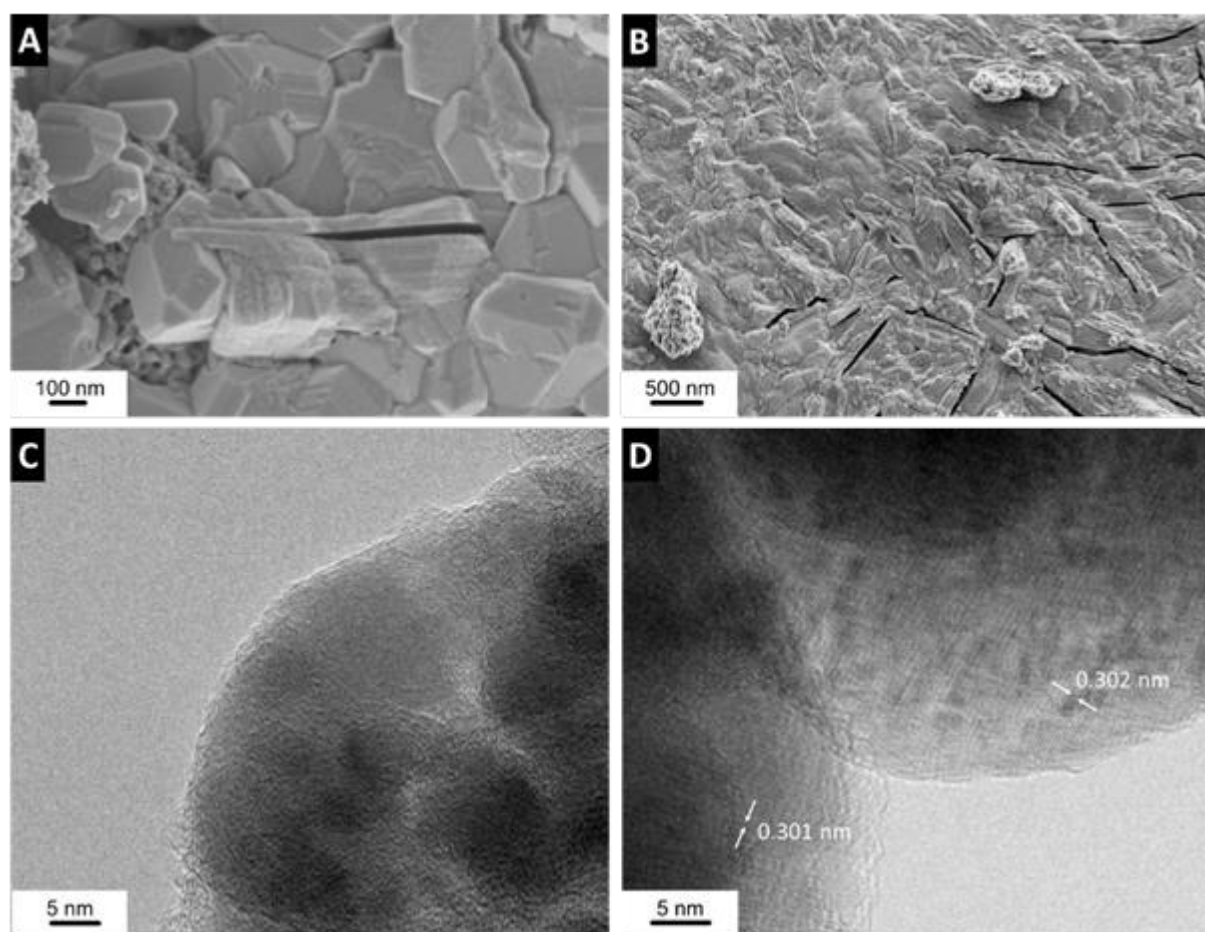


Figure S5. A-B) Scanning electron micrographs of the sulfidized samples. A) CuPB-S and B) CuPB-PDA1-S. C-D) Transmission electron micrographs of CuPB-PDA2-S.

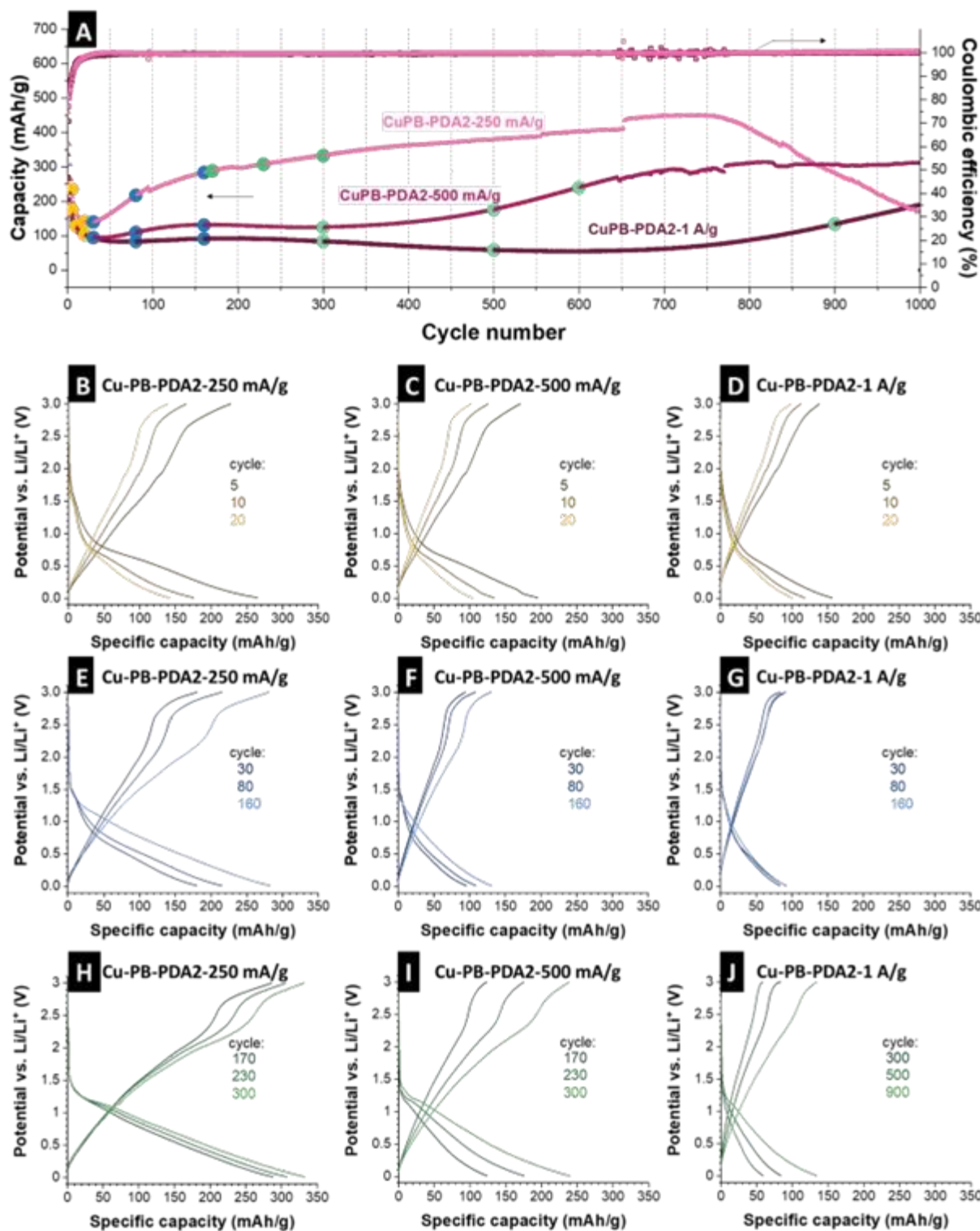


Figure S6. A) Electrochemical cycling stability of the CuPB-PDA2-S and B-J) charge-discharge curves from chosen point in (A)

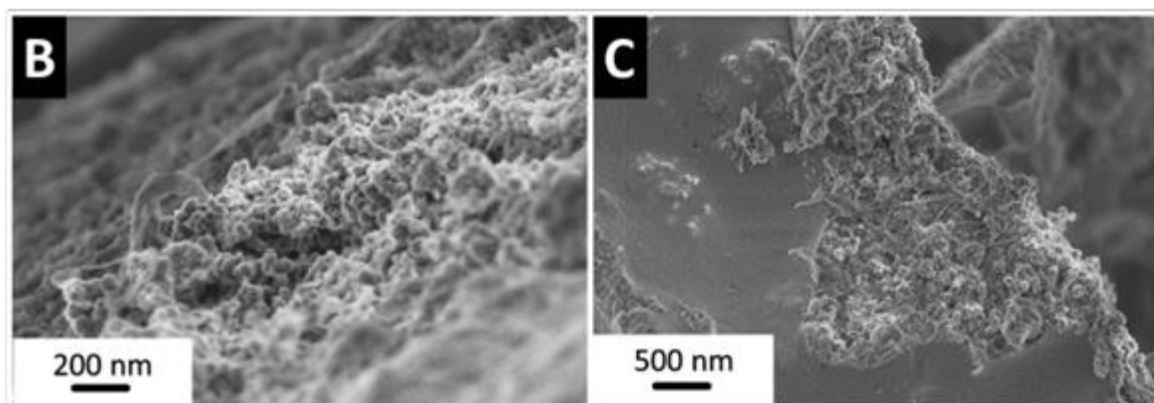
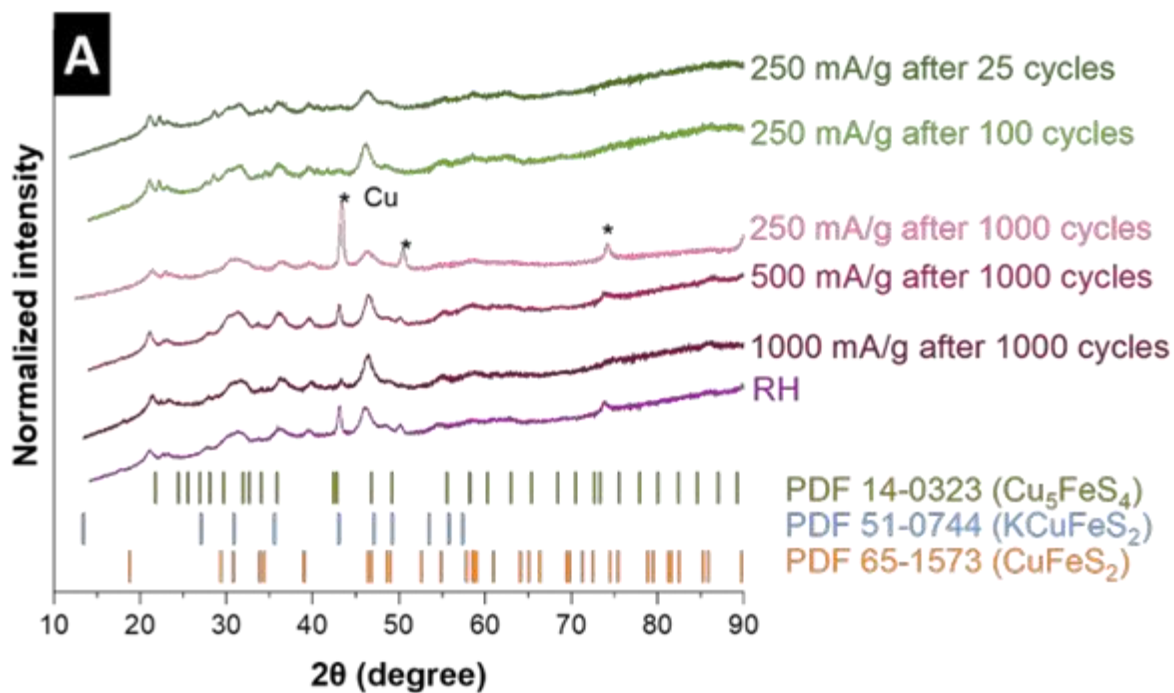


Figure S7. A) post-mortem X-ray diffractograms of cycled electrodes. B-C) Scanning electron micrographs of the coated electrode B) prior to electrochemical testing and C) after the rate handling test.

Table S1. Possible reactions of CuPB-S system under cycling between 0.01-3.0 V vs. Li/Li⁺.(1)

<u>Process</u>	<u>Reaction</u>	<u>Approximate potential / vs. Li/Li⁺</u>
<u>Discharging</u>	$\text{CuFeS}_2 + x\text{Li}^+ + xe^- \rightarrow \text{Li}_x\text{CuFeS}_2$	1.65 V (1 st cycle)
	$\text{LiCuFeS}_2 + \text{Li}^+ + e^- \rightarrow \text{Cu}^0 + \text{Li}_2\text{FeS}_2$	1.5 V (1 st cycle)
	$\text{Li}_x\text{CuFeS}_2 + (4-x)\text{Li}^+ (4-x)e^- \rightarrow \text{Cu}^0 + \text{Fe}^0 + 2\text{Li}_2\text{S}$	Overall reaction
	$\text{Li}_2\text{FeS}_2 + 2\text{Li}^+ + 2e^- \rightarrow \text{Fe}^0 + 2\text{Li}_2\text{S}$	0.70 V
	$\text{Cu}_2\text{S} + 2\text{Li}^+ + 2e^- \rightarrow 2\text{Cu}^0 + \text{Li}_2\text{S}$	~1.6 V (from 2 nd cycle)
	$\text{Li}_{2-x}\text{FeS}_2 + x\text{Li}^+ + xe^- \rightarrow \text{Li}_2\text{FeS}_2$	~1.6 V (from 2 nd cycle)
	$\text{Li}_{2-y}\text{S}_y + y\text{Li}^+ + ye^- \rightarrow \text{Li}_2\text{S}$	< 2.0 V
<u>Charging</u>	$\text{Fe}^0 + 2\text{Li}_2\text{S} \rightarrow \text{Li}_2\text{FeS}_2 + 2\text{Li}^+ + 2e^-$	1.10 V - 1.45 V
	$2\text{Cu}^0 + \text{Li}_2\text{S} \rightarrow \text{Cu}_2\text{S} + 2\text{Li}^+ + 2e^-$	1.90 V
	$\text{Li}_2\text{FeS}_2 \rightarrow \text{Li}_{2-x}\text{FeS}_2 + x\text{Li}^+ + xe^- (0.5 < x < 0.8)$	> 2.0 V
	$\text{Li}_{2-x}\text{FeS}_2 \rightarrow \text{FeS}_{2-y} + \text{Li}_{2-x}\text{S}_y + (2-y)e^-$	~2.4 V

Supplementary References:

1. Zhang Y, Zhao G, Lv X, Tian Y, Yang L, Zou G, et al. Exploration and Size Engineering from Natural Chalcopyrite to High-Performance Electrode Materials for Lithium-Ion Batteries. ACS Applied Materials & Interfaces. 2019;11(6):6154-65.

Surfactant stabilization of vanadium iron oxide derived from Prussian blue analog for lithium-ion battery electrodes

Behnoosh Bornamehr^{1,2}, Hiba El Gaidi^{1,2}, Stefanie Arnold^{1,2}, Emmanuel Pamet ^{1,2}, Volker Presser^{1,2,3,*}

¹ *INM – Leibniz Institute for New Materials, Campus D2 2, 66123, Saarbr cken, Germany*

² *Department of Materials Science & Engineering, Saarland University, Campus D2 2, 66123, Saarbr cken, Germany*

³ *Saarene – Saarland Center for Energy Materials and Sustainability, Campus C4 2, 66123 Saarbr cken, Germany*

Citation:

Bornamehr, B., El Gaidi, H., Arnold, S., Pamet , E. and Presser, V., 2023. Stabilization of iron vanadium Prussian blue derivative enables high-performance lithium-ion battery electrodes. Sustainable Energy & Fuels.

Own contributions:

Conceptualization, Methodology, Investigation, Data Curation, Validation, Writing – original draft



Cite this: DOI: 10.1039/d3se00854a

Surfactant stabilization of vanadium iron oxide derived from Prussian blue analog for lithium-ion battery electrodes†

Behnoosh Bornamehr,^{ab} Hiba El Gaidi,^{ab} Stefanie Arnold,^{ab} Emmanuel Pameté^a and Volker Presser^{id}*^{abc}

Due to their high energy density, Li-ion batteries have become indispensable for energy storage in many technical devices. Prussian blue and its analogs are a versatile family of materials. Apart from their direct use as an alkali-ion battery electrode, they are a promising source for templating other compounds due to the presence of carbon, nitrogen, and metallic elements in their structure, ease of synthesis, and high tunability. In this study, homogeneous iron vanadate derivatization from iron vanadium Prussian blue was successfully carried out using an energy efficient infrared furnace utilizing CO₂ gas. Iron-vanadate is an inherently unstable electrode material if cycled at low potentials vs. Li/Li⁺. Several parameters were optimized to achieve a stable electrochemical performance of this derivative, and the effect of surfactants, such as tannic acid, sodium dodecylbenzene sulfonate, and polyvinylpyrrolidone were shown with their role in the morphology and electrochemical performance. While stabilizing the performance, we demonstrate that the type and order of addition of these surfactants are fundamental for a successful coating formation, otherwise they can hinder the formation of PBA, which has not been reported previously. Step-by-step, we illustrate how to prepare self-standing electrodes for Li-ion battery cells without using an organic solvent or a fluorine-containing binder while stabilizing the electrochemical performance. A 400 mA h g⁻¹ capacity at the specific current of 250 mA g⁻¹ was achieved after 150 cycles while maintaining a Coulombic efficiency of 99.2% over an extended potential range of 0.01–3.50 V vs. Li/Li⁺.

Received 4th July 2023
Accepted 22nd July 2023

DOI: 10.1039/d3se00854a

rsc.li/sustainable-energy

1. Introduction

Li-ion batteries are considered the key technology for portable energy storage, and their market is growing with the energy transition. To meet the increasing requirements for improved power and energy densities and their environmental impact, continuous research is conducted for next-generation battery materials that are more sustainable and offer enhanced electrochemical performance.¹ Many alternatives to commercial battery materials can be synthesized by derivatization from Prussian blue and its analogs (PBAs). While easy and cheap to

synthesize, PBA-derived metal-vanadates have remained unexplored, although they can offer high capacities.²

So far, work on the iron–vanadium (FeV) PBA in aqueous media has shown that the material decomposes and cannot offer a stable capacity. Coating the particles with a more stable PBA, namely with the CuFe, has been reported to create a barrier from the dissolution of FeV, thereby improving the stability.³ To the best of our knowledge, there are no reports on the derivatization from the FeV. For example, PBAs are used in energy storage and conversion as cathodes for commercial Na-ion batteries.⁴ Due to their inherent porous structure arising from the cyanide ligands in the lattice, they have an advantage in ion mass transport.⁵ In parallel, they also are a great precursor for self-templating as they contain metallic precursor elements in their structure and cyanide ligands that can decompose to nitrogen-doped carbon during derivatization. Additionally, PBAs can be prepared in aqueous media at room temperature, are highly tunable in morphology and chemistry, and can be converted to a variety of compounds at temperatures of 300–500 °C.^{6,7}

Target derivative compounds for alkali-ion storage are mainly metal oxides, sulfides, and phosphides due to their high storage capacity.^{8,9} Mixed metal compounds can offer high

^aINM – Leibniz Institute for New Materials, Campus D2 2, 66123 Saarbrücken, Germany. E-mail: volker.presser@leibniz-inm.de

^bDepartment of Materials Science & Engineering, Saarland University, Campus D2 2, 66123 Saarbrücken, Germany

^cSaarene – Saarland Center for Energy Materials and Sustainability, Campus C4 2, 66123 Saarbrücken, Germany

† Electronic supplementary information (ESI) available: Digital images of iron–vanadium oxide self-standing electrode and synthesis solutions, additional characterization of FeV and FVO including SEM, XRD, Raman, TGA, and TEM. Additional electrochemical characterizations. See DOI: <https://doi.org/10.1039/d3se00854a>

capacities due to a higher lithiation degree while distributing the volumetric expansion over multiple steps that otherwise cause pulverization in single metal compounds.¹⁰ Among the mixed vanadium oxides, iron vanadate incorporates low-cost iron in its structure, a rock-forming element with the highest abundance among transition metals. The first report on iron-vanadate as an electrode in Li-ion batteries in Fe_2VO_4 spinel structure was reported with an initial capacity of 250 mA h g^{-1} at 250 mA g^{-1} .¹¹ Further studies in potassium-ion batteries elucidated that Fe_2VO_4 undergoes conversion reactions that break down the mixed metal oxide into vanadium oxide and iron oxide. A capacity loss accompanies this transition if the particles are not confined or protected.¹² Vanadium-iron oxide, compared to the current commercial battery electrode materials, also bears the advantage of easy recovery after its end of life.¹³ Therefore, the dissolution of vanadium during cycling is directly related to its solubility.

Using PBAs for mixed metal oxide derivatization provides multiple advantages from a sustainability point of view. First, the synthesis can be done in pH-neutral aqueous media, avoiding the hazards of organic or low-pH components in preparation and waste management. Second, the synthesis is done at room temperature without autoclaves, heating energy, or pressure, reducing the carbon footprint and energy usage compared to other methods, such as hydrothermal or solid-state synthesis.¹ Third, the synthesis can be scaled to larger volumes due to simplicity. For example, the PBA synthesis, particle coating, and attachment to carbon nanotubes (CNTs) can be done in one step. Additionally, derivatization from PBAs to mixed metal oxides usually requires low energy, employing temperatures lower than $500 \text{ }^\circ\text{C}$ for a duration of 2 h.¹⁴

In this work, we show how to derive homogeneous iron vanadium mixed metal oxide by templating the FeV PBA *via* a low-energy heat treatment and how to prepare self-standing electrodes without using a binder or organic solvents. Multiple parameters in the synthesis, processing, and electrode preparation are then improved to stabilize the material's performance, and their role is investigated. We analyze the effect of different surfactants on the electrochemical stability, namely tannic acid, sodium dodecylbenzene sulfonate, and polyvinylpyrrolidone. The role of surfactant types and their addition to different metal salts are explained following their effect on salt solubility.

2. Experimental

2.1. Synthesis of the FeV

FeV was prepared on CNTs from an aqueous solution with 658.58 mg of potassium ferricyanide ($\text{K}_3\text{Fe}(\text{CN})_6$, 99.0%, Sigma Aldrich), 326 mg of vanadyl sulfate (VO_2SO_4 , 97.0%, Sigma Aldrich), and 50 mg of CNTs (NC7000, Nanocyl).

CNTs served as a network provider and substrate for the FeV particles to form a self-standing electrode. All aqueous solutions were prepared with ultrapure water ($\rho > 18.18 \text{ M}\Omega \text{ cm}$). The formation of the FeV was done by dropwise addition of 100 mL of an aqueous solution of 10 mM vanadyl sulfate at a rate of 40 mL h^{-1} to 100 mL aqueous 10 mM solution of potassium

ferricyanide mixed with 50 mg CNT powder under magnetic stirring. The mixture remained overnight to rest. Multiple rounds of centrifugation and washing in ultrapure water and ethanol obtained the FeV powder after drying at $80 \text{ }^\circ\text{C}$ overnight.

2.2. Synthesis of FeV-PVP/SDBS

FeV-PVP/SDBS1 was prepared by dropwise addition at a 40 mL h^{-1} rate of 100 mL aqueous solution of vanadyl sulfate mixed with 1 g polyvinylpyrrolidone (PVP) or sodium dodecylbenzene sulfonate (SDBS) to a 100 mL aqueous solution of potassium ferricyanide mixed with 50 mg CNTs as a powder under magnetic stirring.

FeV-PVP/SDBS2 was prepared by dropwise addition at a 40 mL h^{-1} rate of 100 mL aqueous solution of potassium ferricyanide powder mixed with 1 g PVP or SDBS to a 100 mL aqueous solution of vanadyl sulfate mixed with 50 mg CNTs under magnetic stirring.

2.3. Oxidation of the FeV

The oxidation of the material was done by heat treatment in an infrared furnace (Behr infrared furnace IRF 10) under 50 : 50 sccm Ar/CO_2 flow. After 30 min of purging, the furnace was heated to $400 \text{ }^\circ\text{C}$ for 1000 s and held for 1 h. The FeV oxidized powder was obtained after cooling in the furnace to room temperature for 1000 s, and the product was labeled FVO. The samples with PVP or SDBS were denoted similarly after heat treatment: FVO-PVP1 or FVO-PVP2 and FVO-SDBS1 or FVO-SDBS2.

2.4. Material characterization

Scanning electron microscopy (SEM) was carried out to characterize the morphology using a ZEISS GEMINI 500 employing an acceleration voltage of 1 kV. Transmission electron microscopy (TEM) was carried out using a 2100F system (JEOL) at a voltage of 200 kV for imaging. For SEM, samples were mounted on an aluminum stub fixed with double-sided copper tape and analyzed without a conductive sputter coating. For TEM, a copper grid coated with lacey carbon was used as the sample holder, and the powder was dispersed in ethanol *via* ultrasonic bath and then dried on the copper grid drop by drop.

To analyze the present phases in the material, X-ray diffraction (XRD) was carried out using a D8 Discover diffractometer (BRUKER AXS) with a copper source ($\text{Cu-K}\alpha$, 40 kV, 40 mA), a Göbel mirror, and a 1 mm point focus. About 10 mg of as-synthesized powder was used. Each angular range of $20^\circ 2\theta$ was covered by a two-dimensional VANTEC detector and recorded for 2000 s. Measurement was carried out on a full range of $20\text{--}80^\circ 2\theta$. Before the measurement, a NIST 1976b corundum standard calibration and peak position adjustment were conducted. The powder samples were fixed by pressing on a glass sample holder with a depth of 0.5 mm. All scans went through background subtraction and were normalized between 0 and 100.

Raman spectroscopy was conducted with a Renishaw inVia Raman microscope employing an Nd-YAG laser and 633 nm

excitation wavelength with a power of 87 μW at the focal point of the sample with a numeric aperture of 0.75. For each sample, spectra from 10 points were recorded with 20 s exposure time and accumulated 20 times. The powder samples were placed on microscope glass slides. Spectra were treated by cosmic ray removal and normalized. The system was calibrated before and after the measurement with a silicon standard.

Thermogravimetric analysis (TGA) on powder materials was performed by a Netzsch TG-209-1 Libra system. Alumina cups cleaned by acid and base washing were used for the measurement, and the change in mass was calibrated to the cup mass. At least 10 mg of as-synthesized powder was used. The mass change was recorded by temperature increase to 800 $^{\circ}\text{C}$ under a heating rate of 5 $^{\circ}\text{C min}^{-1}$ in an inert environment (Ar 99.999%).

Inductively coupled plasma optical emission spectroscopy (ICP OES) on the residual solution after centrifugation was carried out by Horiba Jobin Yvon Ultima 2. A conical atomizer with a pressure of 2.67 bar and a flow of 0.76 L min^{-1} was used with wavelengths of $\lambda = 258.207$ nm for iron and $\lambda = 309.311$ nm for vanadium. The solutions were thinned to 1/100 of their concentration by ultra-pure water.

2.5. Electrode preparation

Sample powders were mixed with different CNT ratios from 5 mass% to 20 mass% of total electrode mass. For FeV mixed with CNT, 30 mg of pure FeV was mixed with CNT, then sonicated for 10 min in EtOH and vacuum filtered on a polytetrafluorethylene (PTFE) filter (Merck). For FeV grown on CNT, the as-synthesized powder was sonicated and filtered after oxidation. The electrodes were then dried overnight at 80 $^{\circ}\text{C}$ and cold rolled in two steps from 150 μm to 120 μm and from 120 μm to 100 μm by a pressure-controlled electric hot rolling press (HR01, MTI). 10 mm discs were punched and used as negative electrodes for electrochemical characterization without further binder use or slurry preparation.

2.6. Electrochemical characterization

Electrodes were tested against a lithium chip (11 mm) in CR2032 coin cells' two-electrode configuration. For electrolyte, 1 M LiPF_6 or 2 M LiTFSI salt in a mixture of ethylene carbonate and dimethyl carbonate (EC:DMC, 1:1 by volume, Sigma, battery grade) was used. For separation between the electrodes, Celgard 2325 (18 mm) and Whatman GF/F glass fiber (18 mm) were used. All cells were rested for 6 h prior to electrochemical testing.

All electrochemical measurements were carried out in a potential window of 0.01–3.50 V vs. Li/Li^+ . Galvanostatic cycling with potential limitation (GCPL) measurement was carried out with an Arbin battery cycler. Cyclic voltammetry (CV) at various rates and electrochemical impedance spectroscopy (EIS) in the frequency range from 100 kHz to 1 mHz was carried out *via* a BioLogic VMP-300 potentiostat/galvanostat. All tests were done in a climate chamber with a regulated temperature of 25 ± 1 $^{\circ}\text{C}$. Specific capacity from GCPL tests was calculated separately for each cell per electrode mass (FVO + CNT

composite mass) with an average of 1.75 ± 0.3 mg. Discharge capacity was divided by charge capacity in each cycle to calculate the Coulombic efficiency.

3. Results and discussion

3.1. Synthesis of FeV and FVO

A schematic representation of the synthesis method is shown in Fig. 1. As the vanadium precursor, vanadyl sulfate was used, which is reported as the recycling product from hydrometallurgical separation from iron.¹³ The synthesis, assembly, and stabilization were carried out in one step by adding the precursors to each other (Fig. 1A). Through room temperature coprecipitation without using acidic media, FeV was prepared (Fig. 1B). Heat treatment was done *via* infrared radiation, which significantly reduces the heating and cooling time compared to conventional tube furnaces with resistive heating (Fig. 1C). Electrode preparation was carried out by direct filtration of the composite suspension in ethanol (Fig. 1D).

The morphology of as-synthesized FeV is shown in Fig. 2A and B. The structure comprises typical nanoparticles in the size range of ~ 4 –10 nm with high aggregation which was retained after oxidation (Fig. 2C and D). Formation of FeV Prussian blue,¹⁵ similar to Thurnball blue, was successful with a unit of M(III)-C-N-M'(II) that accommodates four CN-groups in a primitive unit (Fig. 2E). The X-ray diffractogram data agree with iron vanadium cyanide $\text{V}_{1.5}\text{Fe}(\text{CN})_6$ reflections in a cubic lattice with a space group of $F(0)$ and a lattice parameter of 10.13 \AA , and similar to other PBAs with strong reflections at $\sim 25^{\circ} 2\theta$ and $\sim 35^{\circ} 2\theta$.^{3,16} After successful derivatization to the mixed metal oxide of Fe_2VO_4 , crystallization in cubic lattice space group $Fd\bar{3}m$ and a lattice parameter of 8.42 \AA took place. Conversion to mixed metal oxide was only successful under CO_2 flow which has a less oxidizing nature compared to oxygen.^{17–19} This is in line with early works on the solid-state synthesis of mixed iron–vanadium oxide which is highly dependent on the reducing atmosphere and a high control of $\text{CO}:\text{CO}_2$ is needed for the formation of different iron–vanadium oxides.^{20,21} Here, instead of single metal oxide formation heating to 1000–1200 $^{\circ}\text{C}$ for Fe_2VO_4 formation, the iron–vanadium oxide directly can be derived at a low temperature of 400 $^{\circ}\text{C}$ from its parent PBA.

While in the derivatization of mixed metal oxides from PBAs, usually oxygen or synthetic air is used,²² using synthetic air for FeV oxidation, even when mixed with 50 sccm Ar, did not result in the formation of homogeneous mixed metal oxide. Fig. S1, ESI† shows the images taken from the resulting powders after oxidation under synthetic air. Inhomogeneity in color at the low stream and upstream of the furnace, yellow (Fig. S1B, ESI†) instead of the black color of mixed vanadium/iron oxide shows that the presence of oxygen gas complicates homogeneous derivatization of mixed metal oxide and could also explain the lack of reports on derivatization from vanadium PBAs.

Raman spectroscopy confirms the formation of PBA and oxide derivatization of FVO under CO_2 . Before the heat treatment, successful FeV formation is observed (Fig. 2F) with $\nu(\text{CN})$ bands at 2110 cm^{-1} and 2160 cm^{-1} , representing the typical cyanide ligand stretching vibration in the A_{1g} and E_{1g} modes,

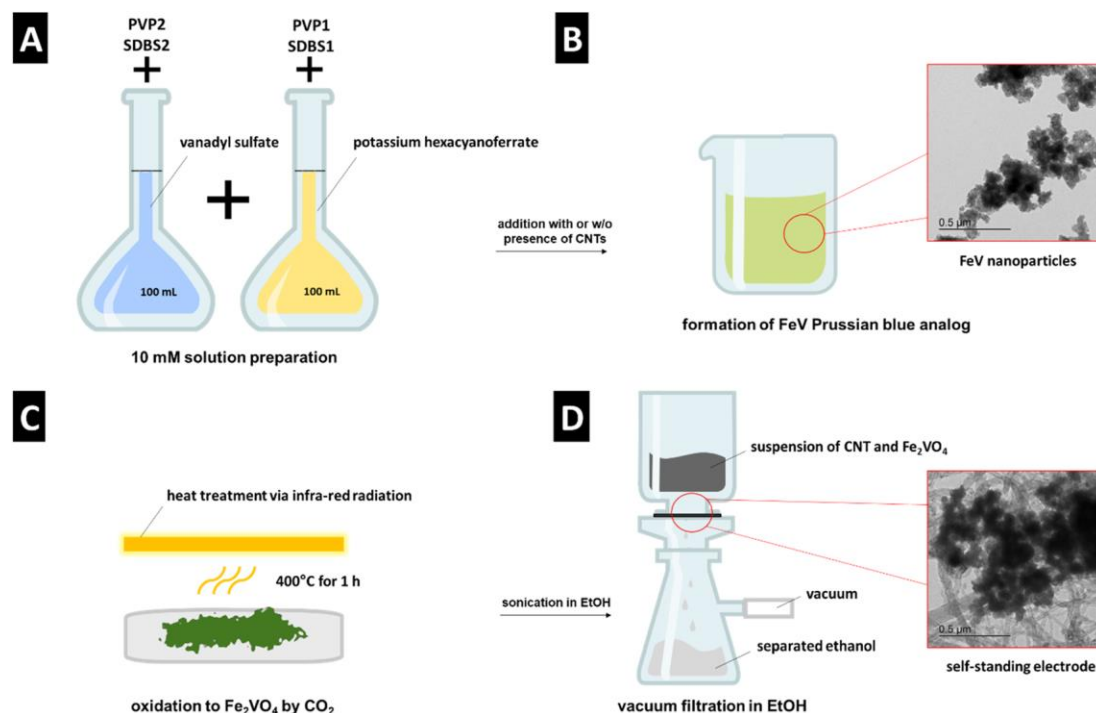


Fig. 1 Schematic representation of (A) and (B) FeV synthesis, (C) heat treatment to FVO, (D) electrode preparation.

respectively.^{16,23} Lower frequency bands correspond to bonding with metallic atoms, such as Fe–C stretching in the 450–620 cm^{-1} spectral window. The band at 960 cm^{-1} that is outside the M–C and M–CN–M vibrations can be an indicator of V=O in the vanadyl group as vanadium–oxygen bands are usually observed in this region.^{3,24,25} After heat treatment, v(CN) bands are absent indicating full derivatization of the precursor. At the same time, D-mode and G-mode appear at 1358 cm^{-1} and 1588 cm^{-1} , respectively, due to the formation of disordered carbon from the presence of CN in the FeV.

Successfully derived mixed metal oxide from FeV was filtered as a self-standing electrode by sonicating the FVO and CNTs mixture. The surface of these self-standing electrodes (Fig. S2, ESI†) was characterized by SEM. Further analysis of the material morphology by SEM (Fig. 3A and B) showed a homogeneous distribution of the FVO in the CNT network and the retained morphology of the FeV template during the heat treatment. The crystallinity of the derived components was approved by TEM with *d*-spacing measurements of 4.9 Å and 2.8 Å, indexed with (111) and (220) plane distances of Fe₂VO₄, respectively (Fig. 3C and D).

Fig. S3, ESI† shows the material synthesis in the presence of tannic acid (TA). Using catechols such as polydopamine and tannins has been reported as a successful strategy to coat Prussian blue derivatives (PBDs) with a carbon coating.²⁶ Data from the XRD and Raman characterization after the synthesis indicate a possible FeV formation but with broad reflections and weak bands (Fig. S3C and D, ESI†). Inhomogeneous structure and loss of the nanoparticles after oxidation show that tannic acid does not form a coating while retaining the material

morphology (Fig. S3B, ESI†). This is assumed to be due to the strong bonding of the catechols to the iron–cyanide complexes and affecting the PBA formation and disturbing subsequent derivatization.²⁶

Therefore, other surfactants, such as PVP and SDBS, were used to form a coating with weaker bonding to the precursor salts. SDBS and PVP have been reported as additives that successfully tune the particle size or enable structure engineering of the materials by selectively covering particle edges and faces.^{27–30} To evaluate the effect of these surfactants on the PBA synthesis, the remaining concentration of Fe and V in the centrifugation supernatant after material synthesis was analyzed by ICP (Table 1). For the synthesis of FeV, concentrations of 402 mg L^{-1} iron and 51 mg L^{-1} vanadium were recorded. This corresponds to a Fe/V ratio of 7.8 that was observed with a yellow solution color, which aligns with the remaining potassium ferricyanide. In all samples with surfactant addition, a higher concentration of the metals was detected compared to the blank FeV. This is the highest for PVP1, showing that adding PVP to the ferricyanide solution (PVP1) complicates the FeV formation the most. In contrast, a successful particle formation has been observed so far in studies on PB³¹ and other PBAs.²⁹

ICP results (Table 1) show for FeV–PVP1, the present iron concentration increases to 532.8 mg L^{-1} and vanadium to 205.4 mg L^{-1} . It has been reported that PVP forms a strong bond with metal ions through their imide unit³² and SDBS forms micelles of M(DBS)_{*x*} (M = metal) in aqueous solutions. Adding the PVP to vanadyl sulfate solution (PVP2) shows a lower concentration of remaining metals in the solution, with 472.2 mg L^{-1} iron and 175.3 mg L^{-1} vanadium. Still, for PVP,

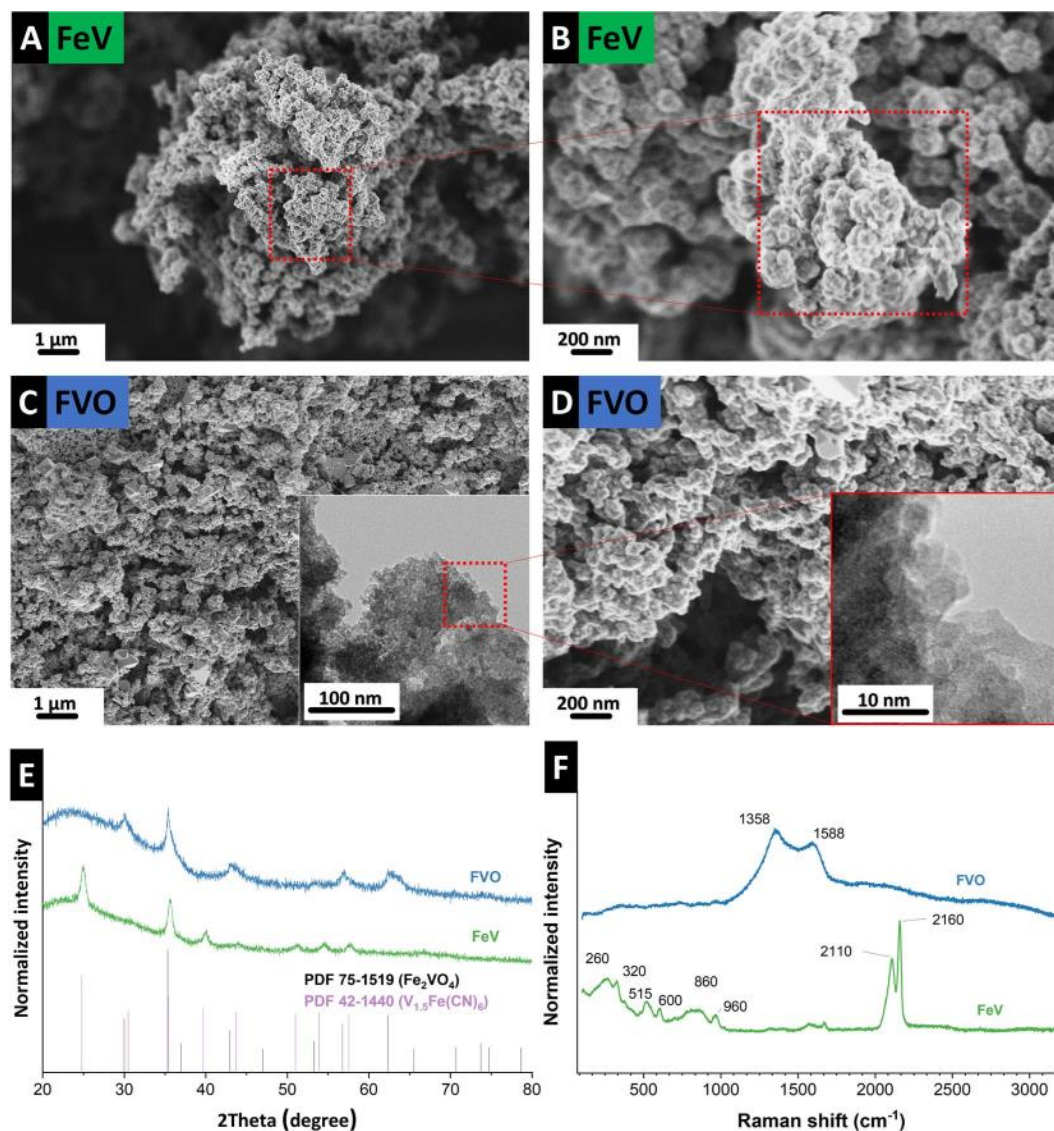


Fig. 2 Scanning electron micrographs of (A) and (B) FeV, (C) and (D) FVO particles after heat treatment, (E) X-ray diffractograms, and (F) Raman spectra of the FeV and FVO particles.

both metals are stabilized in the solvents. This aligns with the green color of the solution after centrifugation resembling the remaining FeV dissolved in the solution (Fig. S4A, ESI[†]).

The dependence of the FeV on the surfactant addition was higher for SDBS, with the Fe/V ratio in the solution changing drastically from 5.3 for SDBS1 to 4.4 for SDBS2. For SDBS1, 381.0 mg L⁻¹ iron and 72.1 mg L⁻¹ vanadium were detected, and for SDBS2 the concentration was less than for SDBS1 with 341.2 mg L⁻¹ iron and 78.2 mg L⁻¹ vanadium. This shows that SDBS, similar to PVP, impedes the FeV formation on CNTs. Compared to the blank FeV, in the presence of SDBS, bonding is stronger to vanadium, but less iron has remained in the solution.³³ When SDBS is first added to iron cyanide, more iron remains in the solution (SDBS1), and when added to the vanadyl sulfate, more vanadium is observed (SDBS2). For both samples with SDBS, FeV was successfully synthesized on CNTs (Fig. S4

and S5, ESI[†]) and retained its nanostructure morphology after oxidation (Fig. 3E, F and H, I).

Further characterization indicated a lack of substantial FeV formation in the presence of PVP as well as metal oxides. This includes a lack of FVO particles on the CNTs (Fig. S6A–C, ESI[†]), XRD reflections, and Raman bands after the treatment (Fig. S6E and F, ESI[†]). Additional TGA analysis under Ar showed a similar mass loss of 11% at 800 °C compared to FVO (Fig. S6D, ESI[†]).

For samples treated with SDBS, a lower intensity of the XRD reflections was observed FVO–SDBS1 sample compared to FVO–SDBS2 after oxidation, in line with the ICP results on the dissolved metals in the supernatant (Fig. 3G). Similar to FVO, reflections of Fe₂VO₄ were observed in FVO–SDBS1 and FVO–SDBS2. Additionally, the formation of FeVO₄ was visible. In FVO–SDBS1, minor peaks of vanadium oxide V₂O₅ and iron oxide Fe₂O₃ were also detected, showing a decrease in the phase homogeneity compared to pristine FVO. The formation of

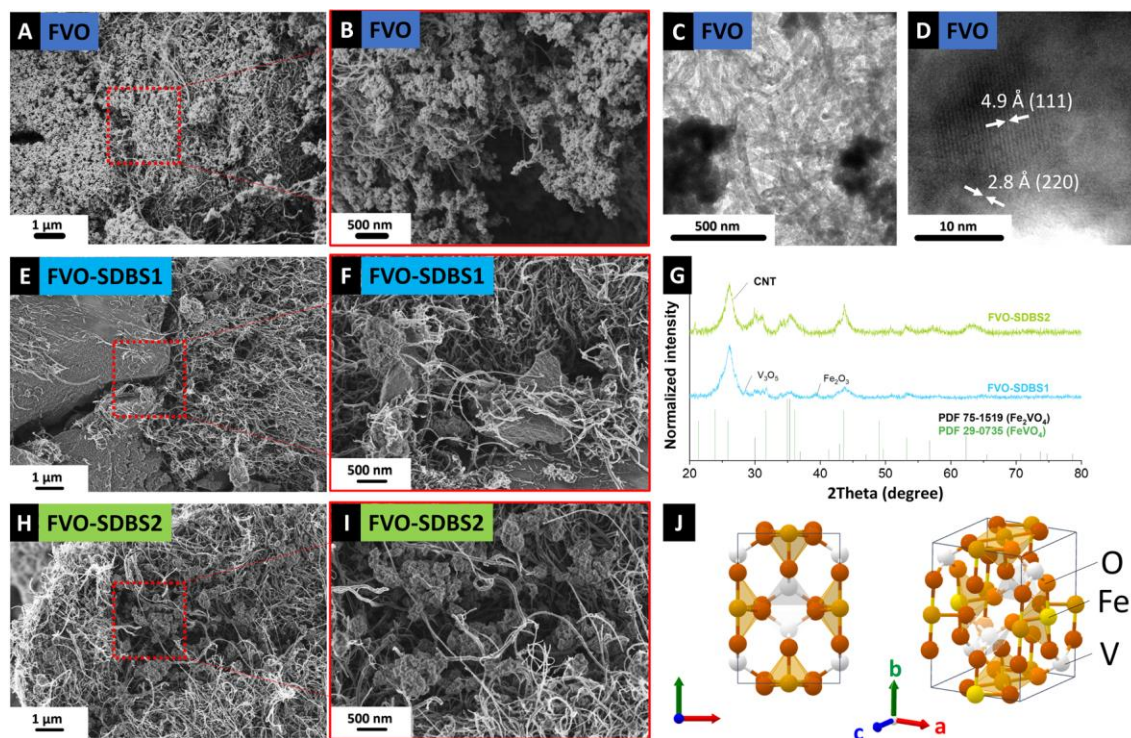


Fig. 3 (A) and (B) Scanning electron micrographs and (C) and (D) transmission electron micrographs of FeV grown *in situ* on CNT after oxidation, (E) and (F) scanning electron micrographs of FeV with SDBS added to hexacyanoferrate after oxidation, (G) X-ray diffractogram of FVO-SDBS1 and FVO-SDBS-2, (H) and (I) scanning electron micrographs of FeV with SDBS added to vanadyl sulfate after oxidation and (J) crystal structure of FeVO₄.

FeVO₄ is assumed to be due to the lost Fe ions in the supernatant and the single metal oxides from defective FeV lattice formation because of the M(DBS) micelle formation.

The formation of single metal oxides can, however, increase the electrochemical stability. These oxides are thermodynamically more stable than the mixed oxide of iron and vanadium and less prone to chemical dissociation during cycling.¹² Moreover, the mixed metal oxide of FeVO₄ provides V⁵⁺ and Fe³⁺ in addition to the V⁴⁺ and Fe²⁺ in Fe₂VO₄ (ref. 34) and therefore contributes to more stable cycling by multi-valence redox reactions³⁵ and causes less mechanical stressing of the particles. FeVO₄ crystallizes in a spinel structure³⁶ with an orthorhombic lattice and is reported as electrochemically active for lithium storage.³⁷

3.2. Electrochemical performance

LiPF₆ and LiTFSI were used as electrolyte salts and improved performance by using LiTFSI was observed similarly as reported in the literature.³⁸ For the cell with LiPF₆, capacity starts with a value of 580 mA h g⁻¹, followed by a short activation in the

first 20 cycles, reaching 615 mA h g⁻¹. A low scattering of the Coulombic efficiencies was recorded in a 95–96% range in the first 40 cycles. After the initial 10 cycles, capacity begins to fall, and the Coulombic efficiency shows a high scattering in parallel, which indicates side reactions.³⁹ The initial capacity increase appears likely because of material activation and access to more electrochemically active particles.⁴⁰ However, with the lack of a protective layer, when the electrolyte accesses the FVO particles, they are continuously etched and disintegrated, resulting in capacity fading. This is a common pitfall for mixed metal components, especially materials that undergo conversion reactions and do not return to the initial chemistry, such as iron–vanadium oxide.⁴¹ Post-mortem analysis of the electrode material observed the morphology change during the process. Transmission electron micrographs show that the electrode stays intact regarding FVO on CNTs, but the FVO particle aggregates swell and become larger after cycling (Fig. S7A, ESI†).

It has been shown in the literature that vanadium is prone to dissolution and electrolyte etching both in aqueous³ and

Table 1 Concentrations of iron and vanadium in the remaining FeV solution after centrifugation determined by ICP

	FeV	FeV-PVP1	FeV-SDBS1	FeV-PVP2	FeV-SDBS2
Fe (mg L ⁻¹)	402.3 ± 6.9	532.8 ± 11.3	381.0 ± 6.2	472.2 ± 6.3	341.2 ± 6.7
V (mg L ⁻¹)	51.3 ± 1.1	205.4 ± 3.5	72.1 ± 0.6	175.3 ± 2.6	78.2 ± 0.9
Fe/V ratio	7.8	2.6	5.3	2.7	4.4

organic media^{38,42} and results in a capacity loss in vanadium-based compounds. Iron–vanadium oxide is also prone to irreversible cycling after undergoing conversion reactions.¹¹ This mixed metal oxide is usually broken into vanadium oxide and iron oxide, which are more thermodynamically stable.^{12,41} However, stability studies on different electrolytes and their molarities indicate a larger electrolyte molecule size, such as in the case of LiTFSI, and higher molarities may impede the fast dissolution of vanadium ions by acting as a diffusion barrier at the surface of electrode particles.³⁸ Fig. 4B shows the stability of the as-grown FeV cycled in 2 M LiTFSI in EC/DMC 1 : 1 (by volume). The initial capacity reaches 700 mA h g⁻¹ after 10 cycles and then stabilizes at around 370 mA h g⁻¹ after a decrease in capacity observed over 100 cycles. Compared to 1 M LiPF₆, the Coulombic efficiencies show less scattering as well. To see if the change of electrolyte salt affects the lithiation mechanism, the electrochemical signatures in measured potential curves were compared. Respective charge and discharge curves in Fig. 4C and D show similar electrochemical thermodynamics of the sample cycled in 1 M LiPF₆ and 2 M LiTFSI, only with the extension of the curves to higher capacities and better retention of the redox processes. This shows that the change in the electrolyte does not introduce new redox reactions but only increases the materials by hampering its etching by the electrolyte. Although the effect of vanadium dissolution

is mitigated here, the capacity fading and Coulombic efficiency scattering indicate the instability of iron vanadate after 100 cycles of conversion, as the FVO particles are not protected by any coating.

Caging of the conversion type materials or formation of composites with electrochemically stable components can decrease capacity fading.⁴³ Here, SDBS is used to form a stable coating on the material. For both FVO–SDBS1 and FVO–SDBS2, an improved cycling behavior is observed compared to the FVO material (Fig. 5A and B). FVO–SDBS2 shows a similar cycling behavior to FVO but with slower kinetics. The initial capacity of FVO–SDBS2 with 520 mA h g⁻¹ is lower than FVO with 700 mA h g⁻¹. This is a result of two combined effects: first, the loss of vanadium due to dissolution when SDBS is added, and second, a lower amount of active material in the total electrode mass due to the presence of SDBS coating, which is not redox active but increases the electrode mass. This capacity then increases to 560 mA h g⁻¹ with further cycling and subsequently decreases, similar to FVO, accompanied by a scattering of the values for the Coulombic efficiency. In general, the use of SDBS surfactant, when added to vanadyl sulfate (SDBS2), delays the material deterioration by the electrolyte but is ineffective in stabilizing the cycling for longer cycles. TGA curves showed the incorporated SDBS coating is about 11 mass% for FVO–SDBS2 and 50 mass% for FVO–SDBS1 (Fig. S8A, ESI†). To elucidate the

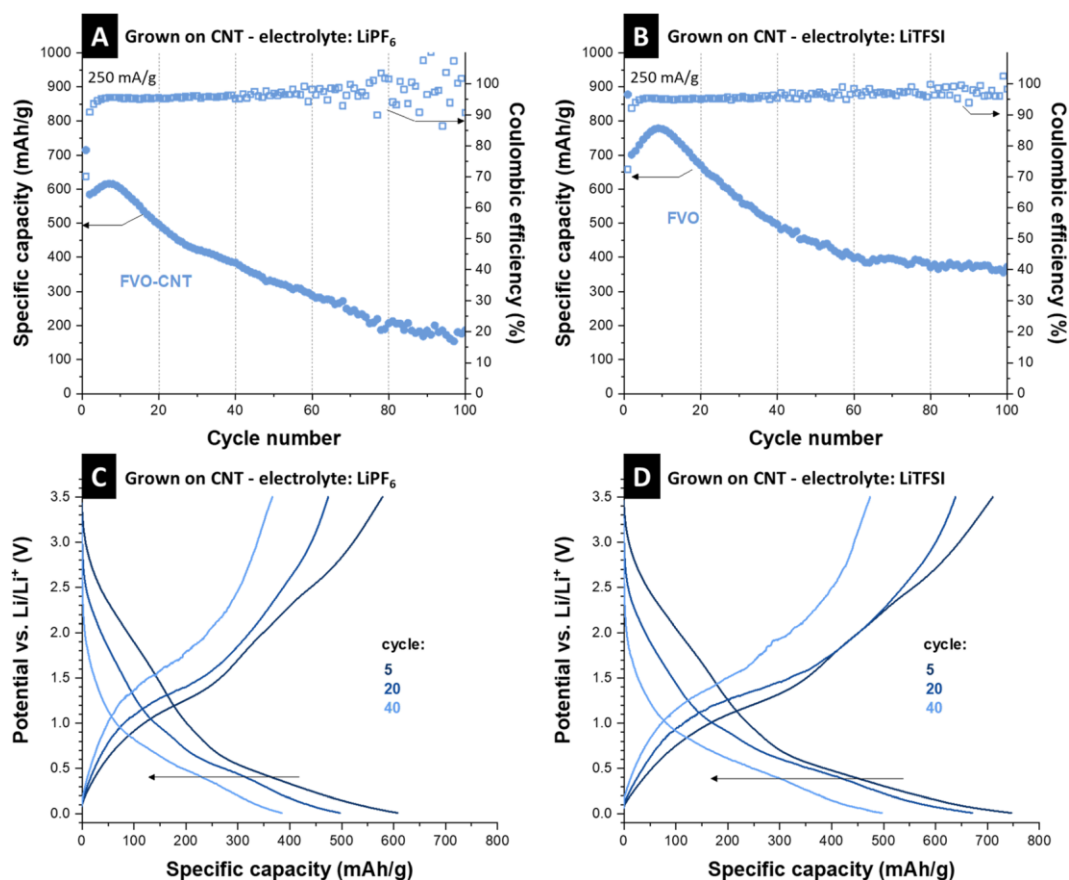


Fig. 4 Stability performances of FVO electrodes at the specific current of 250 mA g⁻¹ in (A) 1 M LiPF₆ in EC/DMC, and (B) 2 M LiTFSI in EC/DMC with their Coulombic efficiencies, and (C) and (D) their respective charge–discharge curves at cycles 5, 20, and 40.

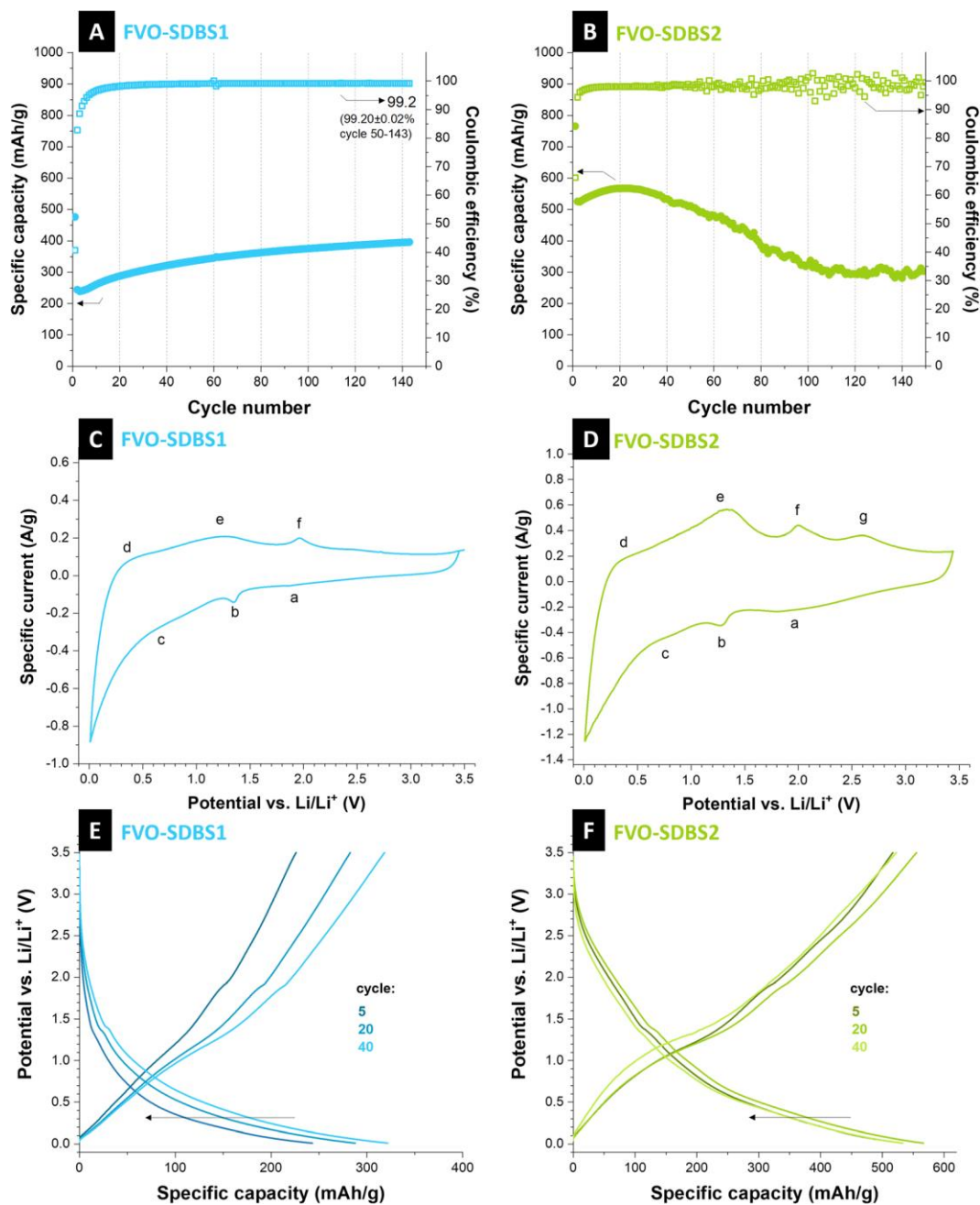


Fig. 5 (A) and (B) Stability of FVO-SDBS1 and FVO-SDBS2 at the specific current of 250 mA g^{-1} , respectively. (C) and (D) The respective cyclic voltammetry at the scanning rate of 0.1 mV s^{-1} , and (E) and (F) the respective galvanostatic charge-discharge curves.

electrochemical behavior of FVO-SDBS1 and FVO-SDBS2 materials under dynamic and non-destructive conditions, electrochemical impedance spectroscopy analysis was conducted. Fig. S8B, ESI,† presents the Nyquist plots obtained from this analysis along with the corresponding equivalent circuit. Both materials exhibit two distinct semi-circles in the high and middle-frequency regions. The high-frequency semi-circle can be ascribed to the bulk electrolyte behavior, originating from the impedance of a layer that forms on the interface between the electrode and electrolyte.⁴⁴ This layer corresponds to the combined carbon layer formed by the SDBS coating and solid

electrolyte interphase (SEI), and its corresponding resistance and capacitance are annotated by EEI (electrode-electrolyte interphase). The higher R_{EEI} for FVO-SDBS2 indicates a thicker coating layer. With 103.2Ω , this is about 90% more resistive than that of FVO-SDBS1 (Table S1, ESI†) since the SDBS coating is less for FVO-SDBS2, this resistance results from the higher etching of the sample as observed in the stability results. The mid-frequency semi-circle corresponds to the electrode polarization (R_{ce}), which is linked to the kinetics of the electrochemical reaction occurring during the charge/discharge process.⁴⁵ With 177.5Ω for FVO-SDBS1 and 207.6Ω for FVO-

SDBS2, slightly more favorable kinetics are present for FVO-SDBS1. A great difference is observed in the values of ESR for the samples. The equivalent series resistance (ESR) of the cell made with the FVO-SDBS1 electrode is lower than that obtained with the device with FVO-SDBS2 materials with 10.8 Ω for FVO-SDBS1 and 52.3 Ω for FVO-SDBS2. Accordingly, the lower ESR value of the FVO-SDBS1 cell is due to the coating, which ultimately provides better electrode-electrolyte contact.⁴⁵ The lower R_{ct} and Warburg resistances for the FVO-SDBS1 cell correlate to the better charge transfer process and diffusional effects of lithium-ion on the host FVO-SDBS1 than the FVO-SDBS2 material.

FVO-SDBS1 shows a different cycling behavior than previous materials. The capacity increase does not end after 10–20 cycles and the materials continuously increase in capacity with more mass accessed by the electrolyte and also no subsequent fading is observed. However, the general capacity values are lower than previous materials. This confirms the lower initial capacity values. The capacity is 250 mA h g^{-1} initially and gradually increases to 400 mA h g^{-1} after 140 cycles while delivering a Coulombic efficiency of 99.2%. In contrast to the previous samples, no capacity fading follows after the initial increase. This shows SDBS coats the active material effectively when added to iron cyanide. As the charge and discharge curves remain the same during cycling and show that the redox processes are not changed, the increase in the capacity can be attributed to the accessibility of more active material during cycling and lithiation. The rate handling of FVO-SDBS1 also shows improved capacity stability compared to the FVO electrode. A high capacity of 740 mA h g^{-1} was achieved under 50 mA g^{-1} for FVO-SDBS1. However, similar to FVO, the material was not capable of delivering storage capacity at higher rates, such as 2500 mA g^{-1} and 5000 mA g^{-1} which shows the high dependency of both materials on diffusion (Fig. S9A, ESI[†]).

Cyclic voltammetry at different rates was carried out for FVO-SDBS1. From specific current values at maximum potential, 0.5 V, and 2.75 V, b -values were calculated (Fig. S10A, ESI[†]). The b -values ranged from 0.64 to 0.71, indicative of a behavior between diffusion-controlled ($b = 0.5$) and non-diffusion-controlled ($b = 1.0$) charge storage (Fig. S10B and C, ESI[†]).⁴⁶

Cyclic voltammograms of FVO-SDBS1 and FVO-SDBS2 showed similar peaks. However, they were more pronounced in the FVO-SDBS2 with a larger integrated area under the cyclic voltammograms area, arising from the higher ratio of the active material in this sample (Fig. 5C and D). Three pairs of current peaks can be indexed, showing multiple electron electrochemical redox reactions. We see oxidation peaks for FVO-SDBS2 at 0.3 V, 1.3 V, 2.0 V, and 2.6 V *vs.* Li/Li⁺. These are less distinct in FVO-SDBS1, indicating lower electrochemical accessibility of the active material caused by the SDBS coating. The sharp oxidation peak at 0.30 V *vs.* Li/Li⁺ and the respective reduction peak at 0.01 V *vs.* Li/Li⁺ displays the Li-intercalation into ordered graphite structure (graphitic layer) of the carbon coating and the MWCNTs and the Li-deintercalation from LiC₆ (LiC₆ → C₆ + Li⁺ + e⁻).⁴⁷ Further, the peak at 1.30 V *vs.* Li/Li⁺ can be attributed to the Li ions extraction in the inner channels of

the CNTs. Finally, the very weak peak at 2.25 V characterizes the extraction of Li ions bonded to surface functional groups.⁴⁸

Anodic peaks at 1.30 V and 2.00 V *vs.* Li/Li⁺ can also be assigned to the multi-step oxidation of Fe⁰ to Fe³⁺ and the delithiation of vanadium oxide (or vanadyl groups).⁴¹ Peaks obtained in the cathodic scan located at 0.80 V, 1.30 V, and 1.80 V *vs.* Li/Li⁺ can be associated with nano stoichiometric Li⁺-intercalated compounds and further conversion formation of iron oxide and vanadium oxide, while lithiation followed by the multi-step reduction of iron back to metallic iron.^{12,41} The obtained reduction and oxidation peaks from cyclic voltammetry agree with the galvanostatic discharge and charge profiles tested at a specific current of 250 mA g^{-1} in a voltage range between 0.01 V and 3.50 V *vs.* Li/Li⁺ as shown in Fig. 5E and F.

As the redox peaks in the cyclic voltammogram are broad and small, in the charge and discharge profiles, no flat plateaus, but rather gradual slopes are observed for different redox reactions with a weak plateau at ~ 1.5 V *vs.* Li/Li⁺, similar to previous reports on FeVO₄ (ref. 37) and Fe₂VO₄ (ref. 40). Studies on mixed iron-vanadium with similarly shaped cyclic voltammograms show this results from the formation of Li_xVO_y and metallic Fe through multi-step reduction.⁴⁰ Further post-mortem analysis after discharge and washing shows that the electrode retains its morphology, and the network of CNTs remains (Fig. S11A, ESI[†]). XRD analysis shows that the main formed phase after cycling is FeVO₄ in an orthorhombic lattice, same as the initial phase present in the electrode with the strongest line at 34° 2θ corresponding to the (112) plane. Additional present reflections can be indexed with Fe₂O₃ (Fig. S11B, ESI[†]).

Table 2 shows the electrochemical performance of comparable studies for lithium-ion storage with values similar to those obtained in this study. Achieved capacity values outperform Fe_{0.12}V₂O₅ nanowire arrays on a Ti foil that are self-standing electrodes similar to this study.⁴⁹ Our results are comparable to Fe₂VO₄ nanowires achieved by Tao *et al.*,⁴⁰ although they used phosphorous additive, which is a high-capacity alloying element and contributes to the total material capacity and increases the conductivity. So far, the present work offers the largest potential window of ~ 3.5 V among other studies while providing stable capacity from conversion reactions. In contrast, other studies rely on limiting the voltage window to reduce capacity fading.^{11,49} With the coating from SDBS surfactant in the present study, stability results outperform all other iron vanadium reports so far. However, the achieved stable capacity is lower than that of the initial (~ 700 – 800 mA h g^{-1}) due to the high mass of SDBS incorporation. Among comparable studies, the capacity values achieved by Luo *et al.*⁴¹ are the highest, comparable to our initial values before stabilization. In their research, surface treatment in ethanol was carried out to form stable porous mixed metal oxide. However, the stability of this treatment faded during cycling. As our surface treatment shows great stability in the current study, an improved conductivity may increase the capacity for iron vanadium oxide further.⁴⁰ Therefore, decreasing the SDBS coating mass or substituting it with similar surfactants that result in a more conductive layer can further enhance the

Table 2 Summary of electrochemical performances of studies on iron vanadate and their composites for use in the lithium-ion battery. AM (active material), EC (ethylene carbonate), DMC (dimethyl carbonates), FEC (fluoroethylene carbonate), PTFE (polytetrafluoroethylene), LiPF₆ (lithium hexafluorophosphate), LiTFSI (lithium bis(trifluoromethane sulfonyl)imide)

Material/reference	AM composition	Potential (V vs. Li/Li ⁺)	Electrode composition	Electrolyte	Capacity	Cycles/capacity retention vs. the first cycle
Fe ₂ VO ₄ porous microparticles/ ⁴¹ Fe ₂ VO ₄ / ¹¹	Fe ₂ VO ₄	0.01–2.50	70% AM/20% super P/10% sodium alginate	1 M LiPF ₆ in EC/DMC (1:1 by volume)	799 mA h g ⁻¹ at 500 mA g ⁻¹	500/78%
Fe ₂ VO ₄ carbon mesoporous nanowires/ ⁴⁰	P-Fe ₂ VO ₄	0.01–3.00	70% AM/20% super P/10% sodium alginate	1 M LiPF ₆ in EC/DMC (1:1 by volume, 5% FEC additive)	486 mA h g ⁻¹ at 5000 mA g ⁻¹	250/109%
Iron vanadate nanowire arrays/ ⁴⁹	Fe _{0.12} V ₂ O ₅ @Ti foil	2.00–3.60	100% AM	1 M LiPF ₆ in EC/DMC (1:1 by volume)	278 mA h g ⁻¹ at 30 mA g ⁻¹	100/82%
Iron vanadate nanowire arrays/ ⁴⁹	Fe _{0.12} V ₂ O ₅ @Ti foil	1.00–4.00	100% AM	1 M LiPF ₆ in EC/DMC (1:1 by volume)	382 mA h g ⁻¹ at 30 mA g ⁻¹	50/81%
This work (FVO–SDBS1)	FeVO₄ and Fe₂VO₄ on CNT	0.01–3.50	100% AM	2 M LiTFSI in EC/DMC (1:1 by volume)	400 mA h g⁻¹ at 250 mA g⁻¹	150/160%

performance compared to other studies on iron–vanadium oxide.

4. Conclusions and outlook

Derivatization of mixed vanadium-iron oxide from its respective FeV Prussian blue analog (PBA) was reported for the first time. FeV formation, assembly on CNT, and coating were in one step at room temperature. Water-based salt of vanadyl sulfate was used for vanadium incorporation, as this salt has been reported as the product of vanadium recovery from iron–vanadium waste. Heat treatment was carried out under CO₂ flow with infrared radiation. Electrodes were prepared by suspension in ethanol and subsequent filtration to decrease the needed heating energy and use of toxic material in the electrode preparation. We use different surfactants to analyze their effect on the electrochemical stability. TA, PVP, and SDBS surfactants have been reported as effective coating agents for morphology design regardless of the order in which the surfactants are added.

We show that for PBAs with higher solubility, such as FeV, the type, and order of the surfactants' addition can directly impede material crystallization and PBA formation. SDBS was shown to be an effective surfactant to stabilize the capacity of FeV only when added to hexacyanoferrate by forming a protective layer. However, both TA and PVP are unsuitable for coating the FeV and stabilizing its derivative. After stabilizing the bare FVO using an SDBS coating, a capacity of 400 mA h g⁻¹ at a rate of 250 mA g⁻¹ after 150 cycles were achieved with a Coulombic efficiency of 99.2%.

Since the coating mass was 50% of the electrode, the capacity can be further increased by optimizing the type and mass of the surfactant to decrease the coating thickness. This work can facilitate the path to derivatization of other complex mixed metal oxides (and other mixed metal components) from their soluble and tricky PBA and show how to stabilize their performance for electrochemical energy storage.

Author contributions

BB: conceptualization, methodology, investigation, data curation, validation, visualization, writing – original draft. HEG: methodology, investigation, data curation, writing – original draft. STA: methodology, validation, writing – original draft. EP: methodology, investigation, data curation, validation, writing – original draft. VP: validation, funding acquisition, writing – review and editing.

Conflicts of interest

The authors have no conflict of interest.

Acknowledgements

This work was part of the electrospun vanadium oxide and sulfide-carbon hybrids project (HEROES-4-Li-Na-batteries) by the German Research Foundation (DFG, Deutsche Forschungsgemeinschaft), project number 452180147. The authors thank Andrea Jung (INM) for carrying out ICP-OES and Samantha Husmann (formerly INM) for her comments on the work. The work of HEG was part of the École Européenne d'Ingénieurs en Génie des Matériaux (EEIGM) carried out at Saarland University. E. P. acknowledges the financial support from the Alexander von Humboldt Foundation.

References

- 1 D. Larcher and J.-M. Tarascon, *Nat. Chem.*, 2015, **7**, 19–29.
- 2 D. Xia, H. Gao, M. Li, F. Gong and M. Li, *Energy Storage Mater.*, 2021, **35**, 169–191.
- 3 T.-U. Choi, G. Baek, S. G. Lee and J.-H. Lee, *ACS Appl. Mater. Interfaces*, 2020, **12**, 24817–24826.
- 4 C. Q. Lim and Z.-K. Tan, *ACS Appl. Energy Mater.*, 2021, **4**, 6214–6220.

- 5 M. Hu, N. L. Torad and Y. Yamauchi, *Eur. J. Inorg. Chem.*, 2012, **2012**, 4795–4799.
- 6 C. Xuan, J. Zhang, J. Wang and D. Wang, *Chem.–Asian J.*, 2020, **15**, 958–972.
- 7 B. Bornamehr, V. Presser, A. J. G. Zarbin, Y. Yamauchi and S. Husmann, *J. Mater. Chem. A*, 2023, **11**, 10473–10492.
- 8 J. B. Goodenough and K.-S. Park, *J. Am. Chem. Soc.*, 2013, **135**, 1167–1176.
- 9 M. Li, J. Lu, Z. Chen and K. Amine, *Adv. Mater.*, 2018, **30**, 1800561.
- 10 Y. Zhao, X. Li, B. Yan, D. Xiong, D. Li, S. Lawes and X. Sun, *Adv. Energy Mater.*, 2016, **6**, 1502175.
- 11 T. Yang, D. Xia, Z. Wang and Y. Chen, *Mater. Lett.*, 2009, **63**, 5–7.
- 12 C. Yang, F. Lv, Y. Zhang, J. Wen, K. Dong, H. Su, F. Lai, G. Qian, W. Wang and A. Hilger, *Adv. Energy Mater.*, 2019, **9**, 1902674.
- 13 M. Tavakoli and D. Dreisinger, *Hydrometallurgy*, 2014, **141**, 17–23.
- 14 J. Chen, L. Wei, A. Mahmood, Z. Pei, Z. Zhou, X. Chen and Y. Chen, *Energy Storage Mater.*, 2020, **25**, 585–612.
- 15 S. F. Kettle, E. Diana, E. M. Marchese, E. Boccaleri and P. L. Stanghellini, *J. Raman Spectrosc.*, 2011, **42**, 2006–2014.
- 16 B. Bornamehr, V. Presser and S. Husmann, *ACS Omega*, 2022, **7**, 38674–38685.
- 17 A. K. Boehm, S. Husmann, M. Besch, O. Janka, V. Presser and M. Gallei, *ACS Appl. Mater. Interfaces*, 2021, **13**, 61166–61179.
- 18 B. Krüner, J. Lee, N. Jäckel, A. Tolosa and V. Presser, *ACS Appl. Mater. Interfaces*, 2016, **8**, 9104–9115.
- 19 A. Tolosa, B. Krüner, S. Fleischmann, N. Jäckel, M. Zeiger, M. Aslan, I. Grobelsek and V. Presser, *J. Mater. Chem. A*, 2016, **4**, 16003–16016.
- 20 M. Wakihara, Y. Shimizu and T. Katsura, *J. Solid State Chem.*, 1971, **3**, 478–483.
- 21 D. Wang, F. Li and B. Yan, *J. Alloys Compd.*, 2019, **797**, 1050–1058.
- 22 C.-H. Chuang, L.-Y. Hsiao, M.-H. Yeh, Y.-C. Wang, S.-C. Chang, L.-D. Tsai and K.-C. Ho, *ACS Appl. Energy Mater.*, 2020, **3**, 11752–11762.
- 23 G. Moretti and C. Gervais, *J. Raman Spectrosc.*, 2018, **49**, 1198–1204.
- 24 R. Fehrmann, S. Boghosian, G. Papatheodorou, K. Nielsen, R. W. Berg and N. Bjerrum, *Inorg. Chem.*, 1989, **28**, 1847–1853.
- 25 N. A. Gvozdik and K. J. Stevenson, *Electrochim. Acta*, 2021, **383**, 138300.
- 26 S.-J. Park, S. S. Shin, J. H. Jo, C. H. Jung, H. Park, Y.-I. Park, H.-J. Kim and J.-H. Lee, *J. Hazard. Mater.*, 2023, **442**, 129967.
- 27 M. Hu, A. A. Belik, M. Imura, K. Mibu, Y. Tsujimoto and Y. Yamauchi, *Chem. Mater.*, 2012, **24**, 2698–2707.
- 28 Q. Zhang, T. Zhang, J. Ge and Y. Yin, *Nano Lett.*, 2008, **8**, 2867–2871.
- 29 L. Liu, Z. Hu, L. Sun, G. Gao and X. Liu, *RSC Adv.*, 2015, **5**, 36575–36581.
- 30 J. Nai, J. Zhang and X. W. D. Lou, *Chem*, 2018, **4**, 1967–1982.
- 31 T. Uemura and S. Kitagawa, *J. Am. Chem. Soc.*, 2003, **125**, 7814–7815.
- 32 M. Hu, S. Furukawa, R. Ohtani, H. Sukegawa, Y. Nemoto, J. Reboul, S. Kitagawa and Y. Yamauchi, *Angew. Chem., Int. Ed.*, 2012, **51**, 984–988.
- 33 A. Hemmatifar, N. Ozbek, C. Halliday and T. A. Hatton, *ChemSusChem*, 2020, **13**, 3865–3874.
- 34 A. Wold, D. Rogers, R. Arnott and N. Menyuk, *J. Appl. Phys.*, 1962, **33**, 1208–1209.
- 35 Z. Gan, L. Chen, F. Xiong, X. Cai, W. Cui, X. Sang, Q. An and L. Wu, *Chem. Commun.*, 2021, **57**, 3615–3618.
- 36 Y. Oka, T. Yao, N. Yamamoto, Y. Ueda, S. Kawasaki, M. Azuma and M. Takano, *J. Solid State Chem.*, 1996, **123**, 54–59.
- 37 N. Yan, Y. Xu, H. Li and W. Chen, *Mater. Lett.*, 2016, **165**, 223–226.
- 38 Y. Maeyoshi, K. Yoshii, M. Shikano and H. Sakaebe, *ACS Appl. Energy Mater.*, 2021, **4**, 13627–13635.
- 39 B. Tratnik, N. Van de Velde, I. Jerman, G. Kapun, E. Tchernychova, M. Tomšič, A. Jamnik, B. Genorio, A. Vizintin and R. Dominko, *ACS Appl. Energy Mater.*, 2022, **5**(9), 10667–10679.
- 40 Y. Tao, N. Yang, C. Liang, D. Huang, P. Wang, F. Cao, Y. Luo and H. Chen, *ChemElectroChem*, 2020, **7**, 2395–2403.
- 41 Y. Luo, D. Huang, C. Liang, P. Wang, K. Han, B. Wu, F. Cao, L. Mai and H. Chen, *Small*, 2019, **15**, 1804706.
- 42 L. Li, Z. Li, A. Yoshimura, C. Sun, T. Wang, Y. Chen, Z. Chen, A. Littlejohn, Y. Xiang and P. Hundekar, *Nat. Commun.*, 2019, **10**, 1764.
- 43 Z.-W. Zhao, T. Wen, K. Liang, Y.-F. Jiang, X. Zhou, C.-C. Shen and A.-W. Xu, *ACS Appl. Mater. Interfaces*, 2017, **9**, 3757–3765.
- 44 N. Ogihara, S. Kawauchi, C. Okuda, Y. Itou, Y. Takeuchi and Y. Ukyo, *J. Electrochem. Soc.*, 2012, **159**, A1034.
- 45 M. Gaberscek, J. Moskon, B. Erjavec, R. Dominko and J. Jamnik, *Electrochim. Solid-State Lett.*, 2008, **11**, A170.
- 46 J. Liu, J. Wang, C. Xu, H. Jiang, C. Li, L. Zhang, J. Lin and Z. X. Shen, *Adv. Sci.*, 2018, **5**, 1700322.
- 47 R. Paul, V. Etacheri, V. G. Pol, J. Hu and T. S. Fisher, *RSC Adv.*, 2016, **6**, 79734–79744.
- 48 X. X. Wang, J. N. Wang, H. Chang and Y. F. Zhang, *Adv. Funct. Mater.*, 2007, **17**, 3613–3618.
- 49 Y. Cao, D. Fang, R. Liu, M. Jiang, H. Zhang, G. Li, Z. Luo, X. Liu, J. Xu and W. Xu, *ACS Appl. Mater. Interfaces*, 2015, **7**, 27685–27693.

Supporting Information

**Surfactant stabilization of vanadium iron oxide derived from
Prussian blue analog for lithium-ion battery electrodes**

Behnoosh Bornamehr^{1,2}, Hiba El Gaidi^{1,2},
Stefanie Arnold^{1,2}, Emmanuel Pameté¹, Volker Presser^{1,2,3,*}

¹ *INM – Leibniz Institute for New Materials, Campus D2 2, 66123, Saarbrücken, Germany*

² *Department of Materials Science & Engineering, Saarland University, Campus D2 2,
66123, Saarbrücken, Germany*

³ *Saarene – Saarland Center for Energy Materials and Sustainability, Campus C4 2, 66123
Saarbrücken, Germany*

* Corresponding author: volker.presser@leibniz-inm.de (VP)

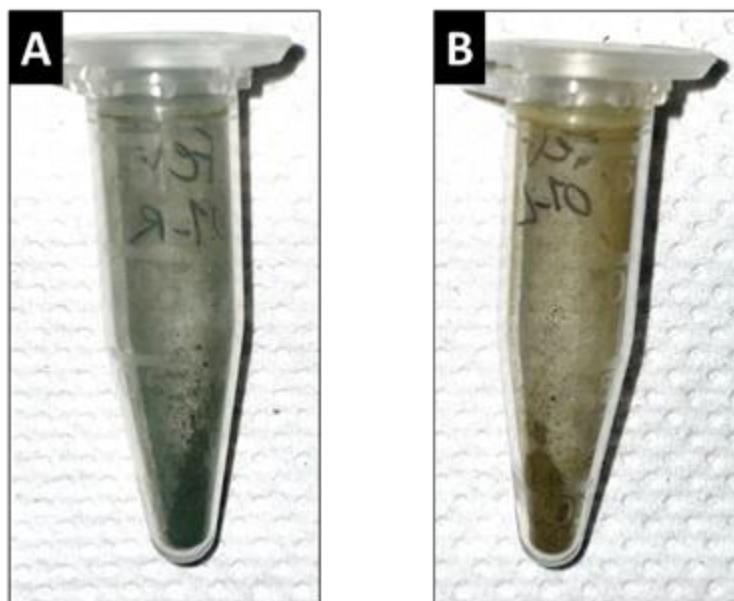


Figure S1. Photographs of FeV oxidation under synthetic air resulting in inhomogeneous oxide formation at **A** low stream and **B** upstream of the furnace.

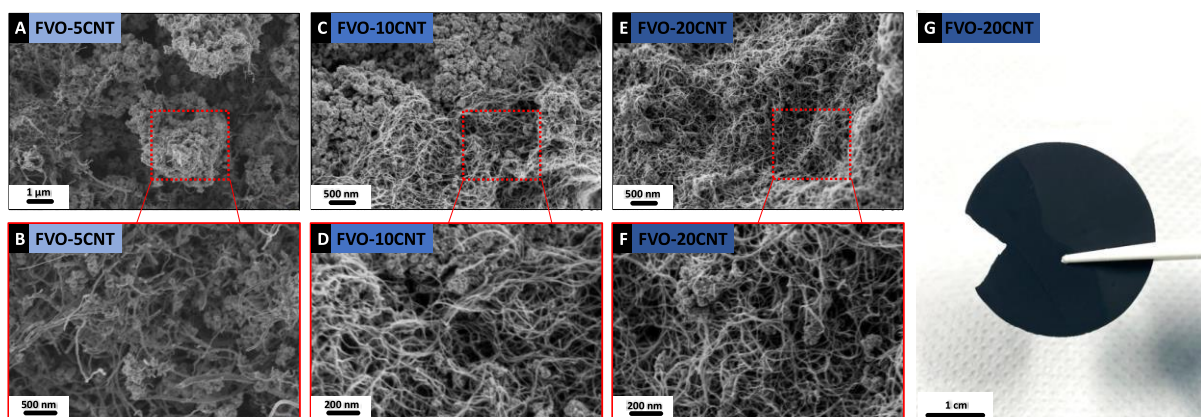


Figure S2. **A-F** Scanning electron micrographs of FVO mixed with different mass ratios (5, 10, 20 mass%) of CNT. **G** Photograph of the filtrated self-standing FVO on CNTs used for cutting the electrodes.

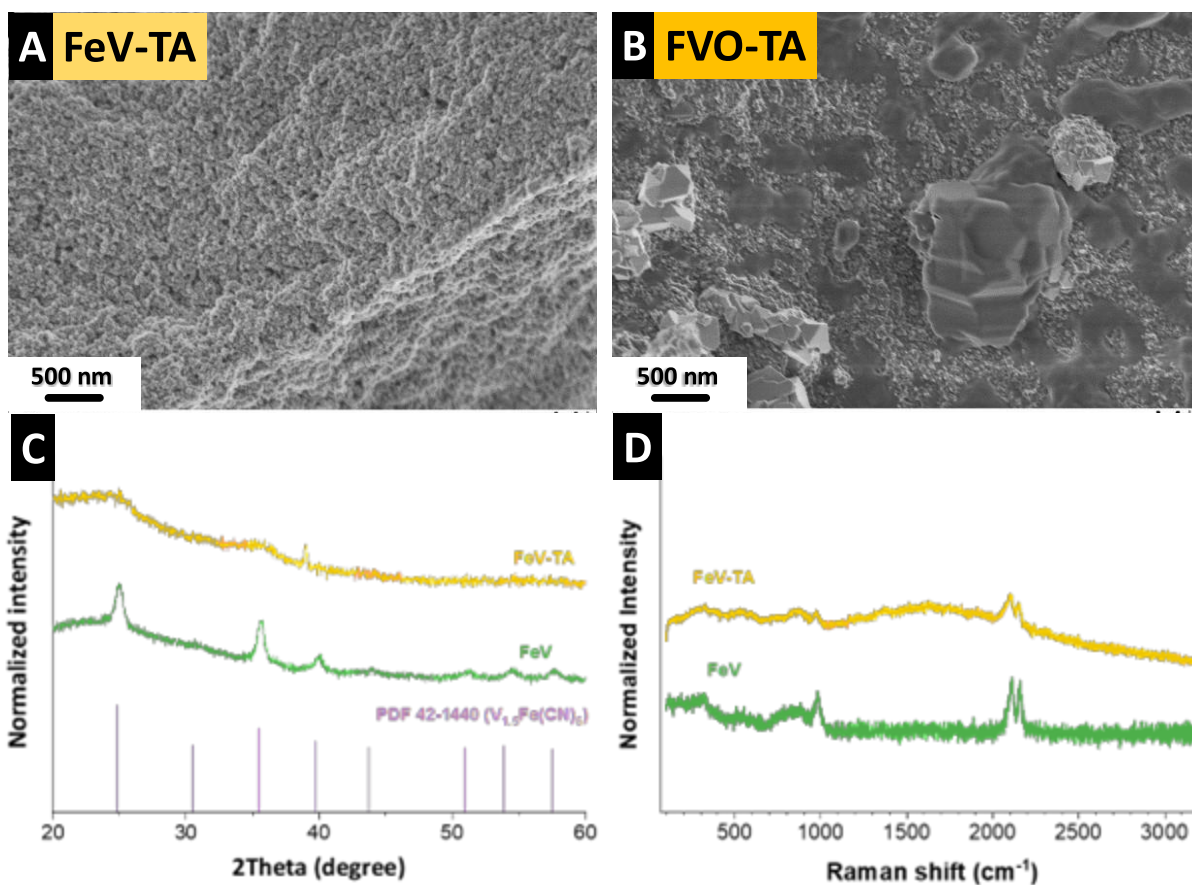


Figure S3. Scanning electron micrographs of **A** FeV synthesized with tannic acid and **B** its resulting oxide. **C** Respective X-ray diffractograms and **D** Raman spectra.

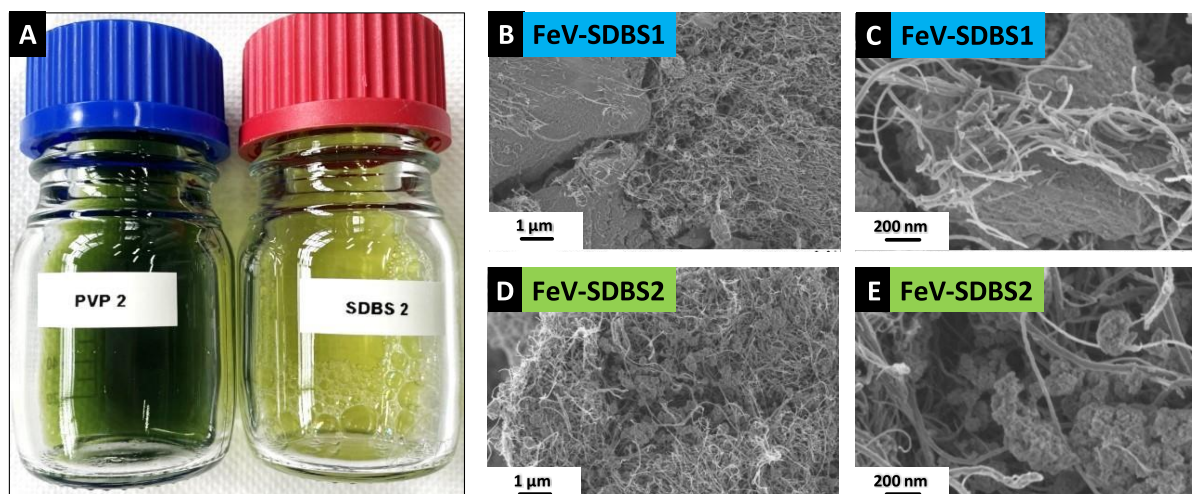


Figure S4. **A** Photograph of the residual supernatants after centrifugation of PVP and SDBS containing synthesis solutions. **B-C** Scanning electron micrographs of FeV-SDBS1 and **D-E** of FeV-SDBS2.

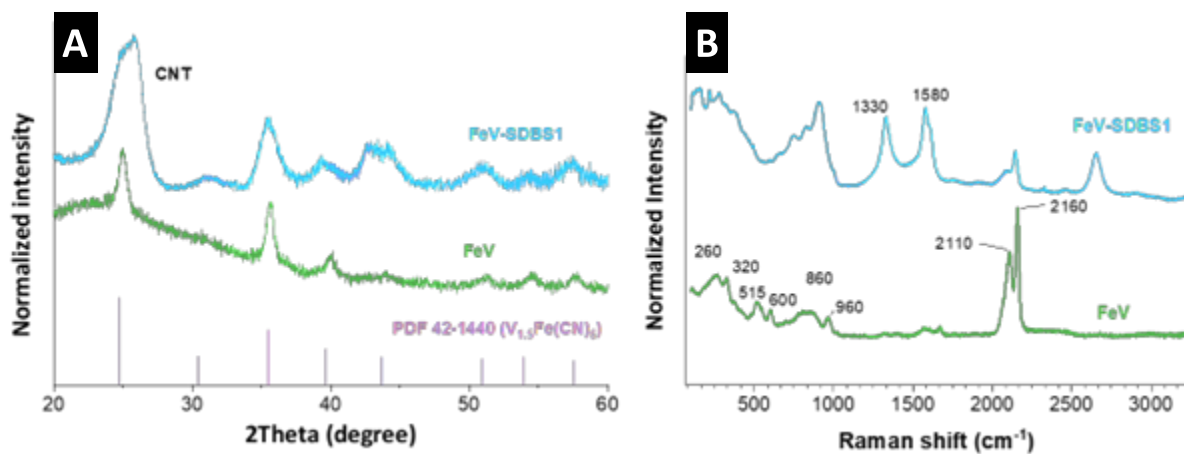


Figure S5. **A** X-ray diffractograms and **B** Raman spectrum of FeV-SDBS1 compared to the FeV.

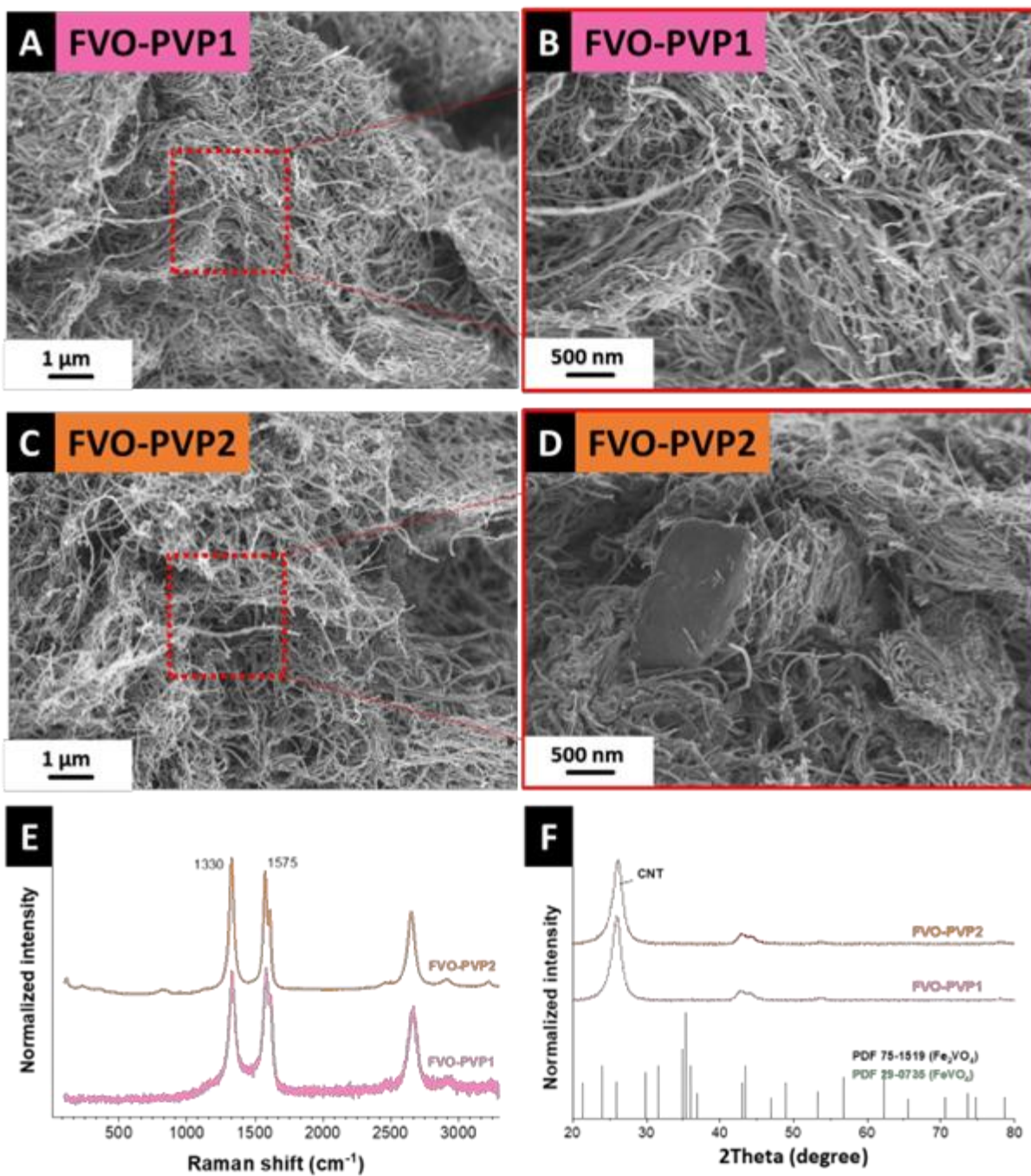


Figure S6. Scanning electron micrographs of **A-B** FeV-PVP1 and **C-D** FeV-PVP2 and their respective **E** Raman spectra and **F** X-ray diffractograms.

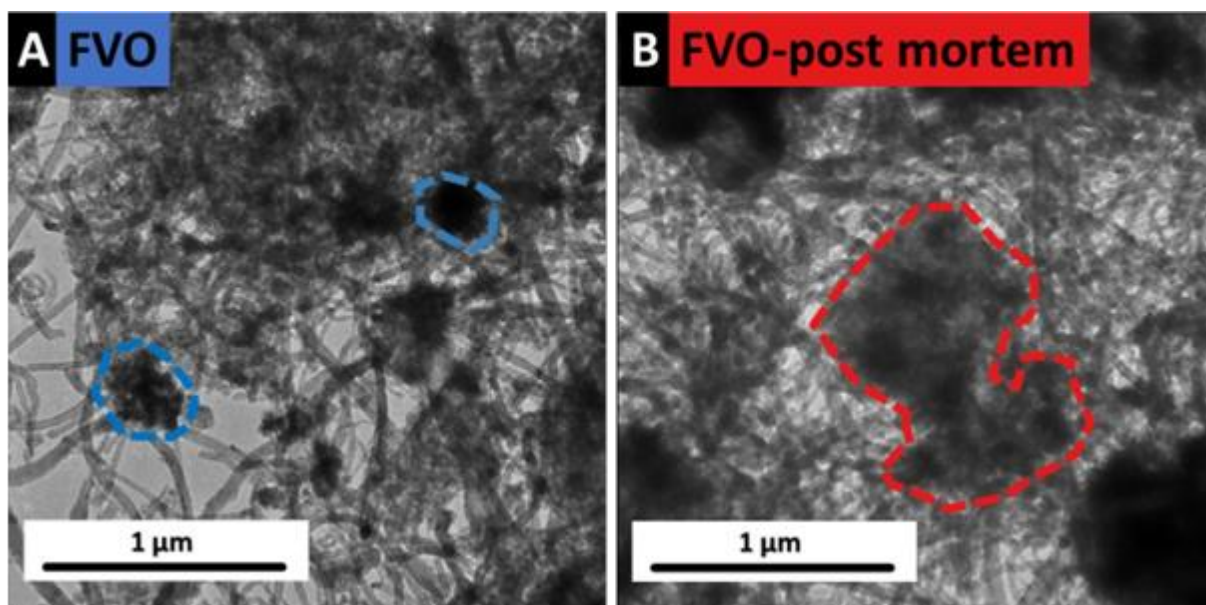


Figure S7. Transmission electron micrographs of the FVO electrode **A** before and **B** after cycling.

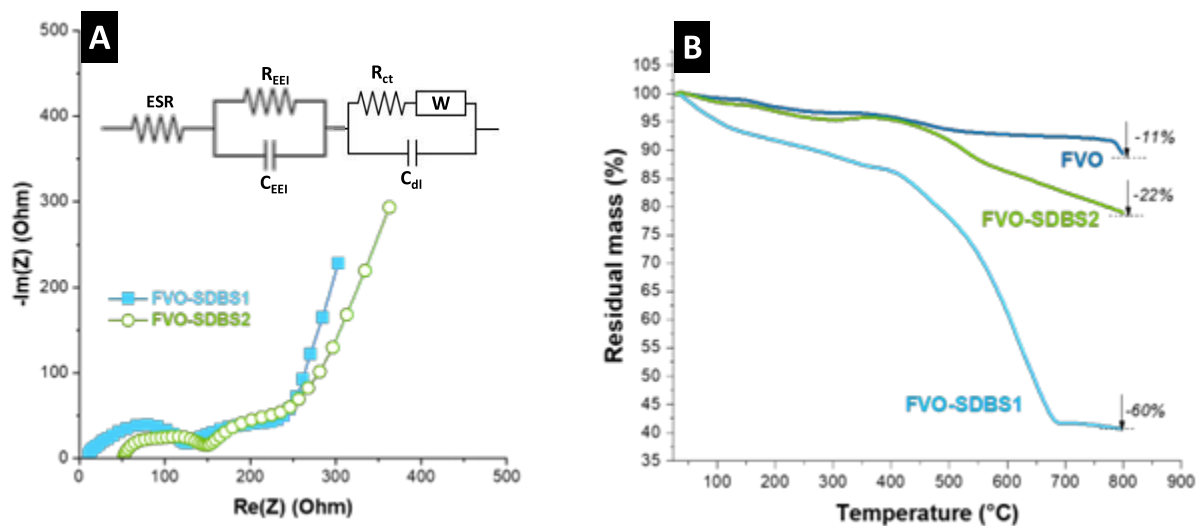


Figure S8. **A** Nyquist plot of FVO-SDBS1 and FVO-SDBS2. The inset shows the corresponding EIS equivalent circuit. **B** TGA curves of FVO, FVO-SDBS1, and FVO-SDBS2 under Ar.

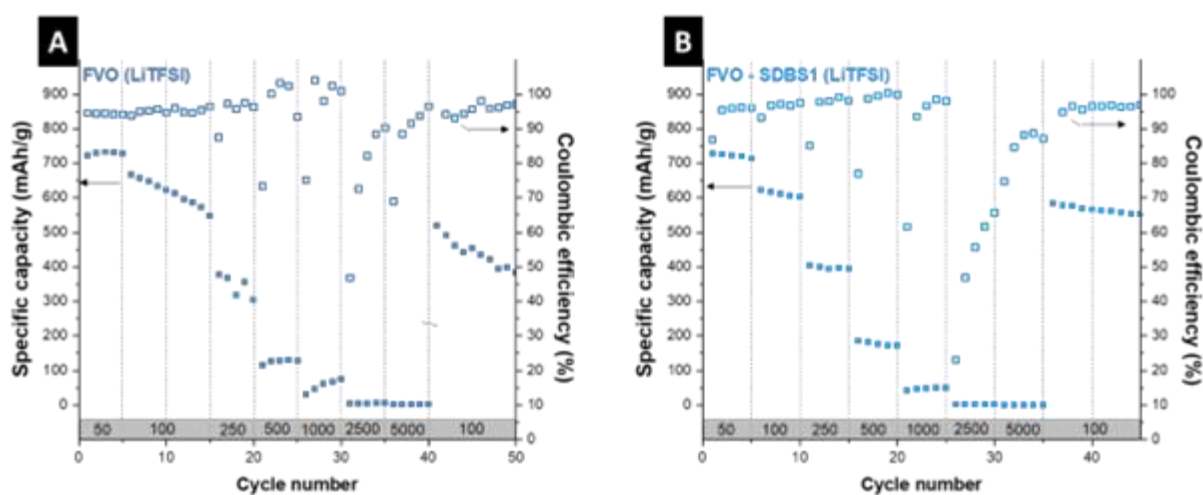


Figure S9. Galvanostatic charge/discharge cycling at 50-5000 mA/g for **A** FVO and **B** FVO-SDBS1.

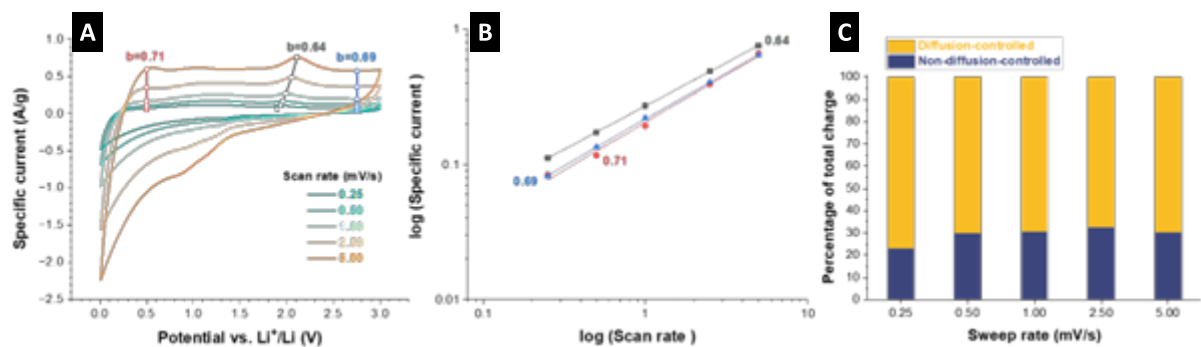


Figure S10. Cyclic voltammetry of FVO-SDBS1 at scan rates of 0.25-5.00 mV/s with their respective b-values at different potentials. **B** Specific current vs. scan rate at the maximum potential of each cycle, as well as potentials 0.5 V vs. Li/Li⁺ and 2.75 V vs. Li/Li⁺. **C** Calculated charge storage percentage from diffusion-controlled and non-diffusion-controlled charge from k_1 and k_2 values at different scan rates.

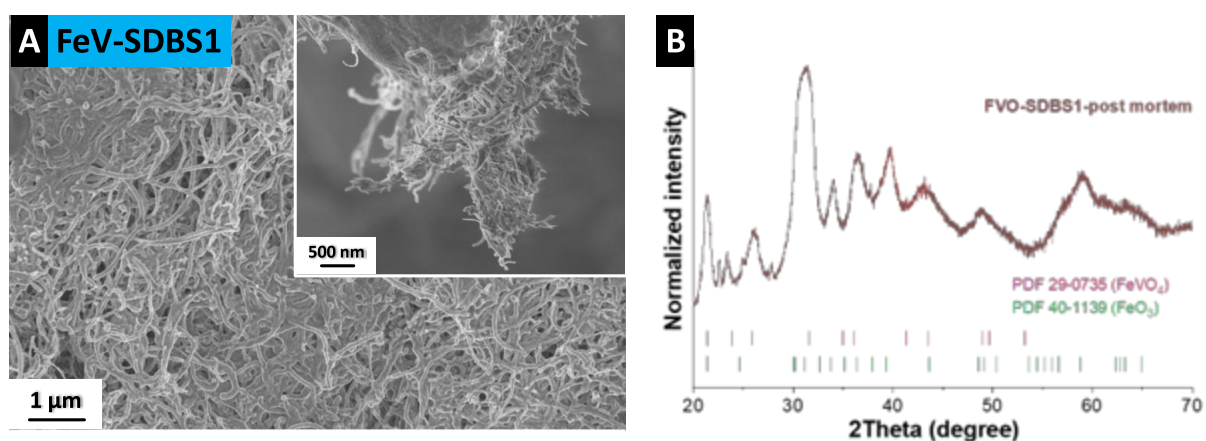


Figure S11. Post-mortem analysis of FVO-SDBS1. **A** Scanning electron micrograph of the electrode surface and **B** X-ray diffractogram of the electrode.

Table S1. Equivalent series resistance (ESR), the resistance of the electrode-electrolyte interphase (R_{EEI}), charge transfer resistance (R_{ct}), and Warburg resistance (R_w) of the tested cells.

Materials	ESR (Ω)	R_{EEI} (Ω)	R_{ct} (Ω)	R_w (Ω)
FVO-SDBS1	10.8	66.1	177.5	219.8
FVO-SDBS2	52.3	103.2	207.6	227.7

Mechanically Stable, Binder-Free, and Free-Standing Vanadium Trioxide/Carbon Hybrid Fiber Electrodes for Lithium-Ion Batteries

Behnoosh Bornamehr^{1,2}, Markus Gallei^{3,4}, Samantha Husmann¹, Volker Presser^{1,2,3*}

¹ *INM – Leibniz Institute for New Materials, Campus D2 2, 66123, Saarbrücken, Germany*

² *Department of Materials Science & Engineering, Saarland University, Campus D2 2, 66123, Saarbrücken, Germany*

³ *Saarene – Saarland Center for Energy Materials and Sustainability, Campus C4 2, 66123 Saarbrücken, Germany*

⁴ *Department of Chemistry, Saarland University, Campus C4 2, 66123 Saarbrücken, Germany*

Citation:

Bornamehr, B., Gallei, M., Husmann, S. and Presser, V., 2023. Mechanically Stable, Binder-Free, and Free-Standing Vanadium Trioxide/Carbon Hybrid Fiber Electrodes for Lithium-Ion Batteries. *Advanced Sustainable Systems*, 7(2), p.2200373.

Own contributions:

Conceptualization, Methodology, Investigation, Data Curation, Validation, Writing – original draft

Mechanically Stable, Binder-Free, and Free-Standing Vanadium Trioxide/Carbon Hybrid Fiber Electrodes for Lithium-Ion Batteries

Behnoosh Bornamehr, Markus Gallei, Samantha Husmann, and Volker Presser*

Binder is a crucial component in present-day battery electrodes but commonly contains fluorine and requires coating processing using organic (often toxic) solvents. Preparing binder-free electrodes is an attractive strategy to make battery electrode production and its end-of-use waste greener and safer. Herein, electrospinning is employed to prepare binder-free and self-standing electrodes. Such electrodes often suffer from low flexibility, and the correlation between performance and flexibility is usually overlooked. Processing parameters affect the mechanical properties of the electrodes, and for the first time it is reported that mechanical flexibility directly influences the electrochemical performance of the electrode. The importance is highlighted when processing parameters advantageous to powder materials, such as a higher heat treatment temperature, harm self-standing electrodes due to deterioration of fiber flexibility. Other strategies, such as conductive carbon addition, can be employed to improve the cell performance, but their effect on the mechanical properties of the electrodes must be considered. Rapid heat treatment achieves self-standing V_2O_3 with a capacity of 250 mAh g^{-1} at 250 mA g^{-1} and 390 mAh g^{-1} at 10 mA g^{-1}

synthesized material by electrospinning has an open and porous structure with a high surface area which can be used in different applications, such as filtering and purification,^[3] as drug carrier mesh in drug delivery,^[4,5] or serving as a template for producing inorganic nanofibers in composites.^[6] An application of the electrospun fibers that is gaining more importance is energy storage and conversion, specifically secondary battery electrodes, due to their simple and versatile synthesis and the ability to modify the surface with conductive coatings or by nanostructuring to improve the capacity and charge transfer.^[7,8]

Electrospun fibers are attractive as they form continuous fibrous morphology, are versatile in transforming a variety of polymers and inorganic substances into nanostructured materials, and can be used to avoid the use of binders to produce self-standing binder-free electrodes.^[9] Binders

are usually high-cost and halogen-containing components in the battery electrode that do not contribute to the capacity and decrease conductivity at their interface with the active material. Accordingly, research has been dedicated to removing binders in the electrode or their substitution by a conductive binder.^[10,11] In addition, electrode processing usually consists of coating slurries composed of the active material, binder, and carbon additive mixed in a solvent, typically highly toxic *N*-methyl-2-pyrrolidone (NMP). Electrospinning can maintain the integrity of the active electrode material without using binders while avoiding the coating process and, thus, using NMP.

Compared to binder-free electrodes synthesized on a substrate such as carbon cloth, carbon nanotubes (CNTs), or other conductive substrates,^[12,13] self-standing electrospun fibers do not have a substrate to give them additional support, and they rely on their mechanical stability.^[14–16] These electrodes can also be a candidate for use in flexible or wearable energy storage devices.^[12] Among materials synthesized by electrospinning for energy storage, vanadium oxides are an attractive candidate due to their various oxide phases, such as VO_2 , V_2O_3 , V_2O_5 , V_3O_7 , and vanadium's multiple oxidation states that give versatility in the design and utilized potential windows for energy storage and conversion.^[17,18] Although electrospinning has great potential as a green synthesis method due to avoiding the use of a binder and one-pot synthesis method without producing

1. Introduction

Electrospinning is a facile synthesis method to produce fibers with a diameter of tens of nanometers to micrometers.^[1,2] The

B. Bornamehr, S. Husmann, V. Presser
INM – Leibniz Institute for New Materials
D2 2, 66123 Saarbrücken, Germany
E-mail: presser@presser-group.com

B. Bornamehr, V. Presser
Department of Materials Science & Engineering
Saarland University
Campus D2 2, 66123 Saarbrücken, Germany

M. Gallei, V. Presser
Saarene – Saarland Center for Energy Materials and Sustainability
66123 Saarbrücken, Germany

M. Gallei
Polymer Chemistry
Saarland University
Campus D4 2, 66123 Saarbrücken, Germany

 The ORCID identification number(s) for the author(s) of this article can be found under <https://doi.org/10.1002/adsu.202200373>.

© 2022 The Authors. Advanced Sustainable Systems published by Wiley-VCH GmbH. This is an open access article under the terms of the Creative Commons Attribution License, which permits use, distribution and reproduction in any medium, provided the original work is properly cited.

DOI: 10.1002/adsu.202200373

side wastes, often studies on the electrospun fibers do not use these fibers directly as self-standing mats and prepare the electrodes by grinding the fibers and coating them on a substrate. In contrast, electrospun fiber mats offers the possibility of better functional material coverage due to the connected pathways.^[19–21] Although it is known that the mechanical properties of electrospun fibers are correlated with their performance,^[22,23] no report is available on the effect of processing parameters on the mechanical properties and application performance.^[24,25] As a result, although self-standing electrodes are investigated, they are mainly treated similarly to powder-based electrodes, which has imposed a gap in knowledge for the parameters that affect electrochemical performance. Our goal is, therefore, to provide a better understanding of the binder-free, electrospun electrodes.

Here we demonstrate that processing parameters such as heat-treatment temperature, atmosphere, and cooling rate interplay with the mechanical stability of the vanadium oxide electrospun fibers as a self-standing electrode. We also show the beneficial impact of adding conductive carbon to the fibers and the challenges faced in this procedure. By developing electrochemical energy storage materials and applications, our work contributes toward the United Nation's Sustainable Development Goal (SDG) number 7 (Affordable and Clean Energy).

2. Experimental Section

2.1. Synthesis of Electrospun Fibers

Vanadium(V) oxytripropoxide (VTIP, 98% metal basis), acetic anhydride (Ac₂O, ≥98% purity), and ethanol (EtOH, analytical standard) were purchased from Sigma-Aldrich. Poly(vinyl acetate) (PVAc, $M_w = 86\,000\text{ g mol}^{-1}$) was purchased from Synthomer. Carbon black was purchased from Nanografi (C-nergy super C65 conductive carbon black). The electrospinning solution was prepared in an MBraun glovebox through sol-gel synthesis according to a previous method with slight modification.^[18] The sol-gel was prepared by mixing 1.93 mL (vanadium triisopropoxy oxide) VTIP, 2.53 mL EtOH, 0.8 mL Ac₂O, and 0.72 g PVAc; this mixture was then stirred for 18 h. For the carbon-containing sample, 100 mg of commercial carbon black (C-nergy super C65) was directly added to the mixture with the other reactants. Samples containing carbon black (CB) were denoted with CB- prefix to the sample name. The solution was viscous and homogeneous the next day and was extracted via a 5 mL syringe to perform electrospinning.

Electrospinning was carried out in an NF-103 V MECC nanofiber system. A blunt tip 21-gauge needle was used to spin the fibers. The humidity and temperature of the electrospinning chamber were set below 20% and between 25 and 30 °C, respectively. The solution was electrospun from a 20 cm height onto an aluminum foil substrate under a potential difference of 28 kV via 1 mL h⁻¹ feeding rate and 1 min intervals for cleaning the needle. The electrospun mat was then put in a climate chamber set to 20 °C and 40% humidity to cross-link for 48 h. Discs of the cross-linked electrospun fiber were punched into 12 mm diameter circles and heat-treated with different treatment parameters.

2.2. Heat-Treatment of Electrospun Fibers

All samples were heat-treated in an inert atmosphere under the Ar gas flow with a 100 cm³ min⁻¹ flow rate. The samples were either heat-treated in a tubular furnace (Carbolite Gero) and denoted with H-prefix, or heat-treated in an infrared furnace (Behr infrared furnace IRF 10) and denoted with IR-prefix to their name. Before any heat treatment, the samples were placed in the middle of the quartz tube and purged with Ar (99.999%), depending on the size of the quartz tube, for 30 and 60 min for the infrared and tubular furnace, respectively. **Table 1** shows the utilized heat treatments for the electrospun discs and the resulting disc diameter after the heat treatment. The cooling in the infrared furnace was done in multiple steps to reduce thermal stress. All the treatments had a holding time of 30 min. The overall heat-treatment duration, including the Ar-purging, heating, and cooling, was 24 h for the tubular furnace and 2 h for the infrared furnace. To assess the reproducibility of the synthesis, the mean disc diameter after the treatment was measured with a caliper by measuring the diameter of 10 discs from each batch. All samples showed a diameter between 9.5 and 10.5 mm equal to ≈20% diameter reduction during the heat treatment.

2.3. Material Characterization

To characterize the structure morphology and elemental analysis, scanning electron microscopy (SEM) and energy-dispersive X-ray spectroscopy (EDX) were performed using a ZEISS GEMINI 500 microscope coupled with an Xmax detector from Oxford instruments. An acceleration voltage of 1 kV for imaging and 15 kV for spectroscopy was utilized. Sample preparation was done by mounting on double-sided sticky copper tape fixed on an aluminum stub without conductive sputter coating. For elemental analysis, at least 20 points were chosen from random locations from fibers on focus, and the average was calculated.

In addition, transmission electron microscopy (TEM) employed a 2100F system (JEOL) at 200 kV. To prepare the samples, a copper grid coated with lacey carbon was used as the substrate, and the fibers were dispersed in ethanol for 5 min in an ultrasound bath and then dried on the copper grid by dropwise addition.

A D8 Discover diffractometer (BRUKER AXS) with a copper source (Cu K_α, 40 kV, 40 mA), a Göbel mirror, and a 1 mm point focus were used for X-ray diffraction and phase analysis. A 2D VANTEC detector was used. Moreover, an angular range of 20° 2θ was used for 1000 s and repeated 3 times to cover a

Table 1. Heat treatment conditions to prepare the vanadium oxide fibers.

	Heating rate [°C min ⁻¹]	Holding temperature [°C]	Average cooling rate [°C min ⁻¹]
H-400	5	400	Furnace cooling
IRF-400	25	400	5.5
CB-IRF-400	25	400	5.5
IRF-700	45	700	9
CB-IRF-700	45	700	9

For all samples: Argon flow of 100 sccm in all steps.

full range of $10\text{--}80^\circ$ 2θ range. The scans were integrated and normalized to (0100).

We used a Renishaw inVia Raman microscope with an Nd-YAG laser and 633 nm excitation wavelength. Spectrometer calibration was done using a silicon standard. The sample was exposed to a power of $87\ \mu\text{W}$ at the focal point with a numeric aperture of 0.75. For each sample, 10 random points under focus were chosen, and the spectra were recorded with a spectral resolution of $1\ \text{cm}^{-1}$ by applying the laser for 20 s and accumulating 5 spectra. All spectra were stripped from cosmic rays and then normalized to (0100).

Thermogravimetric analysis (TGA) was done by a Netzsch TG-209-1 Libra. The mass changes to $700\ ^\circ\text{C}$ were recorded under a heating rate of $5\ ^\circ\text{C}\ \text{min}^{-1}$ in an oxidative (synthetic air) atmosphere with Ar as protective gas.

2.4. Mechanical Testing

Bending tests were performed by a custom-made instrument consisting of a motorized stage with a minimum step size of 6 nm (Q-545.240, PI) for displacement control and two goniometers for alignment correction. Disc samples with a mass of 2–3 mg and a diameter of 9.5–10.5 mm were vertically fixed on a glass sheet with all-purpose glue for the least inference in the testing. In situ observation was done via a tubular optic (12X UltraZoom, Navitar Inc.) and a camera (DMK 33UX252, ImagingSource). For the bending tests, the vertically standing sample was brought to contact with a flat punch connecting to the force sensor (KD45-2 N, ME-Messsysteme) until reaching a maximum displacement of half of the sample diameter. A loading and unloading velocity of 1 and $0.5\ \text{mm}\ \text{s}^{-1}$ were used for moving the flat punch.

2.5. Electrochemical Characterization

Half-cells were assembled by using CR2032 coin cells. Heat-treated discs were directly used as self-standing electrodes to

assemble cells without further punching or coating and used as the working electrode against lithium chip (11 mm) as counter and reference electrode. Whatman GF/F glass fiber and Celgard 2325 punched into 18 mm diameter discs were used as a separator, and $1\ \text{mol}\ \text{L}^{-1}$ LiPF_6 salt in a mixture of ethylene carbonate and dimethyl carbonate (EC:DMC, 1:1 by volume, BASF SelectiLyte) as the electrolyte. A BioLogic VMP300 potentiostat/galvanostat for cyclic voltammetry within a potential window of 0.01–3.5 V versus Li/Li^+ at a scan rate of $0.05\ \text{mV}\ \text{s}^{-1}$ was used. An Arbin Battery Cycler was employed to run galvanostatic charge/discharge with potential limitation measurements in the potential range of 0.01–3.5 V versus Li/Li^+ to test the rate capability and cycling stability at a rate of $250\ \text{mA}\ \text{g}^{-1}$. The electrode mass was, on average, $2.03 \pm 0.77\ \text{mg}$ for all 23 samples: The mass of each electrode was determined individually and used to normalize the electrochemical performance of each electrode. All electrochemical tests were done in a climate chamber held at $25 \pm 1\ ^\circ\text{C}$ to eliminate the effect of temperature fluctuations.

3. Results and Discussion

3.1. Synthesis of Metal Alkoxide Fibers

Figure 1 schematically shows the synthesis and processing steps. After the sol-gel preparation with or without carbon additive, flexible fibers were spun. These fibers are then directly heated and used as electrodes without further use of solvents or polymers. Therefore, it replaces the binder polyvinylidene fluoride (PVDF) in battery electrodes with PVA, which is a water-soluble and biodegradable polymer, and replaces all organic solvents used in synthesis or coating with ethanol which is one of the greenest solvents for synthesis due to its renewable generation, low persistence in the environment and low toxicity.^[26] After heat treatment under different parameters, such as different atmospheres, temperatures, and heating rates, the samples were cyclically bent and tested as cathodes versus Li metal. The parent

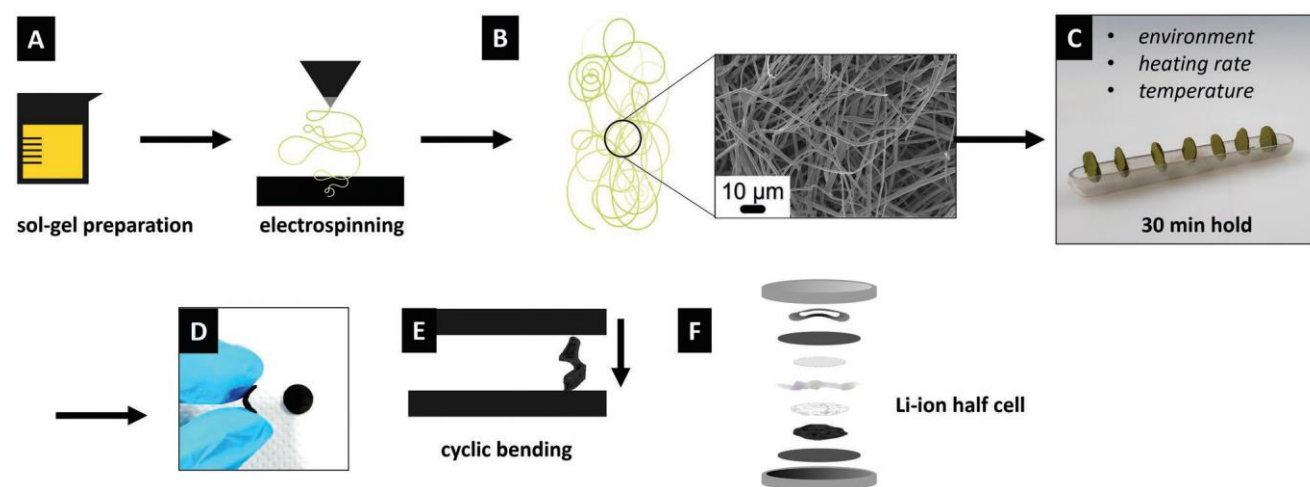


Figure 1. Synthesis and processing procedure to A) prepare a sol-gel as the electrospinning feed and B) electrospun homogeneous fibrous mat, C) punched 12 mm discs from to mat to perform heat-treatments at different conditions with 30 min holding time to D) produce flexible electrodes and be used for E) cyclic bending and F) Li-ion battery electrode.

fibers were prepared from an oxygen-containing vanadium precursor (VTIP) and polymer (PVA) in ethanol. The use of ethanol resulted in a homogeneous fiber morphology without forming beads or droplets due to its quick evaporation.^[27] No additional solvent was used for the fibers with conductive carbon, and the carbon additive was directly added to the solution.

Subsequently, the fibers were treated under different heat-treatment procedures in an infrared furnace at 400 °C for 30 min to form vanadium oxide (VO_x). The effect of the environment was tested as the first parameter affecting the fiber morphology and properties. For this, self-standing as-spun fibers were heat treated in an oxidative environment with a gas flow of 50:50 sccm, Ar/synthetic air, and 100:10 sccm Ar/synthetic air and in an inert environment with Ar only present. At the flow of 50:50 sccm Ar/synthetic air pure crystalline V₂O₅ was achieved (Figure S1A, Supporting Information). This showed similar rod-shaped-vanadium pentoxide nanowires (Figure 2A,B), as reported by Mai et al.^[20] No residual fiber morphology was observed in scanning electron micrographs, and the product showed no mechanical stability and was pulverized upon touch. Better mechanical stability was observed using 100:10 sccm Ar/synthetic air.

Scanning electron characterization showed the fibrous morphology is preserved while large particles are grown from the fibers (Figure 2C,D). X-ray diffraction (XRD) confirmed the present phase is crystalline VO₂ (Figure S1B, Supporting Information). The most homogeneous morphology was achieved under an inert atmosphere (Figure 2E,F). Fibers fully retained their shape while transforming into crystalline V₂O₃, confirmed by XRD and TEM (Figures S1C and S2A,B, Supporting Information). Only the V₂O₃ fibers were self-standing among the samples in different environments. The polymer burning accompanied by the higher oxygen-to-vanadium ratio, led to a disintegration of the fibers, coarsening of VO_x particles, and high brittleness. Therefore, the effect of other processing parameters was investigated using an inert atmosphere, and the oxygen atoms in the VTIP functioned as the oxidation source to form VO_x. A minimum temperature of 400 °C was needed to provide the required energy for achieving crystalline homogeneous vanadium oxide. We observed that the brittleness of the fibers accompanied the formation of VO₂ and V₂O₅ even under short heat treatments. Only the controlled formation of V₂O₃ resulted in a self-standing and flexible electrode with a lower oxygen ratio. This is in line with the reports on self-standing,

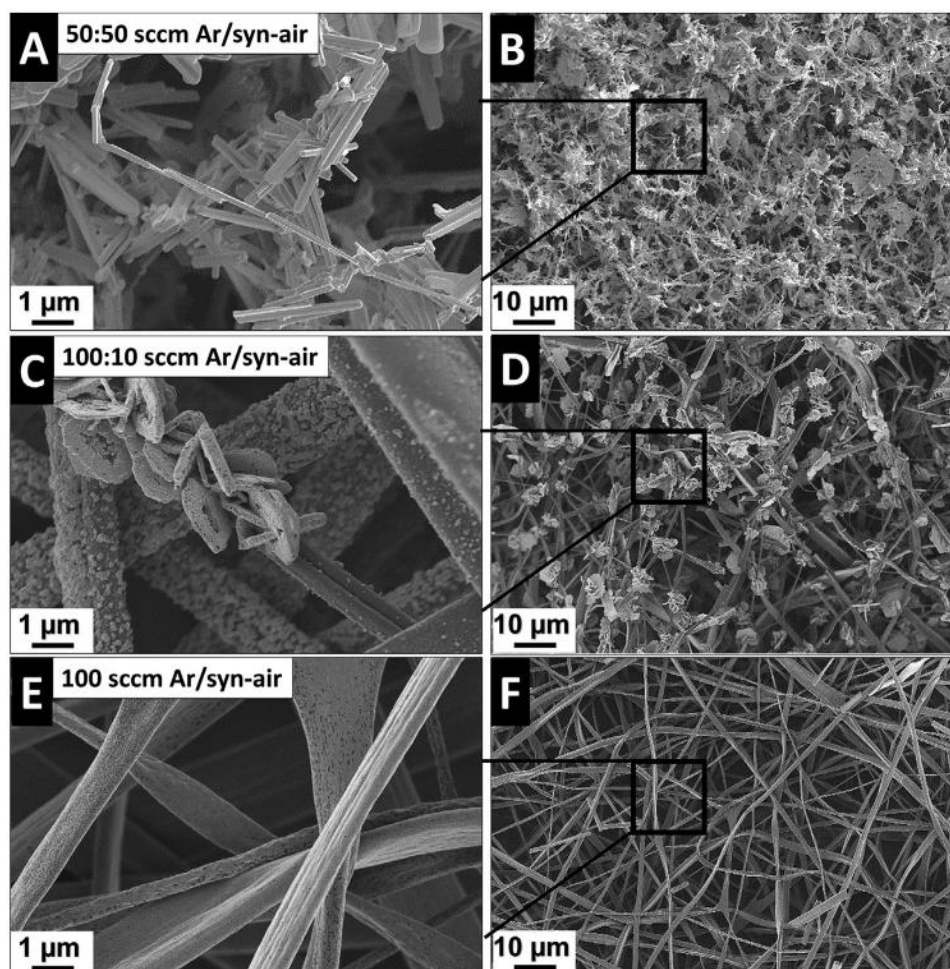


Figure 2. Scanning electron micrographs of heat-treated as-spun fibers for 30 min at 400 °C under A,B) Ar, syn-air/50:50 sccm, C,D) Ar, syn-air/100:10 sccm IRF-700, E,F) Ar/100 sccm.

flexible V_2O_3 , while studies on electrospun fibers of other vanadium oxides do not report flexibility.^[18,20,21,24]

3.2. Heat Treatment of Fibers

After atmosphere optimization for achieving self-standing electrodes, the effect of temperature and heating rate was tested on the properties of the V_2O_3 fibers. For this, the initial heat treatment under Ar was heated to 400 °C in a 1000 s ramp and held for 30 min (IRF-400). The cooling was optimized in multiple steps to minimize the deformation in the samples, as seen by the bending and distortion of the electrospun discs. For this, the cooling from 400 to 50 °C was done in 4 steps of 400–300, 300–200, 200–100, and 100–50 °C. Every step was done with a cooling ramp of 1000 s. The temperatures were optimized to increase the mechanical stability and minimize the deformation caused by the thermal stress in the samples. It was visually observed that the samples were more sensitive to fast cooling than fast heating and showed more deformation during the cooling. Therefore, the cooling was carried out in a step-wise manner. Samples were also heat-treated with multistep heating, but no effect on deformation was observed by changing the heating rate. This means the effect of processing parameters is more pronounced by the thermal contraction of the solid V_2O_3 fibers than when the metal alkoxide is transformed into vanadium oxide. Therefore, the heating was done in a single step, and the cooling was done in multiple steps to achieve flat V_2O_3 discs with the least distortion.

Heat treatments at higher temperatures were also done to achieve a higher crystallinity in the sample and evaluate the effect of the treatment temperature on the electrochemical performance. The heat treatment was optimized to 700 °C for

30 min. Like the IRF-400, the heating was done in a 1000 s ramp from room temperature to 700 °C and held for 30 min. The cooling was done in 4 steps: 700–400, 400–300, 300–200, and 200–100 °C, and each cooling step was done in 1000 s. No control over the temperature was done from 100 °C to RT. Therefore, both heat treatments for IRF-400 and IRF-700 resulted in a 1:36 h duration. The heat-treatments in the infrared furnace were also performed on the carbon-containing fibers leading to samples CB-IRF-400 and CB-IRF-700, respectively (Table 1). The treatment was also done in a tubular furnace at 400 °C for 30 min (sample denoted as H-400). The heating rate was set to 5 °C min⁻¹, and the cooling was done in the furnace overnight, resulting in a slow heat treatment with a total duration of 24 h, including heating and cooling.

The scanning electron micrographs of the samples shown in Figure 3 demonstrate the evolution of the morphology under different synthesis parameters. The as-spun fibers showed a smooth surface, indicating the presence of the polymer coating. In contrast, the cross-section of the fibers (inset of Figure 3A) showed a grainy texture showing vanadium alkoxide particles. After the heat-treatments of IRF-400 and IRF-700, the formation of VO_x particles can be seen while maintaining the fiber morphology (Figure 3B,C). The smooth surface of as-spun was preserved through heat treatments at 400 °C in H-400 (Figure 3D). This can be due to slower diffusion of oxygen with a lower heating and cooling rate and less burning of the PVA shell. The addition of carbon black is observed by the presence of particles in the fibers, which are maintained without the disintegration of the fiber after heat treatment (Figure 3E–G). Transmission electron micrographs show that the V_2O_3 particles formed during the heat treatment are in the order of a few nanometers and contained in the fiber.

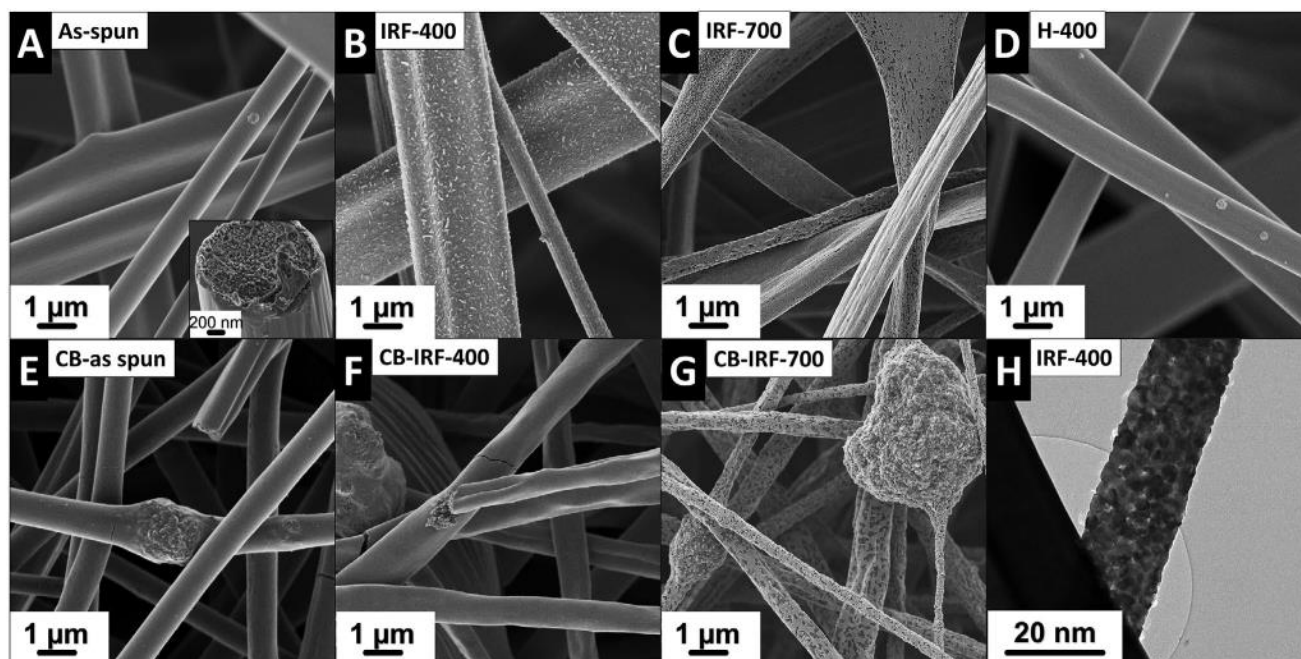


Figure 3. Scanning electron micrographs of A) as-spun VTIP-PVA fibers, inset: cross-section of the fiber. B) H-400, inset: H-400 electrode under bending. C) IRF-400, D) IRF-700, E) as-spun CB-VTIP-PVA, F) CB-IRF-400, G) CB-IRF-700, and H) transmission electron micrograph of IRF-400.

For further morphology analysis, the deviation in the fiber diameter was measured to observe the effect of temperature and heating rate on the diameter of the fibers. For this, 50 points of each sample were measured in the scanning electron micrographs, and their distribution was plotted in Figure 4A. IRF-400 and IRF-700 show a similar fiber diameter distribution with an average of 1.2 ± 0.5 and 1.0 ± 0.5 μm , respectively, while H-400 shows a broader size distribution than the other two with an average of 1.4 ± 0.8 μm . This indicates that the slower heating and cooling rate leads to more heterogeneous fiber diameter distributions. The average diameter of IRF-400 lies below H-400, demonstrating thinner fibers in total, which contribute to sample fragility. IRF-700 shows the lowest average fiber diameter among the three heat-treated fibers.

Homogeneity in the phase was evaluated via X-ray diffraction, and the scans are shown in Figure 4B. For all heat-treated samples, reflections showed a narrow shape and matched the pattern of vanadium trioxide in a rhombohedral lattice, space group $R\bar{3}c$ (167), showing the samples are composed of crystalline V_2O_3 phase. All spectra showed single-phase composition except for the H-400, which presented minor peaks matching other vanadium oxide phases such as VO_2 and V_6O_{11} . The formation of secondary phases can be assigned to the more

prolonged heating and cooling time during the heat treatment, demonstrating higher heterogeneity with slower rates. This duration allows the formation of other oxide phases that are thermodynamically stable at temperatures between room temperature and 400 $^\circ\text{C}$ but are kinetically less favorable than V_2O_3 in the system.

Raman spectroscopy was additionally performed to observe the bands corresponding to the C–C bonding and their evolution in different samples. The spectra are presented in Figure 4C. The spectrum of the as-spun fibers without carbon shows the main bands at 160 , 266 , 474 , 760 , 890 , and 1012 cm^{-1} , which mostly correspond to vanadium-oxygen bonds. Hardcastle et al. studied the correlation of vanadium-oxygen bond distances and the bond orders,^[28] where the longer interatomic distance between oxygen and vanadium corresponded to lower V–O stretching frequencies. Since the as-spun fiber is made of noncrystalline vanadium oxides and VTIP contains bonds between vanadium and oxygen with different oxidation states,^[29] these multiple bands at different frequencies resemble different V–O bond lengths and its stretching (474 , 760 cm^{-1}), bending (266 cm^{-1}), or external modes (160 cm^{-1}). The broad band shape in the spectrum is indicative of the lack of long-range order in the fibers.^[30] Bands in the spectral region

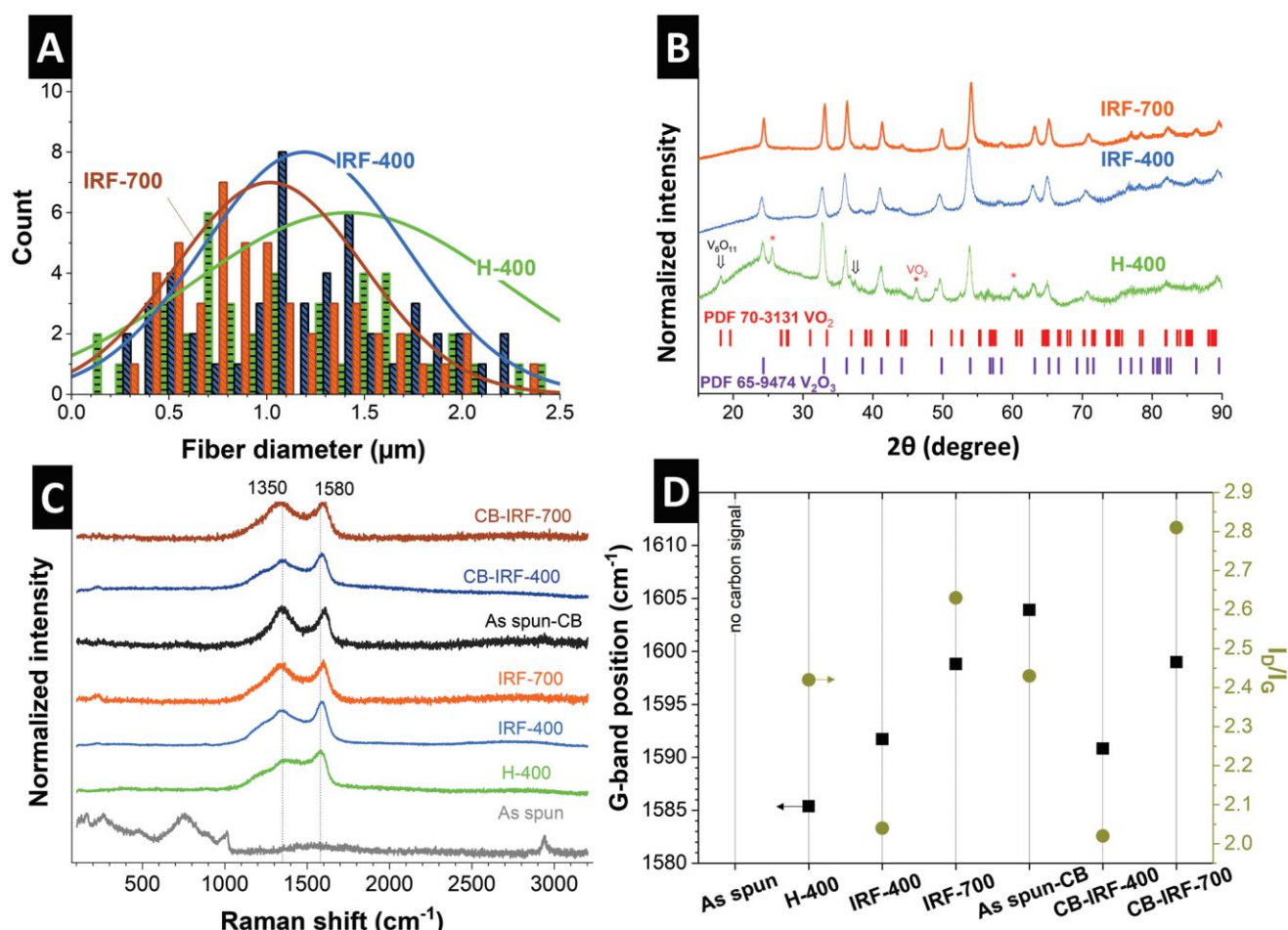


Figure 4. A) Fiber diameter distribution of H-400, IRF-400, and IRF-700. B) X-ray diffractograms of H-400, IRF-400, and IRF-700. C) Raman spectra of as-spun fibers with and without carbon, H-400, IRF-400, IRF-700, CB-IRF-400, and CB-IRF-700, and D) their respective G-band position and I_D/I_G ratio.

of 800–1200 cm^{-1} belong to the vibration of $\text{V}=\text{O}$,^[31] which is present in VTIP. At higher frequencies, a band at $\approx 2940 \text{ cm}^{-1}$ is observed, which is in the CH region^[29] and belongs to the C–H stretching in the CH_3 groups connected to VTIP or the C–H present in the PVA.

All of these bands are hardly distinguished after heat treatment. In all of these samples, C=C and C–C bands belonging to sp^2 -hybridization and sp^3 hybridization were observed as the main present bands (G-band and D-band at 1580 and 1350 cm^{-1} , respectively).^[32] This indicates the presence of conductive carbon in the as-spun fibers due to the carbon black addition and the formation of carbon bonds in the heat-treated samples by removing hydrogen and oxygen atoms in the PVA and forming sp^2 and sp^3 hybridized carbon as a result. The high-frequency band at 2940 cm^{-1} is still observed in the as-spun CB sample due to many C–H bonds but is absent after the heat treatment of PVA. Peak analysis was employed on the D-band and G-band of carbon to investigate the crystallinity and quality of the present carbon in each sample. For this, the G-band position and the ratio of I_D/I_G in different samples calculated from the area under the D-band and G-band are presented in Figure 4D. All samples show a large contribution of the D band and lack of the D-band overtone 2D at 2700 cm^{-1} , indicative of the nanocrystallinity of the carbon in the material. In both carbon-black-containing and parent fibers, the G-band undergoes a blueshift by the heat treatments at 700 °C compared to 400 °C, from 1592 to 1599 cm^{-1} for IRF-400 to IRF-700 and 1591 to 1599 cm^{-1} for CB-IRF-400 to CB-IRF-700, showing more graphitic ordering achieved under higher temperatures. A sharp increase was also observed in I_D/I_G from 2.04 in IRF-400 to 2.63 in IRF-700 and from 2.02 in CB-IRF-400 to 2.81 in CB-IRF-700, which can be due to the coarsening of the vanadium oxide particles and removal of the PVA at a higher temperature, resulting in the defect increase in the carbon shell of the fibers. H-400 showed the lowest G-band position and higher I_D/I_G position than treatments in the infrared furnace. Together, they can imply a lower conductivity of the carbon due to lower graphitization and higher value of defects.

Energy-dispersive X-ray spectroscopy was employed to confirm the presence of oxygen-containing groups and observe the composition change after the heat treatments. Figure 5A shows the elemental analysis for the as-spun and heat-treated samples. All samples show oxygen content of ≈ 22 –33 at%, with carbon-containing samples showing a generally lower amount of oxygen due to the added carbon black. As expected from the synthesis procedure, in the VTIP-CB sample, there is more detected carbon in the fibers than in the VTIP sample. Heat treatments show an increase in vanadium ratio, from 12.6 at% in as-spun fibers to 18.3 at% in H-400, 19.7 at% in IRF-400, and 19.1 at% in IRF-700. Also, in VTIP-CB spun fibers from 10.9 at% to 17.9 at% in CB-IRF-400 and 26.8 at% in CB-IRF-700. Parallel to the vanadium ratio increase in the samples, a general decrease in carbon up to 5 at% is observed. Still, a direct effect of the heat treatment parameters on the elemental composition cannot be concluded. Elemental analysis of the IRF-400 and IRF-700 samples show very similar results, but a different trend is present in the heat-treated samples of VTIP-CB. While in the CB-IRF-400, the carbon ratio stays nearly unchanged and the vanadium ratio increases, in the CB-IRF-700 sample, the carbon percentage decreases drastically. This can indicate the removal of the PVA during the heat treatment. A larger standard deviation for all detected elements also shows less homogeneity caused by PVA removal and particle growth in this sample.

To complement the chemical analysis, thermogravimetric analysis was performed in synthetic air with Ar as the protective gas to calculate the contribution of CB in the carbon content in the fibers after the heat treatment. For this, the samples IRF-400 and CB-IRF-400 were chosen, and their mass change against the temperature is presented in Figure 5B. An initial decrease is observed in both graphs, indicating the fibers' water loss. Following the water loss, a mass increase occurs attributed to the oxidation of V_2O_3 to V_2O_5 . Accompanying this oxidation, a mass decrease starts due to the PVA oxidation and removal. Both V_2O_3 and PVA oxidation end at 400 °C and leave the sample with a plateau at higher temperatures. The difference in the mass of the residues equal to

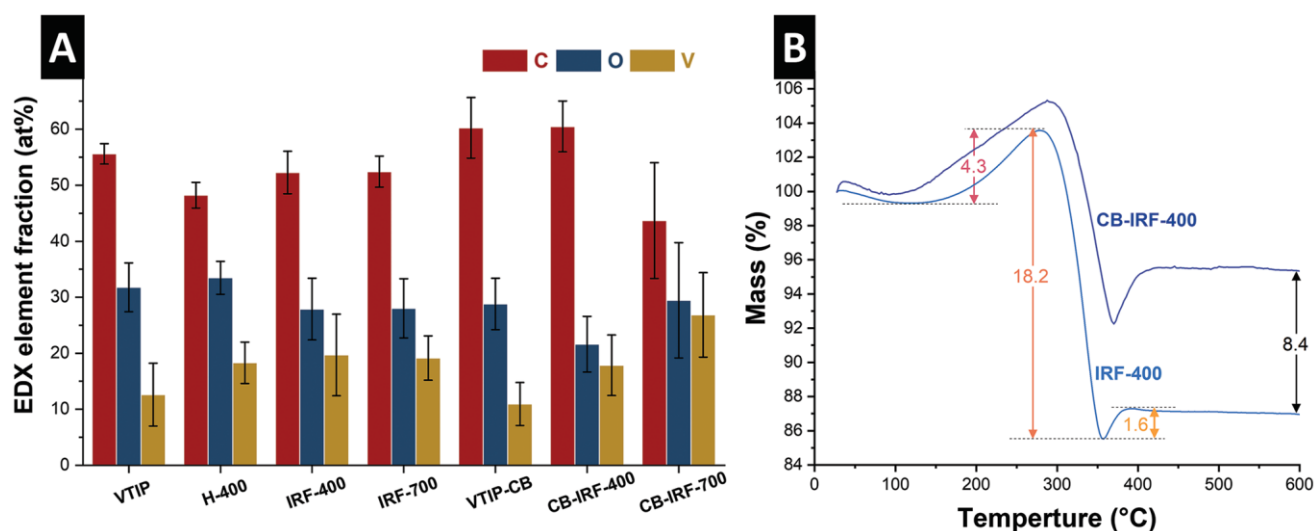


Figure 5. A). Elemental analysis of heat-treated samples by energy-dispersive X-ray spectroscopy. B) Thermogravimetric analysis of IRF-400 and CB-IRF-400 done in synthetic air under 5 °C min^{-1} heating rate.

8.4 mass% indicates the carbon content arising from the CB additive.

3.3. Mechanical Properties of the Fibers

Mechanical stability was examined by cyclic bending of the electrodes to half of their diameter. In contrast to bulk materials, electrospun fibers have low isotropy due to the random, nonwoven fibrous morphology and inhomogeneity in fiber size and direction. Therefore, no standard procedure for examining their mechanical properties has been established. Reports on the mechanical properties of the electrospun fibers can be divided into two groups. One, testing the single fibers via instruments such as AFM and measuring the mechanical properties in the micrometer range,^[14,15] and the other on the macroscopic range and pieces of the electrospun mat.^[14,16] While microscopic measurements can be used for different electrospun fibers and have a higher data precision, they are not scalable to the macroscopic mechanical properties. Additionally, measuring mechanical properties in terms of tensile strength is usually unreproducible when reports on the same materials and conditions are compared.^[22] If the mechanical properties are measured on a microscale, the results vary for different fibers due to the nonwoven nature of the fibers and the difference in size.^[15,33] Therefore, we use macro-bending to analyze the average mechanical behavior under different treatment protocols. The samples were bent to half of their diameter in multiple cycles until crack initiation and subsequent failure (Video S1, Supporting Information). For the fibrous mats, the thickness cannot be directly measured; therefore, samples with similar dimensions (9.5–10 mm) and mass (2.5–3 mg) were chosen to normalize the thickness. No substrate or support, such as polyurethane, was used for the bending to affect the results, and all the samples were bent in their dried state. Different bending rates (mm s^{-1}) were used to observe the sensitivity of the samples to the deformation rate. Each batch tested at least 3 samples to reproduce the results. Despite the samples' anisotropy in fiber morphology, the bending results were similar and in line with the other samples in the same batch.

The samples with an initial defect, such as a crack or a crease, showed a much lower strength and reached failure in the first cycles and could not be compared to samples without initial defects. As-spun fibers were first bent several times under a rate of 1 mm s^{-1} and remained intact for more than 50 cycles. For H-400, the first cracks were observed after 10 cycles of bending to half of the sample diameter, and failure (breaking of the electrode) took place after 50 cycles. H-400 also showed sensitivity to the rate of bending. Under 1 mm s^{-1} , the electrode fractured in the first cycle, while under a bending rate of 0.5 mm s^{-1} , the electrodes withstood 50 cycles before failure. A maximum of 5 mN force was used as the threshold to bend the fibers. The IRF-400 sample showed completely different results compared to H-400. Under the same rate of 0.5 mm s^{-1} , the samples withstood 20 cycles, but all failed before 50 cycles. First cracks were observed earlier than in H-400, namely in the first cycles, before bending 10 times. A maximum of 5 mN was not enough to bend the samples and was increased to 10 mN. This shows higher stiffness of the IRF-samples compared to H-400.

Table 2. Mechanical properties of samples tested via bending.

	Displacement rate [mm s^{-1}]	First cracks [cycle number]	Fracture [cycle number]	Max. compressive load [mN]
As-spun	1	No cracking	No fracture	5
H-400	1	1	<10	5
	0.5	>10	>50	5
IRF-400	0.5	<10	<50	10
CB-IRF-400	0.5	1	<10	50
CB-IRF-700	0.5	Upon assembly	Upon assembly	—

The carbon-containing CB-IRF-400 showed higher brittleness, with early failure after the first cracks. Bending to half the sample diameter was achieved until the maximum force was 50 mN. These failed under 10 cyclic bending, while CB-IRF-700 broke easily when pasting to the testing stage due to extreme brittleness, making further testing impossible. **Table 2** summarizes these results.

The findings show a direct effect of processing parameters on the stability of mechanical flexibility of the fibers under bending. Higher cooling and heating rates and higher temperatures increase the strength of the fibers, which is shown by the maximum needed force to bend the samples while reducing their flexibility. The addition of carbon shows the same trend by hindering the mechanical flexibility of the fibers to undergo bending.

All these observations can be explained by the relation of mechanical performance to the different microstructures of the samples. For comparing the heating and cooling rate, samples H-400 and IRF-400 can be used. The latter, in general, showed higher deformation in the disc, which can be attributed to the thermal strains. Although samples with the least strain were used for bending, the fibers were affected by the thermal stress, and the residual stress in the fibers is probably the reason for the lower resistance of the sample against bending.

The influence of adding carbon can be analyzed by comparing the results of IRF-400 and CB-IRF-400. In the case of CB-IRF-400, the flexibility decreases, but the reason for this brittleness is the extra stress in the fibers due to carbon particles. While the external stress is increased in the fibers due to bending, it creates stress concentration points where there is more inhomogeneity, where the fibers meet the carbon particle in the material, as shown in Figure 3F. Although composed of crystalline V_2O_3 , similar to other samples (Figure S3A, Supporting Information), the brittleness becomes even more severe with a higher treatment temperature that removes the polymer and induces higher thermal stress, as seen for CB-IRF-700.

3.4. Electrochemical Properties of the Fibers

The electrochemical performance of the free-standing fibers was further evaluated. Four samples were chosen to test their performance against lithium chips between 0.01 and 3.5 V versus Li/Li^+ , namely, H-400, IRF-400, CB-IRF-400, and CB-IRF-700.

The cyclic voltammetry of the samples is represented in Figure 6A. The diagram shows very similar voltammograms for all the samples, comprising two peaks in the cathodic sweep at ≈ 1.9 V versus Li/Li⁺ (i) and ≈ 0.8 V versus Li/Li⁺ (ii). These peaks are completed by two oxidation reactions in the anodic sweep at ≈ 1.3 V versus Li/Li⁺ (iii) and ≈ 2.6 V versus Li/Li⁺ (v). An additional anodic peak was observed in the voltammogram of IRF-400 at the potential of ≈ 1.9 V versus Li/Li⁺ (iv). It can be concluded that the lithiation and delithiation mainly occur by two sets of redox peaks at lower and higher potential, as reported in the literature for the V₂O₃ particles.^[24,34–36] Noting the achieved capacity from the rate handling and stability tests and the trend of the capacity change (Figure 6B,C), the predominant lithiation mechanism is through insertion rather than conversion reactions. The galvanostatic charge-discharge profiles (Figure 6D) taken from cycle 150 of the stability test show a similar trend for all sam-

ples, and the lithiation is assumed to take place via insertion in the V₂O₃ lattice by the following reaction^[24,35]



A stability test for 300 cycles in the potential window of 0.01–3.5 V versus Li/Li⁺ was done at a current of 250 mA g⁻¹ (Figure 6B). H-400 showed an initial capacity of 305 mAh g⁻¹, and after a decrease to 280 mAh g⁻¹ in 25 cycles, it stabilized and reached 306 mAh g⁻¹ after 300 cycles. IR-400 showed an initial capacity of 255 mAh g⁻¹ that decreased to 240 mAh g⁻¹ after 15 cycles and showed a similar trend as the H-400. However, the capacity further declined and fell to 216 mAh g⁻¹ after 300 cycles. Its conductive carbon-containing counterpart CB-IRF-400 showed a better performance. Although the initial capacity and decrease were similar to those of IRF-400, the capacity was stabilized at around 250 mAh g⁻¹ for 300 cycles,

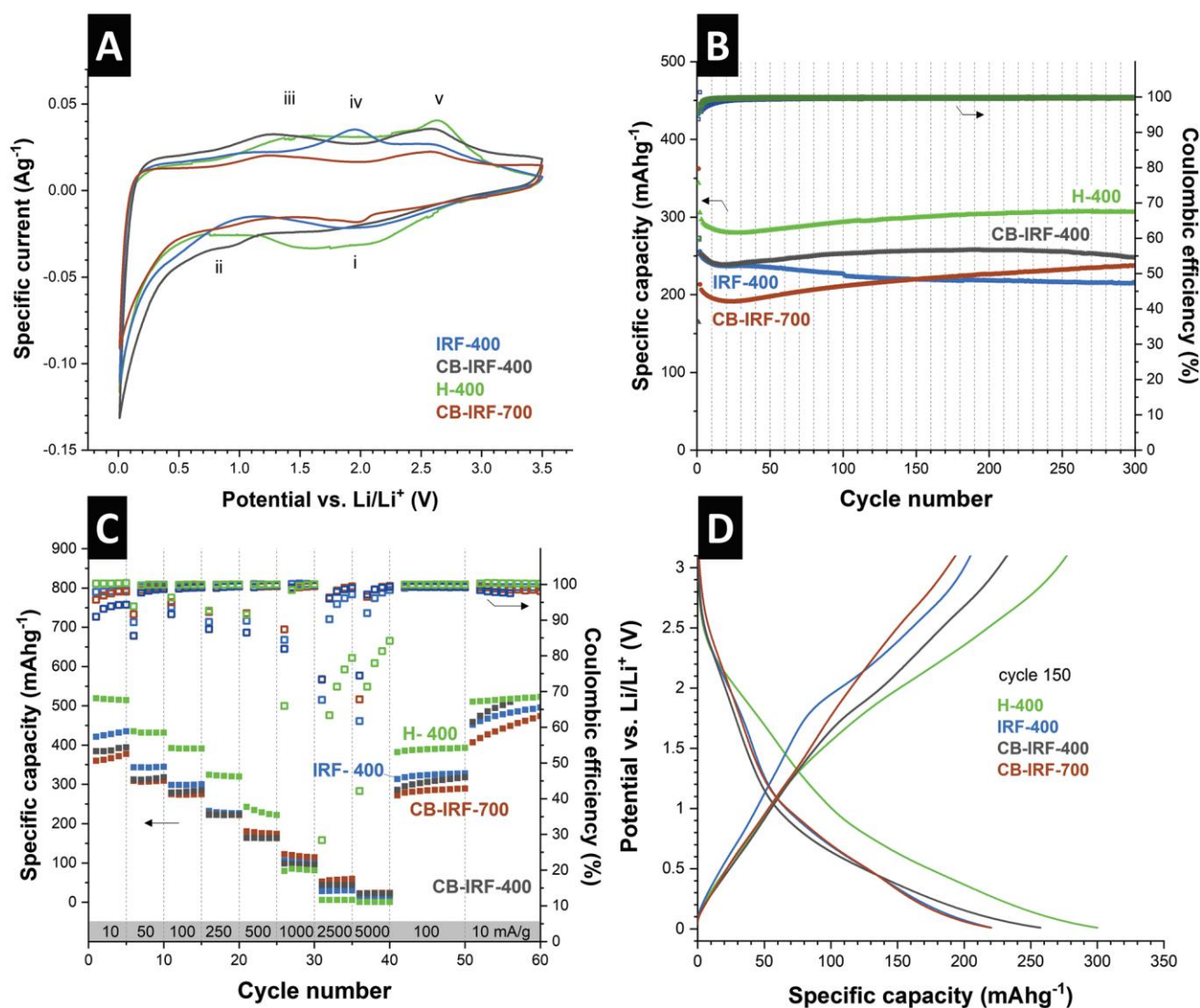


Figure 6. Electrochemical characterization of H-400, IRF-400, CB-IRF-400, and CB-IRF-700 for use as a lithium-ion battery electrode. A) Cyclic voltammograms showing the third cycle at 0.05 mV s⁻¹. B) Stability test at a current rate 250 mA g⁻¹. C) rate handling performance, and D) Galvanostatic charge-discharge curves of the 150th cycle from the stability test at a current rate of 250 mA g⁻¹.

showing a stable performance between H-400 and IRF-400. The CB-IRF-700 sample showed the lowest performance among the four and had an initial capacity of 213 mAh g⁻¹, which decreased to 191 mAh g⁻¹ in 25 cycles and then gradually increased to 238 mAh g⁻¹ after 300 cycles. The H-400 shows the best performance, while CB-IRF-400 and IRF-400 have a lower performance.

This is similar to the results achieved from the mechanical testing of the mats. Since the intactness of the fibers ensures conductive paths for electron movement, it can be deduced that their mechanical stability can directly affect electrochemical performance. This effect can be followed by comparing every two samples in their mechanical and electrochemical performance. The higher cooling rate in the infrared furnace causes more thermal strain on the fibers and makes them more susceptible to breaking. During charging and discharging, the fibers are repeatedly lithiated and delithiated; accordingly, the internal stress from the heat treatment can decrease their ability to buffer the stress from volume change during cycling. As a result, it can be seen that IRF-400 cannot accommodate the capacity of H-400.

Carbon addition makes the fibers more conductive and aids the material with charge transport. This translates into better capacity retention upon long-term cycling, as the carbon ensures conductive pathways even after the mechanical failure of the fibers. Similarly, the presence of carbon enables CB-IRF-400 to outperform IRF-400 at higher rates (Figure 6C). Finally, CB-IRF-700, prepared using a large cooling rate and high-temperature heat treatment, is the most susceptible to breaking, and it shows the lowest performance. Still, the carbon addition in this sample benefits the electrochemical performance, as the comparison with the IRF-700 sample with the same heat treatment but without carbon shows that a lower initial capacity of 121 mAh g⁻¹ is achieved (Figure S3B, Supporting Information).

Therefore, the mechanical properties of the self-standing electrodes can be translated to the electrochemical performance when the chemistry of the samples is the same. For example, when both samples are bare of conductive carbon, electrochemical performance can be directly analyzed by the parameters affecting the brittleness, such as the heat treatment temperature and cooling rate. When the sample's chemical composition is changed by carbon addition, the electrochemical performance enhances, although the carbon addition makes the sample more brittle.

Rate handling was performed at current rates of 10, 50, 100, 250, 500, 1000, 5000 mA g⁻¹ each for 5 cycles and then 10 cycles at rates of 100 and 10 mA g⁻¹ to assess the capacity recovery. All samples went under 5 cycles of conditioning before the rate handling at 10 mA g⁻¹. H-400 showed the highest capacity among the samples, with 520 mAh g⁻¹ at 10 mA g⁻¹ and 390 mAh g⁻¹ at 100 mA g⁻¹. The capacity dropped significantly at higher rates, showing lower conductivity than other samples, as confirmed by Raman analysis (Figure 4C,D). It was again fully recovered and maintained at 100 mAh g⁻¹. The other three samples showed similar rate capability performance with initial capacities of 420, 384, and 360 mAh g⁻¹ for IRF-400, CB-IRF-400, and CB-IRF-700 at 10 mA g⁻¹, respectively. At a higher rate of 2.5 A g⁻¹, CB-IRF-700 retained the highest capacity of 59 mAh g⁻¹, while IRF-400 and CB-IRF-400 showed 30 and

44 mAh g⁻¹, respectively. H-400 lost nearly all of its capacity at 2.5 A g⁻¹. The better performance of carbon-containing samples at a higher rate shows the effect of conductivity and better charge transfer in the fibers. The effect of conductivity can also be observed by the higher Coulombic efficiency in the samples CB-IRF-400 and CB-IRF-700 at higher current rates above 95%, while the Coulombic efficiency for H-400 falls to values below 65% at the highest rates. All samples recovered and maintained their initial capacity at the rate of 10 mA g⁻¹ again, while CB-IRF-400 capacity increased to 520 mAh g⁻¹, close to H-400.

The connectivity of the fibers can explain the observed electrochemical properties. Post mortem scanning electron micrographs of the electrodes after their end of life (Figure S4, Supporting Information) showed the fibers were broken into smaller pieces and lost their initial connection. Since the connectivity of the fibers is the prerequisite for the charge transfer in the material, this elucidates that during cycling, the fiber network loses its connectivity, and through this, its capacity diminishes. Therefore, the parameters mentioned above that affect the capacity can be analyzed through their effect on the connectivity and conductivity of the fibers so that the heat treatment parameter that induces higher thermal stress causes a loss of connectivity in the network and decreases the capacity by isolating the fibers.

4. Conclusions

With the rise of awareness on the sustainability of Li-ion battery electrodes, research has increased in binder-free and NMP-free electrodes. This work aimed to provide a new perspective on preparing flexible electrodes for producing next-generation and more environmentally-friendly electrode materials. We synthesized self-standing vanadium trioxide fibers by electrospinning and subsequent heat treatment. We tested them as Li-ion battery electrodes, showing the relationship between the mechanical and electrochemical performance and how this is affected by processing parameters. We showed that among vanadium oxides, higher oxygen ratios cause fiber brittleness, and particle coarsening. Lower processing temperature was beneficial to the electrode cycling stability. It was observed that lower heating rates affect the performance the most.

Although prolonged heating and cooling induced phase and morphology inhomogeneity, higher mechanical, and electrochemical stability was observed. While in powder materials the synthesis parameters are chosen for the crystallinity and morphology control, in the case of self-standing electrodes, these parameters have to be selected regarding their effect on mechanical flexibility. In the case of faster heating and cooling rates, higher thermal stress is induced in the fibers; therefore, a higher temperature intensifies this effect. This is due to the connection loss between the fibers. More polymer is burned through heat treatments at a higher temperature, and fiber diameter decreases. This can make the fibers more susceptible to breaking under cycling. The same phenomenon occurs when the heat treatment is done with faster heating and cooling rates. This causes the fibers to undergo a greater deformation due to internal thermal stress. Presence of conductive carbon increases the electrochemical stability of the fibers

heat-treated at faster rates by increasing their conductivity, but does not overcome the capacity loss due to the introduced brittleness, as seen by mechanical testing. Therefore, carbon can be added using more mechanically stable species such as CNTs or smaller carbon particles with less aggregation and better dispersion in the sol–gel. Other polymers with higher thermal stability can also improve mechanical properties. PVA has small monomer molecules with –OH functional group per two carbon atoms removed during the heat treatment. This is rather a large mass loss that triggers deformation in the fibers and results in the burning of the carbon atom. Polymers with other monomers and less functional groups can increase flexibility by reducing the diameter and shape loss in the heat treatment and will be used in future works.

Supporting Information

Supporting Information is available from the Wiley Online Library or from the author.

Acknowledgements

This work was part of the electrospun vanadium oxide and sulfide-carbon hybrids project (HEROES-4-Li-NA-batteries) by the German Research Foundation (DFG, Deutsche Forschungsgemeinschaft), Project No. 452180147. The authors thank Zhihao Tien for help with bending tests, Xuan Zhang for useful discussions, and Eduard Arzt (all at INM) for his continuing support.

Open access funding enabled and organized by Projekt DEAL.

Conflict of Interest

The authors declare no conflict of interest.

Author Contributions

B.B.: Conceptualization, Methodology, Investigation, Data curation, Validation, Writing—Original Draft, Writing—Review and Editing. M.G.: Validation, Writing—Review and Editing. S.H.: Methodology, Validation, Supervision, Visualization, Writing—Review and Editing. V.P.: Methodology, Validation, Supervision, Funding Acquisition, Visualization, Writing—Review and Editing.

Data Availability Statement

The data that support the findings of this study are available from the corresponding author upon reasonable request.

Keywords

binder-free electrodes, electrospinning, energy storages, flexible electrodes, vanadium oxide

Received: August 27, 2022

Revised: November 14, 2022

Published online: December 5, 2022

- [1] L. Persano, A. Camposeo, C. Tekmen, D. Pisignano, *Macromol. Mater. Eng.* **2013**, 298, 504.
- [2] D. H. Reneker, I. Chun, *Nanotechnology* **1996**, 7, 216.
- [3] R. Gopal, S. Kaur, Z. Ma, C. Chan, S. Ramakrishna, T. Matsuura, *J. Membr. Sci.* **2006**, 281, 581.
- [4] T. Okuda, K. Tominaga, S. Kidoaki, *J. Controlled Release* **2010**, 143, 258.
- [5] Y. Hong, X. Chen, X. Jing, H. Fan, B. Guo, Z. Gu, X. Zhang, *Adv. Mater.* **2010**, 22, 754.
- [6] M. Ikegame, K. Tajima, T. Aida, *Angew. Chem., Int. Ed. Eng.* **2003**, 42, 2154.
- [7] R. Sahay, P. S. Kumar, R. Sridhar, J. Sundaramurthy, J. Venugopal, S. G. Mhaisalkar, S. Ramakrishna, *J. Mater. Chem. B* **2012**, 22, 12953.
- [8] V. Aravindan, J. Sundaramurthy, P. S. Kumar, Y.-S. Lee, S. Ramakrishna, S. Madhavi, *Sci. Rev. Chem. Commun.* **2015**, 51, 2225.
- [9] M. J. Laudenslager, R. H. Scheffler, W. M. Sigmund, *Pure Appl. Chem.* **2010**, 82, 2137.
- [10] S. He, W. Chen, *Nanoscale* **2015**, 7, 6957.
- [11] Y. Kang, C. Deng, Y. Chen, X. Liu, Z. Liang, T. Li, Q. Hu, Y. Zhao, *Nanoscale Res. Lett.* **2020**, 15, 112.
- [12] D. Chen, Z. Lou, K. Jiang, G. Shen, *Adv. Funct. Mater.* **2018**, 28, 1805596.
- [13] C. Lu, W.-w. Liu, H. Li, B. K. Tay, *Sci. Rev. Chem. Commun.* **2014**, 50, 3338.
- [14] F. Croisier, A. S. Duwez, C. Jerome, A. F. Leonard, K. O. van der Werf, P. J. Dijkstra, M. L. Bennink, *Acta Biomater.* **2012**, 8, 218.
- [15] S. Y. Gu, Q. L. Wu, J. Ren, G. J. Vancso, *Macromol. Rapid Commun.* **2005**, 26, 716.
- [16] Y. Ding, P. Zhang, Z. Long, Y. Jiang, F. Xu, W. Di, *J. Membr. Sci.* **2009**, 329, 56.
- [17] C. F. Armer, J. S. Yeoh, X. Li, A. Lowe, *J. Power Sources* **2018**, 395, 414.
- [18] A. Tolosa, S. Fleischmann, I. Grobelsek, V. Presser, *ACS Appl. Energy Mater.* **2018**, 1, 3790.
- [19] Y. L. Cheah, N. Gupta, S. S. Pramana, V. Aravindan, G. Wee, M. Srinivasan, *J. Power Sources* **2011**, 196, 6465.
- [20] L. Mai, L. Xu, C. Han, X. Xu, Y. Luo, S. Zhao, Y. Zhao, *Nano Lett.* **2010**, 10, 4750.
- [21] C. Ban, N. A. Chernova, M. S. Whittingham, *Electrochem. Commun.* **2009**, 11, 522.
- [22] T. U. Rashid, R. E. Gorga, W. E. Krause, *Adv. Eng. Mater.* **2021**, 23, 2100153.
- [23] S. Y. Chew, T. C. Hufnagel, C. T. Lim, K. W. Leong, *Nanotechnology* **2006**, 17, 3880.
- [24] T. Zhang, L. Zhang, L. Zhao, X. Huang, W. Li, T. Li, T. Shen, S. Sun, Y. Hou, *Small* **2020**, 16, 2005302.
- [25] T. Jin, H. Li, Y. Li, L. Jiao, J. Chen, *Nano Energy* **2018**, 50, 462.
- [26] C. Capello, U. Fischer, K. Hungerbühler, *Trends Green Chem.* **2007**, 9, 927.
- [27] Z. Song, S. W. Chiang, X. Chu, H. Du, J. Li, L. Gan, C. Xu, Y. Yao, Y. He, B. Li, *J. Appl. Polym. Sci.* **2018**, 135, 45787.
- [28] F. D. Hardcastle, I. E. Wachs, *J. Phys. Chem. C: Nanomater. Interfaces* **1991**, 95, 5031.
- [29] J.-C. Panitz, A. Wokaun, *J. Phys. Chem. C: Nanomater. Interfaces* **1996**, 100, 18357.
- [30] P. Shvets, O. Dikaya, K. Maksimova, A. Goikhman, *J. Raman Spectrosc.* **2019**, 50, 1226.
- [31] S.-H. Lee, H. M. Cheong, M. J. Seong, P. Liu, C. E. Tracy, A. Mascarenhas, J. R. Pitts, S. K. Deb, *Solid State Ionics* **2003**, 165, 111.
- [32] A. C. Ferrari, J. Robertson, *Phys. Rev. B* **2000**, 61, 14095.
- [33] L. M. Bellan, J. Kameoka, H. G. Craighead, *Nanotechnology* **2005**, 16, 1095.
- [34] X. Liu, R. Liu, L. Zeng, X. Huang, X. Chen, C. Zheng, Y. Xu, Q. Qian, M. Wei, Q. Chen, *New J. Chem.* **2017**, 41, 5380.
- [35] Y. Sun, S. Jiang, W. Bi, C. Wu, Y. Xie, *J. Power Sources* **2011**, 196, 8644.
- [36] Y. Dong, R. Ma, M. Hu, H. Cheng, J.-M. Lee, Y. Y. Li, J. A. Zapien, *J. Power Sources* **2014**, 261, 184.

ADVANCED SUSTAINABLE SYSTEMS

Supporting Information

for *Adv. Sustainable Syst.*, DOI: 10.1002/adsu.202200373

Mechanically Stable, Binder-Free, and Free-Standing
Vanadium Trioxide/Carbon Hybrid Fiber Electrodes for
Lithium-Ion Batteries

*Behnoosh Bornamehr, Markus Gallej, Samantha
Husmann, and Volker Presser**

**Mechanically stable, binder-free, and free-standing
vanadium trioxide/carbon hybrid fiber electrodes for lithium-ion batteries**

Behnoosh Bornamehr^{1,2}, Markus Gallei,^{3,4} Samantha Husmann¹, Volker Presser^{1,2,3*}

¹ *INM – Leibniz Institute for New Materials, D2 2, 66123, Saarbrücken, Germany*

² *Department of Materials Science & Engineering, Saarland University, Campus D2 2, 66123 Saarbrücken, Germany*

³ *Saarene – Saarland Center for Energy Materials and Sustainability, 66123 Saarbrücken, Germany*

⁴ *Department of Chemistry, Saarland University, Campus D4 2, 66123 Saarbrücken, Germany*

* Corresponding author: volker.presser@leibniz-inm.de

Section S1: Characterization of heat treated fibers

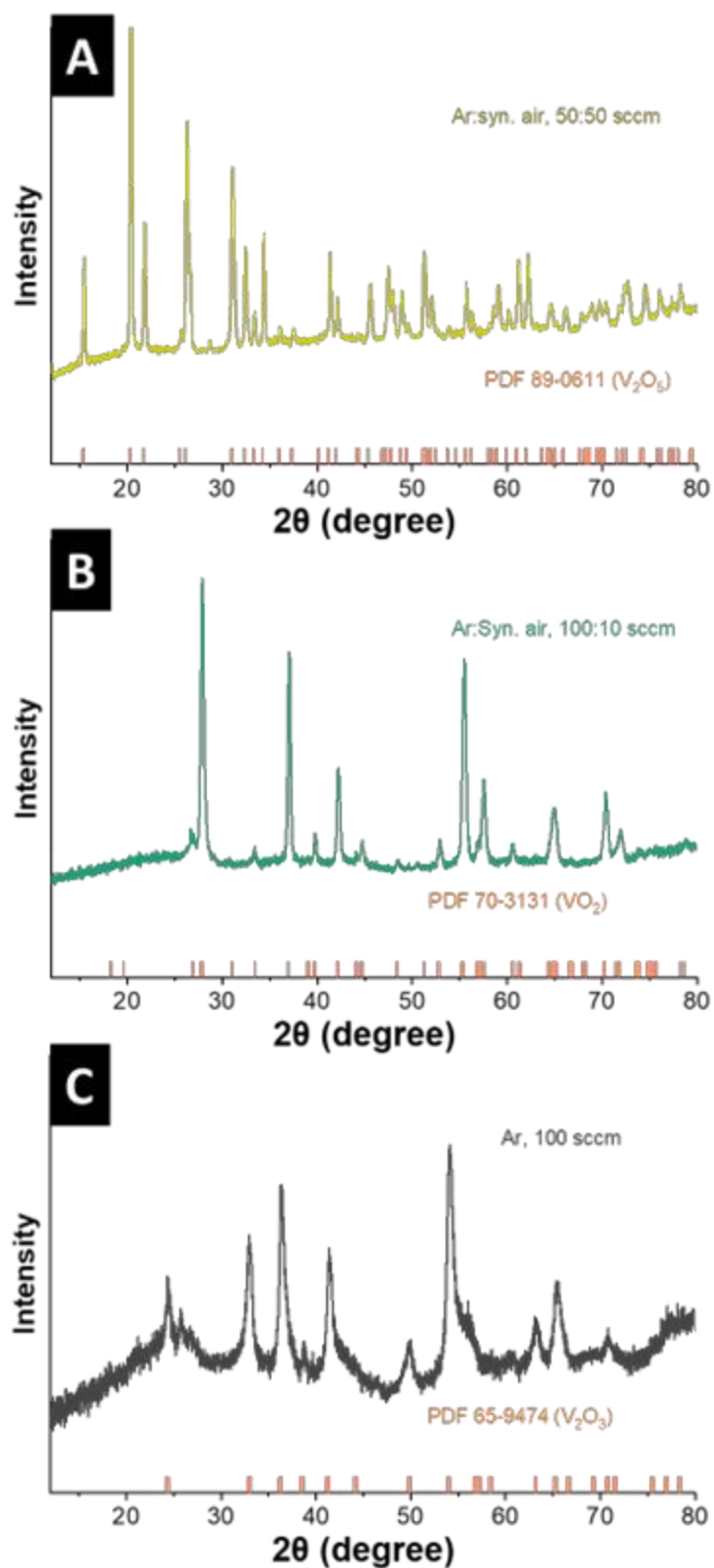


Figure S1. X-ray diffractograms of fibers after treatment for 30 min at 400 °C under gas flow of A) 50:50 sccm Ar: synthetic air, B) 100:10 sccm Ar: synthetic air, and C) 100 sccm Ar.

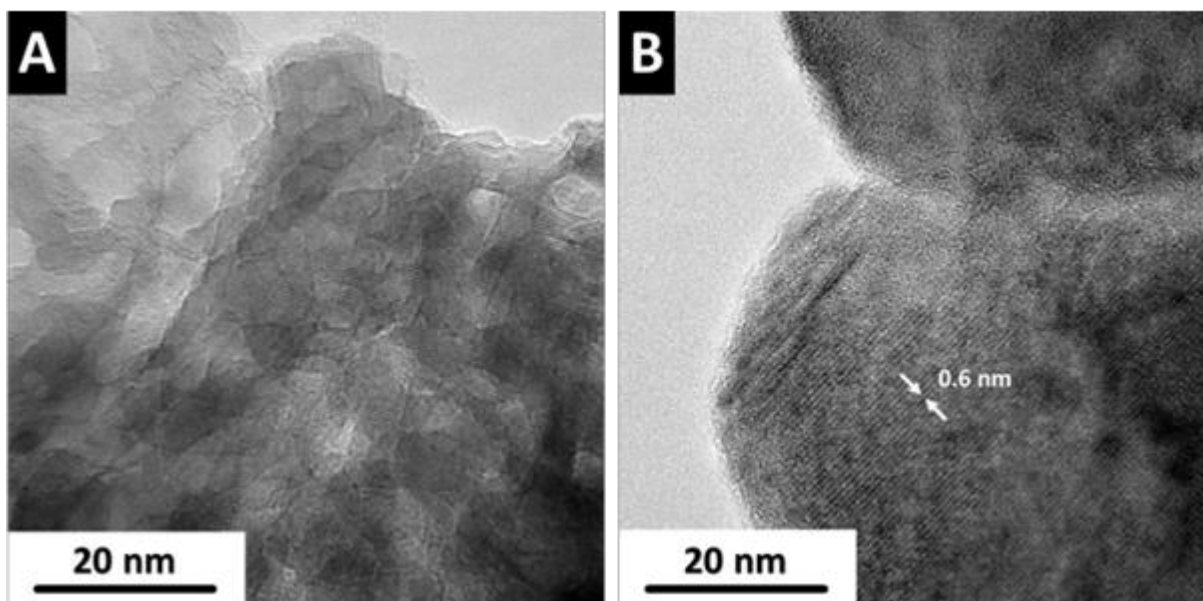


Figure S2. A-B) Transmission electron micrographs of IRF-400 showing nanocrystalline particles of V_2O_3 and amorphous polymer coating.

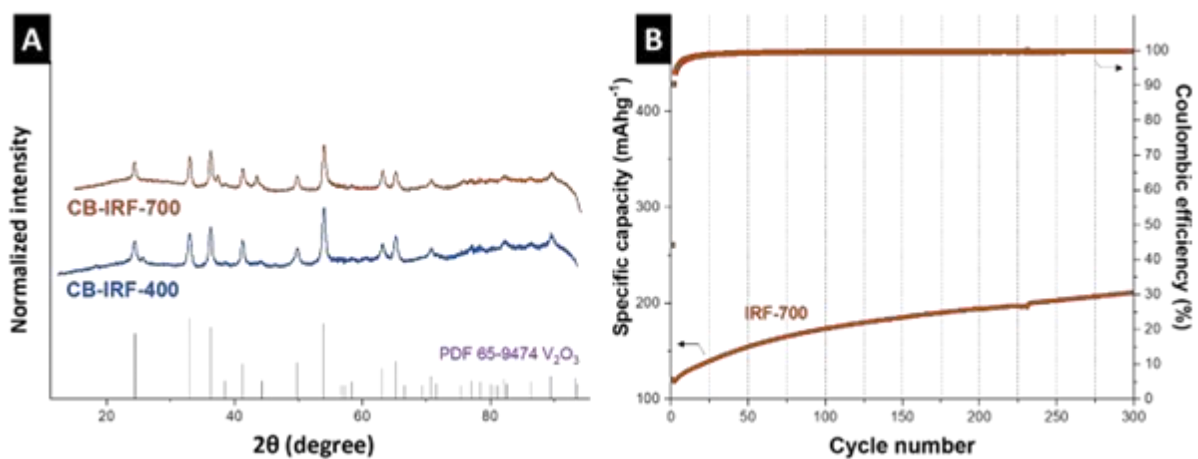


Figure S3. A) X-ray diffractograms of CB-IRF-400 and CB-IRF-700 compatible with V_2O_3 pattern. B) Stability performance of IRF-700 under current rate of 250 mA g^{-1} .

Section S2: Post mortem analysis – scanning electron micrographs

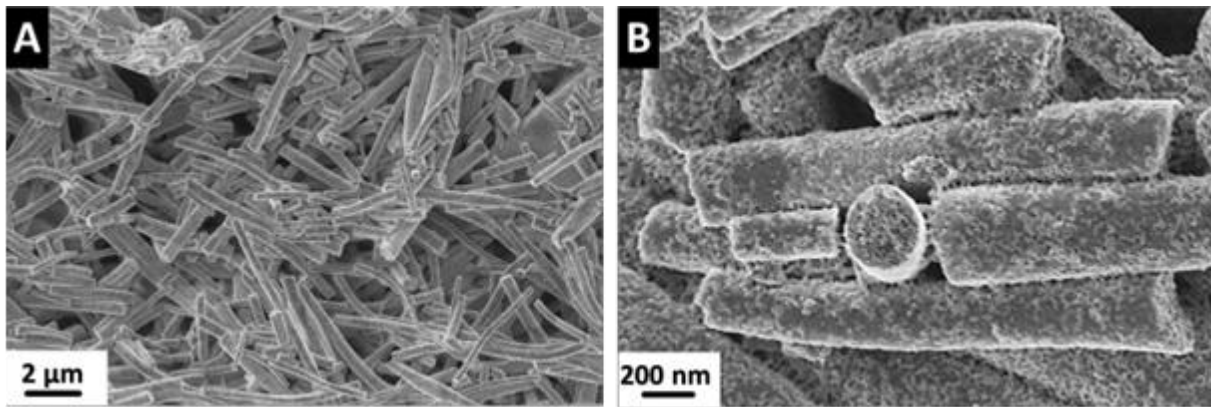


Figure S4. A-B) Scanning electron micrographs of post mortem IRF-400.

Supporting Videos:

S1: Mechanical test of the fiber disc done by the testing setup

S2: Illustration of mechanical flexibility by manual handling

Recent advances in nanoengineering of electrode-electrolyte interfaces to realize high-performance Li-ion batteries

Na-Yeong Kim^{1,†}, Ilgyu Kim^{1,†}, Behnoosh Bornamehr^{2,3}, Volker Presser^{2,3,4}, Hiroyuki

Ueda^{5,6}, Ho-Jin Lee¹, Jun Young Cheong^{7,*}, Ji-Won Jung^{1,*}

¹ School of Materials Science and Engineering, University of Ulsan, Techno saneop-ro 55 beon-gil, Nam-gu, Ulsan 44776, Republic of Korea

² INM – Leibniz Institute for New Materials, Campus D22, 66123 Saarbrücken, Germany

³ Department of Materials Science and Engineering, Campus D22, 66123 Saarbrücken, Germany

⁴ saarene – Saarland Center for Energy Materials and Sustainability, Campus C42, 66123 Saarbrücken, Germany

⁵ Institute for Frontier Materials (IFM), Deakin University, 221 Burwood Highway, Burwood Victoria 3125, Australia

⁶ Battery Technology Research and Innovation Hub (BatTRI-Hub), Deakin University, 5/154 Highbury Road, Burwood, Victoria 3125, Australia

⁷ Bavarian Center for Battery Technology (BayBatt) and Department of Chemistry, University of Bayreuth, Universitätsstraße 30, 95447 Bayreuth, Germany

Citation:

Kim, N.Y., Kim, I., Bornamehr, B., Presser, V., Ueda, H., Lee, H.J., Cheong, J.Y. and Jung, J.W., 2023. Recent advances in nanoengineering of electrode-electrolyte interfaces to realize high-performance Li-ion batteries. *Energy & Environmental Materials*, p.e12622.

Own contributions:

Writing – review and editing

Recent Advances in Nanoengineering of Electrode-Electrolyte Interfaces to Realize High-Performance Li-Ion Batteries

Na-Yeong Kim, Igyu Kim, Behnoosh Bornamehr, Volker Presser*, Hiroyuki Ueda, Ho-Jin Lee, Jun Young Cheong* , and Ji-Won Jung*

A suitable interface between the electrode and electrolyte is crucial in achieving highly stable electrochemical performance for Li-ion batteries, as facile ionic transport is required. Intriguing research and development have recently been conducted to form a stable interface between the electrode and electrolyte. Therefore, it is essential to investigate emerging knowledge and contextualize it. The nanoengineering of the electrode-electrolyte interface has been actively researched at the electrode/electrolyte and interphase levels. This review presents and summarizes some recent advances aimed at nanoengineering approaches to build a more stable electrode-electrolyte interface and assess the impact of each approach adopted. Furthermore, future perspectives on the feasibility and practicality of each approach will also be reviewed in detail. Finally, this review aids in projecting a more sustainable research pathway for a nanoengineered interphase design between electrode and electrolyte, which is pivotal for high-performance, thermally stable Li-ion batteries.

1. Introduction

Since their initial commercialization by Sony in the 1990s, lithium-ion batteries (LIBs) have attracted significant attention and are utilized in various applications, ranging from portable electronics to electric vehicles.^[1–5] The impact of the LIB was also honored by the selection of the 2019 Nobel Prize in Chemistry^[6] and has become one of the most successful recent technologies in our daily lives. The interface and interphase between the electrode and electrolyte have been critical factors in the past and current LIBs since they affect the performance, from cycle retention to rate capability.^[7–10] It is indispensable to have a stable electrode/electrolyte interface at both cathode^[11] and anode^[12] since Li^+ ions reversibly move between the anode and cathode, and an unstable interface in either of the electrodes is detrimental to the electro-

chemical performance of LIBs.

Various factors affect the quality of the interface and interphase between electrode and electrolyte.^[13–15] For instance, various additives in the electrolyte greatly affect the interphase between the electrode and electrolyte,^[16,17] as even a minute change in the types of chemicals used in the electrolyte leads to the formation of interphase with varied composition. There is also a difference between liquid and gel/solid-state electrolytes (SSEs),^[18] where the formed interface between the electrode and electrolyte shows distinct physicochemical properties.

The composition of the electrode-electrolyte interface depends on the chemical mixing of the electrolyte with the cathode and the reduction stability of the electrolyte with Li metal.^[19] For example, when the LiCoO_2 cathode is paired with a garnet-type $\text{Li}_7\text{La}_3\text{Zr}_2\text{O}_{12}$ solid-state electrolyte, the resulting interface may include Li_2CO_3 , La_2O_3 , and $\text{La}_2\text{Zr}_2\text{O}_7$. When a $\text{Li}_2\text{S-P}_2\text{S}_5$ electrolyte is used, the chemical reaction products at the $\text{LiCoO}_2|\text{Li}_2\text{S-P}_2\text{S}_5$ interface may include transition-metal sulfides (such as Co_9S_8 , Mn_2S_3 , Ni_3S_4 , CoNi_2S_4) and polyanions such as PO_4^{3-} and SO_4^{2-} . At the $\text{Li}|\text{solid-state electrolyte (SSE)}$ interface, the reduction decomposition can lead to chemical reaction products such as Li_xS , Li_yP , and Li_zGe (which can form at the $\text{Li}|\text{Li}_{3.25}\text{Ge}_{0.25}\text{P}_{0.75}\text{S}_4$ (LGPS) interface). The electrolyte has a pivotal role in determining whether the interface between the electrode and electrolyte is suitable. In addition to the electrolyte, electrochemical reaction parameters are essential to investigate. For example, the formation cycle(s) condition the morphology and composition of the interphase between the

N.-Y. Kim, I. Kim, H.-J. Lee, Prof. J.-W. Jung
School of Materials Science and Engineering, University of Ulsan, Techno saneop-ro 55 beon-gil, Nam-gu, Ulsan 44776, Korea
E-mail: jwjung4@ulsan.ac.kr
B. Bornamehr, Prof. Dr. V. Presser
INM – Leibniz Institute for New Materials, Campus D22 66123, Saarbrücken Germany
Department of Materials Science and Engineering, Campus D22 66123, Saarbrücken Germany
E-mail: volker.presser@leibniz-inm.de
Prof. Dr. V. Presser
saarene – Saarland Center for Energy Materials and Sustainability, Campus C42 66123, Saarbrücken Germany
Dr. H. Ueda
Institute for Frontier Materials (IFM), Deakin University, 221 Burwood Highway, Burwood Victoria 3125, Australia
Battery Research and Innovation Hub, Deakin University, 5/154 Highbury Road, Burwood Victoria 3125, Australia
Dr. J. Y. Cheong
Bavarian Center for Battery Technology (BayBatt) and Department of Chemistry, University of Bayreuth, Universitätsstraße 30 95447, Bayreuth Germany
E-mail: jun.cheong@uni-bayreuth.de
 The ORCID identification number(s) for the author(s) of this article can be found under <https://doi.org/10.1002/eem2.12622>.

DOI: 10.1002/eem2.12622

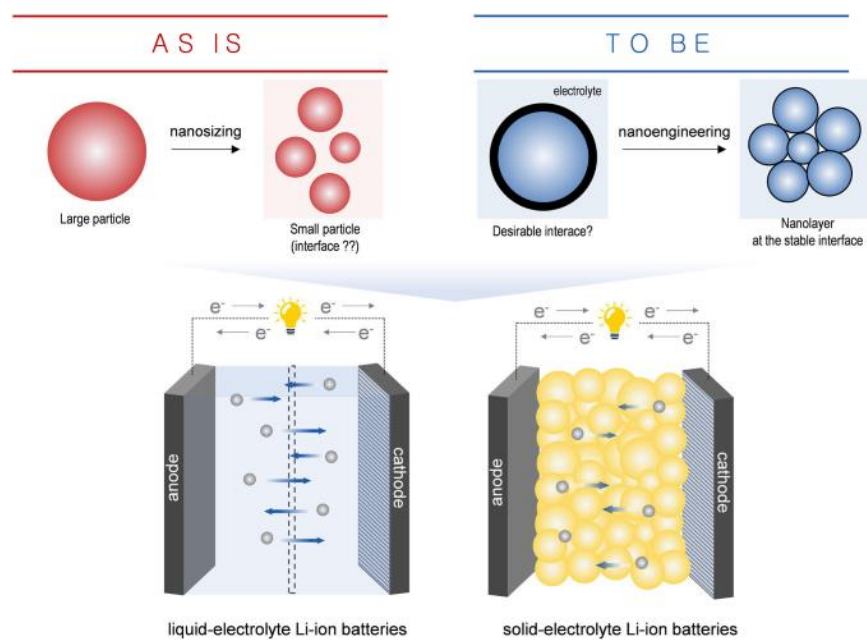


Figure 1. Schematic illustration of a desirable, nanoengineered interface between (electrode and electrode) or (electrode and electrolyte) for liquid- and solid-electrolyte Li-ion batteries.

electrolyte and electrode, where current density in the formation cycle plays a significant role in the interphase between the electrode and electrolyte, hence the electrochemical performance.^[20,21] From a recent study,^[22] electrode materials with smaller particle sizes (240 nm in the study) showed comparably good electrochemical performance compared with a particle size of 810 nm in liquid and gel-like electrolytes, where the formation of various by-products from the electrolyte degradation did not significantly affect the electrochemical performance of smaller particle sizes. This shows that the size of the electrode material particles can be a dominant factor. Nevertheless, as the interface between the electrode and electrolyte involves many factors, it is essential to control the variables to optimize the interface further. So far, most of the adopted approaches were aimed at tuning the surface characteristics of electrode material and/or electrolyte, which need to be summarized and explained further. We focused on and dealt with the interface ‘as is’ and ‘to be’ for liquid- and solid-electrolyte Li-ion batteries in this review (Figure 1).

2. Surface Modification of Interface in Electrode Materials by Nanoscale Layer

2.1. Cathode

The ever-increasing demand for rechargeable battery systems with faster charging and extended utilization requires cathode material with superior rate capabilities and cycle retention. Nanoengineered surface modification of cathode has been extensively carried out^[23] as it leads to enhanced cycle life^[24,25] and superior rate capabilities.^[26,27] In recent years, more in-depth and creative research on improving the cathode capacity has occurred by employing organic and inorganic nanoengineered surficial layers,^[24,25] which made significant research advances.

Several nanoengineered inorganic surficial layers were adopted to realize rechargeable batteries with higher energy and power density. For instance, Song et al.^[28] reported on employing a nano- AlPO_4 coating layer for $\text{Li}_{1.15}\text{Ni}_{0.17}\text{Co}_{0.11}\text{Mn}_{0.57}\text{O}_2$, enhancing the capacity. Such coating processes employ a facile in situ dispersion process, filtering, drying, and heat treatment, where heat treatment condition plays an important role in modulating the electrochemical properties of $\text{Li}_{1.15}\text{Ni}_{0.17}\text{Co}_{0.11}\text{Mn}_{0.57}\text{O}_2$. Figure 2a shows the X-ray diffractograms of the AlPO_4 -coated cathode at various heat treatment conditions, where no apparent change in the overall crystallinity was seen. Based on the elemental mapping (Figure 2b), AlPO_4 is seen on the cathode’s surface. Cycle retention (Figure 2c) and rate capabilities (Figure 2d) highlight the importance of heat treatment temperature on overall electrochemical performance: nano- AlPO_4 coating layer (at 400 °C) for $\text{Li}_{1.15}\text{Ni}_{0.17}\text{Co}_{0.11}\text{Mn}_{0.57}\text{O}_2$ (A-400) exhibits the best electrochemical performance, where the heating temperature has a significant effect on initial Coulombic efficiency, capacity decay per

cycle, and cycle retention at various C-rates. Effective coating of AlPO_4 led to surface protection of $\text{Li}_{1.15}\text{Ni}_{0.17}\text{Co}_{0.11}\text{Mn}_{0.57}\text{O}_2$, which significantly minimizes the formation of reaction by-products (LiF and LiPO_4F_2) shown by 50 cycles of charge and discharge. Similar to this concept, the hybrid surface coating was employed for $\text{LiNi}_{0.8}\text{Co}_{0.1}\text{Mn}_{0.1}\text{O}_2$ cathode using Li_3PO_4 and carbon nanotube (CNT).^[29] Here, the role of Li_3PO_4 and CNT is to improve ionic and electronic conductivity simultaneously, significantly enhancing overall electrochemical performance. Li_3PO_4 coating layer with 4 nm was deposited on NCM, and such a thin nanoscale coating layer allows facile ionic and electronic transport and ensures chemical stability against more extended exposure to air. With effective surface protection from HF corrosion, the structural integrity was well maintained for $\text{LiNi}_{0.8}\text{Co}_{0.1}\text{Mn}_{0.1}\text{O}_2$ cathode with Li_3PO_4 and CNT coating (CNT-LPO-NCM) (Figure 2e). In contrast, the pristine $\text{LiNi}_{0.8}\text{Co}_{0.1}\text{Mn}_{0.1}\text{O}_2$ cathode shows (006)/(102) and (108)/(110) split peaks that are amalgamated, indicating changes in crystalline structures (Figure 2f). Such progressive structure destruction led to a higher metal ion concentration in the electrolyte (Ni, Co, Mn) which further suggests the superior electrolyte stability for CNT-LPO-NCM. The practical role of Li_3PO_4 was also demonstrated for another cathode material (NMC811),^[30–33] where it suppresses electrolyte side reactions while alleviating crack formation after numerous cycling. For the NCM cathode (NMC811), the effects of three typical ionic conductors (Li_3PO_4 , Li_2ZrO_3 , $\text{Li}_4\text{Ti}_5\text{O}_{12}$) were further compared.^[34] The electronic and ionic conductivity improved when Li_3PO_4 was coated, leading to superior rate capabilities. Other metal oxide materials were also adopted for surface modification of the cathode, some of which include $\text{Li}_{1.4}\text{Al}_{0.4}\text{Ti}_{1.6}(\text{PO}_4)_3$,^[35,36] LiInO_2 ,^[37] Al_2O_3 ,^[38–40] Al_2O_3 and LiAlO_2 ,^[41] ZrO_2 ,^[42] LiNbO_3 ,^[43] tungsten oxide,^[44] Li_4SiO_4 ,^[45] Li_3VO_4 ,^[46] TiO_2 ,^[47] Y_2O_3 ,^[48] and SnO_2 ,^[49] and can be used for nanoscale modification in the interphase between cathode and electrolyte. Different methods for stabilizing the metal oxide coatings can be used, such as sol-gel,^[41] atomic layer

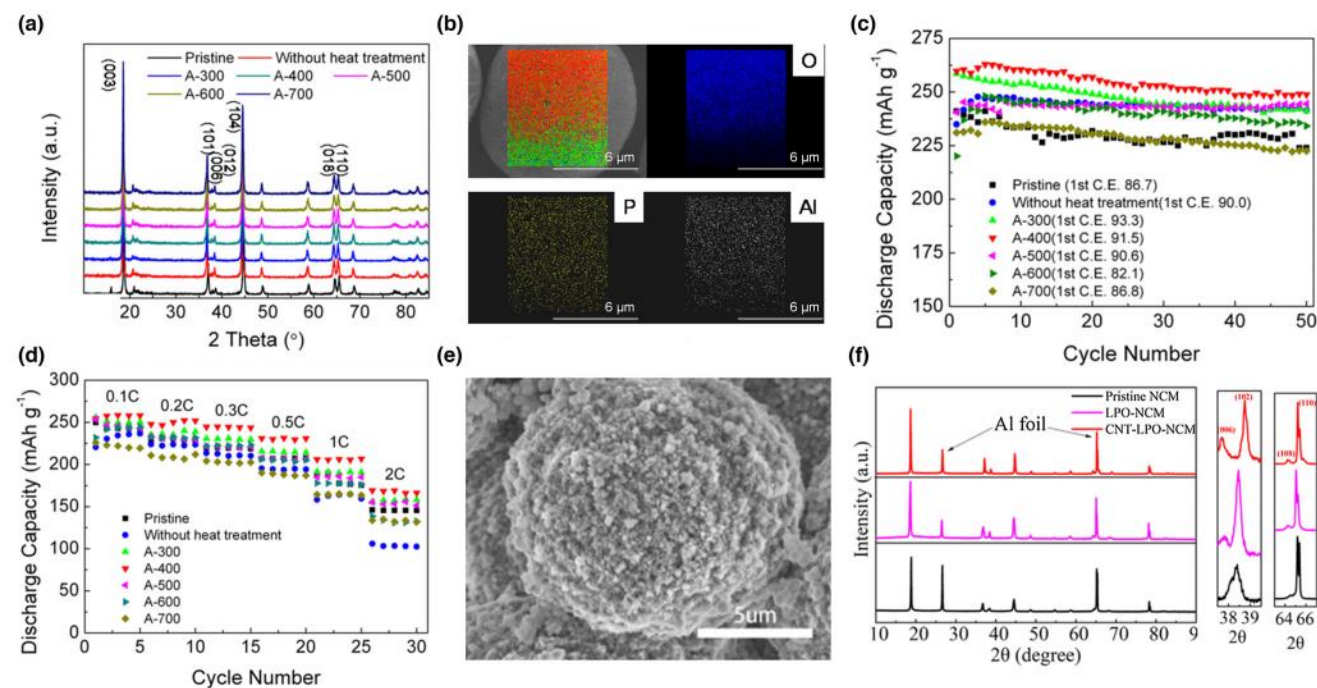


Figure 2. Microstructure and electrochemical performance of cathode with surface modification. a) X-ray diffractograms of 1% nano- AlPO_4 coated cathode at various heat treatment conditions. b) Elemental mapping of nano- AlPO_4 coated cathode at 400 °C. c) Cycle retention characteristics, and d) rate capabilities of various cathode samples. Reproduced with permission.^[28] Copyright 2018, American Chemical Society. e) Scanning electron micrograph of CNT-LPO-NCM after 150 cycles. f) X-ray diffractograms of respective samples after 100 cycles. Reproduced with permission.^[29] Copyright 2019, American Chemical Society.

deposition,^[45] co-precipitation,^[48] and milling procedures such as plasma-assisted milling,^[49] and ball-milling.^[46] Usually, the aim is to deposit a Li-containing phase due to its ionic conductivity so it does not impair the rate capability. Finding the optimum coating thickness is critical for a positive effect, and thicker coatings can impede diffusion^[28] and decrease lattice matching.^[48] In most works, the improvement in the performance is correlated to the protection of the cathode material from HF attack, which is referred to as HF scavenging and restriction of direct electrode/electrolyte contact.^[38–40] This protective effect is greater at higher potentials and temperatures, at which the cathode metals are more likely to dissolve in the electrolyte.^[43] By this protection, these phases also lower the interfacial impedance,^[47] and maintain a gradual potential slope, combating the polarization at the interface.^[35,36] and increasing the charge cut-off voltage.^[44]

In addition to metal oxides, metallic coatings have also shown considerable improvement in electrochemical performance regarding cycle retention and rate capabilities. For instance, highly stabilized $\text{LiNi}_{0.815}\text{Co}_{0.15}\text{Al}_{0.035}\text{O}_2$ secondary particles were achieved by introducing molybdenum (Mo),^[50] which induces a Li_2MoO_4 layer on the outer part and epitaxially grown NiO-like surface. Such coatings give rise to three critical characteristics: i) suppression of cathode-electrolyte side reactions, ii) prevention of structural degradation, and iii) minimization of intergranular cracking. Just with 1 mol % of surficial Mo coating, it shows outstanding rate capabilities (140 mAh g^{-1} at 10C) and cycle retention characteristics (95.7% at 5C after 250 cycles). In addition to Mo, other metals/metal halides and metal sulfides were also doped on the surface of cathodes, such as Zr,^[51,52] MoS_2 ,^[53] LiAlF_4 ,^[54] and S.^[55] Moreover, co-doping of metals and/or metal sulfides/halides were also

adopted to improve the electrochemical performance, such as Na and F,^[56] Cd and S,^[57] and F and LiF.^[58] Instead of using similar elements/compounds, metal and metal oxide surficial modifications were employed simultaneously for some cathodes, including Ti and $\text{La}_4\text{Ni-LiO}_8$.^[59] With a significant change in structural features, a double-shell hybrid nanostructure was also employed for electrochemical performance, the example of which is combining a Li_2SiO_3 coating layer and a cation-mixed layer ($\text{Fm}\bar{3}\text{m}$ phase) and coating them on the surface of NCM811.^[60] With the introduction of a Li_2SiO_3 coating layer (<10 nm), cation-mixed layer increased from 1–2 nm to 5–6 nm, which led to the interfacial stability and structural integrity. Carbon@spinel@layered@spinel@carbon shells that were employed for Li-rich layered oxides,^[61] retaining discharge capacities of 228 and 196 mAh g^{-1} at 1C and 5C, respectively, after 200 cycles. These multi-layer coatings aim to improve the electrochemical performance by increasing the ionic transport, and improving the structural stability.

In addition to the above-mentioned inorganic species, polymer coatings have also been employed to overcome the shortcomings of the inorganic coating layer. For example, constructing a poly(acrylonitrile-co-butadiene) surface layer on a $\text{LiNi}_{0.6}\text{Mn}_{0.2}\text{Co}_{0.2}\text{O}_2$ cathode significantly improved electrochemical performance.^[62] Here, the polymeric surficial layer suppresses side reactions by enlarging the physical contact at solid electrode/solid electrolyte interfaces from points to larger areas during the cycling process and decreasing the interfacial resistance. This resulted in higher cycle retention (75% cycle retention over 400 cycles) and rate capabilities (99 mAh g^{-1} at a rate of 3C) compared to the unprotected cathode. Similarly, a protective conductive polymer (poly(3,4-ethylene dioxithiophene)) was used to coat Ni-rich cathodes

highly conformally.^[63] As a result, it facilitates the transfer of ions and electrons, suppresses the undesired layered to spinel/rock-salt phase transformation, and mitigates intergranular/intragranular mechanical cracking.^[63] In addition, other conductive polymers, such as polyaniline (PANI), have been used as a coating to create a physical barrier between the cathode and the electrolyte.^[64] A 5–7 nm thin PANI layer was uniformly coated onto the Ni-rich NCM811, which effectively hindered side reaction and improved the interface between electrode and electrolyte. PANI has also been co-polymerized with ionically conductive poly(ethylene glycol) to create a homogeneous coating.^[65] A homogeneous and amorphous layer with a thickness of 25–30 nm and 30–35 nm was observed with PANI and PANI/poly(ethylene glycol) composite film, which was sufficient to ensure high ionic conductivity and maintain structural integrity. In contrast to the inorganic coating, these organic counterparts can mitigate the volumetric expansion during cycling, avoid pulverization, and increase the mechanical stability of the cathode material due to their flexibility.^[65] On top of these research advances, Yoon et al.^[66] recently reported a nano-scale Co_xB protective layer on the surface and grain boundary of NCM, which greatly improved the electrochemical performance. This work is important in that interface was controlled at the grain boundary level, where uniform interfaces in both grain boundary and boundaries between primary particles cathode are also necessary to ensure enhanced electrochemical performance.

In summary, inorganic and organic nanoscale coating layers were used for the cathode, and some hybrid inorganic/organic surficial coating layers have been explored. The thickness of the nanoengineered layer was usually below 10 nm, a thin layer that prevented side reactions and contributed to enhanced interfacial stability while allowing facile ionic transport since ionic conductivity is indispensable for the electrochemical performance of the cathode. Many of these studies hint at the importance of nanoscale interfacial engineering on the cathode part, significantly improving the electrochemical performance and properties.

2.2. Anode

From a practical perspective, surface modifications must be applied to micrometer-sized anode particles in contrast to the nanosized anode particles, as the former exhibits higher tap density. For example, Wang et al.^[67] deposited a thin Si coating followed by a graphene cage on Si microparticles (Mp-Si@Si@G), which greatly enhanced the interface between anode and electrolyte and enhanced the electrochemical performance. The Si coating was about 100 nm thick, while the outermost graphene cage coating was only ~7 nm, which were employed as double layers to alleviate the volume changes of Si effectively. The schematic illustration of the fabrication of Mp-Si@Si@G is presented in **Figure 3a**, which undergoes annealing, etching, Si coating, and graphene coating.

To compare the dynamic changes on the interface of the anode, Si microparticles (pristine sample) and Mp-Si@Si@G were analyzed for in situ transmission electron microscopy analysis (Figure 3b–e). Crack formation is observed in the Si microparticles, which leads to an unstable interface between them and the electrolyte. The interface and structure of Mp-Si@Si@G are well maintained during and after lithiation. It is further verified that Si skin lowers the unfavorable electrolyte/electrode contact area and minimizes SEI layer formation for Mp-Si@Si@G , resulting in much superior cycle retention (Figure 3f).

Although Si is actively researched due to its high theoretical capacity (ten times higher than the theoretical capacity of graphite), other anode materials such as graphite are also researched. Tallman et al.^[68] sputtered Cu and Ni nanoscale layers on the graphite to increase the overpotential for Li deposition, thereby suppressing Li plating under high-rate charge conditions. Deposition overpotential can be increased by modifying the graphite interface, which significantly reduces the quantity of plated Li metal by 50%. Heng et al.^[69] suggested a functional film (nano 2,2-dimethylethenylboronic acid) on natural graphite, which greatly enhanced the cycling stability of graphite when it is assembled in a full cell (with $\text{LiNi}_{0.5}\text{Co}_{0.2}\text{Mn}_{0.3}\text{O}_2$ as a cathode). Although the thickness of the film was only about 20 nm, it built a stable

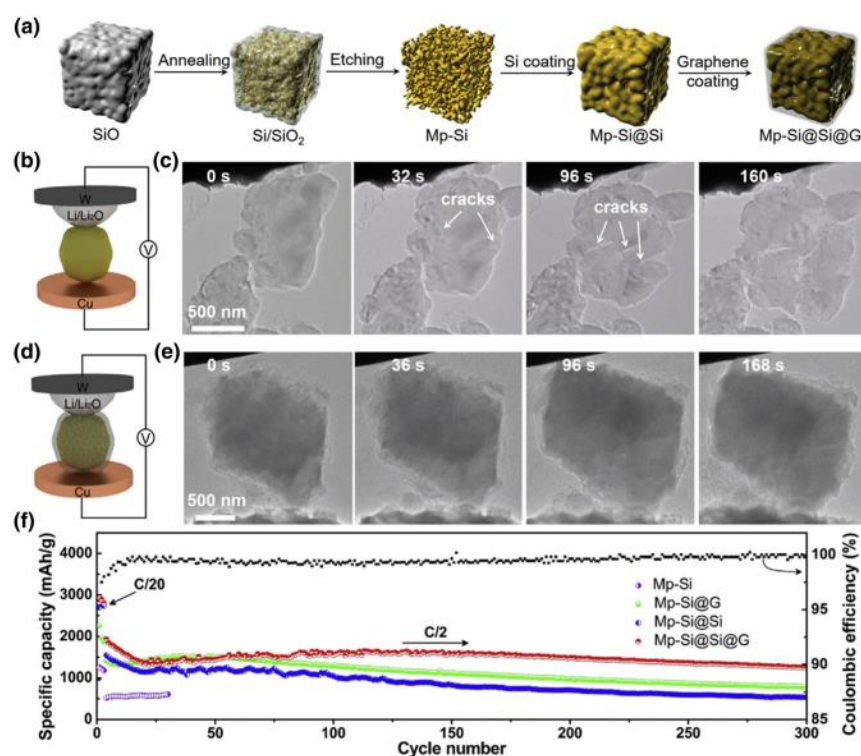


Figure 3. Microstructure and electrochemical performance of anode with surface modification. a) Schematic illustration of the synthesis of graphene cage-encapsulated Si skin-sealed mesoporous Si microparticles (Mp-Si@Si@G). b) Schematic illustration of the in-situ TEM setup for the Si microparticles. c) Time-series TEM snapshots of Si microparticles. d) Schematic illustration of in situ TEM setup of Mp-Si@Si@G . e) Time-series TEM snapshots of Mp-Si@Si@G . f) Capacity retention characteristics of mesoporous Si microparticles (Mp-Si), graphene cage-Si microparticles (Mp-Si@G), Si sealed mesoporous Si (Mp-Si@Si), and Mp-Si@Si@G . Reproduced with permission.^[67] Copyright 2019, Elsevier.

Table 1. Summary of nanoscale layer on electrode materials by surface modification.

Electrode material	Coating material	Method	Layer thickness	References
$\text{Li}_{1.15}\text{Ni}_{0.17}\text{Co}_{0.11}\text{Mn}_{0.57}\text{O}_2$	AlPO_4	Co-precipitation	5–15 nm	[28]
$\text{LiNi}_{0.8}\text{Co}_{0.1}\text{Mn}_{0.1}\text{O}_2$	Li_3PO_4 , carbon nanotube (CNT)	Co-precipitation	4 nm	[29]
$\text{LiNi}_{0.8}\text{Co}_{0.1}\text{Mn}_{0.1}\text{O}_2$	Li_3PO_4	Hydrothermal synthesis	2–4 nm	[34]
$\text{LiNi}_{0.8}\text{Co}_{0.1}\text{Mn}_{0.1}\text{O}_2$	Li_2ZrO_3	Hydrothermal synthesis	2–4 nm	[34]
$\text{LiNi}_{0.8}\text{Co}_{0.1}\text{Mn}_{0.1}\text{O}_2$	$\text{Li}_4\text{Ti}_5\text{O}_{12}$	Hydrothermal synthesis	2–4 nm	[34]
$\text{LiNi}_{0.6}\text{Co}_{0.2}\text{Mn}_{0.2}\text{O}_2$	$\text{Li}_{1.4}\text{Al}_{0.4}\text{Ti}_{1.6}(\text{PO}_4)_3$	Sol–gel method	6 nm	[35]
LiCoO_2	$\text{Li}_{1.4}\text{Al}_{0.4}\text{Ti}_{1.6}(\text{PO}_4)_3$	Solid-state synthesis	~20 nm	[36]
$\text{LiNi}_{0.8}\text{Co}_{0.1}\text{Mn}_{0.1}\text{O}_2$	In_2O_3 & LiInO_2	Co-precipitation	12 nm	[37]
$\text{Li}_{1.256}\text{Ni}_{0.198}\text{Co}_{0.082}\text{Mn}_{0.689}\text{O}_{2.25}$	Al_2O_3	Co-precipitation	3 nm	[38]
$\text{LiNi}_{0.6}\text{Co}_{0.2}\text{Mn}_{0.2}\text{O}_2$	Al_2O_3	Atomic layer deposition	1–4 nm	[39]
$\text{LiNi}_{0.6}\text{Co}_{0.2}\text{Mn}_{0.2}\text{O}_2$, $\text{LiNi}_{0.8}\text{Co}_{0.15}\text{Al}_{0.05}\text{O}_2$	Al_2O_3	Atomic layer deposition	5–10 nm	[40]
$\text{LiNi}_{0.6}\text{Co}_{0.2}\text{Mn}_{0.2}\text{O}_2$	LiAlO_2	Sol–gel method	1 nm	[41]
$\text{LiNi}_{0.6}\text{Co}_{0.2}\text{Mn}_{0.2}\text{O}_2$	ZrO_2	Solvothermal synthesis/ball-milling	5 nm	[42]
$\text{LiNi}_{0.8}\text{Co}_{0.1}\text{Mn}_{0.1}\text{O}_2$	LiNbO_3	Co-precipitation	5–6 nm	[43]
$\text{LiNi}_{0.8}\text{Co}_{0.1}\text{Mn}_{0.1}\text{O}_2$	$\text{Li}_2\text{WO}_4/\text{WO}_3$	Sol–gel method	—	[44]
$\text{LiNi}_{0.8}\text{Co}_{0.15}\text{Al}_{0.05}\text{O}_2$	Li_4SiO_4	Co-precipitation/solid-state method	2–5 nm	[45]
$\text{LiNi}_{0.6}\text{Co}_{0.2}\text{Mn}_{0.2}\text{O}_2$	Li_3VO_4	Ball-milling	6–10 nm	[46]
$\text{LiNi}_{0.6}\text{Mn}_{0.2}\text{Co}_{0.2}\text{O}_2$	TiO_2	Atomic layer deposition	—	[47]
$\text{Li}_{1.2}\text{Mn}_{0.54}\text{Ni}_{0.13}\text{Co}_{0.13}\text{O}_2$	Y_2O_3	Co-precipitation	5–10 nm	[48]
$\text{LiNi}_{0.5}\text{Co}_{0.2}\text{Mn}_{0.3}\text{O}_2$	SnO_2	Plasma-assisted ball-milling	—	[49]
$\text{LiNi}_{0.5}\text{Co}_{0.2}\text{Mn}_{0.3}\text{O}_2$	Li_2MoO_4	Co-precipitation	—	[50]
$\text{LiNi}_{0.8}\text{Co}_{0.1}\text{Mn}_{0.1}\text{O}_2$	Li_2ZrO_3	Co-precipitation	—	[51]
LiNiO_2	Li_2ZrO_3	Co-precipitation	5–10 nm	[52]
$\text{LiNi}_{0.8}\text{Co}_{0.1}\text{Mn}_{0.1}\text{O}_2$	MoS_2	Co-precipitation	14–16 nm	[53]
$\text{Li}_{1.2}\text{Ni}_{0.2}\text{Mn}_{0.6}\text{O}_2$	LiAlF_4	Co-precipitation	5 nm	[54]
$\text{LiNi}_{0.5}\text{Mn}_{1.5}\text{O}_4$	S	Co-precipitation	—	[55]
$\text{LiNi}_{0.6}\text{Co}_{0.2}\text{Mn}_{0.2}\text{O}_2$	Na, F	Co-precipitation	—	[56]
$\text{Li}_{1.2}\text{Ni}_{0.2}\text{Mn}_{0.6}\text{O}_2$	Cd, S	Co-precipitation	—	[57]
$\text{LiNi}_{0.5}\text{Co}_{0.2}\text{Mn}_{0.3}\text{O}_2$	F, LiF	Co-precipitation	—	[58]
$\text{LiNi}_{0.8}\text{Co}_{0.1}\text{Mn}_{0.1}\text{O}_2$	Ti, $\text{La}_4\text{NiLiO}_8$	Co-precipitation	—	[59]
$\text{LiNi}_{0.8}\text{Co}_{0.1}\text{Mn}_{0.1}\text{O}_2$	Li_2SiO_3	Co-precipitation	—	[60]
$\text{LiNi}_{0.8}\text{Co}_{0.1}\text{Mn}_{0.1}\text{O}_2$	Carbon, LiMn_2O_4	Co-precipitation	100 nm	[61]
$\text{LiNi}_{0.6}\text{Mn}_{0.2}\text{Co}_{0.2}\text{O}_2$	Poly(acrylonitrile-co-butadiene) (PAB)	UV polymerization	~10 nm	[62]
$\text{LiNi}_{0.33}\text{Co}_{0.33}\text{Mn}_{0.33}\text{O}_2$, $\text{LiNi}_{0.85}\text{Co}_{0.1}\text{Mn}_{0.05}\text{O}_2$, $\text{Li}_{1.2}\text{Mn}_{0.54}\text{Ni}_{0.13}\text{Co}_{0.13}\text{O}_2$	Poly(3,4-ethylenedioxythiophene) (PEDOT)	Chemical vapor deposition	7–28 nm	[63]
$\text{LiNi}_{0.8}\text{Co}_{0.1}\text{Mn}_{0.1}\text{O}_2$	Poly(vinylpyrrolidone) (PVP), Polyaniline (PANI)	Co-precipitation	5–7 nm	[64]
$\text{LiNi}_{0.8}\text{Co}_{0.1}\text{Mn}_{0.1}\text{O}_2$	Polyaniline (PANI), Polyethylene glycol (PEG)	Co-precipitation	25–35 nm	[65]
$\text{LiNi}_{0.8}\text{Co}_{0.1}\text{Mn}_{0.1}\text{O}_2$	Co_xB	Co-precipitation	~5 nm	[66]
Si	Si, Graphene	Ball-milling, Chemical vapor deposition	107 nm	[67]

SEI layer on the graphite through the in-situ self-polymerization of nano 2,2-dimethylethenylboronic acid molecules. These works demonstrate that the nanoscale surface protection layer helps to build a more stable interface between electrode and electrolyte.

Surface modification was also adopted for Li metal, which exhibits high theoretical capacity (3860 mAh g^{-1}), low density (0.534 g cm^{-3}), and low electrical potential (-3.04 V vs. standard hydrogen electrode).^[66] Li dendrite growth, rupture of the SEI layer, and formation of dead Li contribute to the rapid decay in the electrochemical performance of Li metal,^[70] and some approaches were aimed at tuning the surface properties of Li metal. For instance, a 20-nm-thin Al_2O_3 layer was coated onto the Li metal by sputter coating, which is a simple coating method.^[71] The ionic conductivity of LiAlO_2 was measured as $10^{-7} \text{ S cm}^{-1}$, providing both surface chemical stability and suppression of dendritic growth. Chen et al.^[72] employed LiF coating on Li metal by atomic layer deposition, where a thickness of 8 nm was achieved. Crystalline LiF films achieved a shear modulus of 58 GPa, which is seven times higher than the sufficient value to prevent Li dendritic growth. LiF coating led to a stable Coulombic efficiency of 99.5% over 170 years. In addition to single-layer surface protection, a dual-layer film (organic components such as ROCO_2Li and ROLi on top

(estimated to be 25 nm) and inorganic components such as Li_2CO_3 and LiF on the bottom (estimated to be 50 nm)) was coated onto the Li metal to protect it from the corrosion and regulate the uniform deposition of Li.^[73] It led to a dendrite-free deposition of Li metal, longer cycling stability in symmetric and asymmetric cells, and smaller interfacial polarization (360 mV for dual-layer-film-coated Li metal and 590 mV for reference at a current density of 5.0 mA cm^{-2}). In contrast to surface modification (nanoscale surficial layer) on the cathode, the thickness of the surficial layer on the anode tends to be much larger (sometimes sub-micrometer scale: 100 nm; **Table 1**). Such thicker nanolayers can be attributed to the fact that anode materials (such as Si) tend to undergo massive volume changes ($>300\%$) and morphological evolution (such as the formation of Li dendrites), where thicker nanoscale interphase between electrode and electrolyte is desired.

2.3. Solid Electrolyte

Several recent studies provide an optimized interface between electrodes and the electrolyte through solid electrolyte modification. Among various types of solid electrolytes, $\text{Li}_7\text{La}_3\text{Zr}_2\text{O}_{12}$ (LLZO) is one of the most

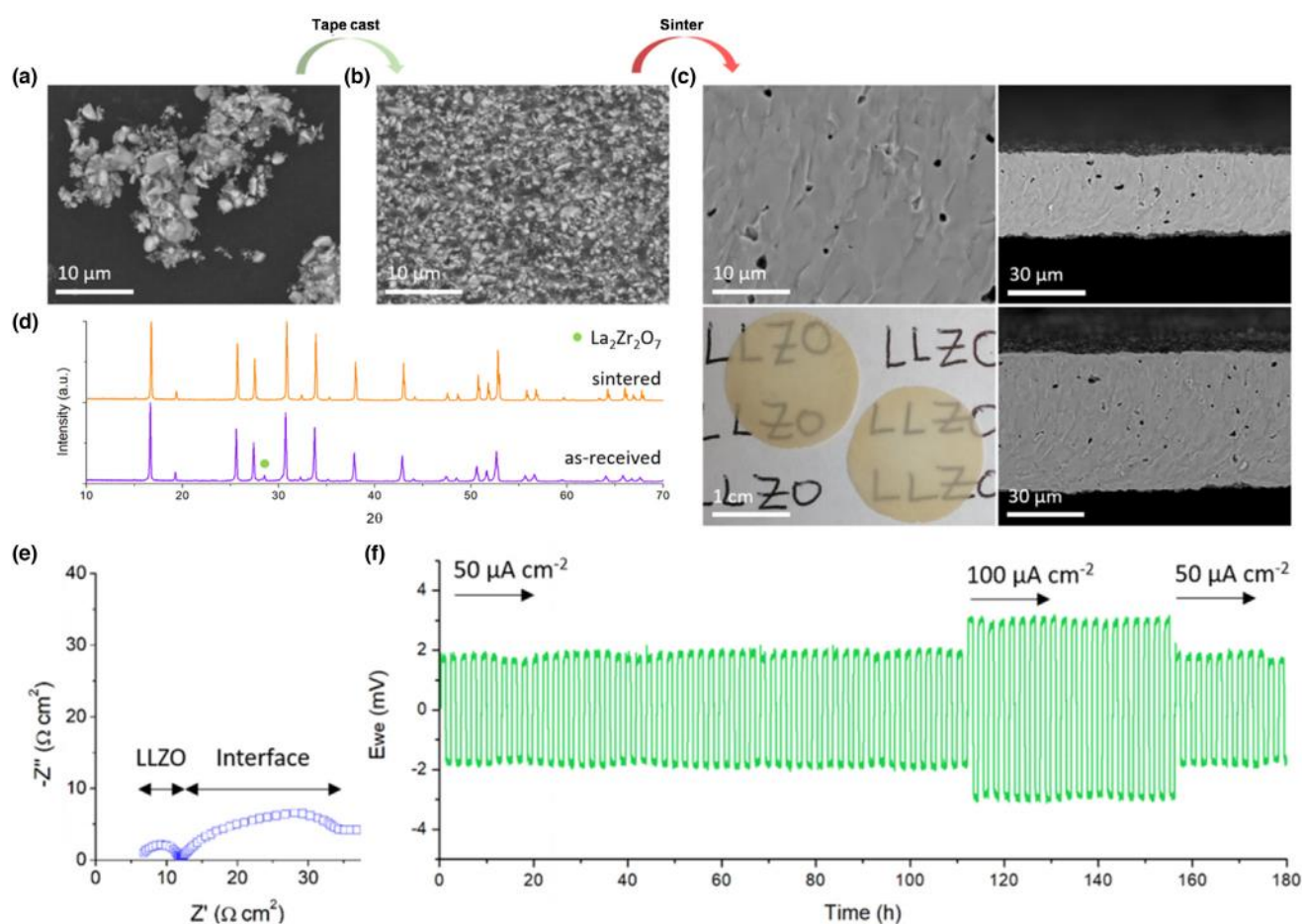


Figure 4. Microstructure and electrochemical performance of LLZO. Scanning electron micrographs of a) LLZO powder and b) fracture surface of tape-cast green tape. c) SEM and optical images of LLZO films sintered in optimal sintering profile. d) X-ray diffractograms of sintered and as-received LLZO film. e) Impedance test (Nyquist plot) and f) DC cycling of Au interface engineered Li/LLZO/Li cell. Reproduced with permission.^[74] Copyright 2020, American Chemistry Society.

promising metal oxide-based solid electrolytes, and much work has been devoted to improving its surficial properties. Recently, Al-substituted LLZO combined with the cathode featuring dual layers (dense LLZO membranes and porous LLZO scaffolds) infiltrated with $\text{LiNi}_{0.6}\text{Mn}_{0.2}\text{Co}_{0.2}\text{O}_2$ while using Li as the counter electrode has been reported.^[74] In this work, tape casting followed by sintering resulted in dense LLZO membranes (Figure 4a–c). X-ray diffraction (Figure 4d) shows that the crystalline peak related to $\text{La}_2\text{Zr}_2\text{O}_7$ disappeared, indicating more crystalline peaks after the sintering process. Electrochemical properties of LLZO were characterized by electrochemical impedance spectroscopy (Nyquist plot, Figure 4e) and electrochemical cycling (Figure 4f) using a Li/LLZO/Li cell configuration. Based on the impedance test, LLZO exhibits an overall cell impedance of $35 \Omega \text{ cm}^2$, while an interfacial impedance is only $12 \Omega \text{ cm}^2$, much lower than previously reported values.^[75,76] As a result, LLZO can stably be cycled at current densities of 50 and $100 \mu\text{A cm}^{-2}$, which leads to stable electrochemical reactions having discharge capacities of 125–135 mAh g^{-1} .

Hybrid polymer-inorganic electrolytes can also induce a suitable interface between the electrode and electrolyte, especially at the cathode–solid–electrolyte interface. Wu et al.^[77] reported functional composite polymer electrolytes with imidazole-modified SiO_2 nanoparticles (300 nm), where a combinatorial effect of both SiO_2 and polyvinylidene fluoride (PVDF)/polyethylene (PE) is present. When imidazole-modified SiO_2 nanoparticles are used, they lead to a more compact and uniform cathode electrolyte interphase (7.5 nm), reducing interfacial resistance and improving cycle retention.^[77] SiO_2 acted as a water/acid scavenger and filler for electrolytes, leading to an increase in charge cut-off voltage to 4.5 V. Another enhanced method is the so-called tri-layer strategy to improve the contact between the electrode and the electrolyte effectively. For example, Zhang et al.^[78] employed a three-dimensional $\text{Li}_{1.5}\text{Al}_{0.5}\text{Ge}_{1.5}(\text{PO}_4)_3$ (LAGP) layer made by templating to form a porous structure that hosts the cathode material by infiltration. This electrolyte is an ionically conductive thin and dense layer that can block dendrite growth. After the cathode addition, the last component is polyethylene glycol bis(amine)-triglycidyl isocyanurate. This solid-state cross-linked polymer fills the gaps between the former two to increase their contact. This compact design maximized cathode loading up to 13 mg cm^{-2} , delivering an areal capacity of 2 mAh cm^{-2} at a rate of 0.1C with a capacity retention of 70% after 50 cycles. Composite solid electrolytes were also recently developed with much progress, some of which include $\text{Li}_3\text{BO}_3\text{-Li}_{6.4}\text{La}_3\text{Zr}_{1.4}\text{Ta}_{0.6}\text{O}_{12}$,^[79] $\text{PEO}_{20}\text{-LiTFSI-Li}_6\text{PS}_5\text{Cl}$,^[80] $\text{Li}_6\text{PS}_5\text{Cl/poly(ethylene oxide)}$,^[81] tantalum-doped lithium lanthanum zirconium oxide,^[82] and poly(ethylene oxide)- $\text{LiClO}_4\text{-Li}_{1.3}\text{Al}_{0.3}\text{Ti}_{1.7}(\text{PO}_4)_3$.^[83] Although the solid electrolyte itself is not nanoscale, adopting proper solid electrolyte results in an enhanced interface between electrode and electrolyte. It can be in nanoscale interphase that contributes to more interfacial stability.

3. Tuning the Interface by Formation of a Solid Electrolyte Interphase Layer

3.1. By Introducing an Artificial Interphase

Forming an artificial solid interphase is a powerful concept for tuning the interface and improving the electrochemical performance. This creates an electrolyte interphase layer on the electrode before cell assembly, which artificially mitigates and solves several issues raised in the conventional LIBs configurations. For instance, an artificial interphase layer

on a cathode material, such as Ni-rich NCM,^[84] can comprise silyl ether functional groups. The latter can be formed by employing wet-coating-based thermal treatment, using dimethoxy-dimethyl silane as an organic solvent. Through in-depth analysis, it has been found that Si-O functional groups were effective in F^- scavenging, leading to fewer side reactions. The as-formed electrode–electrolyte interphase layer improved the interfacial stability of the Ni-rich NCM cathode, leading to higher cycle retention. Jang et al.^[85] formed a chemically induced interphase layer by employing lithium tetra(trimethylsilyl) borate as a functional precursor. The formed coating layer was about 5–8 nm, improving interfacial stability and scavenging fluoride species. Silyl-borate functional groups in the precursor greatly minimize the electrolyte decomposition (along with side reactions) and scavenge fluoride species. Simulation data suggest that it is thermodynamically favorable for lithium tetra(trimethylsilyl) borate to bond to fluoride species, thus mitigating the electrolyte decomposition. As a result, the cell employing such an artificial interphase layer shows stable cycling at a high temperature of 55°C after 100 cycles.

The formation of an artificial interphase layer has also been adopted for anodes, particularly in the case of Li metal. For instance, Li et al.^[86] employed garnet-type $\text{Li}_{6.4}\text{La}_3\text{Zr}_{1.4}\text{Ta}_{0.6}\text{O}_{12}$ (LLZTO)-based artificial interphase layer onto the Cu current collector, where the interphase layer greatly reduces the contact between Li and electrolyte. When sintering the LLZTO together with the Cu current collector, interdiffusion of Cu and Ta_2O_5 takes place, fixing an LLZTO layer on the Cu current collector. Such formation of an artificial interphase layer leads to enhanced Li plating/stripping performance, a long lifespan of 2400 h = 100 days, high rate capabilities with a maximum current density of 20 mA cm^{-2} , and a high areal capacity of 8 mAh cm^{-2} for 100 cycles. Various materials were selected as an artificial interphase layer for Li metal, some of which include covalent organic framework,^[87] $[\text{LiNBH}]_n$ chains,^[88] PIM-1,^[89] LiBAMB-PETMP,^[90] metal–organic framework,^[91] graphene oxide,^[92] carbon nitride/graphene/carbon nitride,^[93] and antimony-doped lithium phosphate.^[94] Furthermore, an artificial interphase layer has also been adopted in other prospective anode materials, such as Si.^[95–98]

Many of these established artificial interphases are thinner than 10 nm and uniform (Table 2), which can effectively prevent the side reaction and enhance interfacial stability. However, also micrometer-sized artificial interphase layers were adopted onto the anode (Cu, Li).^[86,89–92] This showed that both micrometer-scale and nanoscale artificial interphase layers have been adopted onto the anode to improve surface properties, ion and electron transport, and structural integrity after galvanostatic cycling.

3.2. By Introducing Additives

Modulating the electrode/electrolyte interphase is very important to obtain high energy density LIBs,^[99] and such an approach can only be employed by preparing the rationally designed electrolyte, forming a tailored solid electrolyte interphase (SEI) layer. In a typical lowest unoccupied molecular orbital (LUMO) – highest occupied molecular orbital (HOMO) diagram of the electrolyte,^[100] an anode works as a reductant while a cathode works as an oxidant. The gap between the LUMO and HOMO levels is translated to the operation window of the electrolyte and the cell potential window can be calculated. The SEI layer is built at the electrochemical potential of the anode at energies above the LUMO level. Similarly, cathode–electrolyte interphase (CEI) forms at the

Table 2. Summary of interphase layer on electrode materials by artificial interphase layer.

Electrode material	Coating material	Method	Layer thickness	References
DODSi-LiNi _{0.8} Co _{0.1} Mn _{0.1} O ₂	Di-methoxydimethylsilane (DODSi)	Wet-Coating	1%coating – 5.0 nm 2% coating-6.5 nm 10% coating-7.5 nm	[84]
0.05 LTB-LiNi _{0.8} Co _{0.1} Mn _{0.1} O ₂	Lithium tetra(trimethylsilyl) borate(LTB)	Rotary evaporation	5–8 nm	[85]
Cu foil-LLZTO	Li _{6.4} La ₃ Zr _{1.4} Ta _{0.6} O ₁₂ (LLZTO)	Dispersed on and heat treatment	10–20 μm	[86]
COF _{TAPB-PDA}	1,3,5-tris(4-aminophenyl)	Filtration	10 nm	[87]
-Li Li@[LiNBH]n	benzene (TAPB)-terephthaldehyde (PDA) [LiNBH]n layer	Immersed/Heated/cooled/washed and evaporation	140–160 nm	[88]
Li@PIM-1	PIM-1 (polymer of intrinsic microporosity)	Stirred/vacuumed/ dried	4.4 μm	[89]
LP-Li	LiBAMB-PETMP (LP)	Drop casting/ultraviolet expose/dry	1.8 μm	[90]
Cu@Zn-MOF/PVA	Zn-metal organic framework (MOF)/polyvinyl alcohol (PVA)	Spin coating	3.1 μm	[91]
Cu@GO	Graphene oxide (GO)	Spin coating	1.2 μm	[92]
g-C ₃ N ₄ /G/Cu	g-C ₃ N ₄ /graphene/g-C ₃ N ₄	Self-assembly and in-situ calcination reaction	8 nm	[93]
Cu-Sb-doping Li ₃ PO ₄	Sb-doped Li ₃ PO ₄	Radio frequency magnetron sputtering	100 nm	[94]
Si@COF	Covalent organic framework (COF)	Frozen/heating/filtration	5 nm	[95]
Si@LiAlO ₂	LiAlO ₂	Stirring/centrifugation/dry	2 nm	[96]
Si/SiO _x -PBS	Poly(borosiloxane) (PBS)	Drop-casted	—	[97]
P-SiO _x @PTN	Poly-tannins (PTN)	Etching and drying	50–100 nm	[98]

potential of the cathode below the HOMO energy level, thus widening the stable potential window.^[100] For example, Cheng et al.^[101] recently suggested a novel inorganic/polymer CEI by in situ electrochemical oxidation of trace amounts of dual additives. By employing lithium bis(oxalate)borate (LiBOB) and dopamine (DA) as the dual additives, both the cycle retention characteristics and rate capabilities were significantly improved (Figure 5a,b), which could be ascribed to the formation of different interfacial layers. Schematic illustrations of the cathode without and with LiBOB + DA (Figure 5c,d) suggest that a uniform CEI is formed in the case of LiBOB + DA with only a layered phase, different

from conventional electrolyte showing non-uniform CEI with layered and rock-salt phases. The outer layer of the cycled particles in the conventional electrolyte is 20 nm thick. In comparison, that of cycled particles in the modified electrolyte is 2 nm thick, which leads to more facile ionic transport. Furthermore, it protects the cathode from harmful side reactions and phase transition to rock-salt phases, leading to facile Li⁺ ion diffusion.^[101]

Based on experimental evidence and theoretical estimations, a more optimized combination of electrolyte additives can be investigated. Kim et al.^[102] employed 3-(trimethylsilyl)-2-oxazolidinone (TMS-ON), which prevents the hydrolysis of LiPF₆ and scavenges HF in the electrolyte. Both experimental and theoretical analyses were combined to demonstrate the superiority of using TMS-ON. The general issues related to the hydrolysis of LiPF₆ and the formation of reactive species are illustrated in Figure 6a, despite the controversy of whether the water content has detrimental effects on cell performance.^[103,104] LiPF₆, one of the most frequently used salts in the electrolyte, can undergo autocatalytic decomposition to form LiF and PF₅. The formed PF₅ can severely damage the SEI layer formed on the surface of the electrode. Additionally, PF₆⁻ produced by dissociation of LiPF₆ in the electrolyte can react with water to produce HF, which further leaches the transition metal from the cathode and strongly affects the SEI layer.^[102] Therefore, TMS-ON was employed to improve the quality of the SEI layer further. PF₅ stabilizing effects

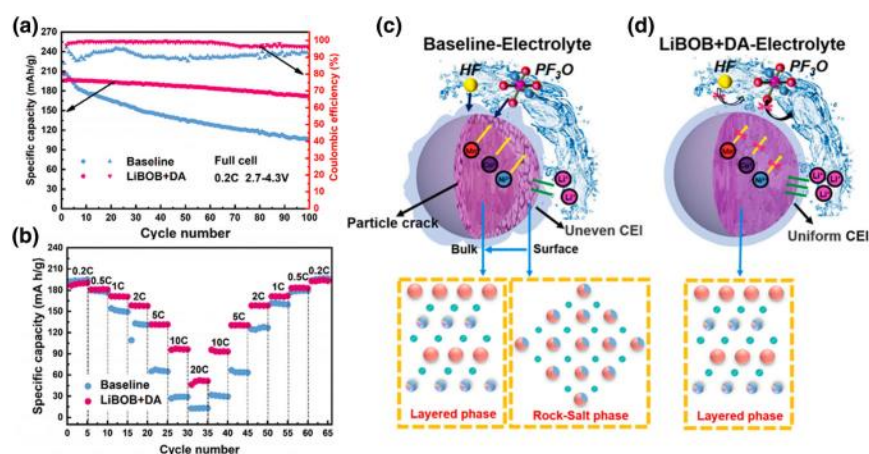


Figure 5. Electrochemical performance and schematic illustration of CEI layer. a) Cycle performance and b) rate capabilities of electrolyte with and without LiBOB + DA. Schematic illustration of the formation of the CEI layer and different phases c) without and d) with LiBOB + DA. Reproduced with permission.^[101] Copyright 2021, Elsevier.

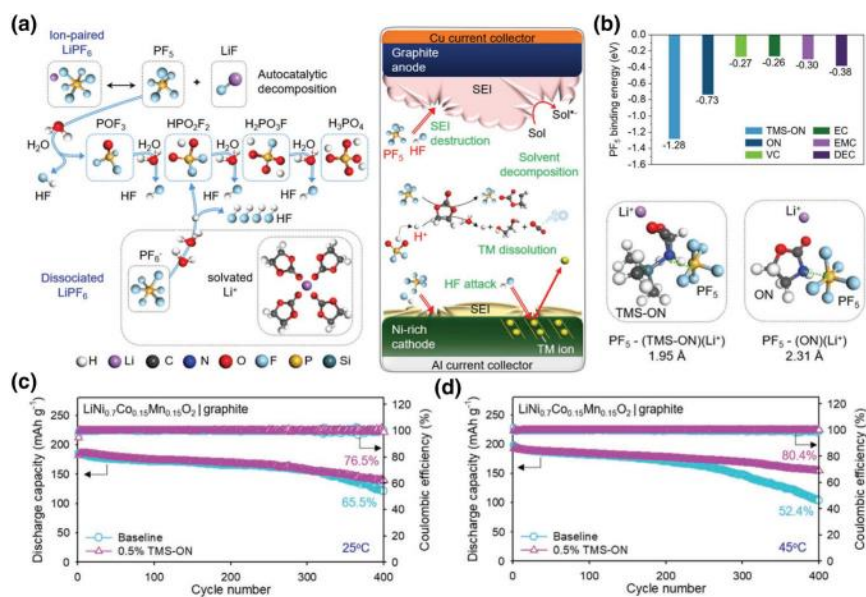


Figure 6. Theoretical and experimental investigation on electrolyte additives. a) Schematic illustration of the chemical decomposition of LiPF₆ (acidic components + reactive species) and related problems. b) PF₅ binding energies of various components coordinated with Li⁺. Cycle retention characteristics of LiNi_{0.7}Co_{0.15}Mn_{0.15}O₂/graphite full cells in a baseline electrolyte and 0.5% (trimethylsilyl)-2-oxazolidinone electrolyte at c) 25 °C and d) 45 °C. Reproduced with permission.^[97] Copyright 2020, Wiley.

by various solvents were theoretically investigated by density functional theory (DFT) calculations (Figure 6b).^[102] TMS-ON shows the highest PF₅ binding energies among 2-oxazolidinone (ON), vinylene carbonate (VC), ethylene carbonate (EC), ethyl methyl carbonate (EMC), and diethyl carbonate (DEC), which suggests that PF₅ binds more strongly

current research is aimed toward solid-state lithium batteries replacing lithium-ion batteries, the research interests in tuning the interface and interphase between electrode and electrolyte are becoming more critical (Scheme 1). Based on the literature,^[110–114] the following points can be concluded and suggested:

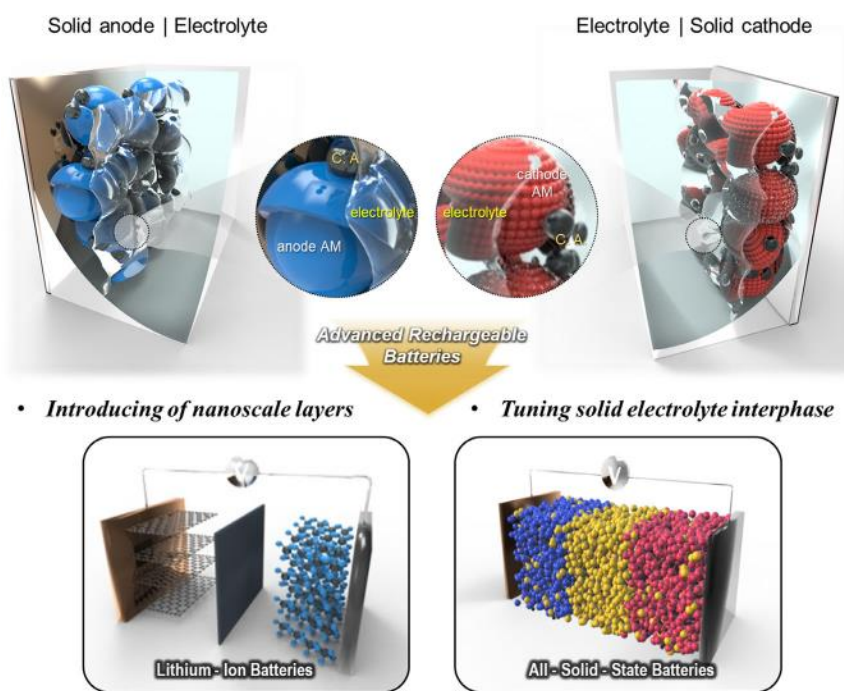
to TMS-ON rather than to the conventional electrolyte. The binding distance of TMS-ON is also very short (1.95 Å), due to the electron-donating nature of TMS functional groups.^[102] Attributed to these characteristics, electrolyte with TMS-ON leads to superior cycle retention both at room temperature (Figure 6c) and 45 °C (Figure 6d). Some other materials were also employed as additives for electrolytes, including Al₂O₃ nanofibers,^[105] Lithium difluorophosphate (LiDFP),^[106] bis(trimethylsilyl)carbodiimide,^[107] N-Allyl-N,N-bis(trimethylsilyl)amine,^[108] and 1-(2-cyanoethyl) pyrrole.^[109] A number of these additives in the electrolytes contribute to the formation of an ultrathin, nanoscale interfacial layer on the electrode (Table 3), which leads to facile ionic and electron transport.

4. Conclusions and Outlook

The interface and interphase between the electrode and electrolyte are essential aspects of research and investigation for various types of batteries, as they are critical to ensure facile ion and electron transport and to improve the state of health in the battery. Especially as the

Table 3. Summary of interphase layer on electrode materials by electrolyte additives.

Electrode material (cathode/anode)	Electrolyte	Additive	CEI/SEI layer thickness (cycles)	References
LiNi _{0.8} Co _{0.1} Mn _{0.1} O ₂ / Graphite	1.4 M Lithium bis(fluorosulfonyl)imide (LiFSI) in dimethyl carbonate (DMC)-ethylene carbonate (EC)-1,1,2,2-tetrafluoroethyl-2,2,3,3-tetrafluoropropyl ether (TTE) (2:0.2:3 by mol)	1,1,2,2-tetrafluoroethyl-2,2,3,3-tetrafluoropropyl ether (TTE)	3 nm/1 nm (100)	[99]
LiNi _{0.8} Co _{0.1} Mn _{0.1} O ₂ /Li	1.1 M Lithium hexafluorophosphate (LiPF ₆) in ethylene carbonate (EC) – diethylene carbonate (DEC) (1:1 by volume)	0.1 M lithium bis oxalate (LiBOB) + 0.1 mass% dopamine (DA)	5 nm/– (200)	[101]
LiNi _{0.7} Co _{0.15} Mn _{0.15} O ₂ / Graphite	1 M Lithium hexafluorophosphate (LiPF ₆) in ethylene carbonate (EC) – ethyl methyl carbonate (EMC)-diethylene carbonate (DEC) (3:4:3, by volume)	0.5 mass% 3-(trimethylsilyl)-2-oxazolidinone (TMS-ON)	3 nm/– (400)	[102]
LiNi _{0.88} Co _{0.09} Al _{0.03} O ₂ / Li	1 M Lithium hexafluorophosphate (LiPF ₆) in ethylene carbonate (EC) -dimethyl carbonate (DMC) (3:7, by volume)	Al ₂ O ₃	200–300 nm/– (300)	[105]
LiNi _{1/3} Co _{1/3} Mn _{1/3} O ₂ / graphite	1 M Lithium hexafluorophosphate (LiPF ₆) – ethylene carbonate (EC)/diethylene carbonate (DEC) (1:3, by mass)	1 mass% Lithium difluorophosphate (LiDFP)	~10 nm/– (100)	[106]
Li _{1.2} Mn _{0.55} Ni _{0.15} Co _{0.1} O ₂ /Li	1 M Lithium hexafluorophosphate (LiPF ₆)-diethylene carbonate (DEC)/ethylene carbonate (EC)/ethyl methyl carbonate (EMC) (2:3:5, by mass)	1 mass% bis(trimethylsilyl)carbodiimide (BTMSC)	6 nm/– (200)	[107]
LiNi _{0.8} Co _{0.15} Al _{0.05} O ₂ / Li	1 M Lithium hexafluorophosphate (LiPF ₆)-diethylene carbonate (DEC)/ethylene carbonate (EC)/ethyl methyl carbonate (EMC) (2:3:5, by mass)	2 mass% N-allyl-N,N-bis(trimethylsilyl)amine (NNB)	10 nm/– (300)	[108]
LiNi _{0.6} Co _{0.2} Mn _{0.2} O ₂ /Li	1 M Lithium hexafluorophosphate (LiPF ₆)-ethylene carbonate (EC)/ethyl methyl carbonate (EMC) (1:2, by mass)	1 mass% 1-(2-cyanoethyl) pyrrole (CEP)	20 nm/– (50)	[109]



Scheme 1. Schematic illustration of nanoengineering of electrode-electrolyte interfaces for advanced Li-ion-based rechargeable batteries.

- 1 The role of the interface and interphase between the electrode and electrolyte will become more critical in the emerging progress from lithium-ion batteries to solid-state lithium batteries.
- 2 Modification in the electrode or electrolyte is the most frequently used method to enhance the interface and interphase between the electrode and electrolyte.
- 3 Instead of adopting only one approach, dual or multiple approaches must simultaneously be taken to improve and optimize the electrode and electrolyte interface.

Different synthetic methods have been employed in the literature to modify the surface of electrode materials. Co-precipitation is usually carried out for surface modification, enabling a thin surface coating.^[32,33] However, its limitations lie in toxic liquid waste and control of pH levels in some cases. Solvothermal/hydrothermal synthesis can employ various solvents, but it also requires an autoclave.^[115] Sol-gel process is a simple method, but it cannot guarantee a uniform coating due to the nature of solution processing. Similar to the sol-gel process, ball-milling is a straightforward method, but it cannot easily control the size of the particle and coating layer.^[116] Atomic layer deposition enables uniform and thin surface coating. Although widely used in the semiconductor industry, it remains a cost-intensive process and might not be scalable in energy storage applications.^[117] UV polymerization is rarely used, but it has the potential to be investigated further. Chemical vapor deposition is useful for the deposition of graphene; However, the processing exhibits similar challenges to atomic layer deposition regarding costs.^[118] Among various used methods for surface modification, atomic layer deposition is most viable for the optimal thickness of the interface since it allows the coating of layers at an atomic scale, as the name indicates. As atomic layer deposition increases production

costs and scalability limitations, alternative methods must also be explored.

In terms of optimal interface composition, electrolyte additive is the most viable approach as the amount of electrolyte additive can lead to the formation of an interphase with a distinct chemical composition, where the amount of electrolyte additive and the chemical composition of the interface are correlated. The goal is to employ a cost-effective and scalable method to form a chemically stable ultrathin interface (<10 nm) with high electric conductivity.

In addition to these points, nanoengineering of the electrode-electrolyte interface and other factors affect the quality of the interphase formed between the electrode and electrolyte. Factors such as applied constant current (or constant voltage) depending on the mass loading of electrode materials and area of the electrode for cycling, formation cycle,^[21] temperature,^[119] and pressure^[120] can also significantly affect the interphase between the electrode and electrolyte. Synergistic technologies are essential to inspect these affecting factors. For example, monitoring gas evolution at the electrode-electrolyte interface, related to unwanted side reactions, can indicate how to

construct the optimal interface. Therefore, differential electrochemical mass spectrometry (DEMS) is a powerful tool for the in-situ detection of gaseous species in rechargeable batteries.^[121,122] Moreover, constant improvement of artificial intelligence (AI, such as ChatGPT) has the potential to systematically evaluate which nanoengineering approach would be optimal for each electrode material in different battery systems and charge/discharge conditions in the future. This will open the door to an exciting path toward advanced energy storage systems that address the growing energy demand.^[119,123]

Acknowledgements

N.-Y.K. and I.K. contributed equally to this work. This work was supported by funding from Bavarian Center for Battery Technology (Baybatt, Hightech Agenda Bayern) and Bayerisch-Tschechische Hochschulagentur (BTHA) (BTHA-AP-2022-45, BTHA-AP-2023-5, and BTHA-AP-2023-12). This work was also supported by the University of Bayreuth-Deakin University Joint Ph.D. Program. This work was also supported by the Regional Innovation Strategy (RIS) through the National Research Foundation of Korea (NRF) funded by the Ministry of Education (MOE) (2021RIS-003). This work was also supported by the National Research Foundation of Korea (NRF) grant funded by the Korea government (MSIT) (No. RS-2023-00213749).

Conflict of Interest

The authors declare no conflict of interest.

Keywords

battery, electrode, electrolyte, interface, lithium, nanoengineering

Received: February 14, 2023
 Revised: March 20, 2023
 Published online: March 23, 2023

- [1] G. E. Blomgren, *J. Electrochem. Soc.* **2017**, *164*, A5019.
- [2] A. Yoshino, *Angew. Chem. Int. Ed.* **2012**, *51*, 5798.
- [3] Y. Wang, B. Liu, Q. Li, S. Cartmell, S. Ferrara, Z. D. Deng, J. Xiao, *J. Power Sources* **2015**, *286*, 330.
- [4] L. Lu, X. Han, J. Li, J. Hua, M. Ouyang, *J. Power Sources* **2013**, *226*, 272.
- [5] J. Duan, X. Tang, H. Dai, Y. Yang, W. Wu, X. Wei, Y. Huang, *Electrochem. Energy Rev.* **2020**, DOI: <https://doi.org/10.1007/s41918-019-00060-4>.
- [6] P. V. Kamat, *ACS Energy Lett.* **2019**, *2019*, 2757.
- [7] H. Wu, G. Chan, J. W. Choi, I. Ryu, Y. Yao, M. T. Mcdowell, S. W. Lee, A. Jackson, Y. Yang, L. Hu, Y. Cui, *Nat. Nanotechnol.* **2012**, *7*, 310.
- [8] J. Chen, X. Fan, Q. Li, H. Yang, M. R. Khoshi, Y. Xu, S. Hwang, L. Chen, X. Ji, C. Yang, H. He, C. Wang, E. Garfunkel, D. Su, O. Borodin, C. Wang, *Nat. Energy* **2020**, *5*, 386.
- [9] N. Ohta, K. Takada, L. Zhang, R. Ma, M. Osada, T. Sasaki, *Adv. Mater.* **2006**, *18*, 2226.
- [10] D. Aurbach, B. Markovsky, G. Salitra, E. Markevich, Y. Talyossef, M. Koltypin, L. Nazar, B. Ellis, D. Kovacheva, *J. Power Sources* **2007**, *165*, 491.
- [11] J. Cabana, B. J. Kwon, L. Hu, *Acc. Chem. Res.* **2018**, *51*, 299.
- [12] X. Yu, A. Manthiram, *Energ. Environ. Sci.* **2018**, *11*, 527.
- [13] H. Yang, J. Lee, J. Y. Cheong, Y. Wang, G. Duan, H. Hou, S. Jiang, I. D. Kim, *Energ. Environ. Sci.* **2021**, *14*, 4228.
- [14] D. Li, H. Guo, S. Jiang, G. Zeng, W. Zhou, Z. Li, *New J. Chem.* **2021**, *45*, 19446.
- [15] J. Yu, S. Liu, G. Duan, H. Fang, H. Hou, *Compos. Commun.* **2020**, *19*, 239.
- [16] H. Bouayad, Z. Wang, N. Dupré, R. Redryvère, D. Foix, S. Franger, J. F. Martin, L. Boutafa, S. Patoux, D. Gonbeau, D. Guyomard, *J. Phys. Chem. C* **2014**, *118*, 4634.
- [17] J. Y. Cheong, J. H. Chang, H. K. Seo, J. M. Yuk, J. W. Shin, J. Y. Lee, I. D. Kim, *Nano Energy* **2016**, *25*, 154.
- [18] X. Yu, A. Manthiram, *Acc. Chem. Res.* **2017**, *50*, 2653.
- [19] Y. Xiao, Y. Wang, S. H. Bo, J. C. Kim, L. J. Miara, G. Ceder, *Nat. Rev. Mater.* **2020**, *5*, 105.
- [20] B. K. Antonopoulos, C. Stock, F. Maglia, H. E. Hoster, *Electrochim. Acta* **2018**, *269*, 331.
- [21] J. Y. Cheong, J. H. Chang, S. H. Cho, J. W. Jung, C. Kim, K. S. Dae, J. M. Yuk, I. D. Kim, *Electrochim. Acta* **2019**, *295*, 7.
- [22] A. Soloy, D. Flahaut, D. Foix, J. Allouche, G. S. Vallverdu, E. Dumont, L. Gal, F. Weill, L. Croguennec, *ACS Appl. Mater. Interfaces* **2022**, *14*, 28792.
- [23] S. T. Myung, K. Amine, Y. K. Sun, *J. Mater. Chem.* **2010**, *20*, 7074.
- [24] S. Kim, W. Cho, X. Zhang, Y. Oshima, J. W. Choi, *Nat. Commun.* **2016**, *7*, 13598.
- [25] X. Ding, D. Luo, J. Cui, H. Xie, Q. Ren, Z. Lin, *Angew. Chem. Int. Ed.* **2020**, *59*, 7778.
- [26] B. J. Kang, J. B. Joo, J. K. Lee, W. Choi, *J. Electroanal. Chem.* **2014**, *728*, 34.
- [27] J. Li, Z. Liu, Y. Wang, R. Wang, *J. Alloys Compd.* **2020**, *834*, 155150.
- [28] J. Song, Y. Wang, Z. Feng, X. Zhang, K. Wang, H. Gu, J. Xie, *ACS Appl. Mater. Interfaces* **2018**, *10*, 27326.
- [29] S. Yang, Q. Fan, Z. Shi, L. Liu, J. Liu, X. Ke, J. Liu, C. Hong, Y. Yang, Z. Guo, *ACS Appl. Mater. Interfaces* **2019**, *11*, 36742.
- [30] S. Deng, X. Li, Z. Ren, W. Li, J. Luo, J. Liang, J. Liang, M. N. Banis, M. Li, Y. Zhao, X. Li, C. Wang, Y. Sun, Q. Sun, R. Li, Y. Hu, H. Huang, L. Zhang, S. Lu, J. Luo, X. Sun, *Energy Storage Mater.* **2020**, *27*, 117.
- [31] Q. Fan, S. Yang, J. Liu, H. Liu, K. Lin, R. Liu, C. Hong, L. Liu, Y. Chen, K. An, P. Liu, Z. Shi, Y. Yang, *J. Power Sources* **2019**, *421*, 91.
- [32] P. Zou, Z. Lin, M. Fan, F. Wang, Y. Liu, X. Xiong, *Appl. Surf. Sci.* **2020**, *504*, 144506.
- [33] W. Zhang, L. Liang, F. Zhao, Y. Liu, L. Hou, C. Yuan, *Electrochim. Acta* **2020**, *340*, 135871.
- [34] M. Wang, Y. Gong, Y. Gu, Y. Chen, L. Chen, H. Shi, *Ceram. Int.* **2019**, *45*, 3177.
- [35] J. Y. Liang, X. X. Zeng, X. D. Zhang, P. F. Wang, J. Y. Ma, Y. X. Yin, X. W. Wu, Y. G. Guo, L. J. Wan, *J. Am. Chem. Soc.* **2018**, *140*, 6767.
- [36] Q. Yang, J. Huang, Y. Li, Y. Wang, J. Qiu, J. Zhang, H. Yu, X. Yu, H. Li, L. Chen, *J. Power Sources* **2018**, *388*, 65.
- [37] Y. Liu, L. Bo Tang, H. Xin Wei, X. Hui Zhang, Z. Jiang He, Y. Jiao Li, J. Chao Zheng, *Nano Energy* **2019**, *65*, 104043.
- [38] X. Wen, K. Liang, L. Tian, K. Shi, J. Zheng, *Electrochim. Acta* **2018**, *260*, 549.
- [39] S. Neudeck, A. Mazilkin, C. Reitz, P. Hartmann, J. Janek, T. Brezesinski, *Sci. Rep.* **2019**, *9*, 5328.
- [40] D. S. Hall, R. Gauthier, A. Eldesoky, V. S. Murray, J. R. Dahn, *ACS Appl. Mater. Interfaces* **2019**, *11*, 14095.
- [41] W. Liu, X. Li, D. Xiong, Y. Hao, J. Li, H. Kou, B. Yan, D. Li, S. Lu, A. Koo, K. Adair, X. Sun, *Nano Energy* **2018**, *44*, 111.
- [42] L. Yao, F. Liang, J. Jin, B. V. R. Chowdari, J. Yang, Z. Wen, *Chem. Eng. J.* **2020**, *389*, 124403.
- [43] X. Li, L. Jin, D. Song, H. Zhang, X. Shi, Z. Wang, L. Zhang, L. Zhu, *J. Energy Chem.* **2020**, *40*, 39.
- [44] D. Becker, M. Börner, R. Nölle, M. Diehl, S. Klein, U. Rodehorst, R. Schmich, M. Winter, T. Placke, *ACS Appl. Mater. Interfaces* **2019**, *11*, 18404.
- [45] J. C. Zheng, Z. Yang, Z. J. He, H. Tong, W. J. Yu, J. F. Zhang, *Nano Energy* **2018**, *53*, 613.
- [46] C. Zhang, S. Liu, J. Su, C. Chen, M. Liu, X. Chen, J. Wu, T. Huang, A. Yu, *Nanoscale* **2018**, *10*, 8820.
- [47] H. Gao, J. Cai, G. L. Xu, L. Li, Y. Ren, X. Meng, K. Amine, Z. Chen, *Chem. Mater.* **2019**, *31*, 2723.
- [48] Q. Chen, L. Luo, L. Wang, T. Xie, S. Dai, Y. Yang, Y. Li, M. Yuan, *J. Alloys Compd.* **2018**, *735*, 1778.
- [49] Z. Chen, Y. Liu, Z. Lu, R. Hu, J. Cui, H. Xu, Y. Ouyang, Y. Zhang, M. Zhu, *J. Alloys Compd.* **2019**, *803*, 71.
- [50] C. Xu, W. Xiang, Z. Wu, Y. Xu, Y. Li, Y. Wang, Y. Xiao, X. Guo, B. Zhong, *ACS Appl. Mater. Interfaces* **2019**, *11*, 16629.
- [51] T. He, Y. Lu, Y. Su, L. Bao, J. Tan, L. Chen, Q. Zhang, W. Li, S. Chen, F. Wu, *ChemSusChem* **2018**, *11*, 1639.
- [52] C. S. Yoon, U. H. Kim, G. T. Park, S. J. Kim, K. H. Kim, J. Kim, Y. K. Sun, *ACS Energy Lett.* **2018**, *3*, 1634.
- [53] X. Qi, Z. Xue, K. Du, Y. Xie, Y. Cao, W. Li, Z. Peng, G. Hu, *J. Power Sources* **2018**, *397*, 288.
- [54] S. Zhao, B. Sun, K. Yan, J. Zhang, C. Wang, G. Wang, *ACS Appl. Mater. Interfaces* **2018**, *10*, 33260.
- [55] L. Wei, J. Tao, Y. Yang, X. Fan, X. Ran, J. Li, Y. Lin, Z. Huang, *Chem. Eng. J.* **2020**, *384*, 123268.
- [56] W. Xiang, C. Q. Zhu, J. Zhang, H. Shi, Y. T. Liang, M. H. Yu, X. M. Zhu, F. R. He, G. P. Lv, X. D. Guo, *J. Alloys Compd.* **2019**, *786*, 56.
- [57] G. Chen, J. An, Y. Meng, C. Yuan, B. Matthews, F. Dou, L. Shi, Y. Zhou, P. Song, G. Wu, D. Zhang, *Nano Energy* **2019**, *57*, 157.
- [58] K. Liu, Q. Zhang, S. Dai, W. Li, X. Liu, F. Ding, J. Zhang, *ACS Appl. Mater. Interfaces* **2018**, *10*, 34153.
- [59] H. Yang, H. H. Wu, M. Ge, L. Li, Y. Yuan, Q. Yao, J. Chen, L. Xia, J. Zhang, Z. Chen, J. Duan, K. Kisslinger, X. C. Zeng, W. K. Lee, Q. Zhang, J. Lu, *Adv. Funct. Mater.* **2019**, *29*, 1808825.
- [60] Q. Ran, H. Zhao, Y. Hu, S. Hao, Q. Shen, J. Liu, H. Li, Y. Xiao, L. Li, L. Wang, X. Liu, *ACS Appl. Mater. Interfaces* **2020**, *12*, 9268.
- [61] Y. Ma, P. Liu, Q. Xie, G. Zhang, H. Zheng, Y. Cai, Z. Li, L. Wang, Z. Z. Zhu, L. Mai, D. L. Peng, *Nano Energy* **2019**, *59*, 184.

- [62] L. P. Wang, X. D. Zhang, T. S. Wang, Y. X. Yin, J. L. Shi, C. R. Wang, Y. G. Guo, *Adv. Energy Mater.* **2018**, *8*, 1801528.
- [63] G. L. Xu, Q. Liu, K. K. S. Lau, Y. Liu, X. Liu, H. Gao, X. Zhou, M. Zhuang, Y. Ren, J. Li, M. Shao, M. Ouyang, F. Pan, Z. Chen, K. Amine, G. Chen, *Nat. Energy* **2019**, *4*, 484.
- [64] Q. Gan, N. Qin, Y. Zhu, Z. Huang, F. Zhang, S. Gu, J. Xie, K. Zhang, L. Lu, Z. Lu, *ACS Appl. Mater. Interfaces* **2019**, *11*, 12594.
- [65] Y. Cao, X. Qi, K. Hu, Y. Wang, Z. Gan, Y. Li, G. Hu, Z. Peng, K. Du, *ACS Appl. Mater. Interfaces* **2018**, *10*, 18270.
- [66] M. Yoon, Y. Dong, J. Hwang, J. Sung, H. Cha, K. Ahn, Y. Huang, S. J. Kang, J. Li, J. Cho, *Nat. Energy* **2021**, *6*, 362.
- [67] J. Wang, L. Liao, H. R. Lee, F. Shi, W. Huang, J. Zhao, A. Pei, J. Tang, X. Zheng, W. Chen, Y. Cui, *Nano Energy* **2019**, *61*, 404.
- [68] K. R. Tallman, B. Zhang, L. Wang, S. Yan, K. Thompson, X. Tong, J. Thieme, A. Kiss, A. C. Marschilok, K. J. Takeuchi, D. C. Bock, E. S. Takeuchi, *ACS Appl. Mater. Interfaces* **2019**, *11*, 46864.
- [69] S. Heng, X. Shan, W. Wang, Y. Wang, G. Zhu, Q. Qu, H. Zheng, *Carbon* **2020**, *159*, 390.
- [70] D. Jin, J. Park, M. H. Ryou, Y. M. Lee, *Adv. Mater. Interfaces* **2020**, *7*, 1902113.
- [71] L. Wang, L. Zhang, Q. Wang, W. Li, B. Wu, W. Jia, Y. Wang, J. Li, H. Li, *Energy Storage Mater.* **2018**, *10*, 16.
- [72] L. Chen, K. S. Chen, X. Chen, G. Ramirez, Z. Huang, N. R. Geise, H. G. Steinrück, B. L. Fisher, R. Shahbazian-Yassar, M. F. Toney, M. C. Hersam, J. W. Elam, *ACS Appl. Mater. Interfaces* **2018**, *10*, 26972.
- [73] C. Yan, X. B. Cheng, Y. Tian, X. Chen, X. Q. Zhang, W. J. Li, J. Q. Huang, Q. Zhang, *Adv. Mater.* **2018**, *30*, 1707629.
- [74] E. Yi, H. Shen, S. Heywood, J. Alvarado, D. Y. Parkinson, G. Chen, S. W. Sofie, M. M. Doeff, *ACS Appl. Energy Mater.* **2020**, *3*, 170.
- [75] C. Wang, Y. Gong, B. Liu, K. Fu, Y. Yao, E. Hitz, Y. Li, J. Dai, S. Xu, W. Luo, E. D. Wachsman, L. Hu, *Nano Lett.* **2017**, *17*, 565.
- [76] G. V. Alexander, S. Patra, S. V. Sobhan Raj, M. K. Sugumar, M. M. Ud Din, R. Murugan, *J. Power Sources* **2018**, *396*, 764.
- [77] J. Wu, X. Zuo, Q. Chen, X. Deng, H. Liang, T. Zhu, J. Liu, W. Li, J. Nan, *Electrochim. Acta* **2019**, *320*, 134567.
- [78] Z. Zhang, S. Chen, X. Yao, P. Cui, J. Duan, W. Luo, Y. Huang, X. Xu, *Energy Storage Mater.* **2020**, *24*, 714.
- [79] D. Wang, Q. Sun, J. Luo, J. Liang, Y. Sun, R. Li, K. Adair, L. Zhang, R. Yang, S. Lu, H. Huang, X. Sun, *ACS Appl. Mater. Interfaces* **2019**, *11*, 4954.
- [80] F. J. Simon, M. Hanauer, F. H. Richter, J. Janek, *ACS Appl. Mater. Interfaces* **2020**, *12*, 11713.
- [81] J. Zhang, C. Zheng, J. Lou, Y. Xia, C. Liang, H. Huang, Y. Gan, X. Tao, W. Zhang, *J. Power Sources* **2019**, *412*, 78.
- [82] H. Chen, M. X. Jing, C. Han, H. Yang, S. Hua, F. Chen, L. L. Chen, Z. X. Zhou, B. W. Ju, F. Y. Tu, X. Q. Shen, S. B. Qin, *Int. J. Energy Res.* **2019**, *43*, 5912.
- [83] X. Ban, W. Zhang, N. Chen, C. Sun, *J. Phys. Chem. C* **2018**, *122*, 9852.
- [84] H. J. Song, S. H. Jang, J. Ahn, S. H. Oh, T. Yim, *J. Power Sources* **2019**, DOI: <https://doi.org/10.1016/j.jpowsour.2019.01.050>.
- [85] S. H. Jang, K. J. Lee, J. Mun, Y. K. Han, T. Yim, *J. Power Sources* **2019**, *410–411*, 15.
- [86] P. Li, X. Dong, C. Li, J. Liu, Y. Liu, W. Feng, C. Wang, Y. Wang, Y. Xia, *Angew. Chem. Int. Ed.* **2019**, *58*, 2093.
- [87] D. Chen, S. Huang, L. Zhong, S. Wang, M. Xiao, D. Han, Y. Meng, *Adv. Funct. Mater.* **2020**, *30*, 1907717.
- [88] Z. Wang, Y. Wang, Z. Zhang, X. Chen, W. Lie, Y. B. He, Z. Zhou, G. Xia, Z. Guo, *Adv. Funct. Mater.* **2020**, *30*, 2002414.
- [89] Q. Yang, W. Li, C. Dong, Y. Ma, Y. Yin, Q. Wu, Z. Xu, W. Ma, C. Fan, K. Sun, *J. Energy Chem.* **2020**, *42*, 83.
- [90] K. Deng, D. Han, S. Ren, S. Wang, M. Xiao, Y. Meng, *J. Mater. Chem. A* **2019**, *7*, 13113.
- [91] L. Fan, Z. Guo, Y. Zhang, X. Wu, C. Zhao, X. Sun, G. Yang, Y. Feng, N. Zhang, *J. Mater. Chem. A* **2020**, *8*, 251.
- [92] Z. T. Wondimkun, T. T. Beyene, M. A. Weret, N. A. Sahalie, C. J. Huang, B. Thirumalraj, B. A. Jote, D. Wang, W. N. Su, C. H. Wang, G. Brunklaus, M. Winter, B. J. Hwang, *J. Power Sources* **2020**, *450*, 227589.
- [93] P. Zhai, T. Wang, H. Jiang, J. Wan, Y. Wei, L. Wang, W. Liu, Q. Chen, W. Yang, Y. Cui, Y. Gong, *Adv. Mater.* **2021**, *33*, 2006247.
- [94] C. Gao, Q. Dong, G. Zhang, H. Fan, H. Li, B. Hong, Y. Lai, *ChemElectroChem* **2019**, *6*, 1134.
- [95] Q. Ai, Q. Fang, J. Liang, X. Xu, T. Zhai, G. Gao, H. Guo, G. Han, L. Ci, J. Lou, *Nano Energy* **2020**, *72*, 104657.
- [96] Q. Ai, D. Li, J. Guo, G. Hou, Q. Sun, Q. Sun, X. Xu, W. Zhai, L. Zhang, J. Feng, P. Si, J. Lou, L. Ci, *Adv. Mater. Interfaces* **2019**, *6*, 1901187.
- [97] S. G. Patnaik, T. P. Jayakumar, Y. Sawamura, N. Matsumi, *ACS Appl. Energy Mater.* **2021**, *4*, 2241.
- [98] J. Guo, W. Wu, J. Wang, T. Zhang, R. Wang, D. Xu, C. Wang, Y. Deng, *Solid State Ion.* **2020**, *347*, 115272.
- [99] X. Zhang, L. Zou, Y. Xu, X. Cao, M. H. Engelhard, B. E. Matthews, L. Zhong, H. Wu, H. Jia, X. Ren, P. Gao, Z. Chen, Y. Qin, C. Kompella, B. W. Arey, J. Li, D. Wang, C. Wang, J. G. Zhang, W. Xu, *Adv. Energy Mater.* **2020**, *10*, 202000368.
- [100] J. B. Goodenough, Y. Kim, *Chem. Mater.* **2010**, *22*, 587.
- [101] F. Cheng, X. Zhang, Y. Qiu, J. Zhang, Y. Liu, P. Wei, M. Ou, S. Sun, Y. Xu, Q. Li, C. Fang, J. Han, Y. Huang, *Nano Energy* **2021**, *88*, 106301.
- [102] K. Kim, D. Hwang, S. Kim, S. O. Park, H. Cha, Y. S. Lee, J. Cho, S. K. Kwak, N. S. Choi, *Adv. Energy Mater.* **2020**, *10*, 2000012.
- [103] J. C. Burns, N. N. Sinha, G. Jain, H. Ye, C. M. VanElzen, E. Scott, A. Xiao, W. M. Lamanna, J. R. Dahn, *J. Electrochem. Soc.* **2013**, *160*, A2281.
- [104] D. J. Xiong, R. Petibon, L. Madec, D. S. Hall, J. R. Dahn, *J. Electrochem. Soc.* **2016**, *163*, A1678.
- [105] Y. Y. Sun, S. Liu, Y. K. Hou, G. R. Li, X. P. Gao, *J. Power Sources* **2019**, *410–411*, 115.
- [106] C. Wang, L. Yu, W. Fan, J. Liu, L. Ouyang, L. Yang, M. Zhu, *ACS Appl. Energy Mater.* **2018**, *1*, 2647.
- [107] J. Lan, Q. Zheng, H. Zhou, J. Li, L. Xing, K. Xu, W. Fan, L. Yu, W. Li, *ACS Appl. Mater. Interfaces* **2019**, *11*, 28841.
- [108] Q. Zheng, L. Xing, X. Yang, X. Li, C. Ye, K. Wang, Q. Huang, W. Li, *ACS Appl. Mater. Interfaces* **2018**, *10*, 16843.
- [109] B. Liao, X. Hu, M. Xu, H. Li, L. Yu, W. Fan, L. Xing, Y. Liao, W. Li, *J. Phys. Chem. Lett.* **2018**, *9*, 3434.
- [110] R. S. Arumugam, L. Ma, J. Li, X. Xia, J. M. Paulsen, J. R. Dahn, *J. Electrochem. Soc.* **2016**, *163*, A2531.
- [111] Y. Zhao, J. Li, J. R. Dahn, *Chem. Mater.* **2017**, *29*, 5239.
- [112] F. Wang, Y. Lin, L. Suo, X. Fan, T. Gao, C. Yang, F. Han, Y. Qi, K. Xu, C. Wang, *Energy Environ. Sci.* **2016**, *9*, 3666.
- [113] H. Chen, J. Chen, W. Zhang, Q. Xie, Y. Che, H. Wang, L. Xing, K. Xu, W. Li, *J. Mater. Chem. A* **2020**, *8*, 22054.
- [114] S. Tan, Z. Shadik, J. Li, X. Wang, Y. Yang, R. Lin, A. Cresce, J. Hu, A. Hunt, I. Waluyo, L. Ma, F. Monaco, P. Cloetens, J. Xiao, Y. Liu, X.-Q. Yang, K. Xu, E. Hu, *Nat. Energy* **2022**, *7*, 484.
- [115] V. K. Suhas, L. P. Gupta, M. Singh, S. K. Chaudhary, *J. Clean. Prod.* **2021**, *288*, 125643.
- [116] R. M. Raihanuzzaman, T. S. Jeong, R. Ghomashchi, Z. Xie, S. J. Hong, *J. Alloys Compd.* **2014**, *615*, S564.
- [117] A. Karimghaloo, J. Koo, H. Sen Kang, S. A. Song, J. H. Shim, M. H. Lee, *Int. J. Precis. Eng. Manuf. Green Technol.* **2019**, *6*, 611.
- [118] Y. Hamedani, P. Macha, T. J. Bunning, R. R. Naik, M. C. Vasudev, *Plasma-Enhanced Chemical Vapor Deposition: Where we are and the Outlook for the Future*, InTech, **2016**. https://books.google.de/books?hl=ko&lr=&id=k3eQDwAAQBAJ&oi=fnd&pg=PA247&dq=Plasma-Enhanced+Chemical+Vapor+Deposition:+Where+We+are+and+the+Outlook+for+the+Future&ots=DiDBKOe8Vy&sig=_9wil6W59N8rGbMrYB-M1v2Tf2w&redir_esc=y#v=onepage&q=Plasma-Enhanced%20Chemical%20Vapor%20Deposition%3A%20Where%20We%20are%20and%20the%20Outlook%20for%20the%20Future&f=false (accessed: April 2023).

- [119] A. Maraschky, R. Akolkar, *J. Electrochem. Soc.* **2020**, *167*, 62503.
- [120] R. M. Kasse, N. R. Geise, E. Sebti, K. Lim, C. J. Takacs, C. Cao, H. G. Steinrück, M. F. Toney, *ACS Appl. Energy Mater.* **2022**, *5*, 8273.
- [121] S. J. Davis, N. S. Lewis, M. Shaner, S. Aggarwal, D. Arent, I. L. Azevedo, S. M. Benson, T. Bradley, J. Brouwer, Y. M. Chiang, C. T. M. Clack, A. Cohen, S. Doig, J. Edmonds, P. Fennell, C. B. Field, B. Hannegan, B. M. Hodge, M. I. Hoffert, E. Ingersoll, P. Jaramillo, K. S. Lackner, K. J. Mach, M. Mastrandrea, J. Ogden, P. F. Peterson, D. L. Sanchez, D. Sperling, J. Stagner, J. E. Trancik, C. J. Yang, K. Caldeira, *Science* **2018**, *360*, eaas9793.
- [122] M. Fichtner, K. Edström, E. Ayerbe, M. Berecibar, A. Bhowmik, I. E. Castelli, S. Clark, R. Dominko, M. Erakca, A. A. Franco, A. Grimaud, B. Horstmann, A. Latz, H. Lorrmann, M. Meeus, R. Narayan, F. Pammer, J. Ruhland, H. Stein, T. Vegge, M. Weil, *Adv. Energy Mater.* **2022**, *12*, 2102904.
- [123] Q. Wang, L. Velasco, B. Breitung, V. Presser, *Adv. Energy Mater.* **2021**, *11*, 2102355.

5 CONCLUSION AND OUTLOOK

This thesis investigated the role of materials design and derivatization engineering for use in energy storage and the challenges that are faced when exploring new compositions. Different metal oxides and metal sulfides hybridized with carbon materials were derived for use in battery electrodes to store lithium and were then tuned in morphology and chemistry to improve their electrochemical performance. Special attention was given in every step to improve the sustainability of the procedure such as using water-based synthesis and low-temperature processing. For derivatization, PBAs were used for self-templating of the active material, and different strategies for tuning the derivative were reviewed such as etching, coating, ion-exchange, and templating. Different methods of derivatization such as thermal, hydrothermal, and liquid were reviewed in parallel to show the great potential PBAs offer as a self-template precursor. With the covered literature, two new PBA derivatives were studied with unique synthesis and derivatization processes using the introduced derivatization strategies.

- Potassium-free and potassium-rich copper iron sulfide were derived for the first time by using H_2S gas. This procedure showed a much shorter time and lower temperatures for mixed-metal sulfide derivatization compared to the reported use of sulfur powder. A treatment time of 10 min at 300 °C resulted in successful sulfidation. Furthermore, an in-situ coating process was carried out during synthesis by applying polydopamine as a carbonaceous precursor. It was shown that this coating decreases the particle size and stabilizes potassium in the lattice, however, at the same time, it hinders sulfur loss during cycling and improves the capacity stability.
- Additionally, iron vanadium oxide was derived for the first time using CO_2 gas. The use of this gas resulted in a homogeneous mixed-metal oxide of vanadium and iron. The choice of the right electrolyte and molarity decreased the vanadium etching and full stabilization was achieved by using surfactants during the synthesis. By following the concentration of the remained metals in the synthesis solution and thermogravimetric analysis, the order and type of effective surfactant were determined.

In addition to the obtained knowledge in the derivatization, two different design strategies were used to create hybrids of metal oxides and it was analyzed how they interact with the

materials composition. CNTs can be employed as a substrate for growth of PBA to create a self-standing electrode and in parallel act as a conductive carbon network between the active material particles. On the other hand, using continuous fibers for self-standing electrodes by electrospinning can be a great strategy for free-standing electrode preparation made of 100% active material and omitting the slurry preparation step, the use of binders, and organic solvents, while at the same time hybridizing the active material with carbon or add other additives in the electrospinning mixture to create a functional composite. The free-standing electrode is reliant on its inherent mechanical properties since it lacks the presence of a binder. Therefore, great care needs to be taken during the synthesis and heat-treatment in order to keep the electrodes easy to handle between each step.

- FeV-CNT composite was synthesized in one step by adding the FeV-PBA precursors to CNT powder. Optimization in the amount of CNT powder in relation to the PBA and surfactant precursor resulted in a homogeneous composite preparation. The composite was also used directly for heat-treatment and by choosing a low oxidizing atmosphere, successful derivatization was carried out while maintaining the design strategy. This resulted in the preparation of self-standing electrode upon filtration in ethanol.
- Free-standing fiber morphology was used to prepare vanadium oxide/carbon hybrid electrodes without the need for slurry preparation. Electrospinning was carried out with and without the use of a carbon powder additive. Subsequent heat treatment under different conditions was carried out as well to analyze the effect of processing parameters on the electrochemical performance and mechanical flexibility. Self-standing electrodes were bent to half of their height until cracking and full failure. In the case of self-standing electrodes, a direct correlation with the electrochemical performance and mechanical flexibility of the electrodes was observed. Higher temperatures, which are commonly preferred for powder electrodes to increase material crystallinity or carbon conductivity, are harmful for self-standing electrodes as they increase the brittleness and loss of conductive paths in the electrode. Therefore, for self-standing electrodes processing parameters are not to be only chosen based on their effect on composition, but also on mechanical properties.

Complementary to the presented results and gained knowledge in design and derivatization, further steps in tuning the electrode and electrolyte interphase were

covered to create a holistic overview of the materials engineering in the Li-based batteries for their main components of electrodes and electrolyte. Separate engineering of the electrode interface at the electrolyte can improve the overall cell performance without compromising the electrode performance or composition. In many cases, this is carried out by applying an artificial layer between the electrode and electrolyte to stabilize their contact interface. This could act as an SEI on the anode side or a protective coating for active materials that are prone to dissolution and etching by electrolyte. Coating via an additional step such as atomic layer deposition, which provides a nanoscale and homogeneous layer is an example of this. Of course, the coating application can be carried out simultaneously during the synthesis or processing of the electrode material. In the presented work on the iron-vanadium oxide from the FeV PBA for example, different surfactants are used to this end. As the particles resulting from the processing are under 20 nm in diameter, they are extensively prone to side reactions during cycling or the dissolution of their active redox metal, in this case, highly soluble vanadium. The used surfactant, if chosen and applied correctly, transforms into a stable coating during the heat-treatment.

The main conclusions and the continuation of the work can be summarized below:

- Although PBAs offer great potential as a functional template due to their water-based synthesis, tunable chemistry and morphology, and easy derivatization, many PBAs and their derivatization are unexplored. In this work, CuFe for derivatization of mixed metal sulfide and FeV for derivatization of mixed metal oxide were studied and it was observed, that for these new derivatives, tuning of the materials composition and morphology is not similar to that of PB or commonly reported PBAs such as CoFe. In the case of CuFe, for example, the use of polydopamine did not only result in coating formation but also affected the synthesis and stabilizing of potassium in the PBA structure.
- For FeV, the use of surfactants also was shown to be dependent on the order in which they are added to the metal salts. So far, these surfactants were mainly reported to successfully tune the morphology and size, but for more complex PBAs such as FeV with high solubility, the use of PVP surfactant caused the dissolution of the PBA by strong bonding to the present metals. Further research is needed in this regard to understand how different PBAs respond to changes in synthesis

parameters. The use of CO₂ and H₂S can also be a great tool to derive new chemistries which were not attainable by using sulfur powder and oxygen gas. This would then enable more complex derivatizations from ternary and quaternary PBAs and their successful derivatization for use in energy storage.

- In electrospun fibers we observed the take on materials design needs to be more holistic rather than focused on the morphology alone. For electrospun fibers, this was observed in the effect of processing parameters on the mechanical properties. The role of different solution properties and electrospinning parameters needs to be revisited with a focus on their effect on the mechanical properties of the electrode. This enables the use of the electrospinning method on a larger scale to produce free-standing electrodes.

6 ABBREVIATIONS

CEI	cathode electrolyte interphase
DEC	diethyl carbonate
DMC	dimethyl carbonate
DMSO	dimethyl sulfoxide
EVs	electric vehicles
EOL	end of life
EMC	ethyl methyl carbonate
EC	ethylene carbonate
EU	European union
HOMO	highest occupied molecular orbital
SHE	hydrogen electrode
LCO	lithium cobalt oxide
LFP	lithium iron phosphate
LMO	lithium manganese oxide
NCA	lithium nickel cobalt aluminum oxide
NMC	lithium nickel manganese cobalt oxide
NMO	lithium nickel manganese oxide
LNO	lithium nickel oxide
LUMO	lowest unoccupied molecular orbital
NMP	N-methyl-2-pyrrolidone
PVdF	polyvinylidene fluoride
PBA	Prussian blue analog
SEI	solid electrolyte interphase
TEP	triethyl phosphate

7 REFERENCES

1. Ritchie, H., M. Roser, and P. Rosado. *CO₂ and greenhouse gas emissions*. 2020; Available from: <https://ourworldindata.org/co2-and-greenhouse-gas-emissions>.
2. Kawamura, H., et al. *Frontier technology issues: lithium-ion batteries: a pillar for a fossil fuel-free economy*. 2021; Available from: <https://www.un.org/development/desa/dpad/publication/frontier-technology-issues-lithium-ion-batteries-a-pillar-for-a-fossil-fuel-free-economy/>.
3. Mitali, J., S. Dhinakaran, and A. Mohamad, *Energy storage systems: A review*. Energy Storage and Saving, 2022.
4. Bhutada, G. *Breaking down the cost of an EV battery cell*. 2022.
5. Intelligence, B.M. *Lithium-ion battery cell prices fall to \$110/kWh, but raw material risk looms large*. 2020.
6. McKinsey. *Battery 2030: Resilient, sustainable, and circular*. 2023 [cited 2023; Available from: <https://www.mckinsey.com/industries/automotive-and-assembly/our-insights/battery-2030-resilient-sustainable-and-circular>.
7. IEA. *Key World Energy Statistics 2020*. 2020; Available from: <https://www.iea.org/reports/key-world-energy-statistics-2020>.
8. Benjamin, P., *The voltaic cell: its construction and its capacity*. 1893: J. Wiley.
9. Cotti, P., *The discovery of the electric current*. Physica B: Condensed Matter, 1995. **204**(1-4): p. 367-369.
10. Ruetschi, P., *Review on the lead—acid battery science and technology*. Journal of Power Sources, 1977. **2**(1): p. 3-120.
11. Dănilă, E. and D.D. Lucache. *History of the first energy storage systems*. in *Paper delivered at the 3rd International Symposium on the History of Electrical Engineering and of Tertiary-Level Engineering Education*. 2010.
12. Roser, M. *Technology over the long run: Zoom out to see how dramatically the world can change within a lifetime*. 2023; Available from: <https://ourworldindata.org/technology-long-run>.
13. Kurzweil, P., *Gaston Planté and his invention of the lead—acid battery—The genesis of the first practical rechargeable battery*. Journal of Power Sources, 2010. **195**(14): p. 4424-4434.
14. Pavlov, D., *Lead-acid batteries: Science and technology*. 2011: Elsevier.
15. Putois, F., *Market for nickel-cadmium batteries*. Journal of Power Sources, 1995. **57**(1-2): p. 67-70.
16. Jeyaseelan, C., et al., *Ni-Cd Batteries*. Rechargeable Batteries: History, Progress, and Applications, 2020: p. 177-194.
17. Blumbergs, E., et al., *Cadmium recovery from spent Ni-Cd batteries: a brief review*. Metals, 2021. **11**(11): p. 1714.
18. Lourenssen, K., et al., *Vanadium redox flow batteries: A comprehensive review*. Journal of Energy Storage, 2019. **25**: p. 100844.
19. Kumar, D., et al., *Progress and prospects of sodium-sulfur batteries: A review*. Solid State Ionics, 2017. **312**: p. 8-16.
20. Winter, M. and R.J. Brodd, *What are batteries, fuel cells, and supercapacitors?* Chemical Reviews, 2004. **104**(10): p. 4245-4270.
21. Li, M., et al., *30 years of lithium-ion batteries*. Advanced Materials, 2018. **30**(33): p. 1800561.

22. Whiting, K. *This is why 'polycrisis' is a useful way of looking at the world right now*. World Economic Forum Annual Meeting 2023; Available from: <https://www.weforum.org/agenda/2023/03/polycrisis-adam-tooze-historian-explains/>.
23. Wigley, T., *The Paris warming targets: emissions requirements and sea level consequences*. Climatic Change, 2018. **147**: p. 31-45.
24. Rechsteiner, R., *German energy transition (Energiewende) and what politicians can learn for environmental and climate policy*. Clean Technologies and Environmental Policy, 2021. **23**: p. 305-342.
25. Belaid, F., A. Al-Sarihi, and R. Al-Mestneer, *Balancing climate mitigation and energy security goals amid converging global energy crises: The role of green investments*. Renewable Energy, 2023. **205**: p. 534-542.
26. IEA. *Share of electricity generation from unabated fossil fuels 2021*. 2023; Available from: <https://www.iea.org/fuels-and-technologies/electricity>.
27. Bhutada, G. *Visualizing the scale of global fossil fuel production*. 2023; Available from: <https://www.visualcapitalist.com/visualizing-the-scale-of-global-fossil-fuel-production/>.
28. Wetzel, D. *Jede Stunde Blackout kostet 600 Millionen Euro*. 2013; Available from: <https://www.welt.de/wirtschaft/article121265359/Jede-Stunde-Blackout-kostet-600-Millionen-Euro.html>.
29. Bundesnetzagentur, *Kennzahlen Der Versorgungsunterbrechungen Strom*. 2017.
30. Xie, J. and Y.-C. Lu, *A retrospective on lithium-ion batteries*. Nature Communications, 2020. **11**(1): p. 2499.
31. Ziegler, M.S., J. Song, and J.E. Trancik, *Determinants of lithium-ion battery technology cost decline*. Energy & Environmental Science, 2021. **14**(12): p. 6074-6098.
32. Castelvechi, D. and E. Stoye. *Chemistry Nobel Honours World-changing Batteries*, . Nature 2019.
33. Whittingham, M.S., *History, evolution, and future status of energy storage*. Proceedings of the IEEE, 2012. **100**(Special Centennial Issue): p. 1518-1534.
34. Cao, X., *Important factors for the reliable and reproducible preparation of non-aqueous electrolyte solutions for lithium batteries*. Communications Materials, 2023. **4**(1): p. 10.
35. Korthauer, R., *Lithium-ion batteries: basics and applications*. 2018: Springer.
36. Fuller, T.F. and J.N. Harb, *Electrochemical engineering*. 2018: John Wiley & Sons.
37. Manthiram, A., *A reflection on lithium-ion battery cathode chemistry*. Nature Communications, 2020. **11**(1): p. 1550.
38. Asenbauer, J., et al., *The success story of graphite as a lithium-ion anode material—fundamentals, remaining challenges, and recent developments including silicon (oxide) composites*. Sustainable Energy & Fuels, 2020. **4**(11): p. 5387-5416.
39. Xu, K., *Navigating the minefield of battery literature*. Communications Materials, 2022. **3**(1): p. 31.
40. Whittingham, M.S., *Lithium batteries and cathode materials*. Chemical Reviews, 2004. **104**(10): p. 4271-4302.
41. Goodenough, J.B. and Y. Kim, *Challenges for rechargeable Li batteries*. Chemistry of Materials, 2010. **22**(3): p. 587-603.
42. Li, J., C. Daniel, and D. Wood, *Materials processing for lithium-ion batteries*. Journal of Power Sources, 2011. **196**(5): p. 2452-2460.
43. Heidrich, B., et al., *Comparative x-ray photoelectron spectroscopy study of the SEI and CEI in three different lithium ion cell formats*. Journal of the Electrochemical Society, 2022. **169**(3): p. 030533.
44. Manthiram, A., *An outlook on lithium ion battery technology*. ACS Central Science, 2017. **3**(10): p. 1063-1069.

45. Goodenough, J.B. and K.-S. Park, *The Li-ion rechargeable battery: a perspective*. Journal of the American Chemical Society, 2013. **135**(4): p. 1167-1176.
46. Simon, P., Y. Gogotsi, and B. Dunn, *Where do batteries end and supercapacitors begin?* Science, 2014. **343**(6176): p. 1210-1211.
47. Spahr, M.E., et al., *Development of carbon conductive additives for advanced lithium ion batteries*. Journal of Power Sources, 2011. **196**(7): p. 3404-3413.
48. Saal, A., T. Hagemann, and U.S. Schubert, *Polymers for battery applications—active materials, membranes, and binders*. Advanced Energy Materials, 2021. **11**(43): p. 2001984.
49. Wu, M., et al., *Toward an ideal polymer binder design for high-capacity battery anodes*. Journal of the American Chemical Society, 2013. **135**(32): p. 12048-12056.
50. Nguyen, V.A. and C. Kuss, *Conducting polymer-based binders for lithium-ion batteries and beyond*. Journal of the Electrochemical Society, 2020. **167**(6): p. 065501.
51. Wang, G., M. Yu, and X. Feng, *Carbon materials for ion-intercalation involved rechargeable battery technologies*. Chemical Society Reviews, 2021. **50**(4): p. 2388-2443.
52. Selim, R. and P. Bro, *Some observations on rechargeable lithium electrodes in a propylene carbonate electrolyte*. Journal of the Electrochemical Society, 1974. **121**(11): p. 1457.
53. Sargent, P. and M. Ashby, *Deformation mechanism maps for alkali metals*. Scripta Metallurgica, 1984. **18**(2): p. 145-150.
54. Jana, A., et al., *Electrochemomechanics of lithium dendrite growth*. Energy & Environmental Science, 2019. **12**(12): p. 3595-3607.
55. Zachman, M.J., et al., *Cryo-STEM mapping of solid–liquid interfaces and dendrites in lithium-metal batteries*. Nature, 2018. **560**(7718): p. 345-349.
56. Besenhard, J. and G. Eichinger, *High energy density lithium cells: Part I. Electrolytes and anodes*. Journal of Electroanalytical Chemistry and Interfacial Electrochemistry, 1976. **68**(1): p. 1-18.
57. Whittingham, M.S., *Electrical energy storage and intercalation chemistry*. Science, 1976. **192**(4244): p. 1126-1127.
58. Mizushima, K., et al., *Li_xCoO₂ (0 < x < 1): A new cathode material for batteries of high energy density*. Materials Research Bulletin, 1980. **15**(6): p. 783-789.
59. Amatucci, G., J. Tarascon, and L. Klein, *CoO₂, the end member of the Li_xCoO₂ solid solution*. Journal of The Electrochemical Society, 1996. **143**(3): p. 1114.
60. Mauler, L., et al., *Technological innovation vs. tightening raw material markets: Falling battery costs put at risk*. Energy Advances, 2022. **1**(3): p. 136-145.
61. Zou, H., et al., *A novel method to recycle mixed cathode materials for lithium ion batteries*. Green Chemistry, 2013. **15**(5): p. 1183-1191.
62. Nitta, N., et al., *Li-ion battery materials: present and future*. Materials Today, 2015. **18**(5): p. 252-264.
63. Lee, S., et al., *Carbon-coated single-crystal LiMn₂O₄ nanoparticle clusters as cathode material for high-energy and high-power lithium-ion batteries*. Angewandte Chemie, 2012. **124**(35): p. 8878-8882.
64. Camargos, P.H., et al., *Perspectives on Li-ion battery categories for electric vehicle applications: A review of state of the art*. International Journal of Energy Research, 2022. **46**(13): p. 19258-19268.
65. Hannan, M.A., et al., *State-of-the-art and energy management system of lithium-ion batteries in electric vehicle applications: Issues and recommendations*. IEEE Access, 2018. **6**: p. 19362-19378.

66. Li, S. and B.C. Church, *Electrochemical stability of aluminum current collector in aqueous rechargeable lithium-ion battery electrolytes*. Journal of Applied Electrochemistry, 2017. **47**: p. 839-853.
67. Frith, J.T., M.J. Lacey, and U. Ulissi, *A non-academic perspective on the future of lithium-based batteries*. Nature Communications, 2023. **14**(1): p. 420.
68. Ponrouch, A. and M.R. Palacín, *Post-Li batteries: Promises and challenges*. Philosophical Transactions of the Royal Society A, 2019. **377**(2152): p. 20180297.
69. Corey, P. *NIST guide to the SI, Chapter 4: The Two Classes of SI Units and the SI Prefixes*. 2016.
70. Greenwood, M., et al., *The Battery Component Readiness Level (BC-RL) framework: A technology-specific development framework*. Journal of Power Sources Advances, 2022. **14**: p. 100089.
71. Brito, M.C., et al., *Sustainable energy systems in an imaginary island*. Renewable and Sustainable Energy Reviews, 2014. **37**: p. 229-242.
72. Liu, Y., Y. Zhu, and Y. Cui, *Challenges and opportunities towards fast-charging battery materials*. Nature Energy, 2019. **4**(7): p. 540-550.
73. Billaud, J., et al., *Magnetically aligned graphite electrodes for high-rate performance Li-ion batteries*. Nature Energy, 2016. **1**(8): p. 1-6.
74. Diederichsen, K.M., E.J. McShane, and B.D. McCloskey, *Promising routes to a high Li⁺ transference number electrolyte for lithium ion batteries*. ACS Energy Letters, 2017. **2**(11): p. 2563-2575.
75. Buss, H.G., et al., *Nonaqueous polyelectrolyte solutions as liquid electrolytes with high lithium ion transference number and conductivity*. ACS Energy Letters, 2017. **2**(2): p. 481-487.
76. Ziegler, M.S. and J.E. Trancik, *Re-examining rates of lithium-ion battery technology improvement and cost decline*. Energy & Environmental Science, 2021. **14**(4): p. 1635-1651.
77. IEA. *Average pack price of lithium-ion batteries and share of cathode material cost, 2011-2021*. 2022 [cited 2023; Available from: <https://www.iea.org/data-and-statistics/charts/average-pack-price-of-lithium-ion-batteries-and-share-of-cathode-material-cost-2011-2021>].
78. OECD, *Security of supply for critical raw materials vulnerabilities and areas for G7 coordination*, in *G7 Leaders' Summit 26-28 June 2022 Schloss Elmau*. 2022.
79. Keersemaeker, M., *Suriname Revisited: Economic Potential of its Mineral Resources*. 2020. 69-82.
80. Mauger, A. and C. Julien, *Critical review on lithium-ion batteries: Are they safe? Sustainable?* Ionics, 2017. **23**: p. 1933-1947.
81. Shahid, S. and M. Agelin-Chaab, *A review of thermal runaway prevention and mitigation strategies for lithium-ion batteries*. Energy Conversion and Management: X, 2022: p. 100310.
82. Hu, L., et al., *Crushing behaviors and failure of packed batteries*. International Journal of Impact Engineering, 2020. **143**: p. 103618.
83. Chen, M., et al., *Performance and safety protection of internal short circuit in lithium-ion battery based on a multilayer electro-thermal coupling model*. Applied Thermal Engineering, 2019. **146**: p. 775-784.
84. Leising, R.A., et al., *Abuse testing of lithium-ion batteries: Characterization of the overcharge reaction of LiCoO₂/graphite cells*. Journal of the Electrochemical Society, 2001. **148**(8): p. A838.
85. Chen, Y., et al., *A review of lithium-ion battery safety concerns: The issues, strategies, and testing standards*. Journal of Energy Chemistry, 2021. **59**: p. 83-99.

86. Liu, K., et al., *Materials for lithium-ion battery safety*. Science Advances, 2018. **4**(6): p. eaas9820.
87. Shen, X., et al., *The underlying mechanism for reduction stability of organic electrolytes in lithium secondary batteries*. Chemical Science, 2021. **12**(26): p. 9037-9041.
88. Lux, S., et al., *The mechanism of HF formation in LiPF₆ based organic carbonate electrolytes*. Electrochemistry Communications, 2012. **14**(1): p. 47-50.
89. Ohzuku, T., et al., *Comparative study of LiCoO₂, LiNi₁₂Co₁₂O₂ and LiNiO₂ for 4 volt secondary lithium cells*. Electrochimica Acta, 1993. **38**(9): p. 1159-1167.
90. Dahn, J., et al., *Thermal stability of Li_xCoO₂, Li_xNiO₂ and λ-MnO₂ and consequences for the safety of Li-ion cells*. Solid State Ionics, 1994. **69**(3-4): p. 265-270.
91. Yang, S., et al., *Reactivity, stability and electrochemical behavior of lithium iron phosphates*. Electrochemistry Communications, 2002. **4**(3): p. 239-244.
92. Larcher, D. and J.-M. Tarascon, *Towards greener and more sustainable batteries for electrical energy storage*. Nature Chemistry, 2015. **7**(1): p. 19-29.
93. Vassilev, S.V., et al., *An overview of the chemical composition of biomass*. Fuel, 2010. **89**(5): p. 913-933.
94. Lee, M., et al., *Redox cofactor from biological energy transduction as molecularly tunable energy-storage compound*. Angewandte Chemie International Edition, 2013. **52**(32): p. 8322-8328.
95. Recham, N., M. Armand, and J.-M. Tarascon, *Novel low temperature approaches for the eco-efficient synthesis of electrode materials for secondary Li-ion batteries*. Comptes Rendus Chimie, 2010. **13**(1-2): p. 106-116.
96. Tarascon, J.-M., et al., *Hunting for better Li-based electrode materials via low temperature inorganic synthesis*. Chemistry of Materials, 2010. **22**(3): p. 724-739.
97. Yuan, C., et al., *Manufacturing energy analysis of lithium ion battery pack for electric vehicles*. CIRP Annals, 2017. **66**(1): p. 53-56.
98. Liu, H., et al., *Advanced electrode processing of lithium ion batteries: A review of powder technology in battery fabrication*. Particuology, 2021. **57**: p. 56-71.
99. Ahmed, S., et al., *Energy impact of cathode drying and solvent recovery during lithium-ion battery manufacturing*. Journal of Power Sources, 2016. **322**: p. 169-178.
100. Wang, M., et al., *Lithium Ion Battery Electrodes Made Using Dimethyl Sulfoxide (DMSO)—A Green Solvent*. ACS Sustainable Chemistry & Engineering, 2020. **8**(30): p. 11046-11051.
101. Chen, C., et al., *Investigating TEP as a greener alternative to NMP in Ni-rich cathode fabrication*. Journal of Energy Chemistry, 2023. **78**: p. 240-245.
102. Lu, Y., et al., *Dry electrode technology, the rising star in solid-state battery industrialization*. Matter, 2022. **5**(3): p. 876-898.
103. Shahjalal, M., et al., *A review on second-life of Li-ion batteries: prospects, challenges, and issues*. Energy, 2022. **241**: p. 122881.
104. Martinez-Laserna, E., et al., *Battery second life: Hype, hope or reality? A critical review of the state of the art*. Renewable and Sustainable Energy Reviews, 2018. **93**: p. 701-718.
105. Börner, M.F., et al., *Challenges of second-life concepts for retired electric vehicle batteries*. Cell Reports Physical Science, 2022. **3**(10).
106. Cao, Y., et al., *Bridging the academic and industrial metrics for next-generation practical batteries*. Nature Nanotechnology, 2019. **14**(3): p. 200-207.
107. Dunn, J., et al., *The significance of Li-ion batteries in electric vehicle life-cycle energy and emissions and recycling's role in its reduction*. Energy & Environmental Science, 2015. **8**(1): p. 158-168.
108. Xiao, J., et al., *From laboratory innovations to materials manufacturing for lithium-based batteries*. Nature Energy, 2023: p. 1-11.

109. Liu, C., Z.G. Neale, and G. Cao, *Understanding electrochemical potentials of cathode materials in rechargeable batteries*. *Materials Today*, 2016. **19**(2): p. 109-123.
110. Manthiram, A., *Electrical energy storage: materials challenges and prospects*. *MRS Bulletin*, 2016. **41**: p. 624-631.
111. Hertzberg, B., A. Alexeev, and G. Yushin, *Deformations in Si–Li anodes upon electrochemical alloying in nano-confined space*. *Journal of the American Chemical Society*, 2010. **132**(25): p. 8548-8549.
112. Grimaud, A., *Batteries: Beyond intercalation and conversion*. *Nature Energy*, 2017. **2**(2): p. 1-2.
113. Wu, F. and G. Yushin, *Conversion cathodes for rechargeable lithium and lithium-ion batteries*. *Energy & Environmental Science*, 2017. **10**(2): p. 435-459.
114. Arico, A.S., et al., *Nanostructured materials for advanced energy conversion and storage devices*. *Nature Materials*, 2005. **4**(5): p. 366-377.
115. Manthiram, A., Y. Fu, and Y.-S. Su, *Challenges and prospects of lithium–sulfur batteries*. *Accounts of Chemical Research*, 2013. **46**(5): p. 1125-1134.
116. Yu, X.Y. and X.W. Lou, *Mixed metal sulfides for electrochemical energy storage and conversion*. *Advanced Energy Materials*, 2018. **8**(3): p. 1701592.
117. Hannah, D.C., et al., *On the balance of intercalation and conversion reactions in battery cathodes*. *Advanced Energy Materials*, 2018. **8**(20): p. 1800379.
118. Zhang, L., et al., *Triggering the in situ electrochemical formation of high capacity cathode material from MnO*. *Advanced Energy Materials*, 2017. **7**(8): p. 1602200.
119. Manthiram, A. and J. Goodenough, *Lithium insertion into Fe₂(SO₄)₃ frameworks*. *Journal of Power Sources*, 1989. **26**(3-4): p. 403-408.
120. Padhi, A., et al., *Effect of structure on the Fe³⁺/Fe²⁺ redox couple in iron phosphates*. *Journal of the Electrochemical Society*, 1997. **144**(5): p. 1609.
121. Wang, Q., et al., *A shuttle effect free lithium sulfur battery based on a hybrid electrolyte*. *Physical Chemistry Chemical Physics*, 2014. **16**(39): p. 21225-21229.
122. Mikhaylik, Y.V. and J.R. Akridge, *Polysulfide shuttle study in the Li/S battery system*. *Journal of the Electrochemical Society*, 2004. **151**(11): p. A1969.
123. Bornamehr, B., V. Presser, and S. Husmann, *Mixed Cu–Fe sulfides derived from polydopamine-coated prussian blue analogue as a lithium-ion battery electrode*. *ACS Omega*, 2022. **7**(43): p. 38674-38685.
124. Liu, Y., et al., *Nanostructured metal chalcogenides confined in hollow structures for promoting energy storage*. *Nanoscale Advances*, 2020. **2**(2): p. 583-604.
125. Cui, L.-F., et al., *Crystalline-amorphous core–shell silicon nanowires for high capacity and high current battery electrodes*. *Nano Letters*, 2009. **9**(1): p. 491-495.
126. Li, X., et al., *Electrospinning-based strategies for battery materials*. *Advanced Energy Materials*, 2021. **11**(2): p. 2000845.
127. Lu, W., et al., *Core-shell materials for advanced batteries*. *Chemical Engineering Journal*, 2019. **355**: p. 208-237.
128. Hu, L. and Q. Chen, *Hollow/porous nanostructures derived from nanoscale metal–organic frameworks towards high performance anodes for lithium-ion batteries*. *Nanoscale*, 2014. **6**(3): p. 1236-1257.
129. Yang, S., P.Y. Zavalij, and M.S. Whittingham, *Hydrothermal synthesis of lithium iron phosphate cathodes*. *Electrochemistry Communications*, 2001. **3**(9): p. 505-508.
130. Li, J., et al., *Microwave solid-state synthesis of spinel Li₄Ti₅O₁₂ nanocrystallites as anode material for lithium-ion batteries*. *Solid State Ionics*, 2007. **178**(29-30): p. 1590-1594.
131. Xu, Y., et al., *Prussian blue and its derivatives as electrode materials for electrochemical energy storage*. *Energy Storage Materials*, 2017. **9**: p. 11-30.

132. Bornamehr, B., et al., *Prussian blue and its analogues as functional template materials: control of derived structure compositions and morphologies*. Journal of Materials Chemistry A, 2023.
133. Liu, N., et al., *A pomegranate-inspired nanoscale design for large-volume-change lithium battery anodes*. Nature Nanotechnology, 2014. **9**(3): p. 187-192.
134. Hu, M., J.-S. Jiang, and Y. Zeng, *Prussian blue microcrystals prepared by selective etching and their conversion to mesoporous magnetic iron (III) oxides*. Chemical Communications, 2010. **46**(7): p. 1133-1135.
135. Zhang, W., et al., *Synthesis of monocrystalline nanoframes of prussian blue analogues by controlled preferential etching*. Angewandte Chemie International Edition, 2016. **55**(29): p. 8228-8234.
136. Devaraju, M.K. and I. Honma, *Hydrothermal and solvothermal process towards development of LiMPO₄ (M= Fe, Mn) nanomaterials for lithium-ion batteries*. Advanced Energy Materials, 2012. **2**(3): p. 284-297.
137. Singh, I. and R. Bedi, *Surfactant-assisted synthesis, characterizations, and room temperature ammonia sensing mechanism of nanocrystalline CuO*. Solid State Sciences, 2011. **13**(11).
138. Torres-Rodríguez, J., et al., *Titania hybrid carbon spherogels for photocatalytic hydrogen evolution*. Carbon, 2023. **202**: p. 487-494.
139. Gu, D. and F. Schüth, *Synthesis of non-siliceous mesoporous oxides*. Chemical Society Reviews, 2014. **43**(1): p. 313-344.
140. Koopmann, A.-K., et al., *Tannin-based nanoscale carbon spherogels as electrodes for electrochemical applications*. ACS Applied Nano Materials, 2021. **4**(12): p. 14115-14125.
141. Salihovic, M., et al., *Monolithic carbon spherogels as freestanding electrodes for supercapacitors*. ACS Applied Energy Materials, 2021. **4**(10): p. 11183-11193.
142. Poolakkandy, R.R. and M.M. Menampambath, *Soft-template-assisted synthesis: a promising approach for the fabrication of transition metal oxides*. Nanoscale Advances, 2020. **2**(11): p. 5015-5045.
143. Aravindan, V., et al., *Electrospun nanofibers: A prospective electro-active material for constructing high performance Li-ion batteries*. Chemical Communications, 2015. **51**(12): p. 2225-2234.
144. Xue, J., et al., *Electrospinning and electrospun nanofibers: Methods, materials, and applications*. Chemical Reviews, 2019. **119**(8): p. 5298-5415.
145. Taylor, G.I., *Disintegration of water drops in an electric field*. Proceedings of the Royal Society of London. Series A. Mathematical and Physical Sciences, 1964. **280**(1382): p. 383-397.
146. Tucker, N., et al., *The History of the Science and Technology of Electrospinning from 1600 to 1995*. Journal of Engineered Fibers and Fabrics, 2012. **7**(2_suppl): p. 155892501200702S10.
147. Zeleny, J., *The discharge of electricity from pointed conductors*. Physical Review (Series I), 1908. **26**(2): p. 129.
148. Zeleny, J., *The discharge of electricity from pointed conductors differing in size*. Physical Review (Series I), 1907. **25**(5): p. 305.
149. Zeleny, J., *The influence of humidity upon the electrical discharge from points in air*. Physical Review (Series I), 1908. **26**(6): p. 448.
150. Zeleny, J., *Instability of electrified liquid surfaces*. Physical Review, 1917. **10**(1): p. 1.
151. Zhao, Y., et al., *Electrospun nanofiber electrodes for lithium-ion batteries*. Macromolecular Rapid Communications, 2023. **44**(4): p. 2200740.
152. Xue, J., et al., *Electrospun nanofibers: New concepts, materials, and applications*. Accounts of Chemical Research, 2017. **50**(8): p. 1976-1987.

153. Koski, A., K. Yim, and S. Shivkumar, *Effect of molecular weight on fibrous PVA produced by electrospinning*. Materials Letters, 2004. **58**(3-4): p. 493-497.
154. Bornamehr, B., et al., *Mechanically stable, binder-free, and free-standing vanadium trioxide/carbon hybrid fiber electrodes for lithium-ion batteries*. Advanced Sustainable Systems, 2023. **7**(2): p. 2200373.
155. Zhang, T., et al., *Free-Standing, Foldable V₂O₃/Multichannel Carbon Nanofibers Electrode for Flexible Li-Ion Batteries with Ultralong Lifespan*. Small, 2020. **16**(47): p. 2005302.
156. Wen, X., et al., *Al₂O₃ coating on Li_{1.256}Ni_{0.198}Co_{0.082}Mn_{0.689}O_{2.25} with spinel-structure interface layer for superior performance lithium ion batteries*. Electrochimica Acta, 2018. **260**: p. 549-556.
157. Yu, X. and A. Manthiram, *Electrode–electrolyte interfaces in lithium–sulfur batteries with liquid or inorganic solid electrolytes*. Accounts of Chemical Research, 2017. **50**(11): p. 2653-2660.
158. Wang, J., et al., *Surface-engineered mesoporous silicon microparticles as high-Coulombic-efficiency anodes for lithium-ion batteries*. Nano Energy, 2019. **61**: p. 404-410.
159. Kim, N.Y., et al., *Recent advances in nanoengineering of electrode-electrolyte interfaces to realize high-performance Li-ion batteries*. Energy & Environmental Materials, 2023: p. e12622.
160. Kim, K., et al., *Cyclic aminosilane-based additive ensuring stable electrode–electrolyte interfaces in Li-ion batteries*. Advanced Energy Materials, 2020. **10**(15): p. 2000012.
161. Cheong, J.Y., et al., *High-rate formation cycle of Co₃O₄ nanoparticle for superior electrochemical performance in lithium-ion batteries*. Electrochimica Acta, 2019. **295**: p. 7-13.
162. Kasse, R.M., et al., *Combined effects of uniform applied pressure and electrolyte additives in lithium-metal batteries*. ACS Applied Energy Materials, 2022. **5**(7): p. 8273-8281.